

**Dissertation**

submitted to the  
Combined Faculty of Mathematics, Engineering and Natural Sciences  
of Heidelberg University, Germany  
for the degree of  
Doctor of Natural Sciences

Put forward by  
**Theodora Xylakis-Dornbusch**  
born in Hamburg, Germany

Oral examination: 09.07.2024



---

**Investigation of the Galactic chemical  
enrichment history with searches for and  
chemical abundance analysis of  
metal-poor stars**

---

*Referees:*

Prof. Dr. rer. nat. Norbert CHRISTLIEB

Prof. Dr. Saskia HEKKER



“Διατήρησε το δικαίωμα σου να σκέφτεσαι, ακόμη και αν σκέφτεσαι λανθασμένα είναι καλύτερο από το να μην σκέφτεσαι καθόλου”

Υπατία η Αλεξανδρινή

*“Reserve your right to think, for even to think wrongly is better than not to think at all”*

Hypatia of Alexandria

# Abstract

This PhD dissertation presents a method for the identification of metal-poor stars with *Gaia* BP/RP spectra. The metal-poor star selection method is based on flux ratios and was developed with *Gaia* BP/RP simulated synthetic spectra. In follow-up work the selection method was updated and applied to *Gaia* DR3 BP/RP spectra with  $E(B - V) \leq 1.5$ . Furthermore, 26 metal-poor candidates were selected for observations, of which 100% had  $[\text{Fe}/\text{H}] < -2.0$ , 57% had  $[\text{Fe}/\text{H}] < -2.5$ , and 8% had  $[\text{Fe}/\text{H}] < -3.0$ . Finally, a catalog of stellar metallicities for 10 861 062 stars was assembled. Moreover, a kinematic analysis and a 1D LTE abundance analysis of limited- $r$  stars was conducted. In addition, the lanthanide mass fractions ( $X_{La}$ ) of all the to date known limited- $r$  stars were calculated and compared to that of the KN AT2017gfo. The results showed that the abundance patterns of the neutron-capture elements of limited- $r$  stars are different depending on whether  $[\text{Ba}/\text{Eu}]$  is below or above  $-0.3$ . Also, the  $X_{La}$  of the KN was found to be higher than the  $X_{La}$ 's of the limited- $r$  stars and in the transition region between the latter and the  $X_{La}$ 's of the  $r$ -I and  $r$ -II stars. Finally, the current sample of limited- $r$  stars is largely born in the Galaxy rather than being accreted.



# Zusammenfassung

Diese Dissertation stellt eine Methode zur Identifizierung metallarmer Sterne mit *Gaia* BP/RP Spektren vor. Die Auswahlmethode dieser Sterne basiert auf Flussverhältnissen und wurde mit simulierten synthetischen *Gaia* BP/RP Spektren entwickelt. In der Folgearbeit wurde die Methode aktualisiert und auf *Gaia* DR3 BP/RP Spektren mit  $E(B - V) \leq 1.5$  angewendet. Darüber hinaus wurden 26 metallarme Kandidaten für Beobachtungen ausgewählt. Davon hatten 100%  $[\text{Fe}/\text{H}] < -2.0$ , 57%  $[\text{Fe}/\text{H}] < -2.5$ , und 8%  $[\text{Fe}/\text{H}] < -3.0$ . Schließlich wurde ein Katalog der Sternmetallizitäten für 10 861 062 Sterne zusammengestellt. Im Weiteren wurde eine kinematische Analyse und eine 1D-LTE-Häufigkeitsanalyse von limited- $r$  Sternen durchgeführt. Zusätzlich wurden die Massenanteile der Lanthanoide ( $X_{La}$ ) aller bisherigen bekannten limited- $r$  Sterne berechnet. Diese wurden mit dem  $X_{La}$  der Kilonova AT2017gfo verglichen. Die Ergebnisse zeigten, dass sich die Häufigkeitsmuster der Neutroneneinfanglemente von den limited- $r$  Sternen unterscheiden, je nachdem, ob  $[\text{Ba}/\text{Eu}]$  unter oder über  $-0.3$  liegt. Außerdem wurde festgestellt, dass der  $X_{La}$  der Kilonova höher ist als der  $X_{La}$  der limited- $r$  Sterne und im Übergangsbereich zwischen letzterem und den  $X_{La}$  der  $r$ -I- und  $r$ -II Sterne liegt. Letztendlich ergab sich, dass die aktuelle Stichprobe von limited- $r$  Sternen größtenteils in der Galaxie geboren ist.



# Contents

<b>Abstract</b>	<b>v</b>
<b>Zusammenfassung</b>	<b>v</b>
<b>1 Introduction</b>	<b>1</b>
1.1 The early Universe	1
1.2 The Milky Way	1
1.3 Metal-poor stars	2
1.4 <i>Gaia</i> BP/RP spectra	3
1.5 Categories of metal-poor stars	6
1.5.1 CEMP stars	6
1.5.2 Neutron-capture signatures	6
1.5.3 <i>r</i> -I and <i>r</i> -II stars	8
1.5.4 Limited- <i>r</i> stars	8
1.6 <i>r</i> -process nucleosynthesis and fission cycling	10
1.6.1 <i>r</i> -process sites and the lanthanide mass fraction	11
<b>2 Methods</b>	<b>13</b>
2.1 Stellar parameters and abundance analysis	13
2.1.1 Model Atmosphere	13
non-LTE	14
2.1.2 Radiative transfer	15
2.1.3 Continuum and line opacities	16
2.1.4 Stellar parameter determination	18
2.1.5 Determination of elemental-abundances	18
Atomic data	20
2.2 Ulysses Simulator	20
2.3 Kinematic analysis	21
2.4 Calculation of the lanthanide mass fractions	24
<b>3 A method for identifying metal-poor stars with <i>Gaia</i> BP/RP spectra</b>	<b>27</b>
<b>4 Metallicities for more than 10 million stars derived from <i>Gaia</i> BP/RP spectra</b>	<b>39</b>
<b>5 The <i>R</i>-Process Alliance: Analysis of Limited-<i>r</i> Stars</b>	<b>49</b>
<b>6 Discussion</b>	<b>65</b>
6.1 Caveat of the selection method	65
6.2 Metal-poor stars in the Galactic bulge	67
6.3 Kinematics of $r_{lim}$ stars	68
6.4 J2140 and the Sequoia accretion event	68
6.5 $X_{La}$ of the $r_{lim}$ stars	70

<b>7 Outlook</b>	<b>71</b>
<b>8 Summary</b>	<b>73</b>
<b>A The effect of extinction on the flux-ratios and selection of the blending fraction <math>\beta</math>.</b>	<b>77</b>
<b>B Additional data on the abundance analysis and kinematics of the sample and literature <math>r_{lim}</math> stars.</b>	<b>81</b>
<b>Bibliography</b>	<b>91</b>
<b>Acknowledgements</b>	<b>101</b>
<b>Declaration of Authorship</b>	<b>103</b>

# List of Figures

1.1	Anatomy of the Milky Way galaxy. Image adopted from K. Brauer. . .	2
1.2	Redshift $z$ versus metallicity of damped Lyman- $\alpha$ systems. . . . .	3
1.3	<i>Gaia</i> focal plane. . . . .	4
1.4	<i>Gaia</i> CCD. . . . .	5
1.5	The abundance universality in the $r$ -process abundances of RPE stars, as shown by Roederer et al., 2022. The scaled Solar residual $r$ -process pattern (red line) is also plotted. Top panel: in the top the light $r$ -process elements are scaled to Zr, and in the bottom the dispersions of the $\log \epsilon(X/Zr)$ abundance ratios are shown. Bottom panel: as in the top, but here the heavy elements are scaled to Eu, and the dispersions of the $\log \epsilon(X/Eu)$ abundance ratios are shown. Figure is adopted from Roederer et al., 2022. . . . .	9
1.6	The abundance difference between Solar and $r$ -process stars. The limited- $r$ star HD 122563 exhibits clearly a neutron-capture element abundance pattern that is gradually decreasing with increasing atomic number. Figure adopted from Cowan et al., 2021. . . . .	10
1.7	$X_{La}$ from $r$ -process site models. Model L17 from Lippuner et al., 2017, W16 from Wu et al., 2016, S18 from Siegel, Barnes, and Metzger, 2019, N15 from Nishimura, Takiwaki, and Thielemann, 2015, and E15 from Eichler et al., 2015. Figure adopted from Ji, Drout, and Hansen, 2019. . .	12
2.1	Left panel: Equivalent width of an absorption line. Figure adopted from Trypsteen and Walker, 2017. Right panel: The curve of growth. . .	19
6.1	$\chi^2$ test. . . . .	66
A.1	Ratio of the flux-ratios post- and pre-dereddening. The effect of reddening has a greater impact on the $fr_{G/CaNIR}$ flux-ratio compared to the $fr_{CaHK/Hfi}$ . This would be expected, since the Calcium Near Infrared Triplet (Ca NIR) is located far more in the red than the other components of the flux-ratios, and is thus much less affected by extinction. . . . .	77
A.2	Blending fraction $\beta$ versus the metallicity of the stars selected from Cutoff2. A significant fraction of false positives, with $[Fe/H] < -1$ , are found to have large values of the blending fraction $\beta$ . . . . .	78
A.3	Selection of the maximum value of the blending fraction $\beta$ for the quality cut purpose. The $\beta$ of the minimum contamination for stars at and below the metallicity shown on the x-axis, is shown in the left panel. In the right panel we calculated the difference between the completeness achieved with the $\beta$ from the left plot, and the maximum possible completeness at the same metallicity bin. All stars were selected through Cutoff1. . . . .	78

A.4 Completeness, success rate and contamination of the stars that were selected from below Cutoff1 (left panel) and Cutoff2 (right panel). The stars were selected from a reddened flux-ratio plane, i.e. no dereddening was performed. . . . . 79

# List of Tables

1.1	Nomenclature for of the different metal-poor star regimes. . . . .	6
1.2	Sub-classes of CEMP stars. . . . .	7
1.3	Metal-poor stars with neutron-capture signatures. . . . .	8
B.6	Line information. . . . .	81
B.1	Uncertainties for the abundances of J003859+272551 due to the uncertainties in stellar parameters. . . . .	85
B.2	Uncertainties for the abundances of J20313531 due to the uncertainties in stellar parameters. . . . .	86
B.3	Uncertainties for the abundances of J21402305 due to the uncertainties in stellar parameters. . . . .	87
B.4	Inferred orbital parameters for the $r_{lim}$ stars. $R_{max}$ is the projection of the apocenter of the orbit on the Galactic plane $R_{max} = \sqrt{r_{ap}^2 - Z_{max}^2}$ , and $IA = \arctan(Z_{max}/R_{max})$ . . . . .	88
B.5	Mean uncertainties of the inferred orbital parameters for the $r_{lim}$ stars. . . . .	89



# List of Abbreviations

<b>1D</b>	<b>One-Dimensional</b>
<b>2D</b>	<b>Two-Dimensional</b>
<b>3D</b>	<b>Three-Dimensional</b>
<b>AC</b>	<b>ACross scan</b>
<b>AGB</b>	<b>Asymptotic Giant Branch</b>
<b>AL</b>	<b>ALong scan</b>
<b>BB</b>	<b>Big Bang</b>
<b>BH</b>	<b>Black Hole</b>
<b>BP</b>	<b>Blue Photometer</b>
<b>CCDs</b>	<b>Charge-Coupled Devices</b>
<b>CCSN</b>	<b>Core-Collapse Supernova</b>
<b>CEMP</b>	<b>Carbon Enhanced Metal Poor</b>
<b>DEC</b>	<b>DEClination</b>
<b>DR</b>	<b>Data Release</b>
<b>EMP</b>	<b>Extremely Metal Poor</b>
<b>EW</b>	<b>Equivalent Width</b>
<b>FoV</b>	<b>Field of View</b>
<b>GC</b>	<b>Galactic Center</b>
<b>GSE</b>	<b>Gaia-Sausage-Enceladus</b>
<b>HES</b>	<b>Hamburg ESO Survey</b>
<b>hfs</b>	<b>hyperfine structure</b>
<b>IS</b>	<b>Isotopic Shifts</b>
<b>KN</b>	<b>KiloNova</b>
<b>LAMOST</b>	<b>Large Sky Area Multi-Object Spectroscopic Telescope</b>
<b>LEPP</b>	<b>Light Element Primary Process</b>
<b>LSF</b>	<b>Line Spread Function</b>
<b>LTE</b>	<b>Local Thermodynamic equilibrium</b>
<b>MR</b>	<b>Magneto-Rotational</b>
<b>MW</b>	<b>Milky Way</b>
<b>NIR</b>	<b>Near-InfraRed</b>
<b>NLTE</b>	<b>Non-Local Thermodynamic equilibrium</b>
<b>NS</b>	<b>Neutron Star</b>
<b>PIGS</b>	<b>Pristine Inner Galaxy Survey</b>
<b>PopII</b>	<b>Population III</b>
<b>RA</b>	<b>Right Ascension</b>
<b>RPA</b>	<b>R-Process Alliance</b>
<b>RPE</b>	<b>R-Process Enhanced</b>
<b>RP</b>	<b>Red Photometer</b>
<b>SMSS</b>	<b>SkyMapper Southern Sky survey</b>
<b>SNe</b>	<b>Supernovae</b>
<b>SNR</b>	<b>Signal-to-Noise Ratio</b>
<b>TDI</b>	<b>Time Delay Integration</b>

<b>UV</b>	<b>UltraViolet</b>
<b>VMP</b>	<b>Very Metal Poor</b>

Αυτό το πόνημα είναι αφιερωμένο στον Ίωνα και στην μητέρα μου.



# Chapter 1

## Introduction

### 1.1 The early Universe

The world as we know it today started, as is the accepted consensus to date, with an explosion known as the Big Bang (BB). Shortly after, the first elements formed, namely H, He, and Li. The first stars formed a few hundred million years after the BB, at about  $z \approx 30$  (Klessen and Glover, 2023), setting forth the forging of the heavier elements - "metals" - via nuclear fusion in the stellar interiors and during the end of life explosions of the stars. However, element species such as  ${}^6\text{Li}$ ,  ${}^9\text{Be}$  and  ${}^{10}\text{B}$ , were exclusively formed via cosmic ray spallation (Vangioni-Flam and Cassé, 1999).

### 1.2 The Milky Way

The Milky Way is a spiral – possibly barred – galaxy, and is the second most massive member of the Local Group, containing several hundred billion stars. Its structure consists of a disk, a bulge, and a stellar halo. The disk is divided into three components: the thin-disk which has a scale height of about 300 pc, the thick-disk with a scale height of about 900 pc, and the metal-weak thick-disk, which is a vertical extension of the thick-disk. The Galactic center (GC), where a supermassive ( $\sim 4 \times 10^6 M_\odot$ ) black hole resides, is surrounded by a luminous dense region with ongoing star formation, the bulge. In the disk and the bulge – which are old structures – young stars are mostly found. It is believed though, that some of the most ancient stars could still reside there, because the MW should have formed from the inside out (Diemand, Madau, and Moore, 2005; Tumlinson, 2009). Howes et al., 2015 found EMP stars in the bulge, as did Reggiani et al., 2020. A part of the ongoing *Pristine* survey is dedicated to the study of the inner Galaxy, namely the *Pristine Inner Galaxy Survey* (PIGS) Arentsen et al., 2020b. With the use of data from the *Gaia* Survey (see Section 1.4), Rix et al., 2022 found an ancient metal-poor population ( $-2.7 < [\text{M}/\text{H}] < -1.5$ ) that has a Gaussian extent of only  $\sigma_{\text{GC}} \sim 2.7$  kpc around the GC.

Furthermore, the disk and bulge structures are surrounded by the stellar halo, which exhibits a far lower stellar density. The stars found in the halo are predominantly older – most of the metal-poor stars are found there – and they are either found single or in binaries (field stars). In the halo reside also globular clusters and satellite dwarf galaxies which orbit the MW. The disruption of some dwarf galaxies from the gravitational pull of the MW is manifested in stellar streams that span across the sky. An example of such a disruption is the Sagittarius Stream, which starts in the homonymous dwarf galaxy and extends throughout the halo. Finally, the halo extends to more than 100 kpc away from the GC.

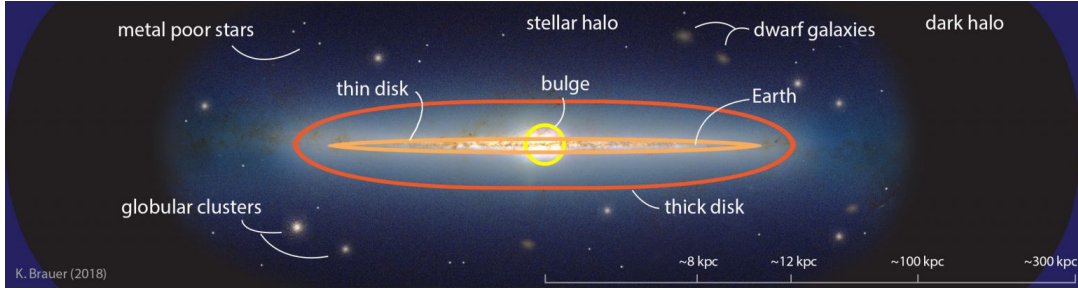


FIGURE 1.1: Anatomy of the Milky Way galaxy. Image adopted from K. Brauer.

### 1.3 Metal-poor stars

The knowledge of BB nucleosynthesis and the pioneering work of Burbidge et al., 1957 and Cameron, 1957, supported the concept that stars deficient in metals (elements heavier than He) are old. The idea is, that the surface of the star generally retains the chemical make-up of the gas cloud from which it formed. Hence, a star that was born from a metal-free cloud – Population III (PopIII) stars – should be void of metals, that is, nothing but H, He, and Li should be observable in the stellar spectrum. Therefore, the discovery and thorough study of metal-poor stars grants us a glimpse into the past, that gives us evidence to reconstruct the evolutionary path of the stars, including their chemical enrichment history, learn about their birth-places, deduce information pertaining to chemical-enrichment channels, and also learn about the history of Galaxy formation and assembly.

In order to determine whether the amount of metals in the stellar atmosphere of a star is low, we compare it to the Sun. Specifically, the relative abundance of an element X in a star is

$$[X/H] = \log \left( \frac{N_X}{N_H} \right)_* - \log \left( \frac{N_X}{N_H} \right)_\odot \quad (1.1)$$

where  $N_X, N_H$  are the number densities of atoms of element X and of H, respectively. Astronomers tend to use the Fe abundance (Fe instead of all elements heavier than He) as a proxy for the metal content (metallicity) in the atmosphere of a star. Rafelski et al., 2012 showed that the cosmic metallicity decreases with increasing redshift up to  $z \sim 5$ , which corroborates the idea that metal-poor stars are old. Further, it shows that studying stars with very low Fe content, is equivalent to studying stars at high redshifts (Frebel and Norris, 2013). Since the discovery of metal-poor stars in the beginning of the second half of the twentieth century, many surveys have been dedicated to their search. The HK objective-prism survey of Beers, Preston, and Shtetman (Beers, Preston, and Shtetman, 1985; Beers, Preston, and Shtetman, 1992) and the Hamburg/ESO survey (HES) (Christlieb et al., 2008) were among the first large surveys for metal-poor stars. Recent surveys of metal-poor stars are the Large Sky Area Multi-Object Spectroscopic Telescope (LAMOST) survey (Zhao, 2005), the SkyMapper Southern Sky survey (SMSS) (Wolf et al., 2018), and the *Pristine* survey (Starkenburg et al., 2017).

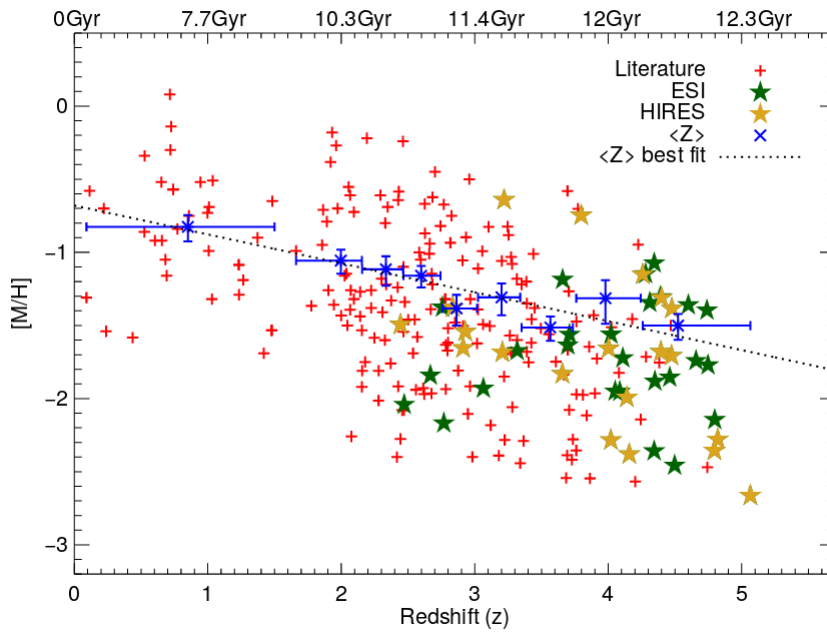


FIGURE 1.2: Redshift versus DLA metal abundance  $[M/H]$ . Figure adopted from Rafelski et al. 2012.

## 1.4 *Gaia* BP/RP spectra

In 2013 the European Space Agency (ESA) launched a space mission called *Gaia* (Gaia Collaboration et al., 2016), in order to do a full sky survey of all the objects brighter than  $G = 20.7$  mag. Since then, the Gaia Collaboration has done four data releases (DR1, DR2, EDR3, and DR3) providing to the community astrometric, kinematic, photometric, and spectrophotometric data for more than 1.4 billion sources. Specifically, the kinematic and astrometric data include parallaxes, positions, proper motions, and radial velocities which have helped astronomers paint a more detailed picture of how the Galaxy assembled, for example by tracing accretion events (for example the *Gaia*-Sausage-Enceladus (GSE) event; Belokurov et al., 2018; Helmi et al., 2018).

The spectrophotometric data for more than 219 million stars with  $9 < G \leq 21.43$  mag were released to the public in 2022 as part of *Gaia* DR3 (Gaia Collaboration et al., 2023; De Angeli et al., 2023). These data present a unique opportunity to look for new metal-poor stars. Therefore, extensive work was carried out by the author of this dissertation for the development of a method to find new metal-poor stars with *Gaia* BP/RP spectra.

The low-resolution spectra were taken by the on board *Gaia* slitless blue and red photometers (BP and RP, respectively). In order to complete a full sky survey, the *Gaia* satellite is spinning around itself. The satellite has two telescopes (two fields of view; FoV), so when *Gaia* is spinning the sources are scanned first by the leading FoV and then – after 106 min – by the second one. However, the light collected by both FoV is projected on a common focal plane where two different rows of charge-coupled devices (CCDs) are located, the BP and RP. Each row of CCDs – namely, BP and RP – consists of 7 CCDs, and each CCD has 4500 pixels in the along scan (AL) direction (which is the transit direction) and 1966 pixels in the across scan (AC) direction (the direction perpendicular to AL). A schematic representation of both the

focal plane and CCDs are shown in Figures 1.3 and 1.4, respectively. Further, the incoming light is being dispersed by two different slitless prisms before it is recorded by the BP and RP CCDs. The wavelength range covered by both BP and RP is different, which is also the case for the spectral dispersion due to wavelength dependence. Particularly, the wavelength range and spectral dispersion for BP are 330-680 nm and 3 to 27 nm/pixel, respectively, and 640-1050 nm and 7 to 15 nm/pixel, respectively, for RP. The resolving power  $R = \frac{\lambda}{\Delta\lambda}$  of the spectra is less than 100, and it depends on wavelength and position on the focal plane.

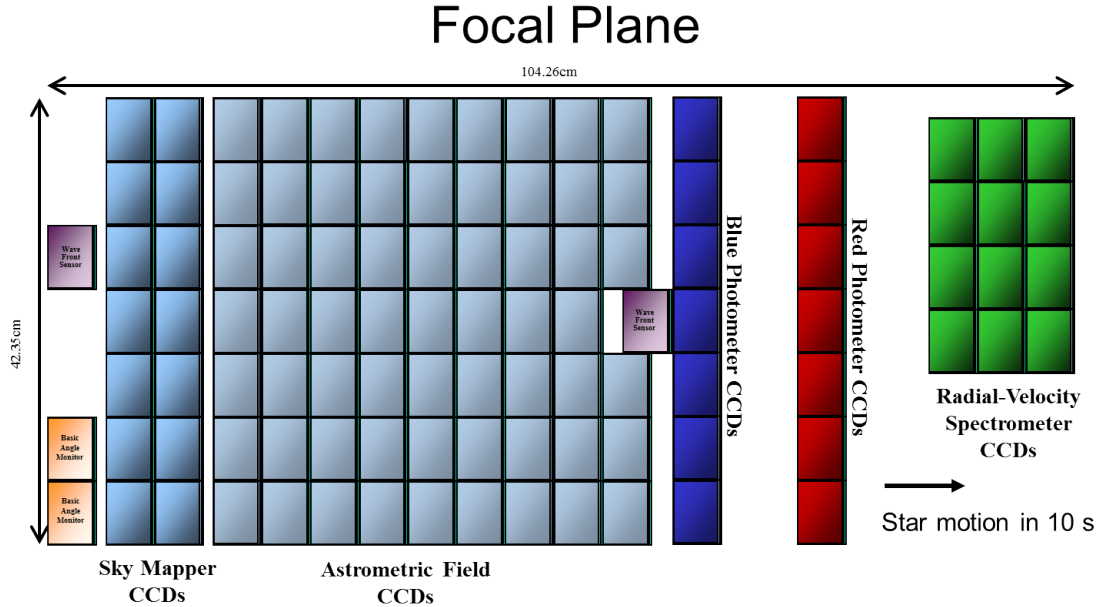


FIGURE 1.3: *Gaia* focal plane. Figure adopted from ESA.

As already mentioned, the satellite is spinning and as a result each object's image is transiting the focal plane during the observation. For that reason, the CCDs are operating in a mode called time delay integration (TDI). This means that each recorded image is being read continuously at a given rate instead of being read at the end of a predetermined exposure time (as usually done during observations). The reading rate is such, that the light collected by each CCD is integrated during the transit over that same CCD, which results in a maximum CCD transit time (or exposure time) of 4.4 seconds (Carrasco et al., 2021). For each transit only a selected window of pixels around the detected light is being downloaded and integrated. This window has a size of  $60 \times 12$  pixels. The download of the pixels in that window produces a two-dimensional (2D) spectrum which is – for sources with  $G \geq 11.5$  mag – subsequently collapsed to a one-dimensional (1D) spectrum through the binning of the 12 pixels in the AC direction.

The integration of the flux that is recorded by BP and RP is also included in the released *Gaia* data, constituting the magnitude in these bands, namely  $G_{BP}$  and  $G_{RP}$ , respectively. The *Gaia*  $G$  magnitude is obtained from the flux integration of the astrometric field CCDs.

Further, transits of sources that are part of binaries or that are located in crowded regions of the sky, can be affected by blending. This effect can be significant for the  $G_{BP}$  and  $G_{RP}$  magnitudes, because the window of the pertinent flux acquisition is large, whereas for the  $G$  magnitude – for which the data is being collected from a window that is 12 or 18 pixels wide – it is negligible. Riello et al., 2021 proposed

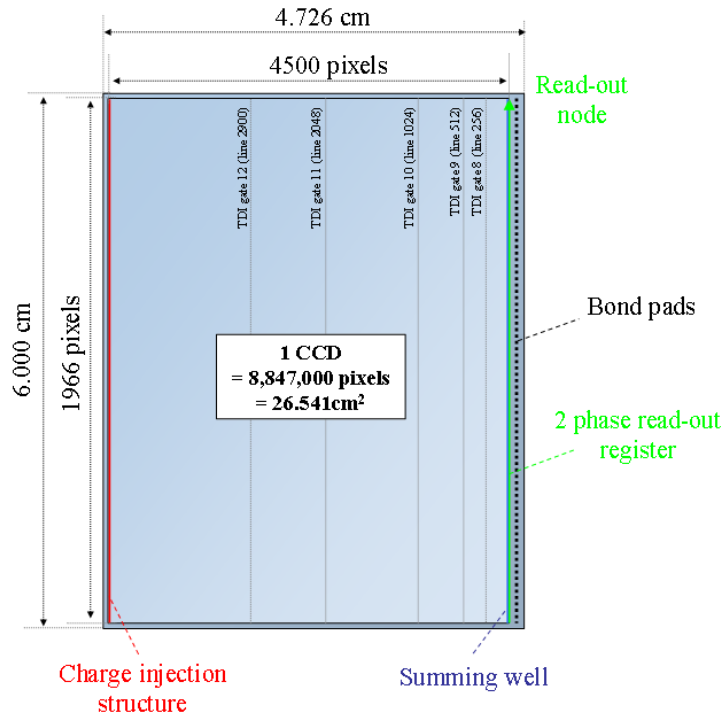


FIGURE 1.4: *Gaia* CCD. Figure adopted from ESA.

a metric of quality for the BP and RP photometry that accounts for blending, the blending fraction  $\beta$ . This is defined by Riello et al., 2021 as the sum of the number of blended transits in BP and RP divided by the sum of the number of observations in BP and RP. Or, in terms of *Gaia* DR3 archive spectroscopic tables,

$$\beta = \frac{(\text{bp\_n\_blended\_transits} + \text{rp\_n\_blended\_transits})}{(\text{bp\_n\_transits} + \text{rp\_n\_transits})}$$

Riello et al., 2021 note, however, two caveats. First,  $\beta = 0.0$  does not mean that a source is not affected by blending, because *Gaia* might not be able to resolve a close-by source. Secondly, a  $\beta > 0$  should not always be taken at face value, because the flux ratio of the target source to the blending source is not considered in the blending fraction, which for example can mean that the blending source might be too faint to effect the flux of the target source.

The *Gaia* BP/RP spectra that were released with DR3 do not come in the common format of a spectrum. Particularly, the raw data from the satellite – which were collected as described above – were processed, so that for each source, the data of multiple transits (all the epoch spectra) were combined into a single mean spectrum (internally calibrated spectrum; Carrasco et al. 2021; De Angeli et al. 2023). These mean spectra were calibrated to a self-consistent mean instrument, that is, they were brought onto a common flux and pixel (pseudo-wavelength) scale. Subsequently, a calibration of the internally calibrated spectra to the absolute reference system of physical flux and wavelength was done (externally calibrated spectra; Montegriffo et al. 2023). The data products that were delivered to the community were the expansion coefficients and respective covariance matrices, separately, for BP and RP internally and externally calibrated spectra. For details on how to access the BP/RP

spectra see De Angeli et al., 2023 and Montegriffo et al., 2023.

## 1.5 Categories of metal-poor stars

The degree in which a metal-poor star is deficient in Fe – compared to the Sun – brings about various metal-poor regimes. The nomenclature, which was proposed by Beers and Christlieb, 2005 and extended by Frebel, 2018, is presented in Table 1.1. However, the metal-content deficiency of these stars, is not their only interesting trait. Many metal poor stars show various chemical abundance signatures, which can facilitate the understanding and exploration of the different heavy element nucleosynthesis channels, as well as the chemical evolution history of the Milky Way (MW) and its satellite dwarf galaxies.

TABLE 1.1: Nomenclature for of the different metal-poor star regimes.

Term	Metallicity	Acronym
Super metal-rich	$[\text{Fe}/\text{H}] > +0.5$	SMR
Solar	$[\text{Fe}/\text{H}] \sim 0.0$	—
Metal-poor	$[\text{Fe}/\text{H}] < -1.0$	MP
Very metal-poor	$[\text{Fe}/\text{H}] < -2.0$	VMP
Extremely metal-poor	$[\text{Fe}/\text{H}] < -3.0$	EMP
Ultra metal-poor	$[\text{Fe}/\text{H}] < -4.0$	UMP
Hyper metal-poor	$[\text{Fe}/\text{H}] < -5.0$	HMP
Mega metal-poor	$[\text{Fe}/\text{H}] < -6.0$	MMP
Septa metal-poor	$[\text{Fe}/\text{H}] < -7.0$	SMP
Octa metal-poor	$[\text{Fe}/\text{H}] < -8.0$	OMP
Giga metal-poor	$[\text{Fe}/\text{H}] < -9.0$	GMP

### 1.5.1 CEMP stars

Metal-poor stars that are enhanced in C, are called carbon-enhanced metal-poor (CEMP) stars. CEMP stars were first defined by Beers and Christlieb, 2005 as stars with  $[\text{C}/\text{Fe}] \geq +1.0$ . Aoki et al., 2007 redefined the class of CEMP stars by implicating in the categorization the evolutionary stage of the star. Specifically,

$$\begin{aligned}
 [\text{C}/\text{Fe}] > +0.7 \text{ when } \log(L/L_{\odot}) \leq 2.3 \\
 [\text{C}/\text{Fe}] > [+3.0 - \log(L/L_{\odot})] \text{ when } \log(L/L_{\odot}) > 2.3
 \end{aligned}
 \tag{1.2}$$

where  $\log(L/L_{\odot})$  is the ratio of the luminosity of the star compared to that of the Sun. Furthermore, in the case that CEMP stars show an enhancement in heavy elements that are produced via the slow or/and rapid neutron-capture processes, more sub-classes have been determined (Table 1.2; Beers and Christlieb, 2005; Aoki et al., 2007).

### 1.5.2 Neutron-capture signatures

The vast majority of the elements beyond the iron-peak are formed via the slow- and rapid-neutron-capture processes (*s*-process and *r*-process, respectively) (Burbidge et

TABLE 1.2: Sub-classes of CEMP stars.

Carbon-enhanced metal-poor stars	
CEMP-r	CEMP and $[\text{Eu}/\text{Fe}] > +1.0$
CEMP-s	CEMP and $[\text{Ba}/\text{Fe}] > +1.0$ and $[\text{Ba}/\text{Eu}] > +0.5$
CEMP-r/s	CEMP and $0.0 < [\text{Ba}/\text{Eu}] < +0.5$
CEMP-no	CEMP and $[\text{Ba}/\text{Fe}] < 0$

al., 1957; Cameron, 1957). The neutron-capture entails the successive addition of neutrons to a seed, resulting in the formation of heavy elements. The  $s$ -process proceeds with the slow (compared to  $\beta$ -decay) addition of neutrons to an Fe nucleus, producing nuclei near the valley of  $\beta$  stability. It has been well studied, and it occurs in asymptotic giant branch (AGB) stars and massive stars ( $M_* > \sim 10 M_\odot$ ) (for a review see Lugaro et al., 2023). On the other hand, the  $r$ -process – which is fast compared to  $\beta$ -decay – proceeds far away from the valley of  $\beta$  stability. It produces neutron-rich nuclei that are radioactive, and eventually  $\beta$ -decay to the valley of stability. The site(s) of the  $r$ -process are still under investigation, with the exception of neutron star (NS)-NS mergers, which were confirmed as such after the observation of the light curve of the kilonova (KN) AT2017gfo which was compatible with the decay of  $r$ -process material (Smartt et al., 2017). Other candidate sites, that have yet to be confirmed, are fast-rotating massive stars that end their lives as supernovae (SNe) (called collapsars), magneto-rotational (MR) core-collapse supernovae (CCSN), and quark deconfinement SNe (for a recent review see Cowan et al., 2021).

Metal-poor stars that are enhanced in neutron-capture elements and thus show specific abundance signatures, can help us understand better the physics of the heavy element formation sites, as well as the chemical evolution and assembly of the MW. In order to do so, we use the Sun as a comparison. The case is laid out as follows: both  $s$ - and  $r$ -process contribute each, approximately, 50% of elements heavier than Fe in the Solar System, with the first synthesizing most of the Ba (85%) and the second most of Eu (97%). Further, the Solar isotopic abundances have been well studied, due to measurements of the abundances in the Solar spectrum and in meteorites (Lodders, Palme, and Gail, 2009; Asplund et al., 2009). In addition, the  $s$ -process has been studied thoroughly, enabling the calculation of the  $s$ -process fractions (Arlandini et al., 1999; Käppeler et al., 2011; Busso et al., 2021), and then subtracting those from the total Solar isotopic abundances. The residual is assumed to be the  $r$ -process contribution to the total amount of heavy elements in the Solar System. With both the  $s$ - and  $r$ -process contributions at hand, we are able to characterize and study the different neutron-capture signatures that we observe in metal-poor stars (Table 1.3).

However, astronomers have also discovered CEMP and other metal-poor stars whose abundance patterns differ from both the  $s$ - and  $r$ -process patterns. It was long believed that those patterns of the CEMP stars are the result of the superposition of the yields of both nucleosynthesis channels. But, for most of those stars, the models of an intermediate neutron-capture process ( $i$ -process; Cowan and Rose 1977) has been shown to reproduce fairly well the observed abundance distributions (Hempel et al., 2016; Goswami and Goswami, 2020). Nonetheless, Gull et al., 2018 recently showed that the VMP giant star RAVE J0949-1617, is a CEMP  $r/s$  star. RAVE J0949-1617 was possibly formed from a previously  $r$ -process enriched gas cloud, and was then further enriched with C and  $s$ -process material via mass transfer from a more

massive companion.

TABLE 1.3: Metal-poor stars with neutron-capture signatures.

Acronym	Criteria	Signature
<i>r</i> -I	$0.3 \leq [\text{Eu}/\text{Fe}] \leq +0.7$ and $[\text{Ba}/\text{Eu}] < 0.0$	Main <i>r</i> -process
<i>r</i> -II	$[\text{Eu}/\text{Fe}] > +0.7$ and $[\text{Ba}/\text{Eu}] < 0.0$	Main <i>r</i> -process
<i>r</i> -lim	$[\text{Eu}/\text{Fe}] < +0.3$ , $[\text{Sr}/\text{Ba}] > +0.5$ and $[\text{Sr}/\text{Eu}] > 0.0$	Limited- <i>r</i> process
<i>s</i>	$[\text{Ba}/\text{Fe}] > +1.0$ , $[\text{Ba}/\text{Eu}] > +0.5$ and $[\text{Ba}/\text{Pb}] > -1.5$	<i>s</i> -process
<i>r/s</i>	$0.0 < [\text{Ba}/\text{Eu}] < +0.5$ and $-1.0 < [\text{Ba}/\text{Pb}] < -0.5$	<i>r</i> - and <i>s</i> -processes
<i>i</i>	$0.0 < [\text{La}/\text{Eu}] < +0.6$ and $[\text{Hf}/\text{Ir}] \sim +1.0$	<i>i</i> -process

### 1.5.3 *r*-I and *r*-II stars

Metal-poor stars that are enriched in *r*-process elements, are called *r*-process enhanced (RPE) stars, and are divided in the categories of *r*-I and *r*-II stars (Christlieb et al., 2004; Beers and Christlieb, 2005; Frebel, 2018; Holmbeck et al., 2020a), depending on their level of enrichment (see Table 1.3). It has been shown in many studies that the scaled distributions of the *r*-process elemental abundances of RPE stars match very well the Solar residual *r*-process pattern, suggesting that this nucleosynthesis channel is robust. The abundance distributions of RPE stars are typical scaled to match the Solar Eu abundance, since Eu is almost entirely synthesized by the *r*-process. This universality, however, is only observable for elements with  $55 < Z < 73$ , whereas the light neutron-capture elements with  $32 < Z < 56$ , show a large scatter (Snedden, Cowan, and Gallino, 2008). Recently, Roederer et al., 2022 studied the abundances of eight stars that have different degrees of Eu enrichment;  $-0.22 \leq [\text{Eu}/\text{Fe}] \leq +1.32$ . Roederer et al., 2022 did a novelty and scaled the light *r*-process elements Se to Te to Zr, and those with  $Z \geq 56$  to Eu. They found that despite the variations between light and heavy elements, they are not entirely decoupled. Further, the scaling to Zr revealed a universality among the light elements Se, Sr, Y, Zr, Nb, Mo, and Te. However, the star-to-star scatter for Ru, Rh, Pd, and Ag, remained. Lastly, concerning the origin of RPE stars, recent studies of large samples of such stars have shown that a large fraction of the *r*-I and *r*-II stars were probably accreted to the MW (Roederer, Hattori, and Valluri, 2018; Gudin et al., 2021; Shank et al., 2023).

The many open questions concerning the *r*-process nucleosynthesis has sparked, in recent years, the dedicated effort of a team of astronomers around the world, the *R*-Process Alliance (RPA), to find and study more RPE stars (Hansen et al., 2018a; Sakari et al., 2018; Ezzeddine et al., 2020; Holmbeck et al., 2020b). The RPA has discovered, to date, 72 new *r*-II stars, 232 new *r*-I stars, and 42 new limited-*r* stars (see Section 1.5.4).

### 1.5.4 Limited-*r* stars

The ample abundance analyses of metal-poor stars in the literature have not only revealed the universality of the *r*-process pattern, but have also highlighted cases where this universality is not met. Specifically, this observed deviation from the Solar *r*-process residual pattern is manifested by an abundance distribution that is

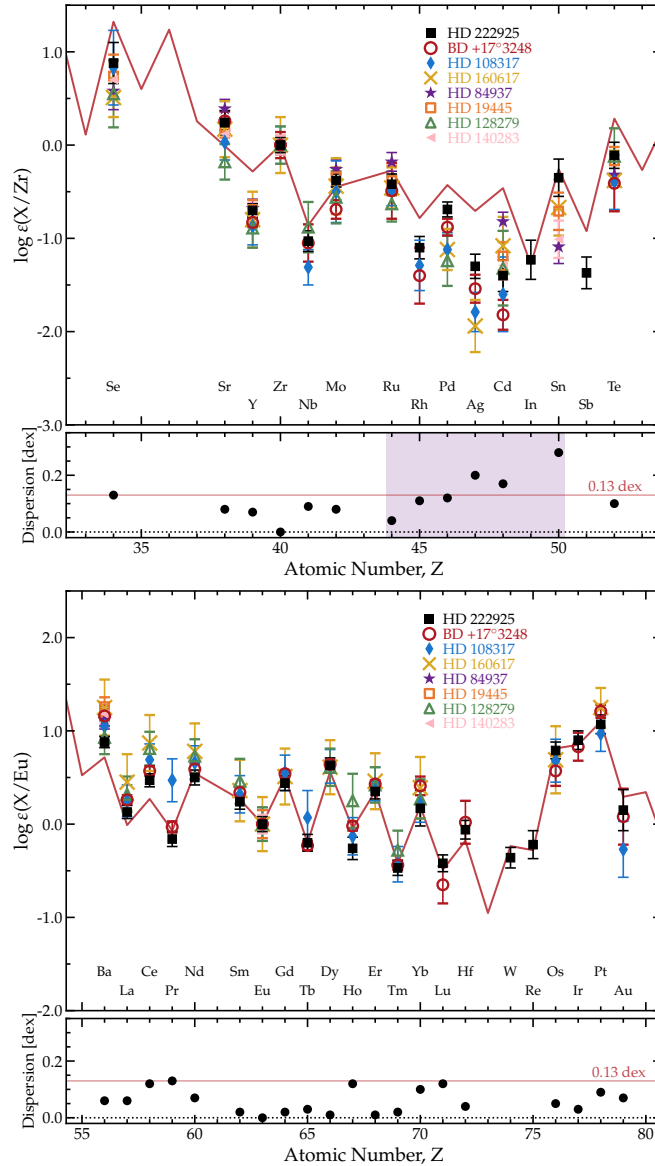


FIGURE 1.5: The abundance universality in the  $r$ -process abundances of RPE stars, as shown by Roederer et al., 2022. The scaled Solar residual  $r$ -process pattern (red line) is also plotted. Top panel: in the top the light  $r$ -process elements are scaled to Zr, and in the bottom the dispersions of the  $\log \epsilon(X/Zr)$  abundance ratios are shown. Bottom panel: as in the top, but here the heavy elements are scaled to Eu, and the dispersions of the  $\log \epsilon(X/Eu)$  abundance ratios are shown. Figure is adopted from Roederer et al., 2022.

decreasing with increasing atomic number. As a result, the scaled abundance pattern of such a star will manifest higher – than the solar pattern – first-peak abundances, while in contrast most stars do not (Frebel, 2018). The first star that was observed with such a signature was HD 122563 (Snedden and Parthasarathy, 1983; Honda et al., 2006; Honda et al., 2007). This variations in the  $r$ -process signatures, along with the scatter in the light elements, led to efforts to explore the possibility of the existence of a secondary  $r$ -process: the weak  $r$ -process (Hansen et al., 2012) or the light element primary process (LEPP) (Travaglio et al., 2004). According to Frebel, 2018, this  $r$ -process should be called limited, due to a limited neutron-capture rate,

which then leads to the observed "truncated"  $r$ -process element production. Possible formation sites for the limited  $r$ -process are electron-capture supernovae (SNe), magneto-rotational (MR) and regular core-collapse supernovae (CCSN), and quark deconfinement SNe (Cowan et al., 2021; Nishimura et al., 2017). The stars that exhibit an abundance signature consistent with the limited  $r$ -process are called limited- $r$  stars ( $r_{lim}$ ).

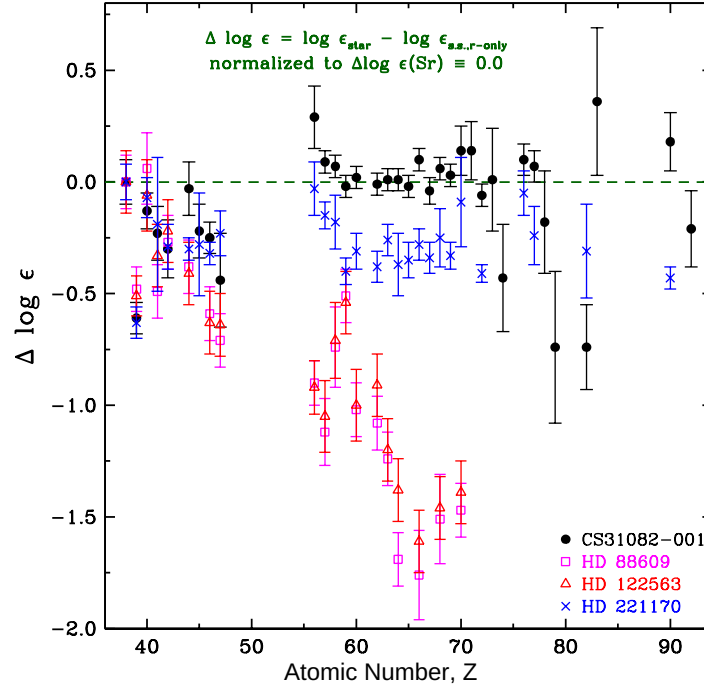


FIGURE 1.6: The abundance difference between Solar and  $r$ -process stars. The limited- $r$  star HD 122563 exhibits clearly a neutron-capture element abundance pattern that is gradually decreasing with increasing atomic number. Figure adopted from Cowan et al., 2021.

## 1.6 $r$ -process nucleosynthesis and fission cycling

As already briefly discussed, the  $r$ -process nucleosynthesis produces about 50% of the elements heavier than Fe, and all the elements heavier than  $^{209}\text{Bi}$ . However, it is still poorly understood, and even though we now know that NSMs are one of the production sites of  $r$ -process elements, it has not been shown that NSMs can account for the  $r$ -process material that is found in the Galaxy. In this context, a part of this dissertation is allocated to the exploration of the origin of the  $r$ -process elements in  $r_{lim}$  stars.

The conditions in which  $r$ -process nucleosynthesis takes place are extreme, since it requires very high temperatures ( $T > 10^9$  K) and neutron densities ( $> 10^{20} \text{cm}^{-3}$ ). So, one of the most important quantities which predicts whether a potential  $r$ -process event is viable, is the electron fraction of the matter involved. This is defined as

$$Y_e \equiv \frac{n_p}{n_n + n_p} \quad (1.3)$$

where  $n_p$  and  $n_n$  are the densities of protons and neutrons, respectively. In normal conditions ordinary matter has usually more protons than neutrons. The condition that is generally required for an *r*-process to take place is  $Y_e < 0.5$ . When the required conditions for an *r*-process are met, seed nuclei capture neutrons while their atomic number  $Z$  remains constant, and as a result their mass number  $A$  changes. Thus, seeds are moving along their isotopic chains by capturing neutrons, and as the number of neutrons increases, the rate of  $\beta$ -decay also increases. On the other hand, as the seeds become more neutron-rich, the capture on neutrons is slowing down. The effect of both the faster  $\beta$ -decay and the slower neutron capture is, that the seed-nuclei will stop capturing neutrons and advance to the next consecutive element, as soon as  $\beta$ -decay is fast enough to challenge the neutron capture (Holmbeck, Sprouse, and Mumpower, 2023). The Solar and RPE metal-poor stars abundance patterns have given us clues as to how the abundance distribution of the final stable nuclei of an *r*-process nucleosynthesis looks like. Specifically, there are three abundance peaks, in the sense that more of some particular elements are being synthesised compared to other elements. These peaks occur at  $Z = 34 - 36$  (first peak),  $Z = 52 - 54$  (second peak), and  $Z = 76 - 78$  (third peak). These peaks are the result of the decay of unstable neutron-rich nuclei that have magic numbers of neutrons.

When an *r*-process produces elements heavier than Pb, the unstable heavy neutron-rich nuclei besides experiencing decay ( $\beta$  or  $\alpha$ ), may also undergo fission, which means that they can split up in two or more fission-fragments. The elements up to the actinides are synthesised via neutron capture and  $\beta$ -decay, but as soon as the nucleosynthesis process takes place at the region of actinides, nuclei can experience spontaneous,  $\beta$ -delayed, and/or neutron-induced fission (see Holmbeck, Sprouse, and Mumpower 2023 for a review). Further, the fission-fragments – once produced – operate within the *r*-process as new seed nuclei and thus continue to capture neutrons, ultimately affecting the final neutron-capture element abundances. A high enough neutron-to-seed ratio can lead to multiple fission cycles, where each time the fission-fragments can capture neutrons until heavy nuclei are formed which then fission again to lighter fragments and so on and so forth. However, it is still not clear which of all the fission channels is more important in shaping the *r*-process nucleosynthesis.

### 1.6.1 *r*-process sites and the lanthanide mass fraction

Thus far, the only observational evidence that we have of *r*-process nucleosynthesis is the KN AT2017gfo which is the electromagnetic counterpart of the gravitational wave event GW170817 (Abbott et al., 2017). Because the *r*-process produces neutron-rich unstable nuclei within 1-2 s, their decay to the valley of stability through  $\beta$ ,  $\alpha$ , and fission decays releases a lot of energy, which can be observed as electromagnetic emission. The study of such an emission in the form of spectra or light curves, can provide us with information about the ejected material and the physical parameters of both the progenitor system and its explosion. Furthermore, the high opacity of the lanthanides, if present, will dominate the opacity of spectra (or light curves), and therefore affect their shape. This was also confirmed by the light curves and spectra of the KN AT2017gfo. On that account, a comparison between the observations and the models can give us information about the presence and amount of lanthanides – and thus *r*-process material – in the spectra (or light curves). Particularly, the calculation and comparison of the lanthanide mass fraction ( $X_{La}$ ) of metal-poor stars, to the  $X_{La}$  of different models, allows us to probe the possible nucleosynthesis channels. Ji, Drout, and Hansen, 2019 present a compilation of  $X_{La}$ 's derived from models of

$r$ -process sites, specifically, models of NSM disk winds and tidal ejecta (Wu et al., 2016; Lippuner et al., 2017; Eichler et al., 2015), collapsar disk winds (Siegel, Barnes, and Metzger, 2019), and magnetorotationally driven jets from SN (Nishimura, Takiwaki, and Thielemann, 2015). They note that all the models have the possibility to reproduce the highest  $X_{La}$  observed in RPE metal-poor stars (see Figure 1.7), however, Ji, Drout, and Hansen, 2019 warn not to make a direct comparison with the metal-poor star  $X_{La}$  distribution due to nuclear data uncertainties and simplifications of the models compared to actual astrophysical events. For more detail see Ji, Drout, and Hansen, 2019. The  $X_{La}$ , as used in this dissertation, is the ratio of the lanthanides to the rest of the  $r$ -process material.

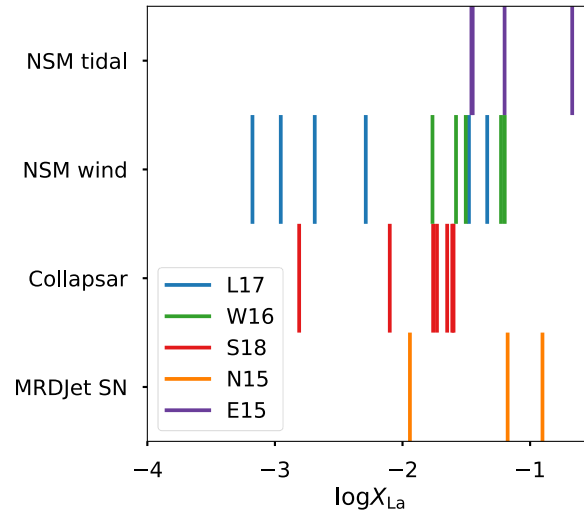


FIGURE 1.7:  $X_{La}$  from  $r$ -process site models. Model L17 from Lippuner et al., 2017, W16 from Wu et al., 2016, S18 from Siegel, Barnes, and Metzger, 2019, N15 from Nishimura, Takiwaki, and Thielemann, 2015, and E15 from Eichler et al., 2015. Figure adopted from Ji, Drout, and Hansen, 2019.

## Chapter 2

# Methods

In this chapter, I shall describe the various tools that I used to conduct the research presented in this thesis. The tools that I used were a simulator of the *Gaia* BP/RP spectra, abundance and kinematic analysis, and I calculated the lanthanide mass fraction of *r*-process stars.

### 2.1 Stellar parameters and abundance analysis

The surface of stellar atmospheres retains, to a large extent, the chemical make-up of the star's birth-cloud. This makes the determination of stellar atmospheric elemental abundances a powerful tool in the investigation of matters ranging from BB nucleosynthesis, to nucleosynthesis channels of heavy elements and Galaxy assembly history.

In order to infer chemical abundances from stellar spectra, one needs to first determine the astrophysical parameters that govern the star, that is, effective temperature ( $T_{\text{eff}}$ ), surface gravity ( $\log g$ ), metallicity ( $[\text{Fe}/\text{H}]$ ), and microturbulent velocity ( $\xi$ ). To achieve that, we need a model of the stellar atmosphere and atomic and molecular data that account for the possible transitions; their cross section (how likely they are to happen) and the energy they require to happen.

#### 2.1.1 Model Atmosphere

A model of a stellar atmosphere is essentially a dataset of all the atmospheric state parameters as a function of depth. This is done by stratifying the atmosphere in a finite number of layers, and by making several assumptions that simplify the task. The assumptions on which a classical 1D local thermodynamic equilibrium (LTE) model atmosphere is based on, are

- the atmosphere is plane parallel, 1D, and thus depends only on the vertical height
- LTE holds
- the atmosphere is in hydrostatic equilibrium
- radiative equilibrium
- there are no sources or sinks of energy
- energy is transported through radiation and convection
- free electron and free heavy particles follow the Maxwell-Boltzmann distribution

- the atmosphere does not depend on time

In the stellar interior we can make the assumption that the collisions of all the particles are random or uncorrelated. Hence, we can describe their distributions – the photons' included – with their most probable macrostate. That means, that they are in thermodynamic equilibrium, and only temperature is needed to describe their state. But, the strict thermodynamic equilibrium is only valid up to a certain boundary, which in the stellar case, is the atmosphere of the star. The reason for this is the nature of the photons (Bosons), which enables them to travel greater distances before interacting (mean free path) and eventually escape the stellar surface. This is manifested by the net radiation transport outside the star. However, we can assume that locally, that is, when small distances are travelled by all gas particles, the temperature is not changing. So, we can assign a temperature to each depth-slab in the star, by assuming that the energy that is created in the center and transverses each slab of constant temperature is conserved (radiative equilibrium). LTE is described by the following distributions:

$$f(\mathbf{v})d\mathbf{v} = \left(\frac{m}{2\pi kT}\right)^{3/2} \exp\left(\frac{-m\mathbf{v}^2}{2kT}\right)d\mathbf{v} \quad (2.1)$$

which is the Maxwell-Boltzmann velocity distribution, and  $m$ ,  $k$ , are the particle mass and Boltzmann constant, respectively. Next,

$$\frac{N_j}{N_i} = \frac{g_j}{g_i} \exp\left[\frac{-(E_j - E_i)}{2kT}\right] \quad (2.2)$$

is the Boltzmann excitation equation.  $N_j, N_i$  are the number of atoms in the energy levels  $E_j, E_i$  with statistical weights  $g_j, g_i$ , respectively. The energy levels are measured from the ground state, and the statistical weights are the number of states with the same energy  $E_{i,j}$ , that is, the degeneracy of the energy states. Lastly, the Saha ionization equation

$$\frac{n_I}{n_{I+1}} = n_e \frac{U_I}{2U_{I+1}} \left(\frac{h^2}{2\pi m k T}\right)^{3/2} \exp\left(\frac{\chi_I}{kT}\right) \quad (2.3)$$

where  $n_I, n_{I+1}$  is the number density ( $n = N/V$ ) of atoms in the ionization state  $I$  and  $I + 1$ , respectively,  $U_{I,I+1}$  are the respective partition functions with  $U = \sum_1^\infty g_i \exp(E_i/kT)$ , and  $\chi_I$  is the ionization potential from state  $I$  to  $I + 1$ . From the ionization equilibrium we can find how the pressure changes with depth. Equations 2.1, 2.2, and 2.3 describe the state of LTE macroscopically, while microscopically LTE is achieved when all processes are in absolute balance with their inverses ( $A \rightleftharpoons B$ ). Further, the assumption of LTE enables us to set the source function  $S_\nu$  equal to the radiation intensity of a black body, that is, the Planck function  $B(\lambda, T) = \frac{2hc^2/\lambda^5}{e^{hc/\lambda kT} - 1}$  where  $h$  is Planck's constant. Finally, in 1D LTE stellar atmosphere models, convection is treated via the mixing-length theory. This theory is essentially describing the convective mean-free path of a gas bubble, that is, the distance it travels until it mixes in with the surroundings. In this study I used 1D LTE model atmospheres.

### non-LTE

The stellar atmospheric model that I described above is based – among other – on the assumption of LTE. The basic assumption for LTE is that the particle collisions set the energy distribution of matter, however, the energy distribution of radiation may

deviate from LTE, but the influence of this non-LTE (NLTE) radiation on the energy distribution of matter is neglected. This can be a fairly well approximation when we deal with the stellar interior, as the mean-free path of photons is small – due to the high density and temperature – compared to the range in which temperature and pressure change. However, close to the stellar surface the existence of the various interactions between radiation and matter – such as stimulated emission, bound-free absorption – become important as the density of matter is low and the mean-free path is greater than the matter’s scale height. As a result, the radiation transition rates dominate the collisional ones, so that the Boltzmann and Saha equations cannot describe anymore the populations of atomic energy levels. Instead, the statistical equilibrium equations are used for the NLTE case. Also, the source function  $S_\nu$  is not anymore described by the Planck function, since the scattering of the photons contributes to the local energy emission, resulting in a dependence of  $S_\nu$  from the radiation field. Consequently, the statistical equilibrium and radiative transfer equations need to be solved simultaneously when NLTE model atmospheres are calculated.

Applying NLTE has several effects, when compared to the LTE counterpart. For example, if the mean intensity  $J_\nu$  of the radiation field is greater than the Planck function  $B_\nu(T_{\text{eff}})$ , that is  $J_\nu > B_\nu(T_{\text{eff}})$ , then over-ionization and over-excitation manifest. This means that the LTE counterpart atmosphere shows the respective excited and ionized states less populated, so the measured abundances from the respective absorption lines will be underestimated. When the opposite happens, that is  $J_\nu < B_\nu(T_{\text{eff}})$ , there is a shortage of ionizations which leads to the net over-recombination to the upper levels, specifically in the infrared. Both effects are manifested in neutral atoms. For a review on the NLTE radiative transfer in cool stars see Bergemann and Nordlander, 2014.

### 2.1.2 Radiative transfer

The stellar atmosphere is the part of a star from which the electromagnetic radiation that an observe can see, is emitted. It’s chemical composition consists mainly of hydrogen (H) and helium (He), while the metals are very sparse. Particularly, astronomers characterize the stellar atmospheres by using the mass fractions  $X$ ,  $Y$ , and  $Z$  of H, He, and metals, respectively, that comprise it. Once again, we use the Sun as a prototype. Asplund, Amarsi, and Grevesse, 2021 report the Solar mass fractions at the surface of the Sun to be  $X = 0.7438 \pm 0.0054$ ,  $Y = 0.2423 \pm 0.0054$ ,  $Z = 0.0139 \pm 0.0006$ .

The energy that is produced in the stellar cores via nuclear fusion, is the one that manifests as light escaping from the stellar surface, which we can observe. But, as a ray makes its way through the stellar interior outwards, its energy will not remain (generally) constant. Absorption or scattering of the radiation, as well as spontaneous emission alter the light that ultimately escapes the stellar atmosphere. The absorption and scattering coefficients result in the extinction coefficient  $\kappa_\nu$ , which is defined as

$$\kappa_\nu = \alpha_\nu + \sigma_\nu \quad (2.4)$$

where  $\alpha$  and  $\sigma$  are the linear absorption and scattering coefficients, respectively. Here we will consider only the absorption coefficient. The spontaneous emission coefficient for an isotropic emitter (or a distribution of randomly oriented emitters) is

$$j_\nu = \frac{P_\nu}{4\pi} \quad (2.5)$$

where  $P_\nu$  is the radiated power per volume and frequency. Now we can define the source function, which is the ratio of the emission coefficient to the absorption coefficient  $S_\nu \equiv \frac{j_\nu}{\alpha_\nu}$ . Further, if the absorption varies with distance, then we can define the optical depth as

$$\tau_\nu = \int_{s_0}^{s_1} \alpha_\nu(s) ds \quad (2.6)$$

$\tau_\nu$  is dimensionless and it describes how opaque an atmosphere is. An optically thick atmosphere (or opaque) has  $\tau > 1$ , while an optically thin (or transparent) atmosphere has  $\tau < 1$ .

We will now consider the specific intensity of the radiation  $I_\nu$ .  $I_\nu$  is defined as the energy of all the rays travelling in a direction that is within a solid angle  $d\Omega$  of the direction of the given ray with frequency  $\nu$ , and that are passing through a surface  $dA$  – which is normal to the direction of all the rays – in time  $dt$

$$I_\nu = \frac{dE}{dAdT d\Omega d\nu} \quad (2.7)$$

The energy that is being radiated through the stellar interior is affected by absorption and emission, but ultimately some of it escapes the surface of the star. The radiation transport can be described by the radiative transfer equation

$$\frac{dI_\nu}{ds} = -\alpha_\nu I_\nu + j_\nu, \quad (2.8)$$

$$\frac{dI_\nu}{d\tau_\nu} = -I_\nu + S_\nu \quad (2.9)$$

Radiation transport, however, is not the only way that energy is being transported through the stellar interior. There is also energy transport through convection, which is the movement of hotter and lighter bubbles of gas upwards, that is replaced by cooler and heavier gas bubbles that sink. Convection will occur when the radiative temperature gradient is greater in magnitude than the adiabatic temperature gradient. That is, when

$$\left| \frac{dT}{dr} \right|_{rad} > \left| \frac{dT}{dr} \right|_{ad} \quad (2.10)$$

When that happens, convection will dominate the energy transport, because it is very efficient. However, near the stellar surface convection is rather inefficient due to the lower – than the stellar interior – density and temperature, and so the mixing-length theory is sufficient in describing the effect convection has on the structure of the stellar atmosphere.

### 2.1.3 Continuum and line opacities

The opacity  $\kappa_\nu$  (or extinction coefficient) in a stellar atmosphere can be the result of a combination of different interactions between the photons and matter. The sources of opacity are

- bound-bound transition: this transition involves the absorption of a photon resulting in an absorption (or emission) line at a specific wavelength. This means that  $\kappa_{\nu,bb}$  is considerable only at wavelengths (or frequencies) that correspond to the energy difference of two atomic levels. The absorption can only take

place when photons have energies in a specific range  $\Delta\nu$  centered on  $\nu_0$  which is the frequency of the transition. These transitions are a source of opacity at discrete wavelengths (line opacity).

- bound-free transition: this is the photo-ionization, where an electron is expelled from the atom after a photon of energy equal or greater than the ionization potential ( $E \geq \chi_\nu$ ) of a specific atomic energy level is absorbed. This is a source of continuum opacity ( $\kappa_{\nu,bf}$ ).
- free-free transition: this transition entails the encounter of a free electron and an ion forming temporarily an unbound system capable of absorbing a photon of any energy. This is also a source of continuum opacity ( $\kappa_{\nu,ff}$ ).
- electron scattering: this is the scattering of photons by free electrons where the energy of the scattered photon remains the same. Electron scattering is independent of wavelength and thus is a source of continuum opacity.

In cool stars the main source of continuum opacity is the photoionization of  $\text{H}^-$  (bound-free transition), because the extra electron in this ion has a low ionization potential of  $0.754 \text{ eV}$ . This energy corresponds to a photon with  $\lambda = 1.64 \mu\text{m}$ , meaning that all the photons with  $\lambda < 1.64 \mu\text{m}$  can ionize  $\text{H}^-$ . In warmer stars (A and B stars) the main sources of the continuum opacity are the photoionization of neutral H and free-free absorption, while in O stars there is also contribution from electron scattering and He photoionisation.

As mentioned above, bound-bound absorption happens for photons with an energy (or frequency or wavelength) in a specific range  $\Delta E = h\Delta\nu$  centered on the wavelength of the transition  $\lambda_0$ . This essentially is described by Heisenberg's uncertainty principle  $\Delta E \Delta t \geq \hbar/2$ , and it causes the spectral lines to be broader. Another mechanism that broadens the spectral lines is due to thermal motions of the atoms in the gas. It is called Doppler broadening, because the thermal motions of the atoms cause the observer to see from his/her rest frame a different frequency of the emitted (or absorbed) photons than an observer moving with the atoms would. If we also consider turbulent velocities that are associated with macroscopic velocity fields, then the effective line broadening due to the Doppler effect is  $\Delta\nu_D = \nu_0/c(2kT/m_a + \zeta^2)^{1/2}$ , where  $m_a$  is the mass of the atom and  $\zeta$  is the root mean-square of turbulent velocities. If the turbulence is small compared to the scale of a mean free path, then  $\zeta$  is called microturbulence. Lastly, collisions between the atoms and other gas particles can result in perturbations of the energy levels of the atoms. This broadening effect is called collisional or pressure broadening. Both the natural and pressure broadening can be described by a Lorentzian profile, while the Doppler broadening is described by a Gaussian profile. The convolution of both profiles is a Voigt profile, which is often used to fit spectral lines.

The pressure broadening, depending on the force that is causing the perturbation of the energy levels, can be classified as follows

- linear Stark broadening due to the homonymous effect, which is the splitting and shifting of spectral lines due to the influence of an externally applied electric field. The shift in energy is linearly proportional to the strength of the electric field.
- resonance broadening, which occurs when the particle that causes the perturbations of the atomic energy levels is of the same type as the emitting particle.

- quadratic Stark effect, where the cause is the same as for the linear one, but here the shift in energy is proportional to the square of the strength of the electric field.
- van der Waals broadening, where the van der Waals forces are causing the perturbation of the atomic energy levels of the emitting particle.

### 2.1.4 Stellar parameter determination

In order to perform an analysis of a stellar spectrum, we need to construct a model atmosphere. To do that, we need to assign a set of stellar parameters  $T_{\text{eff}}$ ,  $\log g$ ,  $[\text{Fe}/\text{H}]$ , and  $\zeta$  to that model. The choice of that set is the stellar parameter determination process, which can be done in various ways. If we have spectra of high quality, that is, high signal-to-noise ratio (SNR) and high resolution, we can resort in the use of the abundantly present and detectable Fe I and Fe II lines to determine the stellar parameters spectroscopically. However, metal-poor stars are not as abundant in Fe lines, so we can resort in other methods.

In this thesis,  $T_{\text{eff}}$  was determined photometrically. This means, that the differences between the magnitudes of the star in different passbands, namely the color-index, was used to calculate the effective temperature from a calibration relationship between the color(s),  $T_{\text{eff}}$ , and  $[\text{Fe}/\text{H}]$  (Casagrande et al., 2010). For that purpose an initial  $[\text{Fe}/\text{H}]$  is chosen. Then  $\log g$  can be determined from the fundamental relation

$$\log(g/g_{\odot}) = \log(M/M_{\odot}) - 4 \log(T_{\text{eff}}/T_{\text{eff},\odot}) + 0.4(M_{\text{bol}} - M_{\text{bol},\odot}) \quad (2.11)$$

where  $M_{\text{bol}} = BC_V + V + 5 \log \varpi + 5 - 3.1E(B - V)$ ,  $M_{\text{bol},\odot} = 4.75$ ,  $\log T_{\text{eff},\odot} = 3.7617$ ,  $\log g_{\odot} = 4.438$ , and  $\varpi$  is the parallax of the star. Following, one can measure the equivalent widths (EWs) (see Section 2.1.5) of Fe I and Fe II lines in order to determine  $[\text{Fe}/\text{H}]$  and the  $\zeta$ .  $\zeta$  is determined as the value that assures that there is no correlation between the reduced equivalent width ( $\log(W_{\lambda}/\lambda)$ ) of the lines and the respective derived abundance. All the stellar parameters are correlated, that is, when one changes the others are affected as well. As a result, the stellar parameter determination procedure is an iterative process.

### 2.1.5 Determination of elemental-abundances

The last step now is ready to be taken. With the  $T_{\text{eff}}$  and  $\log g$  at hand, we can measure the abundances. Specifically, we can link the number of the absorbing atoms or ions that create a specific absorption line with the strength of that line. In order to do so, we can use the EW  $W_{\lambda}$  of the spectral line, which is defined as the width of a rectangular strip – with a height equal to that of the continuum – that has the same area as the absorption line.

$$W_{\lambda} = \int \frac{F_c - F_{\lambda}}{F_c} d\lambda \quad (2.12)$$

where  $F_c, F_{\lambda}$  are the flux of the continuum and of the line, respectively. This method, however, can only be applied to single lines, that is, lines that are not blended with other ones. Then, we can deduce from the curve of growth – which is the relation between the logarithm of the column density of absorbing atoms  $\log \mathcal{N}$  and the EW of the line  $\log W_{\lambda}$  – the abundance. Figure 2.1 shows on the left the equivalent width of a spectral line, and on the right the curve of growth. The curve of growth shows

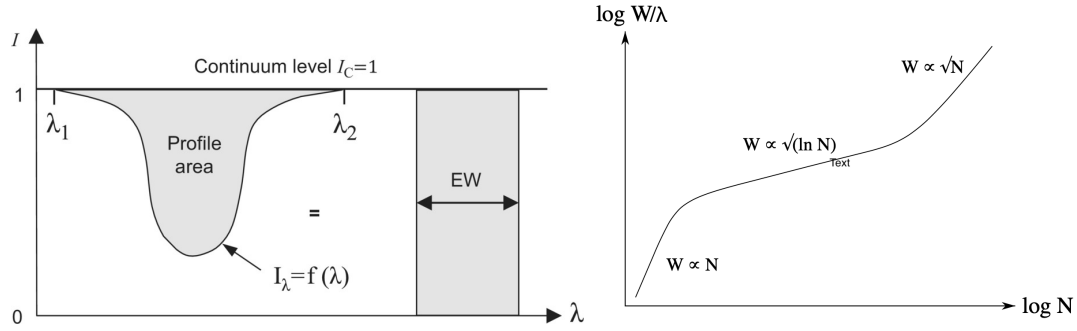


FIGURE 2.1: Left panel: Equivalent width of an absorption line. Figure adopted from Trypsteen and Walker, 2017. Right panel: The curve of growth.

a different relation between  $\log \mathcal{N}$  and  $\log W_\lambda$ , as the line strength increases ( $\mathcal{N}$  increases). Particularly, when the lines are weak – few absorbers – then  $W_\lambda \propto \mathcal{N}$ . This linear relationship breaks down, when the line saturates. The further addition of absorbers increases slowly the EW, by widening the wings of the line while the middle part of it is flat, and  $W_\lambda \propto \sqrt{\ln \mathcal{N}}$ . As the abundance continues to grow, the wings grow deeper and  $W_\lambda \propto \sqrt{\mathcal{N}}$ . For weak lines, the equation that relates the EW with  $\mathcal{N}$ , and thus the abundance, is

$$\log \left( \frac{W_\lambda}{\lambda} \right) = \log C + \log A + \log(gf\lambda) - \frac{5040}{T} \chi - \log(\kappa_\nu) \quad (2.13)$$

where  $C$  is a constant for a given star,  $g$  is the statistical weight of the respective transition, and  $f$  the oscillator strength – which is the probability of the transition happening –  $\chi$  is the excitation potential, and  $\kappa_\nu$  is the continuum absorption coefficient.  $\log A$  is the number density of atoms of element  $A$  ( $N_A$ ) relative to the number density of hydrogen atoms ( $N_H$ ). Then, the absolute abundance of element  $A$  is defined as follows

$$\log \epsilon(X) = \log \frac{N_A}{N_H} + 12 \quad (2.14)$$

where the number 12 comes from defining the abundance of element  $A$  with respect to the number of hydrogen atoms fixed at a trillion ( $N_H = 10^{12}$ ), that is  $\log \epsilon(H) = \log N_H = 12$ . The abundance of an element  $X$  relative to the Solar abundance of that same element is given by equation 1.1.

Another way to estimate elemental abundances, is to use spectral synthesis. In this way, one can estimate also abundances of blended lines, or even of extensive molecular bands. In this dissertation I used both equivalent width measurements and spectral synthesis, using the 1D LTE radiative transfer code M00G (Snedden, 1973; Sobeck et al., 2011) and the software smhr (Casey, 2014; Ji et al., 2020).

Both the Saha and Boltzmann equations (2.3, 2.2), as well as equation 2.13 depend on the stellar parameters of the star. This has as a result that a change in the stellar parameters leads to a change in the measured abundances. For the abundance analysis that I conducted, I provide a comprehensive table showing the uncertainty in the abundance due to the uncertainty in the stellar parameters  $T_{\text{eff}}$ ,  $\log g$ ,  $[\text{Fe}/\text{H}]$ , and  $\xi$ .

### Atomic data

The final ingredient, without which the described abundance analysis is not possible, is the atomic and molecular data of the relevant transitions. This data is comprised of the wavelength  $\lambda_0$  of the transition, the respective excitation energy, its oscillator strength  $f$ , its damping coefficients, and in case of a molecular transition, the dissociation energy of the molecule. This set of data is called a line list. The oscillator strength is given in combination with the statistical weight, describing the probabilities of all the possible transitions. Further, the damping coefficients describe the line-broadening and depend on temperature. Cool stars are dominated by van der Waals broadening, while the Stark effect dominates in hot stars. Finally, some spectral lines present hyperfine structure (hfs) and isotopic shifts (IS). Hfs is due to the interaction between the electrons with the nucleus, which leads to line splittings or shifts. One kind of hfs are the IS, which happen due to the difference in mass and size of the isotopes. Specifically, the difference in size results in different electric potentials and electric fields inside the nuclei.

## 2.2 Ulysses Simulator

Ulysses is a simple simulator that can quickly generate end-of-mission sampled mean BP/RP spectra (Astraatmadja, 2015). The simulator, however, does not generate the spectra by itself, but it needs a spectrum of a source to be given as input. It is designed in such a way, that the user can control the various parameters of the model instrument, choose whether or not to add noise to the spectra, and apply extinction to the flux of the input spectra. For each input source Ulysses generates and delivers the BP/RP spectra, the  $G_{BP}$  and  $G_{RP}$  magnitudes, the wavelength of the spectrum, the astrometric errors, the photometric errors, noise-free *UBVRI* photometry and the respective extinctions, and the extinction  $A_{RVS}$  (in the RVS band).

I will now briefly describe the simple model that Astraatmadja, 2015 used for the modelling of the 1D *Gaia* mean BP/RP spectra. For a detailed description see Astraatmadja, 2015. The light of a source has a specific spectral energy distribution,  $N(\lambda)$ , which is given in photons  $s^{-1} m^{-2} nm^{-1}$ . After it gets collected by the telescope(s) (that is comprised of 6 mirrors) it passes through a filter and a prism, and then it gets recorded by the CCD(s). All of these components have their own transmissivity as a function of wavelength, which needs to be accounted for. At the focal plane, the light gets dispersed by the prism at the AL direction. The 1D dispersed spectrum, before reaching the CCD, is

$$S(\kappa) = (D \times H)\tau \int_{\lambda} N(\lambda)T_m(\lambda)T_p(\lambda)Q(\lambda)L_{\lambda}(\kappa - \kappa_{\lambda})d\lambda \quad (2.15)$$

where  $\kappa_p(\lambda, \kappa_0) = \kappa_{\lambda} - \kappa_0$  is the position of the monochromatic light  $\lambda$  given as the offset from the reference point  $\kappa_0$ ,  $D \times H$  is the telescope pupil area (AL  $\times$  AC size),  $\tau$  is the TDI integration time per CCD,  $T_m(\lambda)$  is the total transmissivity of the mirrors,  $T_p(\lambda)$  is the total transmissivity of the prism,  $Q(\lambda)$  is the CCD quantum efficiency at 160 K, and  $L_{\lambda}$  is the monochromatic line spread function (LSF) at wavelength  $\lambda$ . For BP and RP there is an LSF for every CCD and telescope combination. Ulysses is using only one LSF for each of the BP and RP photometers, which is the mean of the respective normalised LSFs. Further, the actual spectrum recorded by the CCD, is limited to a window of  $K$  pixels in the AL direction

$$S(k) = \int S(\kappa)\delta(\kappa - \kappa_0)d\kappa + \epsilon_s(k), k = 0, \dots, K - 1 \quad (2.16)$$

where  $\delta(x)$  is the smearing function, and  $\epsilon_s(k)$  is the noise added due to the measurement process. The adopted smearing function is

$$\Pi(x) = \begin{cases} \frac{1}{2}, & \text{for } x = \pm 0.5, \\ 1 & \text{for } -0.5 < x < +0.5, \\ 0 & \text{elsewhere.} \end{cases} \quad (2.17)$$

In Ulysses the FITS convention was used, which means that the centers of pixels were placed at integer values of the continuous coordinate system  $\kappa$ , and the size of each pixel was considered to be of one unit. The spectra can be oversampled. That is, a spectrum is observed  $n_{over}$  times and each time the position of the wavelengths on the focal plane is shifted in the AL direction. In the end, the final spectrum is obtained by combining all the spectra, but now the size of the spectrum is the size of the window ( $K$  pixels) multiplied by the oversampling  $n_{over}$ .

Furthermore, the noisy end-of-mission spectra are generated first as noise-free, and then the noise is added. The noise model was adopted from Jordi et al., 2010

$$f_{noisy}(\kappa) = f_{noise-free}(\kappa) + r_G(0|1)\sigma_{EOM,\kappa}, \quad (2.18)$$

where  $r_G(0|1)$  is randomly drawn from a Gaussian distribution with  $\mu = 0$  and  $\sigma = 1$ , and  $\sigma_{EOM,\kappa}$  is the standard deviation of the noise-free flux measurement at pixel  $k$ .

$$\sigma_{EOM,\kappa} = \sqrt{m^2\sigma_{str}^2 \frac{n_{over}}{n_{tr}} + \sigma_{cal}^2} \quad (2.19)$$

where  $n_{tr}$  is the number of transits,  $m = 1.2$  is the overall mission margin which accounts for unknown sources of error,  $\sigma_{str}$  and  $\sigma_{cal}$  are the uncertainties in the observed flux and of the flux internal calibration, respectively.

## 2.3 Kinematic analysis

I performed a kinematic analysis of the three stars that I studied, as well as of the  $r_{lim}$  stars in literature. Such an analysis entails the knowledge of the position and velocities of a star, so that its orbit can be calculated. The positions – right ascension ( $RA$ ) and declination ( $DEC$ ) – the velocities – proper motions in  $RA$  and  $DEC$  – and radial velocities were adopted from *Gaia* DR3 (Gaia Collaboration et al., 2023), and the distances were adopted from Bailer-Jones et al., 2021. The software that I used to calculate the orbits is `galpy` (Bovy, 2015).

The orbit of a stellar body is the trajectory it travels on, whilst under the influence of a gravitational field. In order to describe the gravitational field, we need to know the distribution of mass that creates the field. For the MW a good approximation is to consider axisymmetric mass distributions and thus, an axisymmetric potential. The bar and the spiral arms of the MW, however, are non-axisymmetric but can be well described as perturbations of the axisymmetric system. The axisymmetry means

that the mass distribution is not changing – is symmetric – with respect to rotation around the axis that is perpendicular to the disk. This fact points to the choice of cylindrical coordinates, since then, instead of a potential  $\Phi(R, \phi, z)$  one needs only  $\Phi(R, z)$ , which we also can assume to be symmetric about the plane ( $z = 0$ ).

According to Hamilton's principle, a dynamical system will – within a specified time interval  $t_1$  to  $t_2$  – always follow the path that minimizes the action. The action is the time integral of the difference between the kinetic and potential energies. The mathematical formulation of this principle is

$$\delta \int_{t_1}^{t_2} (T - V) dt = 0 \quad (2.20)$$

where  $\mathcal{L} = T - V$ . Furthermore, if we make use of the Euler-Lagrange equation, then

$$\frac{d}{dt} \left( \frac{\partial \mathcal{L}}{\partial \dot{\mathbf{x}}} \right) - \frac{\partial \mathcal{L}}{\partial \mathbf{x}} \quad (2.21)$$

If we substitute  $\mathcal{L}$  with  $T - V$ , then we have  $\frac{d}{dt}(m\dot{\mathbf{x}}) = -\frac{\partial V}{\partial \mathbf{x}}$ , which is essentially Newton's second law of motion ( $\mathbf{F} = m\mathbf{a}$ ). Transforming from Cartesian to cylindrical coordinates, we have the following relations

$$x = R \cos \phi, \quad (2.22)$$

$$y = R \sin \phi, \quad (2.23)$$

$$z = z \quad (2.24)$$

The respective velocities are

$$\dot{x} = \dot{R} \cos \phi - R \dot{\phi} \sin \phi, \quad (2.25)$$

$$\dot{y} = \dot{R} \sin \phi + R \dot{\phi} \cos \phi, \quad (2.26)$$

$$\dot{z} = \dot{z} \quad (2.27)$$

Since we are dealing only with gravitational forces when it comes to stellar orbits, and the mass of a star does not influence its orbit, we can treat the star as a particle of a unit mass. Therefore, all relevant quantities will be considered to be per unit mass.

The kinetic energy in cylindrical coordinates is

$$K = \frac{1}{2}(\dot{x}^2 + \dot{y}^2 + \dot{z}^2) = \frac{1}{2}(\dot{R}^2 + R^2 \dot{\phi}^2 + \dot{z}^2) \quad (2.28)$$

Hence, the motion is described by the following Lagrangian

$$\mathcal{L} = \frac{1}{2}[\dot{R}^2 + (R\dot{\phi})^2 + \dot{z}^2] - \Phi(R, z) \quad (2.29)$$

whose momenta are calculated via  $p_i = \frac{\partial \mathcal{L}}{\partial \dot{q}_i}$  and are  $p_R = \dot{R}$ ,  $p_\phi = \dot{\phi}R^2$ , and  $p_z = \dot{z}$ . The relation between the Lagrangian and the respective Hamiltonian equation is

$$H = \sum_i p_i \dot{q}_i - \mathcal{L} \quad (2.30)$$

resulting, for this case, in

$$H = \frac{1}{2} \left( p_R^2 + \frac{p_\phi^2}{R^2} + p_z^2 \right) + \Phi(R, z) \quad (2.31)$$

The respective equations of motion can be derived via Hamilton's equation  $\dot{p}_i = -\frac{\partial H(q,p)}{\partial q_i}$ , and are

$$\dot{p}_R = \frac{p_\phi^2}{R^3} - \frac{\partial \Phi}{\partial R}, \quad (2.32)$$

$$\dot{p}_\phi = 0, \quad (2.33)$$

$$\dot{p}_z = -\frac{\partial \Phi}{\partial z} \quad (2.34)$$

These equations of motion cannot be solved analytically for realistic potentials/mass distributions, but they can be solved numerically. Further, equation 2.33 shows that  $p_\phi$  does not change with time and is, therefore, a constant of motion ( $p_\phi = \dot{\phi}R^2 = \text{constant}$ ). Particularly,  $p_\phi$  describes the angular momentum about the  $z$ -axis (that is,  $p_\phi = L_z$ ). If we now define the effective potential  $\Phi_{eff}(R, z, L_z)$  as

$$\Phi_{eff}(R, z, L_z) = \frac{p_\phi^2}{2R^2} + \Phi(R, z) = \frac{L_z^2}{2R^2} + \Phi(R, z) \quad (2.35)$$

we only need to describe the stellar orbit in the 2D space that matches the respective angular momentum  $L_z$ . The  $(R, z)$  plane of the orbit is referred to as the meridional plane. For more details on the orbits of bodies in axisymmetric (and other) potentials, see Binney and Tremaine, 2008.

For the study that I conducted, I used the axisymmetric gravitational potential of McMillan, 2017. McMillan, 2017 divides the MW into six axisymmetric components: the bulge, the dark-matter halo, the thin- and thick-disc, and HI and molecular gas ( $H_2$ ) discs. For the bulge, they adopt an axisymmetric approximation of the model from Bissantz and Gerhard, 2002, and the density profile of the bulge is

$$\rho_b = \frac{\rho_{0,b}}{(1 + r'/r_0)^\alpha} \exp \left[ -(r'/r_{cut})^2 \right], \quad (2.36)$$

where  $r' = \sqrt{R^2 + (z/q)^2}$  in cylindrical coordinates,  $\alpha = 1.8$ ,  $r_0 = 0.075$  kpc,  $r_{cut} = 2.1$  kpc, and  $q$  – which is the axis ratio – is  $q = 0.5$ . The total mass of the bulge is  $M_b = 8.9 \times 10^9 M_\odot \pm 10\%$ .

Both the thin- and thick discs are modelled so that their mass density declines exponentially. The corresponding density profile is

$$\rho_d(R, z) = \frac{\Sigma_0}{2z_d} \exp \left( -\frac{|z|}{z_d} - \frac{R}{R_d} \right), \quad (2.37)$$

where  $z_d$  and  $R_d$  are the scale height and the scale length, respectively, and  $\Sigma_0$  is the central surface density. For the thin-disk  $z_{d,thin} = 300$  pc and  $R_{d,thin} = 2.6 \pm 0.52$  kpc, and for the thick-disk  $z_{d,thick} = 900$  pc and  $R_{d,thick} = 3.6 \pm 0.72$  kpc.

The HI and molecular gas discs are modelled also exponentially, but they have a hole in the middle with a scale length  $R_m$ . The respective density profile – for both – is

$$\rho_d(R, z) = \frac{\Sigma_0}{4z_d} \exp\left(-\frac{R_m}{R} - \frac{R}{R_d}\right) \operatorname{sech}^2(z/2z_d), \quad (2.38)$$

where  $\Sigma_{0,\text{HI}} = 53.1 M_\odot \text{pc}^{-2}$ ,  $z_{d,\text{HI}} = 0.085 R_{m,\text{HI}} = 4 \text{ kpc}$ , and  $R_{d,\text{HI}} = 7$  for the HI gas disc, and  $\Sigma_{0,\text{H}_2} = 2180 M_\odot \text{pc}^{-2}$ ,  $z_{d,\text{H}_2} = 0.045 R_{m,\text{H}_2} = 12 \text{ kpc}$ , and  $R_{d,\text{H}_2} = 1.5$  for the molecular ( $\text{H}_2$ ) gas disc. McMillan, 2017 notes, that these gas discs are important to be considered, because they deepen the potential well near the Sun causing stars that reach large distances from the Galactic plane to have high  $v_z$  when they pass near the Sun. For details of the model see McMillan, 2017.

Lastly, for the dark matter halo McMillan, 2017 considers a spherically symmetric halo with

$$\rho_h = \frac{\rho_{0,h}}{x^\gamma (1+x)^{3-\gamma}}, \quad (2.39)$$

where  $x = r/r_h$  and  $r_h$  is the scale radius, and  $\gamma = 1$  (which is the NFW profile from Navarro, Frenk, and White 1996). The virial mass of the MW – which is defined as the radius of a sphere that is centered on the GC and has a mean density that is 200 times larger than the critical density  $\rho_{\text{crit}} = \frac{3H_0^2}{8\pi G}$  – is adopted from Moster, Naab, and White, 2013 and taken as a prior

$$M_* = M_v \times 2N \left[ \left(\frac{M_v}{M_1}\right)^{-\beta} + \left(\frac{M_v}{M_1}\right)^\gamma \right], \quad (2.40)$$

where  $N = 0.0351$ ,  $\log_{10} M_1 = 11.59$ ,  $\beta = 1.376$ , and  $\gamma = 0.608$  at redshift zero ( $z = 0$ ). The value of the Hubble constant was adopted from Komatsu et al., 2011 ( $H = 70.4 \text{ km s}^{-1} \text{ Mpc}^{-1}$ ).

## 2.4 Calculation of the lanthanide mass fractions

In order to compare the lanthanide mass fraction ( $X_{La}$ ) of the KN AT2017gfo with that of the  $r_{\text{lim}}$  stars, I computed the  $X_{La}$ 's of the latter (for the stars that I analysed and for those in the literature). The recipe that I used is introduced in Ji, Drout, and Hansen, 2019, and I will present it here.

As already discussed in the theoretical introduction, a key parameter for the  $r$ -process is the electron fraction  $Y_e$ . Low  $Y_e$  ( $Y_e \lesssim 0.25$ ) ejecta have high neutron densities, and produce heavy  $r$ -process elements including the lanthanides and actinides, which have high opacities. The high opacity is due to the configuration of their electrons (open  $4f$ -shells), which causes many electronic transitions (hence many absorption lines) in the optical wavelengths. On the other hand, the high  $Y_e$  ( $Y_e \gtrsim 0.25$ ) ejecta, which are neutron-poor, produce mostly the low opacity  $r$ -process elements of the first peak. Ji, Drout, and Hansen, 2019 separated the  $r$ -process elements in three different groups, based on their opacity and formation conditions ( $Y_e$ ). Elements with low opacity that belong to the first peak and have been formed in high  $Y_e$  ejecta comprise the mass fraction  $M_A$ .  $M_B$  is comprised of elements that have low opacity and belong to the second and third  $r$ -process peak, thus, they were formed in low  $Y_e$  ejecta. Lastly, the lanthanides and actinides comprise  $M_C$  (low  $Y_e$  and high opacity). Ji, Drout, and Hansen, 2019 take into account only the lanthanides, due to

the lack of observational data for the actinides. They argue that the abundances of actinides are not high enough to significantly alter  $M_C$ .

They define three different mass ratios:

$$H \equiv \frac{M_C}{M_B + M_C} \quad (2.41)$$

$$f \equiv \frac{M_A}{M_B + M_C} \quad (2.42)$$

$$X_{La} \equiv \frac{M_C}{M_A + M_B + M_C} \quad (2.43)$$

$H$  essentially accounts for the part of the  $r$ -process that exhibits a universality, that is, the relative distribution of the respective elements (second peak, third peak, and lanthanides) is exceptionally similar when comparing the Solar (residual)  $r$ -process abundance pattern to that of metal-poor stars.  $f$  is the fraction of the mass of the elements that formed in neutron-poor ejecta to that of elements that formed in neutron-rich ones. Lastly,  $X_{La}$  is the fraction of the mass of lanthanides to the mass of the total mass of material synthesized during the  $r$ -process. Also,

$$X_{La} = \frac{H}{1 + f} \quad (2.44)$$

In this dissertation the mass ratios were calculated as follows:  $M_A$  consists of the elements with  $31 \leq Z \leq 49$ ,  $M_B$  of those with  $49 < Z < 58$  and  $71 < Z < 86$ , and  $M_C$  of those with  $57Z \leq 71$ . Following Ji, Drout, and Hansen, 2019, we calculate  $H$  by using only the Solar  $r$ -process isotopic abundances, since, as discussed above,  $H$  traces the universality of the  $r$ -process. In this dissertation the isotopic abundances of Sneden, Cowan, and Gallino, 2008 were adopted. In order to convert them to mass fractions, I used the following relation from Hinkel, Young, and Wheeler, 2022

$$\sum_i N_i A_i = \sum_i (10^{A(Q_i)_*}) A_i \quad (2.45)$$

where  $A(Q_i)_*$  is the absolute stellar abundance of all the species  $i$  of the element  $Q$  and  $A(Q_i)_* \equiv \log_{10}(Q_i) = \log(q) + 12$  where  $Q \approx q \times 10^{12}$ , and  $A_i$  is the atomic mass number. I found  $H \approx 0.135$ , which agrees with the value Ji, Drout, and Hansen, 2019 found ( $H = 0.14 \pm 0.02$ ). Lastly,  $f$  is calculated by

$$f \equiv \frac{M_{A,\odot}}{M_{B,\odot} + M_{C,\odot}} 10^{\Delta \log \epsilon} \quad (2.46)$$

where  $\Delta \log \epsilon$  is the difference between the median of  $\log \epsilon(X_A)_* - \log \epsilon(X_A)_\odot$  with  $X_A$  being the elements comprising  $M_A$ , and the median of  $\log \epsilon(X_{B,C})_* - \log \epsilon(X_{B,C})_\odot$  with  $X_{B,C}$  being the elements comprising  $M_B$  and  $M_C$ .



## Chapter 3

# A method for identifying metal-poor stars with *Gaia* BP/RP spectra

This chapter presents the study that I conducted with the purpose of developing a method to identify new metal-poor candidates with *Gaia* BP/RP low-resolution spectra. The study is presented in the form of a manuscript that was published in the journal *Astronomy & Astrophysics (A&A)* Volume 666, A58. This research was conducted by the author of this dissertation. Discussions with and comments from the co-authors N. Christlieb, K. Lind, and T. Nordlander were very valuable in improving the final published manuscript.

# A method for identifying metal-poor stars with *Gaia* BP/RP spectra<sup>★</sup>

T. Xylakis-Dornbusch<sup>1,★★</sup> , N. Christlieb<sup>1</sup>, K. Lind<sup>2</sup>, and T. Nordlander<sup>3,4</sup>

<sup>1</sup> Zentrum für Astronomie der Universität Heidelberg, Landessternwarte, Königstuhl 12, 69117 Heidelberg, Germany  
e-mail: [txylaki@lsw.uni-heidelberg.de](mailto:txylaki@lsw.uni-heidelberg.de)

<sup>2</sup> Department of Astronomy, Stockholm University, AlbaNova University Center, 106 91 Stockholm, Sweden

<sup>3</sup> Research School of Astronomy and Astrophysics, Australian National University, Canberra, ACT 2611, Australia

<sup>4</sup> ARC Centre of Excellence for All Sky Astrophysics in 3 Dimensions (ASTRO 3D), Australia

Received 19 April 2022 / Accepted 12 July 2022

## ABSTRACT

**Context.** The study of the oldest and most metal-poor stars in our Galaxy promotes our understanding of the Galactic chemical evolution and the beginning of Galaxy and star formation. However, they are notoriously difficult to find, with only seven stars at  $[\text{Fe}/\text{H}] < -5.0$  having been detected to date. Thus, the spectrophotometric data of 219 million sources which became available in the third *Gaia* Data Release comprise a very promising dataset for the identification of metal-poor stars.

**Aims.** We want to use the low-resolution *Gaia* Blue Photometer/Red Photometer (BP/RP) spectra to identify metal-poor stars. Our primary aspiration is to help populate the poorly constrained tail of the metallicity distribution function of the stellar halo of the Galaxy.

**Methods.** We developed a metal-poor candidate selection method based on flux ratios from the BP/RP *Gaia* spectra, using simulated synthetic spectra.

**Results.** We found a relation between the relative iron abundance and the flux ratio of the Ca H & K region to that of the H $\beta$  line. This relation is temperature and surface gravity dependent, and it holds for stars with  $4800 \text{ K} \leq T_{\text{eff}} \leq 6300 \text{ K}$ . We applied it to noisy simulated synthetic spectra and inferred  $[\text{Fe}/\text{H}]$  with an uncertainty of  $\sigma_{[\text{Fe}/\text{H}]} \lesssim 0.65$  dex for  $-3 \leq [\text{Fe}/\text{H}] \leq 0.5$  and  $G = 15\text{--}17$  mag, which is sufficient to identify stars at  $[\text{Fe}/\text{H}] < -2.0$  reliably. We predict that by selecting stars with inferred  $[\text{Fe}/\text{H}] \leq -2.5$  dex, we can retrieve 80% of the stars with  $[\text{Fe}/\text{H}] \leq -3$  and have a success rate of about 50%, that is one in two stars we select would have  $[\text{Fe}/\text{H}] \leq -3$ . We do not take into account the effect of reddening, so our method should only be applied to stars which are located in regions of low extinction.

**Key words.** stars: Population III – surveys – stars: Population II – stars: abundances – stars: late-type

## 1. Introduction

The *Gaia* survey (Gaia Collaboration 2016) poses an unprecedented opportunity to understand the structure, history, and evolution of our Galaxy better. Aside from the astrometry and photometry for over a billion stars, *Gaia* has also delivered spectrophotometric data in its third Data Release (*Gaia* DR3), which was made public on June 13, 2022. This could serve as a tool to map out the Galaxy in terms of the relative iron abundance  $[\text{Fe}/\text{H}]$  – which is a proxy for the total amount of metals in a star – and consequently find new metal-poor stars. Stars deficient in elements heavier than helium, called metal-poor stars, are usually very old, with ages comparable to that of the Universe (Frebel & Norris 2013). The basic idea is that stellar atmospheres preserve, to a large extent, the makeup of their birth cloud, hence a metal deficient star should have formed along with the first few generations of stars after the Big Bang. That is why these objects are very interesting, and they can facilitate our understanding of the past, even though they can be found close by. In

particular, they can be used as tracers of the evolution of the elements and of the Galaxy, help us understand how the distribution of the first population of stars (Pop III) looked, and assist in constraining Big Bang nucleosynthesis further (Frebel 2010; Beers & Christlieb 2005; Sneden et al. 2008).

The *Gaia* Collaboration itself, through the Data and Analysis Consortium (DPAC), has already, and will also in the future, deliver astrophysical parameters using the *Gaia* data. With the astrometric and photometric data of *Gaia* DR2, Andrae et al. (2018) delivered temperatures, extinctions and reddening. DPAC also used the *Gaia* DR3 Blue Photometer / Red Photometer (BP/RP) spectra to estimate metallicities of stellar objects (Creevey et al. 2022; Fouesneau et al. 2022; Andrae et al. 2022). Liu et al. (2012) predicted that Aeneas – which is a Bayesian method employed by DPAC for the stellar parameter estimation – would estimate the metallicity with an accuracy of 0.1–0.2 dex, given that the extinction is  $A_0 < 2$  mag and that the magnitude is  $G = 15$  mag. Now with *Gaia* DR3 available, Andrae et al. (2022) estimated  $[\text{M}/\text{H}]$  values for several million sources, and provide information on how to use them.

The search for metal-poor stars is as pertinent as ever now. The ongoing photometric SkyMapper Southern Sky (SMSS) survey is actively searching for extremely metal-poor stars ( $[\text{Fe}/\text{H}] < -3$  dex according to the classification of Beers & Christlieb 2005). With its DR1.1, the SkyMapper team found that 40% of their candidates had  $[\text{Fe}/\text{H}] < -2.75$  dex and only

<sup>★</sup> Full Table A.1 and a table with all the coefficients of the method are only available at the CDS via anonymous ftp to [cdsarc.u-strasbg.fr](ftp://cdsarc.u-strasbg.fr) (130.79.128.5) or via <http://cdsarc.u-strasbg.fr/viz-bin/cat/J/A+A/666/A58>

<sup>★★</sup> Member of the International Max Planck Research School for Astronomy & Cosmic Physics at the University of Heidelberg (IMPRS-HD).

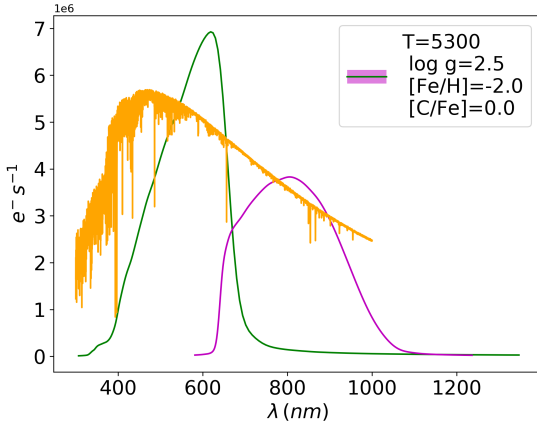


**Fig. 1.** Synthetic spectrum before (orange) and after (green and magenta) simulation. The spectrum has  $T_{\text{eff}} = 5300$  K,  $\log g = 2.5$  dex,  $[\text{Fe}/\text{H}] = -2$  dex and  $[\text{C}/\text{Fe}] = 0.0$  dex.

$\approx 7\%$  had  $[\text{Fe}/\text{H}] > -2$  dex, that is an efficacy of  $\approx 93\%$  in finding stars with  $[\text{Fe}/\text{H}] < -2$  dex (Da Costa et al. 2019). SkyMapper also led to the discovery of the star with the lowest detected Fe abundance (Nordlander et al. 2019). The *Pristine* survey, which is being carried out in the northern hemisphere, was tailored to find metal-poor stars with a narrow-band filter centered on the metallicity-sensitive Ca II H & K lines (Starkenburg et al. 2017). *Pristine* has a 56% reported efficacy of finding stars with  $[\text{Fe}/\text{H}] < -2.5$  dex and 23% for stars with  $[\text{Fe}/\text{H}] < -3$  dex (Aguado et al. 2019). The objective of this work is to develop a recipe that can efficiently identify metal-poor stars, and especially stars within and below the extremely metal-poor regime ( $[\text{Fe}/\text{H}] < -3$  dex). In Sect. 2, we present the reasoning of our approach for this endeavor, as well as the tools we used. We also describe the parameter space where our method is applicable, along with a detailed description of the development of our technique. Further, in Sect. 3 we present our results from applying our method on noise-free and noisy spectra. Therein, we also investigate the dependence of our procedure on the different astrophysical parameters, and we additionally study the effect of extinction. Lastly, we explore the expected efficiency of our technique.

## 2. Methods

For this work, we used the Ulysses Simulator (Astraatmadja 2015) and synthetic spectra (Nordlander et al. 2019; see Sects. 2.1.2 and 2.1.1, respectively) in order to simulate the spectrophotometric data of BP and RP, respectively, on board *Gaia*. The very low resolution of the expected BP/RP spectra (see Fig. 1) inclined us to use integrated fluxes of different parts of the spectra, such that a relation varying with metallicity could be found. Those spectral areas had to be sensitive to the change in metallicity and also to at least one other quantity that can be known a priori or that can be directly derived from the spectra themselves.

### 2.1. Data and simulations

Choosing the temperature and surface gravity space for our dataset was the first critical step for our method. The desired relation has to hold in that parameter space, which would then allow us to use those parameters as priors when applying the method described in this paper. Additionally, the dataset has to cover a

**Table 1.** Initial parameter space of the synthetic spectra.

Parameter	Range	Step
$T_{\text{eff}}$ (K)	$3500 \leq T_{\text{eff}} \leq 7800$	100
$\log g$ (dex)	$0.5 \leq \log g \leq 5.0$	0.5
$[\text{Fe}/\text{H}]$ (dex)	$-7.0 \leq [\text{Fe}/\text{H}] \leq 0.5$	0.5
$[\text{C}/\text{Fe}]$ (dex)	$-1.5 \leq [\text{C}/\text{Fe}] \leq 6.0$	0.5

**Notes.** The metallicity and carbon enhancement combinations are restricted to physically meaningful combinations (see Fig. 2).

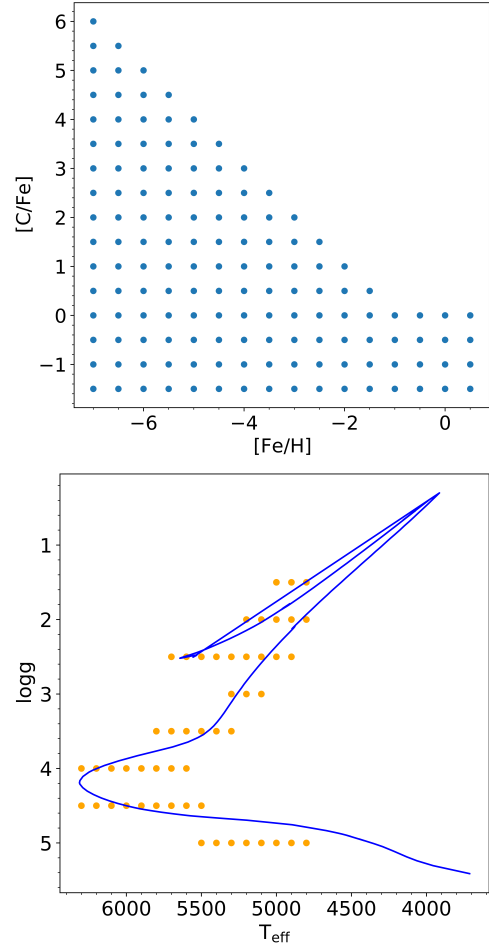


**Fig. 2.** Parameter space we used to develop our method. *Top plot:* each point in the top plot represents a specific combination of relative carbon and iron abundances. Our entire dataset is comprised of all the meaningful temperature and surface gravity combinations (see bottom plot) for each and every one of these relative abundance combinations. *Bottom plot:* a PARSEC isochrone of 12 Gyr and  $[\text{Fe}/\text{H}] = -3.0$  dex, which we used to determine the astrophysical parameters of our preliminary dataset. Overplotted are the temperature-surface gravity pairs of the final parameter space we used to develop our method.

wide metallicity range, so that both metal-poor and metal-rich stars can be covered, and we can ultimately distinguish between them. Since low metallicities are involved in the process, the last important factor that we have to pay attention to is the carbon enhancement that has been observed in many metal-poor stars (Beers & Christlieb 2005; Frebel & Norris 2015; Arentsen et al. 2021). The initial dataset parameters are shown in Table 1 and Fig. 2.

**Table 2.** Configuration of the Ulysses simulator which we used in order to construct our method.

Parameter	Value
$G$ magnitude (mag)	15
spectrum oversampling	4
number of transits	75
Extinction $A_0$	0.0

**Notes.** The method is described in Sect. 2.1.2. The same configuration was used for the test and applications described in Sect. 3, apart from the magnitude and extinction which are explicitly mentioned when they have different values than in the table above.

### 2.1.1. Synthetic spectra

For this work, we used synthetic spectra from a one dimensional (1D) grid where local thermodynamic equilibrium (LTE) is assumed (Nordlander et al. 2019), that was computed with the Turbospectrum code (Alvarez & Plez 1998; Plez 2012) and MARCS model atmospheres (Gustafsson et al. 2008). Nordlander et al. (2019) adopted the Solar chemical composition from Asplund et al. (2009); for  $[\text{Fe}/\text{H}] < -1.0$ ,  $[\alpha/\text{Fe}] = +0.4$  was adopted; for models with  $-1.0 < [\text{Fe}/\text{H}] < 0.0$ , a relationship of  $[\alpha/\text{Fe}] = +0.4 \cdot [\text{Fe}/\text{H}]$  was used. The models take continuum scattering into account and use  $v_{\text{mic}} = 1 \text{ km s}^{-1}$  for models with  $\log g \geq 4.0$ . Models with  $\log g \leq 3.5$  take spherical symmetry into account and assume  $v_{\text{mic}} = 2 \text{ km s}^{-1}$ . The line data are a combination of atomic data from VALD3 (Ryabchikova et al. 2015) and molecular data from a variety of sources; here the primary molecular line list is the one for CH from Masseron et al. (2014). This grid also contains spectra with varying carbon abundances, which we used for this work.

### 2.1.2. Ulysses

Ulysses (Astraatmadja 2015) is a simulator which takes spectra as input and delivers the equivalent BP/RP spectrum as it would be observed from *Gaia*. The final DR3 BP/RP spectra will be a combination of many different epoch observations, spanning up to the entire time of the missions' operation. That is why the input spectrum is being convolved with an averaged line spread function (LSF). For each of the two spectrophotometers (BP and RP), an averaged LSF exists, which is the product of all the LSFs of the different CCDs and telescopes. The parameters of Ulysses that can be tuned, among others, are the number of transits – which are the number of times an object was observed – the amount of interstellar extinction  $A_0$ , the apparent magnitude of the source, as well as the spectrum oversampling. The spectrum oversampling is essentially the number of spectra that will be combined into the final BP/RP spectrum. Each spectrum is sampled over 60 pixels, but for different observations, different parts of the spectrum are being sampled, so that there will be more than 60 pixels of data in the end. Carrasco et al. (2021) present a model for the internal calibration of the BP/RP spectra, in particular how to produce a mean spectrum from all the epoch spectra of the same source. The extinction curve models that Ulysses implements are those of Cardelli et al. (1989) and Fitzpatrick (1999). We selected the Fitzpatrick (1999) models for our simulations, after determining both models produce very similar results.

The core products of Ulysses are noise-free BP/RP spectra, noise-free *Gaia* photometry, and extinctions. Other outputs

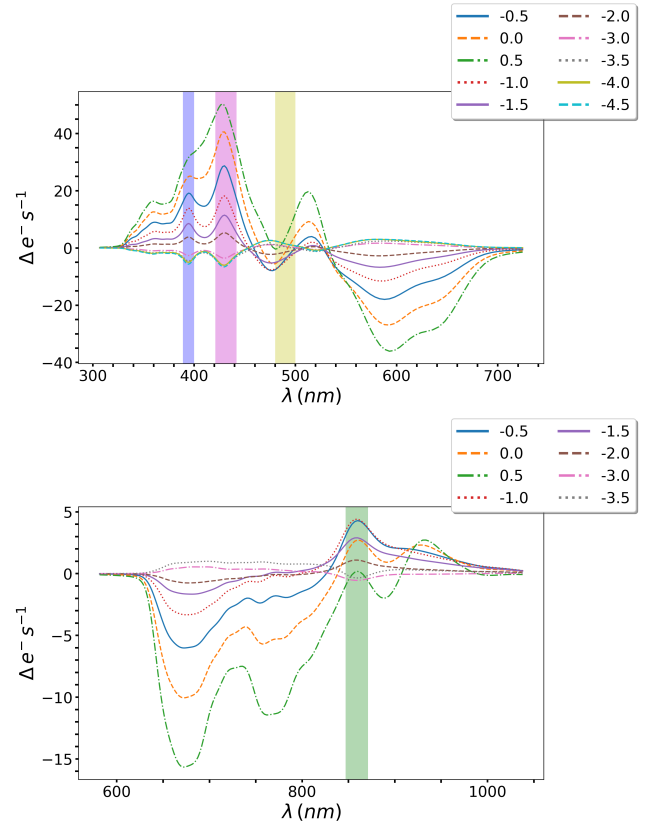


**Fig. 3.** Differential BP (top panel) and RP (bottom panel) spectra of Solar  $[\text{C}/\text{Fe}]$ -scaled stars, with different  $[\text{Fe}/\text{H}]$ . Each differential spectrum results from *reference spectrum* – *spectrum*, where  $[\text{Fe}/\text{H}]_{\text{ref}} = -2.5$ . The shaded areas correspond to the regions we used for our flux ratios, i.e., the Ca II H & K region (purple), the  $G$ -band (magenta), the  $\text{H}\beta$  (yellow), and the Ca II NIR (green) regions.

are also possible, for instance the end-of-mission noisy spectra, which are being generated with the addition of noise to the noise-free spectra. The noise model employed by Ulysses is the one from Jordi et al. (2010). An overview of the configuration we used to simulate our data is shown in Table 2.

### 2.1.3. Parameter space

A  $\chi^2$  test of the simulated spectra showed that they carry enough information in the region of the Ca II H & K lines to distinguish between metal-rich stars and stars with  $[\text{Fe}/\text{H}] < -2.0$ . However, this was observed only for stars with  $T_{\text{eff}} \geq 4800$  and also depending on their surface gravity. A 12 Gyr and  $Z = 0.001$  isochrone (Bressan et al. 2012) was used to choose realistic  $T_{\text{eff}}\text{-}\log g$  pairs for the preliminary dataset (see Fig. 2).

## 2.2. Flux ratios

Differential simulated spectra were used to find out how the flux changes with changing metallicity. For this exercise, we used the spectra with  $[\text{Fe}/\text{H}] = -2.5$  dex as a reference, and we subtracted the spectra of lower and higher metallicity that had all the other astrophysical parameters identical to the reference spectrum (Fig. 3). The regions we expected to be  $[\text{Fe}/\text{H}]$  sensitive were the Ca II H & K and  $G$ -band wavelength ranges, which was confirmed: the lower the metallicity of the object, the higher the flux. The regions of the spectra that cover the Ca II near-infrared triplet as well as the  $\text{H}\beta$  absorption line

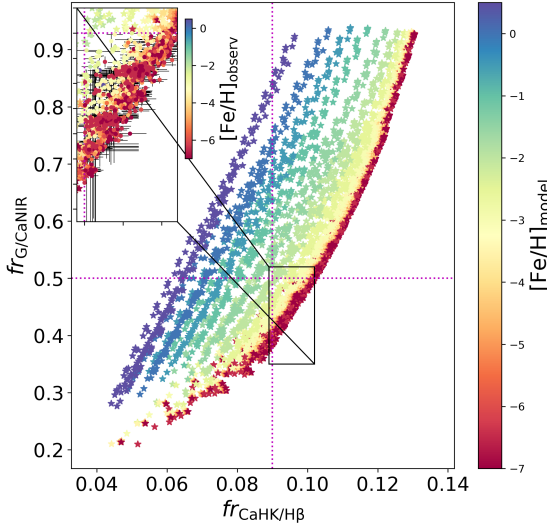


**Fig. 4.** Smoothly changing metallicity for model stars of  $G=15$  mag. On the inset plot, it is shown how well the noisy simulated flux ratios track the modeled (noiseless) ones.

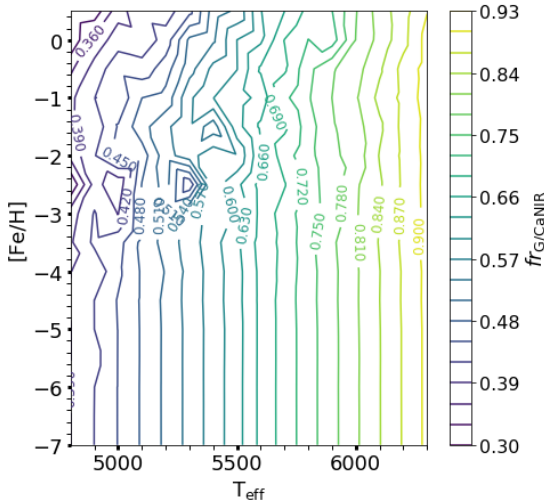


**Fig. 5.**  $fr_{G/CaNIR}$  is an effective temperature indicator; however, it does not carry information regarding the iron abundance.

showed a greater sensitivity to the change in all the other stellar parameters compared to  $[Fe/H]$ . Using the ratios of the aforementioned spectral regions, that is the ratio of the integrated Ca H & K flux to that of the  $H\beta$  region ( $fr_{CaHK/H\beta}$ ), and that of the  $G$  band integrated flux to the Ca NIR triplet ( $fr_{G/CaNIR}$ ), we can see a relation with metallicity (Fig. 4). Figure 4 was created from our entire dataset, that is temperature, surface gravity (Fig. 2), and all physically meaningful  $[C/Fe]$ – $[Fe/H]$  combinations, in other words  $[C/Fe] + [Fe/H] \leq -1$  dex for  $[Fe/H] \leq 0.5$  and  $-1.5 \geq [C/Fe] \geq 0$  for  $[Fe/H] \geq -0.5$ .

### 2.3. Metallicity-temperature- $fr_{CaHK/H\beta}$ relation

The relation between  $fr_{CaHK/H\beta}$ ,  $fr_{G/CaNIR}$ , and  $[Fe/H]$  that is emerging in Fig. 4 encouraged us to try to find a relation of the form  $F(fr_{CaHK/H\beta}, fr_{G/CaNIR}) = [Fe/H]$ . In this venture, we found that  $fr_{G/CaNIR}$  is – by itself – an indicator for the effective temperature (see Fig. 5), but it does not carry

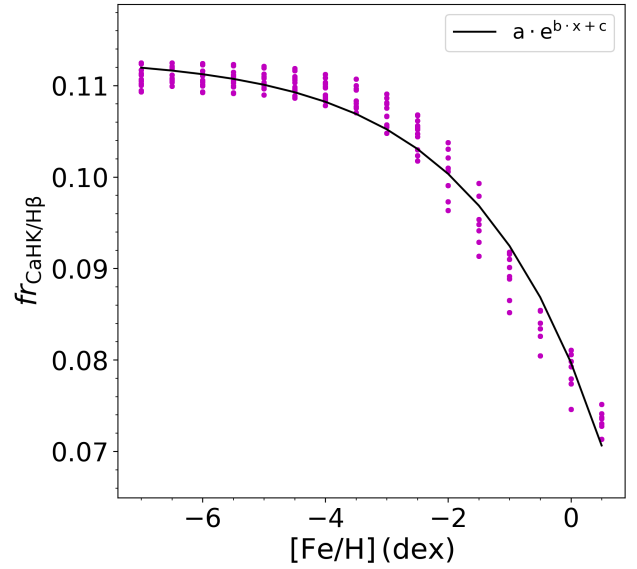


**Fig. 6.** Exponential decline of  $fr_{CaHK/H\beta}$  with increasing  $[Fe/H]$ , for a roughly constant  $fr_{G/CaNIR}$ . This behavior starts to break down for  $T_{\text{eff}} < 4800$  K. The scatter at each iron abundance reflects the different carbon enhancement and surface gravity, as well as a moderate ( $\sim 300$  K) variation in temperature.

any information about the metallicity. On the other hand, for constant  $fr_{G/CaNIR}$ , the metallicity is changing smoothly with the change of  $fr_{CaHK/H\beta}$  (Fig. 6), hence  $fr_{CaHK/H\beta}$  carries information concerning the iron abundance. There is, however, a scatter that accounts for variations in  $T_{\text{eff}}$ ,  $\log g$ , and  $[C/Fe]$ . So, since  $fr_{G/CaNIR}$  is not metallicity-sensitive, as mentioned above, but rather a temperature indicator, we thought it best to proceed with the objective of developing a relation which is comprised of  $fr_{CaHK/H\beta}$  and some relevant stellar parameters. The usage of stellar parameters makes the range of applicability more straightforward to implement, and subsequently more user-friendly. By inspecting Fig. 6, we assessed that the therein  $fr_{CaHK/H\beta}$ – $[Fe/H]$  correlation can be described with an exponential relation (Figs. 4 and 6), which was confirmed by the residuals of the fit. This exponential relation can then be expressed with respect to the temperature and surface gravity of the model stars (Fig. A.1), enabling us to use them as priors, for example from *Gaia* itself (Andrae et al. 2018). Finally, we can use the iso- $fr_{CaHK/H\beta}$  lines (see Fig. A.1), as well as the effective temperatures and surface gravities, in order to infer the metallicity:

$$F(fr_{CaHK/H\beta}, T_{\text{eff}}, \log g) = [Fe/H] \quad (1)$$

$$F = -(T_{\text{eff}} \cdot \log g) \cdot e^{b \cdot fr_{CaHK/H\beta} + c} + d, \quad (2)$$

where  $b$ ,  $c$ , and  $d$  are  $T_{\text{eff}}$  and  $\log g$  dependent coefficients.

The coefficients  $b, c, d$  are the result of fitting Eq. (2) to  $fr_{CaHK/H\beta}$ –metallicity pairs of a roughly constant temperature –  $T_{\text{eff}} \pm 30$  K – and constant surface gravity (see Fig. A.2) for metallicities greater than  $-3.5$  dex. The aforementioned  $fr_{CaHK/H\beta}$ – $[Fe/H]$  pairs result from the iso- $fr_{CaHK/H\beta}$  lines.

## 3. Results

We first tested our method on the very same data we used to construct it, and then we examined how it is influenced by different stellar parameters. Finally, we applied our method to noisy spectra.

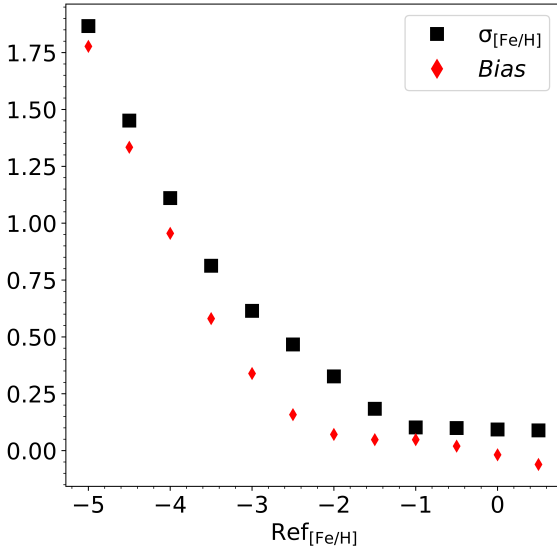


**Fig. 7.**  $\sigma$  and bias of the inferred metallicities of our noise-free spectra of  $G = 15$  mag.

### 3.1. Testing on the model spectra

We applied our method on the same model spectra we used to find relation 2. Figure 7 shows that our method works very well for stars with  $[\text{Fe}/\text{H}] \geq -3$  dex since  $\sigma_{[\text{Fe}/\text{H}]} \leq 0.6$  dex. Specifically, for red giant branch stars  $\sigma_{[\text{Fe}/\text{H}]} = 0.6$  and for turnoff stars,  $\sigma_{[\text{Fe}/\text{H}]} \approx 0.3$  at  $[\text{Fe}/\text{H}] = -3$ . Further, even for stars with  $[\text{Fe}/\text{H}] = -3.5$  dex,  $\sigma$  is smaller than 1.0 dex. On the other hand, we can identify stars with  $[\text{Fe}/\text{H}] \geq -1$  very accurately, that is to say with  $\sigma_{[\text{Fe}/\text{H}]} \approx 0.1$  dex. The bias of these results (see Fig. 7), which we defined as  $[\text{Fe}/\text{H}]_{\text{inf}} - [\text{Fe}/\text{H}]_{\text{ref}}$ , shows that our method tends to overestimate the metallicity for  $[\text{Fe}/\text{H}]_{\text{ref}} \leq -1$ , in other words it assigns higher values than the true ones. The benefit of this result is that the inferred metallicities that are in and below the metal-poor range are most probably as low as or even lower than the true ones (see Sect. 3.3). Further, the way the difference between the bias and  $\sigma$  decreases as we go to lower  $[\text{Fe}/\text{H}]_{\text{ref}}$  indicates that there is a point below which we cannot distinguish metallicities, and that is around  $[\text{Fe}/\text{H}]_{\text{ref}} = -3.5$  dex.

### 3.2. Application on noisy spectra and the dependence on stellar parameters

We subsequently applied our method to noisy spectra. For each of our model spectra ( $G = 15$  mag), we generated 20 noisy ones: we inferred the metallicity with  $\sigma_{[\text{Fe}/\text{H}]} \leq 0.6$  dex for  $[\text{Fe}/\text{H}] \geq -3$  dex (Fig. 8). Again, the uncertainty in inferring metallicity for metal-poor stars ( $[\text{Fe}/\text{H}] = -1$ ) and above is very low with  $\sigma_{[\text{Fe}/\text{H}]} \lesssim 0.12$  dex. Further we sought to determine how our method performs in the different temperature bins. For this purpose, we computed  $\sigma_{[\text{Fe}/\text{H}]}$  for all spectra of the same temperature, surface gravity, and relative carbon abundance (Fig. A.3). We found that the dependence on temperature is linked with  $[\text{C}/\text{Fe}]$ . When  $[\text{C}/\text{Fe}] \leq 0.0$  dex, our method performs slightly better for lower effective temperatures of the same  $\log g$  when  $[\text{Fe}/\text{H}] < -4$ . In contrast, when the iron abundance is greater than  $-4$ , performance becomes independent of  $T_{\text{eff}}$ . When  $[\text{C}/\text{Fe}] > 0$ , performance has a similar behavior for  $[\text{Fe}/\text{H}] < -4$ , that is to say it is better for lower temperatures.

However, above that threshold, the effect is reversed: the performance is much better for higher effective temperatures. That phenomenon is intensified as  $[\text{C}/\text{Fe}]$  grows. We expected that we could determine the metallicity for lower temperatures more accurately since the Ca H & K lines are stronger in cooler stars compared to hotter ones, even down to very low metallicities. This, as stated above, is the case for  $[\text{C}/\text{Fe}] \leq 0$ , but not above that threshold. The reason for this is probably due to the many carbon lines that arise as a result of the high carbon enhancements, which in turn are also stronger at lower effective temperatures and, consequently, our method assigns higher metallicities to those spectra. Furthermore, we investigated the dependence on different relative carbon to iron abundances, for which we already have some information as stated above. To test that, we separated our data into surface gravity and  $[\text{C}/\text{Fe}]$  bins, and calculated the error of the inferred metallicities (Fig. A.4). There is an obvious difference in the performance pattern for stars below and above  $[\text{C}/\text{Fe}] = 0$  dex. At and below that threshold,  $\sigma_{[\text{Fe}/\text{H}]}$  is almost independent of  $[\text{C}/\text{Fe}]$ . Above it, however, the performance declines as the relative carbon abundance is rising. This effect though is attenuated as temperature rises.

Another factor we considered is the extinction  $A_p$ . We used synthetic spectra with  $T_{\text{eff}} = 5500$  K,  $\log g = 3.5$  dex,  $[\text{Fe}/\text{H}] = -2$  dex, and all possible  $[\text{C}/\text{Fe}]$  combinations – for which  $[\text{Fe}/\text{H}] + [\text{C}/\text{Fe}] \geq -1$  is true – and passed them through Ulysses generating spectra of two kinds for each model: a noiseless spectrum and 20 noisy ones. We expected that the performance would decline with greater extinction, which is what we observed (see Fig. 9). We validated this result by performing the above exercise for a collection of spectra with varying astrophysical parameters. As extinction rises,  $fr_{\text{CaHK}/\text{H}\beta}$  and  $fr_{\text{G}/\text{CaNIR}}$  decrease, in other words the model star appears to be colder and the Ca H & K features are less distinguishable. When we use Fig. 4 as a reference, a model star with increasing extinction shifts left and downwards in the plot. However, according to Christlieb et al. (2008), about 90% of stars at high galactic latitudes (i.e., at  $|b| \geq 20^\circ$ ) have a reddening that is smaller than 0.06 ( $E(B - V) \leq 0.06$ ), which corresponds to  $A_p < 0.19$ . Thus, the issue of extinction is outside the scope of this paper, but we consider addressing its effect in our follow-up work.

Lastly, we wanted to find out for which magnitude our method starts to break down. Hence, we generated noisy spectra (one noisy spectrum for each set of stellar parameter combinations) of magnitudes  $G = 16, 17, 18$  mag. Up to 17 mag, the performance of our method is roughly on the same levels of precision (Fig. 8), and at 18 mag,  $\sigma_{[\text{Fe}/\text{H}]} < 0.85$  for  $[\text{Fe}/\text{H}] \geq -3$ . Our method does not seem to break down, but it rather gets less precise as the magnitude rises. Even so, at 18 mag, we can infer metallicities down to  $-2$  dex with an uncertainty of  $\sigma_{[\text{Fe}/\text{H}]} \leq 0.6$  dex.

### 3.3. Predicted success rate

Lastly, an application of our method to a simulated dataset ( $G = 15$  mag) of realistic  $[\text{Fe}/\text{H}]$  and  $[\text{C}/\text{Fe}]$  distributions (Fig. 10) served the purpose of assessing the expected success rate of our method. Additionally, this test enabled us to set the metal-poor threshold, that is to say the derived  $[\text{Fe}/\text{H}]$  value below which metal-poor stars can be selected, with the greatest efficiency and completeness. We constructed the aforementioned dataset in the following manner: (a) we randomly drew  $T_{\text{eff}} - \log g - [\text{Fe}/\text{H}] - [\text{C}/\text{Fe}]$  combinations from our parameter space; (b) then we replaced the metallicity and carbonicity values by drawing new ones from two different metallicity distribution functions (MDF)

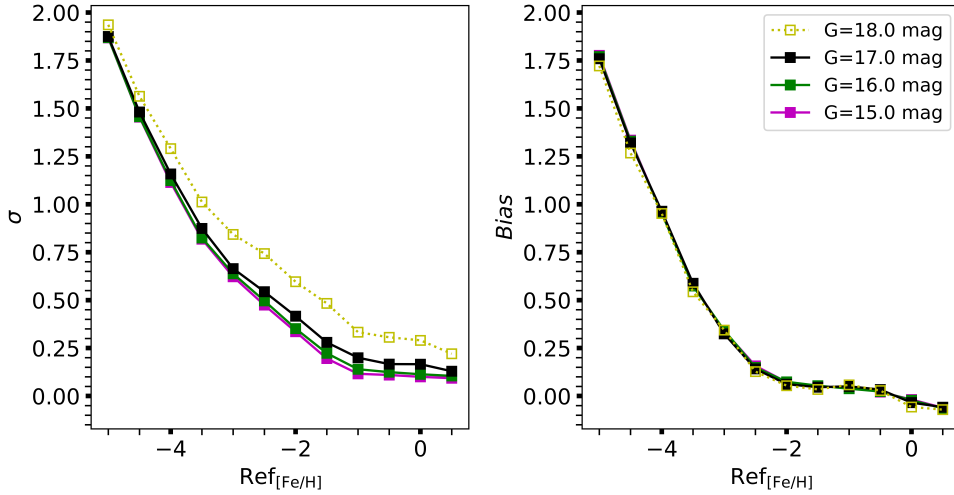


**Fig. 8.**  $\sigma$  and bias of the inferred metallicities of noisy spectra of different magnitudes:  $G = 15, 16, 17, 18$  mag.

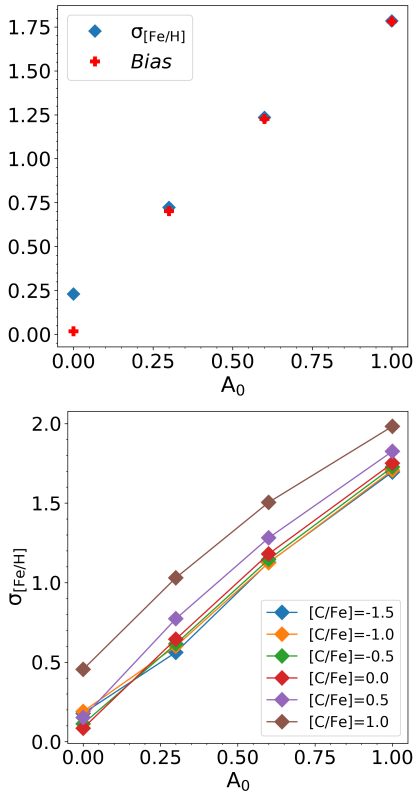


**Fig. 9.** Testing the dependence of metallicity inference on different extinction coefficients has the following expected outcome: the higher the extinction, the higher the uncertainty. We used one set of stellar parameters and metallicity, i.e.,  $T_{\text{eff}} = 5500$  K,  $\log g = 3.5$  dex, and  $[\text{Fe}/\text{H}] = -2$  dex, but various relative carbon abundances. On the *top* are the  $\sigma_{[\text{Fe}/\text{H}]}$  and bias in bins of extinctions, and in the *bottom* the results are also in bins of different  $[\text{C}/\text{Fe}]$ .

of halo stars, and from two carbonicity distribution functions, respectively. Specifically, we used the MDF from [Youakim et al. \(2020\)](#) when the initially drawn metallicity was  $> -2$  dex, and the MDF from [Placco et al. \(2014\)](#) otherwise. Concerning the carbonicity, we used the respective carbon-enhancement distribution for the [Placco et al. \(2014\)](#) MDF ([Placco et al. 2014](#)),

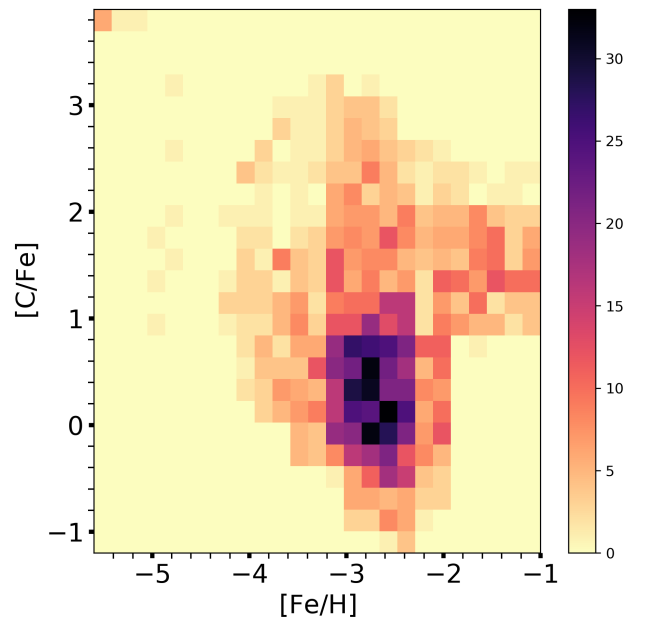


**Fig. 10.** Metallicity and carbonicity of the simulated dataset we used to predict the success rate of our method. The color bar designates the number of models in each  $[\text{Fe}/\text{H}]$ – $[\text{C}/\text{Fe}]$  bin.

and we used the  $[\text{C}/\text{Fe}]$  distribution from [Yoon et al. \(2016\)](#) for  $[\text{Fe}/\text{H}] > -2$ .

We found that when we selected all stars with an inferred  $[\text{Fe}/\text{H}]_{\text{inf}} \leq -2.5$ , we recovered 80% of stars with  $[\text{Fe}/\text{H}] \leq -3$ , and we had a contamination of about 2% of stars with metallicities above  $-2.5$ . It should be noted, however, that these “contamination” stars all have  $[\text{Fe}/\text{H}] < -2$ . Furthermore, about 55% of the stars with  $[\text{Fe}/\text{H}]_{\text{inf}} \leq -2.5$  have a reference  $[\text{Fe}/\text{H}] \leq -3$ , which means that one in two of the selected stars would at least be extremely metal-poor ( $[\text{Fe}/\text{H}] \leq -3$ ). If we were to select the metallicity threshold at  $[\text{Fe}/\text{H}]_{\text{inf}} \leq -3$ , the hit rate for stars below  $-3$  would increase to 9 out of 10. We would, however, fail to detect about 75% of stars with  $[\text{Fe}/\text{H}] \leq -3$  (see [Fig. 11](#)). The overall results of this test are detailed in [Fig. 11](#). Specifically, we show how the success rate, the completeness,

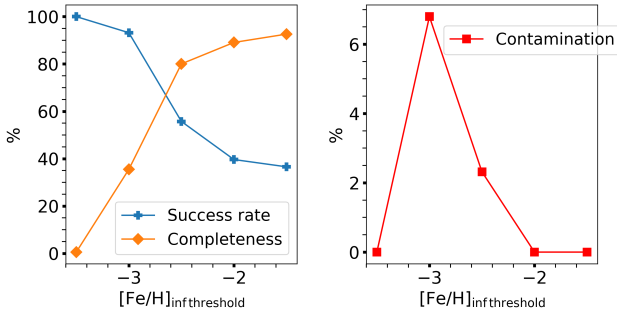


**Fig. 11.** Calculation of the success rate, the completeness (*left plot*), and the contamination (*right plot*) for threshold values  $[\text{Fe}/\text{H}]_{\text{inf threshold}} = -3.5, -3.0, -2.5, -2.0$ . The contamination was calculated with reference to the threshold metallicity, whereas the completeness and the success rate were calculated with reference to model spectra with  $[\text{Fe}/\text{H}] \leq -3$ .

and the contamination change by selecting a different threshold, that is for  $[\text{Fe}/\text{H}]_{\text{inf threshold}} = -2.0, -2.5, -3.0, -3.5$  dex. We define the success rate as the percent of the selected stars that actually have  $[\text{Fe}/\text{H}]_{\text{ref}} \leq -3.0$ , the completeness as the percent of the total number of stars with  $[\text{Fe}/\text{H}]_{\text{ref}} \leq -3.0$  that have  $[\text{Fe}/\text{H}]_{\text{inf}} \leq [\text{Fe}/\text{H}]_{\text{inf threshold}}$ , and the contamination as the percent of selected stars that have  $[\text{Fe}/\text{H}]_{\text{ref}} > [\text{Fe}/\text{H}]_{\text{inf}}$ .

#### 4. Conclusions

We developed a method using flux ratios of metallicity-sensitive regions from the *Gaia* BP/RP low resolution spectra in order to find new metal-poor stars. This method is applicable when stars have  $4800 \text{ K} \geq T_{\text{eff}} \leq 6300 \text{ K}$ . We took into account the fact that a large fraction of metal-poor stars are carbon enhanced, and thus used a grid of synthetic spectra with varying  $[\text{Fe}/\text{H}]$  and  $[\text{C}/\text{Fe}]$ . We found an exponential relation between the metallicity and the  $fr_{\text{CaHK}/\text{H}\beta}$  flux ratio, which is temperature and surface gravity dependent. Therefore, our method requires both of those stellar parameters as priors. We first applied our method to the very same noiseless data ( $G = 15$  mag) we used to construct it, and  $[\text{Fe}/\text{H}]$  was inferred with an uncertainty of  $\sigma \approx 0.6$  dex at  $[\text{Fe}/\text{H}] \leq -3.0$  dex. Our method's performance was approximately on the same level for noisy spectra of the same and greater magnitudes, that is  $\sigma \approx 0.65$  for  $[\text{Fe}/\text{H}] \leq -3.0$  dex and  $G = 15, 16, 17$  mag. We found that the performance depends on temperature, but in conjunction with the relative carbon abundance: for Solar  $[\text{C}/\text{Fe}]$  and below, performance is slightly better for lower temperatures of the same surface gravity when determining  $[\text{Fe}/\text{H}] \approx -3.5$ . For  $[\text{Fe}/\text{H}] \geq -3$ , the performance is practically independent of  $T_{\text{eff}}$ . When  $[\text{C}/\text{Fe}] > 0$ ,  $\sigma_{[\text{Fe}/\text{H}] \approx -3.5}$  is as in the Solar case, that is it is lower for lower  $T_{\text{eff}}$ . However, the determination of the metallicity above  $-3.5$  dex presents a lower uncertainty at higher temperatures of the same  $\log g$ . A dependence of the performance from the relative carbon-to-iron abundance is observed when  $[\text{C}/\text{Fe}] > 0$ . Further, even for

spectra of 18th magnitude, we can determine metallicities down to  $-2$  with an uncertainty of  $\sigma_{[\text{Fe}/\text{H}]} < 0.6$  dex, which is sufficient for identifying metal-poor stars. Nevertheless, we find that the overall performance of our method deteriorates with rising extinction  $A_0$ . Lastly, we predict that by selecting stars with  $[\text{Fe}/\text{H}]_{\text{inf}} \leq -2.5$  dex, we achieve a completeness of 80% of the stars with  $[\text{Fe}/\text{H}] \leq -3$ , and that one in two stars we select is extremely metal-poor. Our method will be applied to *Gaia* DR3 data and the results will be published in a forthcoming paper.

*Acknowledgements.* This work was funded by the Deutsche Forschungsgemeinschaft (DFG, German Research Foundation) – Project-ID 138713538 – SFB 881 (“The Milky Way System”, subproject A04). KL acknowledges funds from the European Research Council (ERC) under the European Union’s Horizon 2020 research and innovation program (Grant agreement no. 852977) and funds from the Knut and Alice Wallenberg foundation. This research was supported by the Australian Research Council Centre of Excellence for All Sky Astrophysics in 3 Dimensions (ASTRO 3D), through project number CE170100013. This work was supported by computational resources provided by the Australian Government through the National Computational Infrastructure (NCI) under the National Computational Merit Allocation Scheme and the ANU Merit Allocation Scheme (project y89).

#### References

- Aguado, D. S., Youakim, K., González Hernández, J. I., et al. 2019, *MNRAS*, **490**, 2241
- Alvarez, R., & Plez, B. 1998, *A&A*, **330**, 1109
- Andrae, R., Fouesneau, M., Creevey, O., et al. 2018, *A&A*, **616**, A8
- Andrae, R., Fouesneau, M., Sordo, R., et al. 2022, *A&A*, in press, <https://doi.org/10.1051/0004-6361/202243462>
- Arentsen, A., Starkenburg, E., Aguado, D. S., et al. 2021, *MNRAS*, **505**, 1239
- Asplund, M., Grevesse, N., Sauval, A. J., & Scott, P. 2009, *ARA&A*, **47**, 481
- Astraatmadja, T. L. 2015, Technical Report GAIA-C8-TN-MPIA-TLA-001, Max Planck Institute for Astronomy, Heidelberg
- Beers, T. C., & Christlieb, N. 2005, *ARA&A*, **43**, 531
- Bressan, A., Marigo, P., Girardi, L., et al. 2012, *MNRAS*, **427**, 127
- Cardelli, J. A., Clayton, G. C., & Mathis, J. S. 1989, *ApJ*, **345**, 245
- Carrasco, J. M., Weiler, M., Jordi, C., et al. 2021, *A&A*, **652**, A86
- Christlieb, N., Schörck, T., Frebel, A., et al. 2008, *A&A*, **484**, 721
- Creevey, O. L., Sordo, R., Pailler, F., et al. 2022, *A&A*, in press, <https://doi.org/10.1051/0004-6361/202243688>
- Da Costa, G. S., Bessell, M. S., Mackey, A. D., et al. 2019, *MNRAS*, **489**, 5900
- Fitzpatrick, E. L. 1999, *PASP*, **111**, 63
- Fouesneau, M., Frémat, Y., Andrae, R., et al. 2022, *A&A*, accepted, [arXiv:2206.05992]
- Frebel, A. 2010, *Astron. Nachr.*, **331**, 474
- Frebel, A., & Norris, J. E. 2013, in *Planets, Stars and Stellar Systems* (Springer), 55
- Frebel, A., & Norris, J. E. 2015, *ARA&A*, **53**, 631
- Gaia Collaboration (Prusti, T., et al.) 2016, *A&A*, **595**, A1
- Gustafsson, B., Edvardsson, B., Eriksson, K., et al. 2008, *A&A*, **486**, 951
- Jordi, C., Gebran, M., Carrasco, J. M., et al. 2010, *A&A*, **523**, A48
- Liu, C., Bailer-Jones, C. A. L., Sordo, R., et al. 2012, *MNRAS*, **426**, 2463
- Masseron, T., Plez, B., Van Eck, S., et al. 2014, *A&A*, **571**, A47
- Nordlander, T., Bessell, M. S., Da Costa, G. S., et al. 2019, *MNRAS*, **488**, L109
- Placco, V. M., Frebel, A., Beers, T. C., & Stancliffe, R. J. 2014, *ApJ*, **797**, 21
- Plez, B. 2012, *Turbospectrum: Code for spectral synthesis*
- Ryabchikova, T., Piskunov, N., Kurucz, R. L., et al. 2015, *Phys. Scr.*, **90**, 054005
- Snedden, C., Cowan, J. J., & Gallino, R. 2008, *ARA&A*, **46**, 241
- Starkenburg, E., Martin, N., Youakim, K., et al. 2017, *MNRAS*, **471**, 2587
- Yoon, J., Beers, T. C., Placco, V. M., et al. 2016, *ApJ*, **833**, 20
- Youakim, K., Starkenburg, E., Martin, N. F., et al. 2020, *MNRAS*, **492**, 4986

## Appendix A: Additional figures and data.

The figures in the appendix are described in Sections 2.3 and 3.2. Figures A.1 and A.2 describe the way we developed our method, whereas Figures A.3 and A.4 detail the dependence of our method on effective temperature and relative carbon abundance. In Table A.1 we provide the entire dataset that we used to produce Figure 4, so that the interested readers can apply our method themselves.

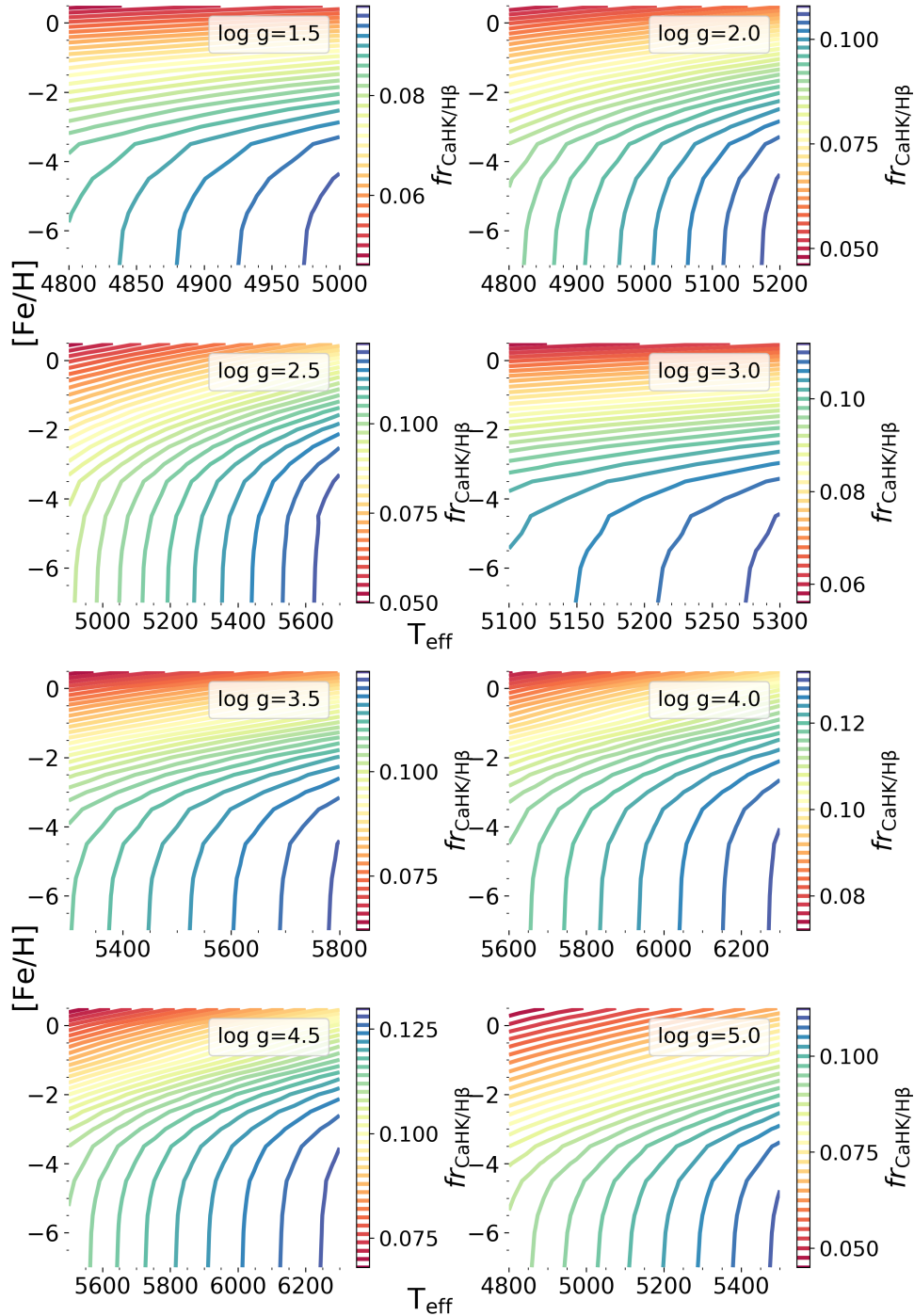


**Fig. A.1.** Contour plots where the third dimension are iso-flux lines, in particular for the  $fr_{\text{CaHK/H}\beta}$  flux ratio. Those iso- $fr_{\text{CaHK/H}\beta}$  lines are temperature-sensitive up to about  $[\text{Fe}/\text{H}] = -3.5$  dex, and then they become metallicity-sensitive, hence we can use them to find a relation from which we can infer  $[\text{Fe}/\text{H}]$ . Because the metallicity sensitivity starts at  $[\text{Fe}/\text{H}] = -3.5$ , we cannot distinguish iron abundances below that threshold, but rather identify whether they are below or above it.

**Table A.1.** Noise-free  $fr_{\text{CaHK}/\text{H}\beta}$  and  $fr_{\text{G}/\text{CaNIR}}$  flux ratios and their respective astrophysical parameters.

$a/a$	$fr_{\text{G}/\text{CaNIR}}$	$fr_{\text{CaHK}/\text{H}\beta}$	$T_{\text{eff}}$ (K)	$\log g$ (dex)	[Fe/H] (dex)	[C/Fe] (dex)
0	0.353852	0.056188	4800.0	5.0	-0.5	-0.5
1	0.361829	0.056728	4800.0	5.0	-0.5	-1.0
2	0.365205	0.056951	4800.0	5.0	-0.5	-1.5
3	0.337023	0.054872	4800.0	5.0	-0.5	0.0
4	0.288912	0.050126	4800.0	5.0	-0.5	0.5
5	0.187117	0.038496	4800.0	5.0	-0.5	1.0
6	0.122764	0.032674	4800.0	5.0	-0.5	1.5
7	0.086716	0.033368	4800.0	5.0	-0.5	2.0
8	0.324806	0.050360	4800.0	5.0	0.0	-0.5
9	0.333351	0.050936	4800.0	5.0	0.0	-1.0
10	0.336977	0.051179	4800.0	5.0	0.0	-1.5
11	0.305943	0.048967	4800.0	5.0	0.0	0.0
12	0.227209	0.042632	4800.0	5.0	0.0	0.5
13	0.144015	0.034670	4800.0	5.0	0.0	1.0
14	0.097575	0.032297	4800.0	5.0	0.0	1.5
15	0.073156	0.034265	4800.0	5.0	0.0	2.0
...	...	...	...	...	...	...
8963	0.471143	0.097089	5000.0	1.5	-7.0	0.0
8964	0.471170	0.097088	5000.0	1.5	-7.0	0.5
8965	0.471178	0.097102	5000.0	1.5	-7.0	1.0
8966	0.471137	0.097087	5000.0	1.5	-7.0	1.5
8967	0.471192	0.097109	5000.0	1.5	-7.0	2.0
8968	0.471005	0.097071	5000.0	1.5	-7.0	2.5
8969	0.470596	0.097043	5000.0	1.5	-7.0	3.0
8970	0.469710	0.096964	5000.0	1.5	-7.0	3.5
8971	0.466643	0.096713	5000.0	1.5	-7.0	4.0
8972	0.458394	0.095966	5000.0	1.5	-7.0	4.5
8973	0.439977	0.094247	5000.0	1.5	-7.0	5.0
8974	0.409192	0.090923	5000.0	1.5	-7.0	5.5
8975	0.368257	0.084704	5000.0	1.5	-7.0	6.0

**Notes.** Figure 4, as well as our model, was produced from this dataset.

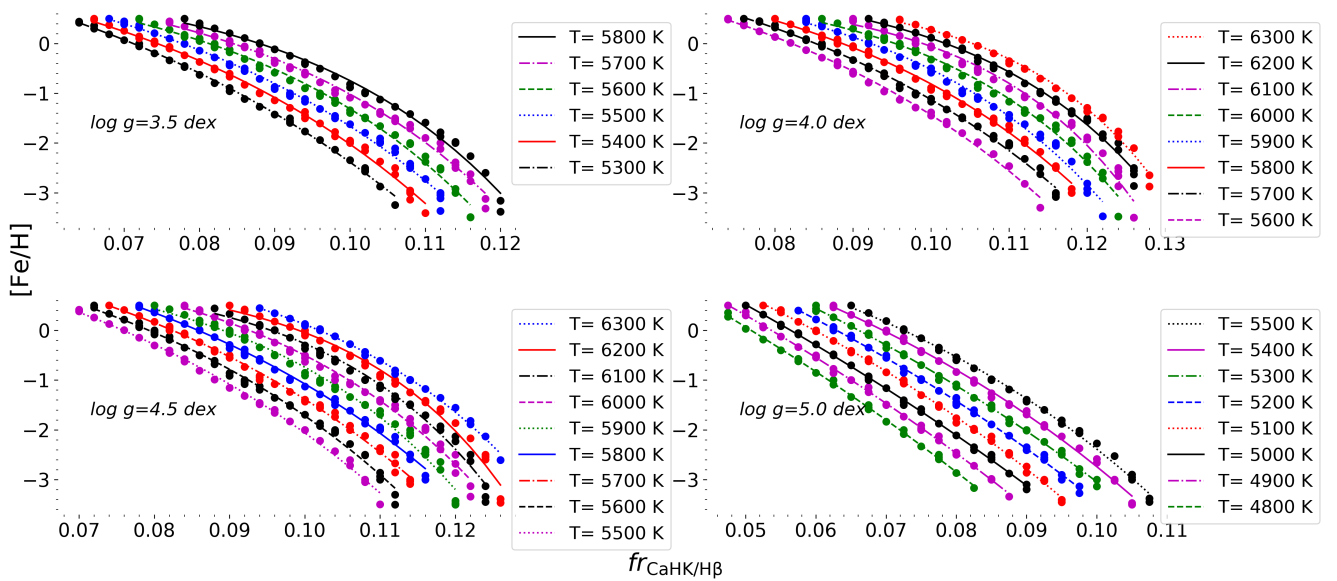


**Fig. A.2.** We fit Equation (2) in the metallicity- $fr_{\text{CaHK}/\text{H}\beta}$  space for each temperature-surface gravity pair from our parameter space (see Figure 2). Some of those fits are shown in the above panels.

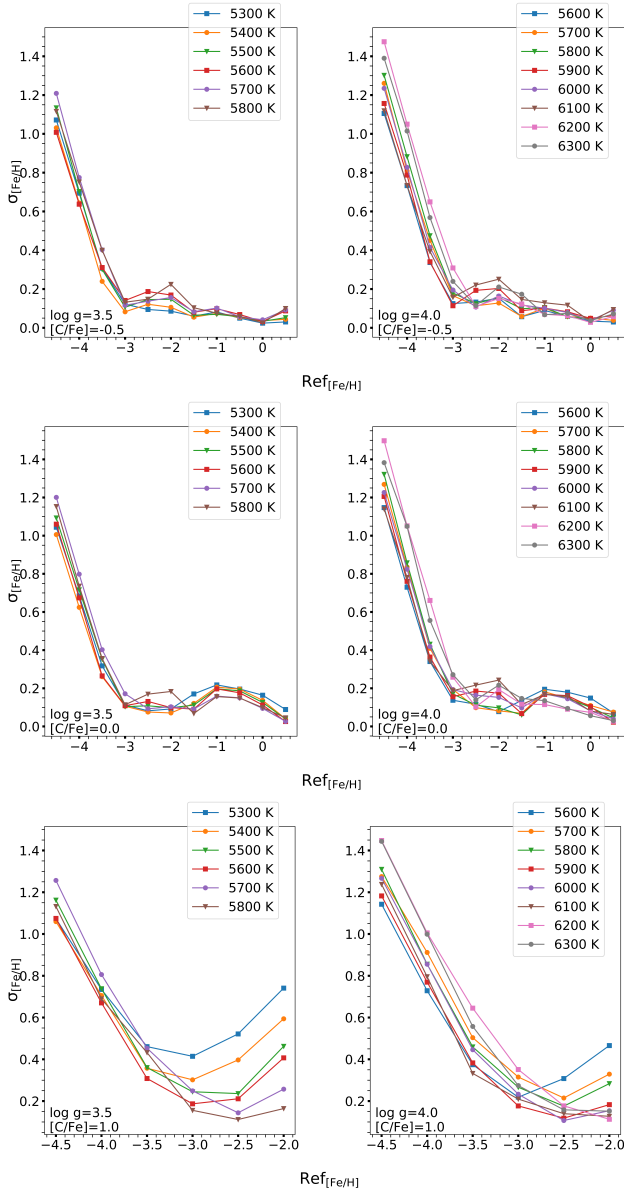


**Fig. A.3.** Temperature dependence of the performance of our method is twofold. When  $[C/Fe] \leq 0$ , the uncertainty is slightly better for lower temperatures up to  $[Fe/H] \sim -3.5$ , and above that, it becomes almost independent of  $T_{\text{eff}}$ . When  $[C/Fe] > 0$ , the pattern is the same as above for  $[Fe/H]$  up to  $\sim -3.5$ ; whereas, above  $-3$  dex, lower temperatures render higher uncertainties.

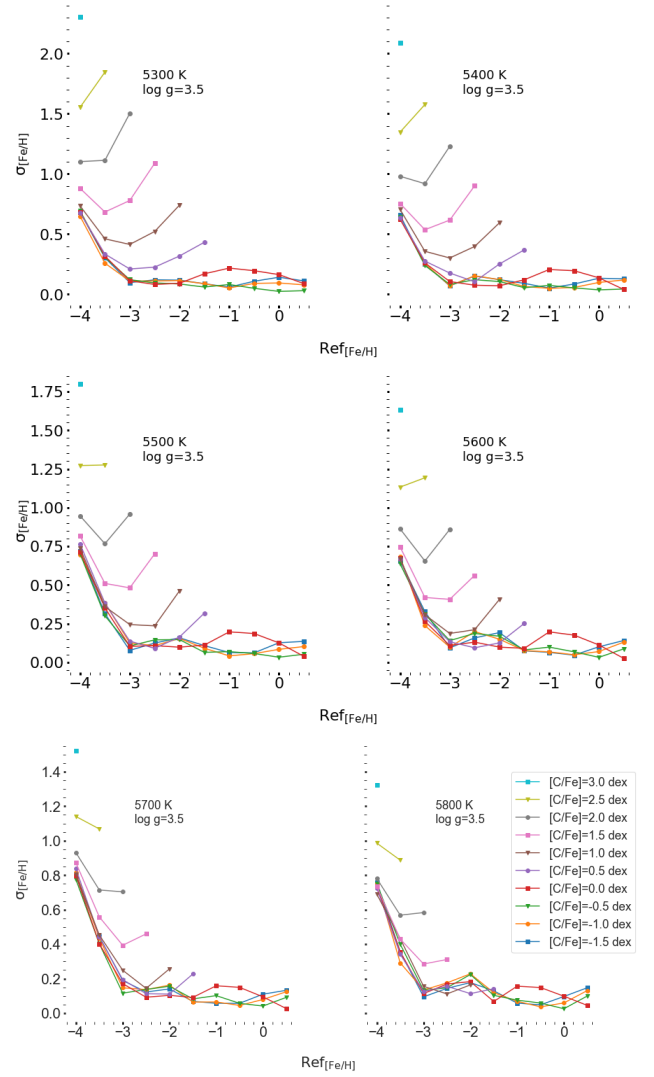


**Fig. A.4.** Computation of  $\sigma_{[Fe/H]}$  for all temperatures corresponding to  $\log g = 3.5$  dex, and all bins of  $[C/Fe]$ . The manner in which the performance of our method depends on the relative carbon abundances relates to whether or not  $[C/Fe] \leq 0$  dex: at and below a Solar value,  $\sigma_{[Fe/H]}$  is practically independent of carbon, but above it the uncertainty rises as carbon-enhancement increases. The last effect lessens as temperature rises. The same exercise was performed for all surface gravities of our parameter space, and the results were similar.

## Chapter 4

# Metallicities for more than 10 million stars derived from *Gaia* BP/RP spectra

The following manuscript (PaperII) is accepted for publication in *A&A* with the following author list: T. Xylakis-Dornbusch, N. Christlieb, T. T. Hansen, T. Nordlander, K. B. Webber, and J. Marshall. The research therein is a follow-up study on the 'A method for identifying metal-poor stars with *Gaia* BP/RP spectra' (PaperI) work. Specifically, I applied the method from PaperI to *Gaia* DR3 BP/RP spectra. The application process mandated the modification of the recipe that was developed in PaperI. Following, I verified the fine-tuned selection method by selecting metal-poor candidates which were subsequently observed and analyzed. The observations were carried out by K. B. Webber, and the spectra reduction and stellar parameter determination was done by T. T. Hansen, while I provided the dereddened magnitudes. All other scientific work was carried out by the author of this dissertation. Discussions with and comments from the co-authors T. Nordlander, T. T. Hansen, and N. Christlieb helped improve this manuscript. Additional figures are provided in the Appendix [A](#).

# Metallicities for more than 10 million stars derived from *Gaia* BP/RP spectra <sup>★</sup>

T. Xylakis-Dornbusch , N. Christlieb , T.T. Hansen , T. Nordlander , K. B. Webber  and J. Marshall 

<sup>1</sup> Zentrum für Astronomie der Universität Heidelberg, Landessternwarte, Königstuhl 12, 69117 Heidelberg, Germany  
e-mail: txylaki@lsw.uni-heidelberg.de

<sup>2</sup> Department of Astronomy, Stockholm University, AlbaNova University Center, SE-106 91 Stockholm, Sweden

<sup>3</sup> Research School of Astronomy and Astrophysics, Australian National University, Canberra, ACT 2611, Australia

<sup>4</sup> ARC Centre of Excellence for All Sky Astrophysics in 3 Dimensions (ASTRO 3D), Australia

<sup>5</sup> George P. and Cynthia Woods Mitchell Institute for Fundamental Physics and Astronomy, Texas A&M University, College Station, TX 77843, USA

<sup>6</sup> Department of Physics & Astronomy, Texas A&M University, 4242 TAMU, College Station, TX 77843, USA

April 26, 2024

## ABSTRACT

**Context.** The third *Gaia* Data Release, which includes BP/RP spectra for 219 million sources, has opened a new window into the exploration of the chemical history and evolution of the Milky Way. The wealth of information encapsulated in these data is far greater than their low resolving power ( $R \sim 50$ ) would suggest at first glance, as shown in many studies. We zeroed in on the use of these data for the purpose of the detection of "new" metal-poor stars, which are hard to find yet essential for understanding several aspects of the origin of the Galaxy, star formation, and the creation of the elements, among other topics.

**Aims.** We strive to refine a metal-poor candidate selection method that was developed with simulated *Gaia* BP/RP spectra with the ultimate objective of providing the community with both a recipe to select stars for medium and high resolution observations, and a catalog of stellar metallicities.

**Methods.** We used a dataset comprised of GALAH DR3 and SAGA database stars in order to verify and adjust our selection method to real-world data. For that purpose, we used dereddening as a means to tackle the issue of extinction, and then we applied our fine-tuned method to select metal-poor candidates, which we thereafter observed and analyzed.

**Results.** We were able to infer metallicities for GALAH DR3 and SAGA stars with color excesses up to  $E(B - V) < 1.5$  and an uncertainty of  $\sigma_{[\text{Fe}/\text{H}]_{\text{inf}}} \sim 0.36$ , which is good enough for the purpose of identifying new metal-poor stars. Further, we selected 26 metal-poor candidates via our method for observations. As spectral analysis showed, 100% of them had  $[\text{Fe}/\text{H}] < -2.0$ , 57% had  $[\text{Fe}/\text{H}] < -2.5$ , and 8% had  $[\text{Fe}/\text{H}] < -3.0$ . We inferred metallicities for these stars with an uncertainty of  $\sigma_{[\text{Fe}/\text{H}]_{\text{inf}}} \sim 0.31$ , as was proven when comparing  $[\text{Fe}/\text{H}]_{\text{inf}}$  to the spectroscopic  $[\text{Fe}/\text{H}]$ . Finally, we assembled a catalog of metallicities for 10 861 062 stars.

**Key words.** stars: Population II - Catalogs - Surveys

## 1. Introduction

The oldest stars that are still alive today and located nearby have metallicities of less than  $-3$  (Beers & Christlieb 2005). These extremely metal-poor (EMP) stars are rare and difficult to find. They are the descendants of the first generation of stars. Hence, EMP stars carry information that can shed light on the properties of their predecessors as well as on how the latter exploded and ended their lives. Consequently, finding a large number of new EMP stars for which detailed studies of their chemical composition could be conducted is of the essence since such investigations would provide constraints on the assembly of the Galaxy, on the initial mass function of the first stars, and on the

nucleosynthesis processes that formed the heavy elements. The *Gaia* Survey (Gaia Collaboration et al. 2016) released in 2022 the low-resolution ( $R \sim 50$ ) *Gaia* BP/RP spectra for 219 million sources (De Angeli et al. 2023), and there have already been many studies that have provided metallicity estimates for several thousands to millions of objects by extracting information from BP/RP spectra, often with the use of additional data from *Gaia* itself (for example Radial Velocity Spectrometer (RVS) spectra; Katz et al. 2023) or other surveys. Bellazzini et al. (2023) derived metallicities for  $\sim 700\,000$  stars, and Andrae et al. (2023a) delivered a catalog of stellar parameters, including the metallicity, using a Bayesian forward-modeling approach (Bailer-Jones et al. 2013). Yao et al. (2024) used a classification algorithm, XGBoost (Chen & Guestrin 2016), to identify 188 000 very metal-poor star candidates. Rix et al. (2022) used the machine learning algorithm XGBoost to estimate  $[M/H]$  for 2 million

\* Table 3 is only available in electronic format at the CDS via anonymous ftp to cdsarc.u-strasbg.fr (130.79.128.5) or via <http://cdsweb.u-strasbg.fr/cgi-bin/qcat?J/A+A/>.

stars, with 18 000 of them in the very- and metal-poor regime. Andrae et al. (2023b) produced a new catalog that improved on the one of Rix et al. (2022). The new catalog was assembled by training the XGBoost algorithm on stellar parameters taken from the Data Release 17 (DR17) of the Sloan Digital Sky Survey's (SDSS) APOGEE survey (Abdurro'uf et al. 2022) and from Li et al. (2022), who derived stellar parameters for 400 extremely and ultra metal-poor stars. Andrae et al. (2023b) delivered a catalog for  $\sim 175$  million stars, with a mean precision of 0.1 dex for  $[M/H]$ . Zhang et al. (2023) used a forward model to estimate the effective temperature, surface gravity, metallicity, distance, and extinction for 220 million stars. In order to do so, they used the *Gaia* XP-based data-driven models along with 2MASS (Skrutskie et al. 2006) and WISE (Schlafly et al. 2019) photometry. The forward model was then trained and validated on stellar parameters from the LAMOST survey (Wang et al. 2022), yielding  $[Fe/H]$  with a typical uncertainty of 0.15 dex. Martin et al. (2023) used the BP/RP spectra to derive synthetic photometry of the Ca H & K region based on the narrow-band photometry of the Pristine Survey (Starkenburger et al. 2017). They updated the Pristine metallicity inference model so that it is exclusively based on *Gaia* magnitudes ( $G$ ,  $G_{BP}$ , and  $G_{RP}$ ) and produced a catalog of metallicities for more than 52 million stars. Martin et al. (2023) showed that their photometric metallicities are accurate down to  $[Fe/H] \sim -3.5$  and are thus very much suited for the study of the metal-poor Galaxy. Another study that took advantage of the BP/RP spectra in order to derive stellar parameters and/or metallicities is Cunningham et al. (2023). Xylakis-Dornbusch et al. (2022) (Paper I) developed an empirical method based on flux ratios of synthetic *Gaia* BP/RP spectra for the purpose of identifying new metal-poor stars. Specifically, the flux ratios were those of the Ca H & K lines to the  $H\beta$  region ( $fr_{CaHK/H\beta}$  with  $388\text{nm} < \lambda < 401\text{nm}$  and  $479\text{nm} < \lambda < 501\text{nm}$ ) and the G-band region to the Ca near-infrared (NIR) triplet ( $fr_{G/CaNIR}$  with  $420\text{nm} < \lambda < 444\text{nm}$  and  $846\text{nm} < \lambda < 870\text{nm}$ ). It was shown that for a roughly constant  $fr_{G/CaNIR}$ , the  $fr_{CaHK/H\beta}$  exponentially declines as metallicity increases. This work is a follow-up to Paper I and aims at verifying the metal-poor star selection recipe presented therein by applying it to *Gaia* DR3 BP/RP spectra. The paper is laid out in the following manner: In Section 2 we describe the dataset we used for the purpose of validating the method in Paper I as well as how we addressed the issue of extinction, which was not dealt with in our previous work. We close the section with a description of the modifications we performed on the selection procedure and metallicity estimation of the metal-poor candidate stars compared to that introduced in Paper I. Next, we present in Section 3 the results of the method verification, including the expected success rate in selecting stars that are very metal poor ( $[Fe/H] < -2$ ) and below this threshold and the purity of that ensemble. Then we investigate the plausibility of OBA stars being selected as metal-poor stars via our method. Furthermore, in Section 5 we describe the application of our fine-tuned recipe by selecting candidate metal-poor stars and subsequently observing them. We then present the results of our observations. Finally, in Section 6 we present a catalog of metallicities including stars in both the metal-poor and metal-rich regimes.

## 2. Methods

For the verification of the selection process, we used stellar parameters from high- and medium-resolution surveys and studies along with the respective flux dereddened *Gaia* BP/RP spectra.

The software *Gaia*XPy<sup>1</sup> was used to generate the *Gaia* BP/RP spectra, and `dust_extinction`<sup>2</sup> and `dustmaps`<sup>3</sup> (Green 2018) were used to deredden the spectral flux.

### 2.1. Dataset

The dataset we used for this work is comprised of two different cross-matches with *Gaia* BP/RP externally calibrated spectra (?Gaia Collaboration et al. 2023, 2016). The first cross-match was with the Stellar Abundances for Galactic Archaeology (SAGA) database (Suda et al. 2008, 2011; Yamada et al. 2013; Suda et al. 2017), and the second was with the Galactic Archaeology with HERMES data release 3 (GALAH DR3) (Buder et al. 2021). Both datasets together consist of 21 812 stars. We applied quality cuts on the aforementioned dataset by finding correlations between falsely identified metal-poor stars and quality parameters and ended up with 20 850 stars. Since this procedure could only be done after the application of our method to the dataset, we elaborate on it in both this section as well as in the results section. The quality cuts we applied were twofold: one with respect to the quality of the stellar parameters of the dataset and another stemming from the quality of the *Gaia* BP/RP spectra themselves as well as from the effect of reddening. Concerning the first, stars for which there was no reliable metallicity estimate from GALAH were dropped (`flag_fe_h=0`). The mean uncertainty in the iron abundance for the remaining GALAH stars is 0.12 dex. We did not use any quality flag for the SAGA stars, but we resorted to the provided iron abundance uncertainties ( $\bar{\sigma}_{SAGA} \sim 0.17$  dex). The GALAH  $[Fe/H]$  were computed using  $A(Fe)_{\odot} = 7.38$  (for details see Buder et al. 2021), while the SAGA database utilizes the Asplund et al. (2009) solar chemical composition, that is,  $A(Fe)_{\odot} = 7.50$ . We considered this difference in the normalization of the metallicities of the two components comprising our dataset to be negligible since our aim is not to deliver high-precision iron abundances but rather to identify metal-poor stars. Further, as appears in the Kiel Diagram (Figure 1), the final dataset we used spans from dwarf to giant stars, with most of the GALAH stars having disk-like kinematics (Buder et al. 2021) and a mean distance of  $\bar{D} \sim 1.9$  kpc (distances taken from Bailer-Jones et al. 2018) and the SAGA stars having  $\bar{D} \sim 1.8$  kpc (distances taken from Fouesneau et al. 2023) and belonging to the Galactic halo. Regarding the spectra quality, we set a limit to the blending fraction  $\beta$  of the BP/RP spectra and the color excess ( $E(B - V)$ ). The former was defined by Riello et al. (2021) as "... the sum of the number of blended transits in BP and RP divided by the sum of the number of observations in BP and RP." We slightly modified the definition to

$$\beta = \frac{(\text{bp\_n\_blended\_transits} + \text{rp\_n\_blended\_transits} + \text{bp\_n\_contaminated\_transits} + \text{rp\_n\_contaminated\_transits})}{(\text{bp\_n\_transits} + \text{rp\_n\_transits})},$$

and we set  $\beta \leq 0.5$ . Finally, complementary to our work in Paper I, we included objects in our dataset whose reddening is well above  $E(B - V) = 0.06$  (see Figure 2), which mandates that we tackle the issue of extinction.

<sup>1</sup> Software available at <https://gaia-dpci.github.io/GaiaXPy-website/>, version: DOI v2.0.1: 10.5281/zenodo.7566303.

<sup>2</sup> [https://github.com/karllark/dust\\_extinction](https://github.com/karllark/dust_extinction)

<sup>3</sup> <https://github.com/gregreen/dustmaps>

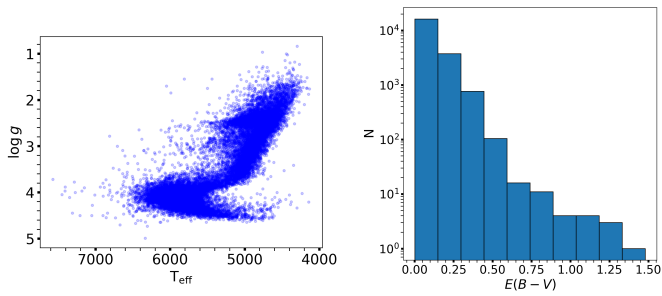


**Fig. 1.** Kiel Diagram of the dataset. **Fig. 2.** Histogram of the reddening distribution of our dataset.

## 2.2. Reddening

As a first approach, we aimed at finding a reddening independent index, similar to Bonifacio et al. (2000a). Since the region of the  $H\beta$  line is part of the  $fr_{CaHK/H\beta}$  ratio (see Paper I for details), we decided to test if the Strömgren  $\beta$  index withstands extinction and replaced the  $H\beta$  region in  $fr_{CaHK/H\beta}$  with the former. The results were not what we had anticipated: The  $\beta$  index changed with extinction, even though it showed a sensitivity to effective temperature. As we were not able to define a reddening-independent metallicity calibration, we instead sought to implement reddening corrections for the metallicity calibration by means of dereddening the spectra. Therefore, we used the dust maps of Schlegel et al. (1998) (SFD) re-calibrated by Schlafly & Finkbeiner (2011), the extinction model of Fitzpatrick (1999), and  $R_v = 3.1$  to deredden the externally calibrated BP/RP spectra. We repeated the above procedure using the extinction model of Cardelli et al. (1989) and found that the resulting flux ratios have minimal differences with those calculated with the Fitzpatrick (1999) model. We chose the SFD maps because they cover the entire sky. Considering the fact that the SFD maps account for the foreground dust, our stars needed to be distant enough or at a galactic latitude great enough for the distance dependence to be neglected. The SAGA stars are halo stars and are thus distant enough ( $D \geq 1$  kpc; Schlafly & Finkbeiner 2011). In total, 81% of the stars in our dataset are either at a distance of  $D \geq 1$  kpc or at a latitude of  $|b| > 30^\circ$ . For the remaining 19%, we calculated the reddening correction from Bonifacio et al. (2000b). For most of the stars, we found no or a very small ( $<0.001$  mag) correction. Only for 4% of the total sample, we found  $E(B - V)$  corrections  $\geq 0.02$  mag, so applying such a correction would have a negligible effect on the distribution in the dereddened flux-ratio plane (Figure 3).

## 2.3. Application of the method

In Paper I we provided coefficients for different pairs of  $T_{\text{eff}}$  and  $\log g$  for the estimation of  $[\text{Fe}/\text{H}]$ . We calibrated the coefficients for application to the real data, but the results did not correspond to the theoretical expectations. Further, the problem of acquiring well-defined effective temperatures and surface gravities for millions of stars so that the metal-poor ones among them could be identified became apparent. We decided to use only quantities that could be directly derived from the spectra (i.e. the flux ratios). The plane of the  $fr_{CaHK/H\beta}$  and  $fr_{G/CaNIR}$  flux ratios (see Figure 3) enabled us to find the loci of metal-poor ( $[\text{Fe}/\text{H}] < -1.0$ ) and further metal-deficient stars. The gray lines in Figure 3 represent different metallicity regimes, with the stars below the dashed-dotted and dotted lines being metal poor ( $[\text{Fe}/\text{H}] < -1$ ) and very metal poor ( $[\text{Fe}/\text{H}] < -2$ ), respectively.

## 3. Results

The results in the right panel of Figure 3 depict a clear correlation between metallicity  $fr_{CaHK/H\beta}$  and  $fr_{G/CaNIR}$  flux ratios. The left panel shows the flux ratios before dereddening, and the right panel shows the dereddened values. We overplotted a dashed-dotted line (Cutoff1) and a dotted line (Cutoff2) to designate flux-ratio areas where objects with  $[\text{Fe}/\text{H}]_{\text{ref}} \leq -1$  and  $[\text{Fe}/\text{H}]_{\text{ref}} \leq -2$ , respectively, are primarily found ( $[\text{Fe}/\text{H}]_{\text{ref}}$  is the reference  $[\text{Fe}/\text{H}]$ ). By selecting metal-poor stars in this way, we found that there was a correlation between a high blending fraction  $\beta$  and contaminants (i.e. stars with  $[\text{Fe}/\text{H}]_{\text{ref}} > -1$ ). We chose the  $\beta$  such that there is a balance between acceptable contamination and completeness since a greater  $\beta$  means a greater number of stars. We defined the completeness as the ratio of the number of selected stars below a certain metallicity threshold to the total number of stars in the dataset that have  $[\text{Fe}/\text{H}]_{\text{ref}} \leq \text{threshold}$ , the success rate as the percent of the selected stars that have  $[\text{Fe}/\text{H}]_{\text{ref}}$  below a certain specified value, and the contamination as the percent of selected stars that have a metallicity above the specified threshold.

The results in Figure 3 were generated after the application of the quality cuts described above. By choosing all the stars below Cutoff1 in Figure 3, we were able to recover from the GALAH-SAGA sample more than 98% of the stars with  $[\text{Fe}/\text{H}] \leq -2$ , all the ultra metal-poor stars ( $[\text{Fe}/\text{H}] \leq -4$ ), and 70% of the stars  $[\text{Fe}/\text{H}] < -1$ . We recorded a success rate of  $\sim 80\%$ ,  $44\%$ , and  $20\%$  for stars with  $[\text{Fe}/\text{H}] \leq -1, -1.5$ , and  $-2$ , respectively. When we selected stars below Cutoff2, we made a trade-off between the success rate and the completeness. We still recovered more than 90% and 94% of the very and extremely metal-poor stars, respectively, but we lost about 40% of those with  $-2 < [\text{Fe}/\text{H}] \leq -1$  compared to the other Cutoff1. The success rate increased significantly to  $\sim 99\%$ ,  $95\%$ , and  $60\%$  for stars with  $[\text{Fe}/\text{H}] \leq -1, -1.5$ , and  $-2$ , respectively (summarized in Figure 4). As before, we selected all the stars that fell below the same dotted and dashed-dotted line without dereddening (left panel of Figure 3) for comparison and calculated the statistics as above. Even though the completeness for different metallicity categories are fairly similar and in some cases even slightly better, the success rate is much lower, and consequently, the contamination is much higher.

Further, we found that by selecting the metal-poor candidates through the flux-ratio plane, we could extrapolate the theoretical method described in Paper I to a broader parameter space. Specifically, the recipe in Paper I was developed for FGK stars in the effective temperature range of 4800-6300 K, and in this study, we retrieved metal-poor stars that have  $4636 \text{ K} \leq T_{\text{eff}} \leq 7150 \text{ K}$ .

Finally, we estimated the iron abundances of our dataset as follows. First, we randomly sampled our GALAH-SAGA dataset and split it into two equal parts. We divided the flux ratios of the first sampled sub-dataset into  $fr_{G/CaNIR}$  bins. Then, we split each of those bins into metallicity bins, for which we calculated the mean  $fr_{CaHK/H\beta}$ . Next, we found the best fits to the sets of  $fr_{CaHK/H\beta}$  -  $[\text{Fe}/\text{H}]$  pairs (Figure 5), which we subsequently used to estimate the iron abundance of the second sub-dataset. We used the following function to perform the fittings:

$$fr_{G/CaNIR} = -a \cdot fr_{CaHK/H\beta}^b + c, \quad (1)$$

where  $a$ ,  $b$ , and  $c$  are the coefficients of the best fit, which are shown in Table 1. The respective results of the metallicity estimation are presented in Figure 6. We were able to infer  $[\text{Fe}/\text{H}]$

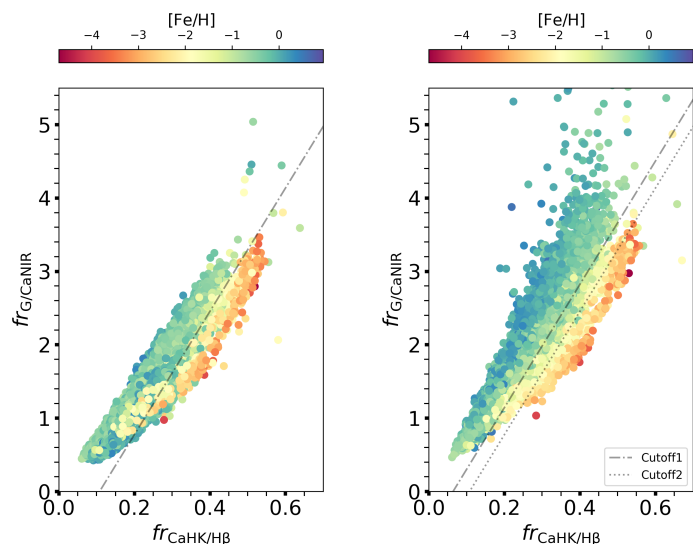


**Fig. 3.** Flux ratios of raw (left panel) and dereddened (right panel) fluxes from *Gaia* BP/RP spectra. The color-coding reflects the metallicity of the stars of the dataset we used. Below the dashed-dotted and dotted lines are the flux-ratio areas where stars with  $[\text{Fe}/\text{H}] \leq -1$  and  $[\text{Fe}/\text{H}] \leq -2$ , respectively, are primarily found.

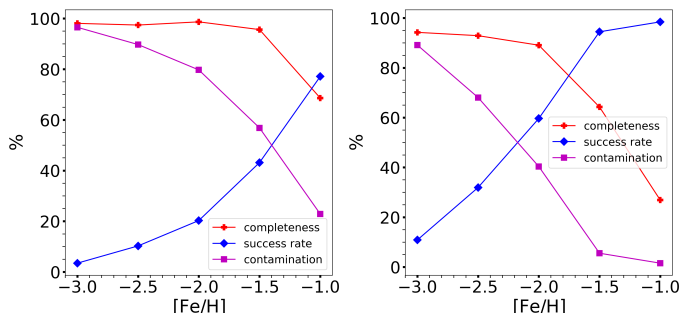


**Fig. 4.** Completeness, success rate, and contamination of the stars that were selected from below the dashed-dotted (left panel) and dotted line (right panel). The stars were selected from a dereddened flux-ratio plane.

**Table 1.** Coefficients of the best fit.

$a$	$b$	$c$	$f_{\text{r}_{\text{G}/\text{CaNIR}}}$
17.497139	1.119316	2.506009	[1.3-1.8]
22.219935	1.512732	2.800237	[1.8-2.3]
29.101554	2.624439	1.18252	[2.3-2.8]
32.268827	3.351201	0.815609	[2.8-3.3]

**Notes.** The  $f_{\text{r}_{\text{G}/\text{CaNIR}}}$  values are the ranges of applicability of each set of coefficients.

with an uncertainty of  $\sigma_{[\text{Fe}/\text{H}]_{\text{inf}}} \sim 0.36$  dex. This precision is sufficient to reliably identify metal-poor stars.

#### 4. OBA stars

OBA stars are young hot stars that can present emission lines in their spectra. When OB stars are highly reddened, they can appear as K-type stars. Hence, good reddening values are essential to tell them apart from metal-poor FGK stars. Also, young or accreting stars can show emission lines at various spectral regions, including the Ca H&K absorption lines. Consequently, the emission in the Ca II H&K lines results in a net weak absorption line

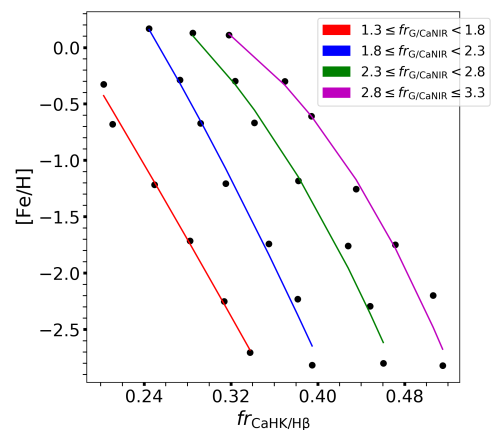


**Fig. 5.** Best fits to the  $f_{\text{r}_{\text{CaHK}/\text{H}\beta}} - [\text{Fe}/\text{H}]$  pairs. The different line colors convey the  $f_{\text{r}_{\text{G}/\text{CaNIR}}}$  range of applicability.

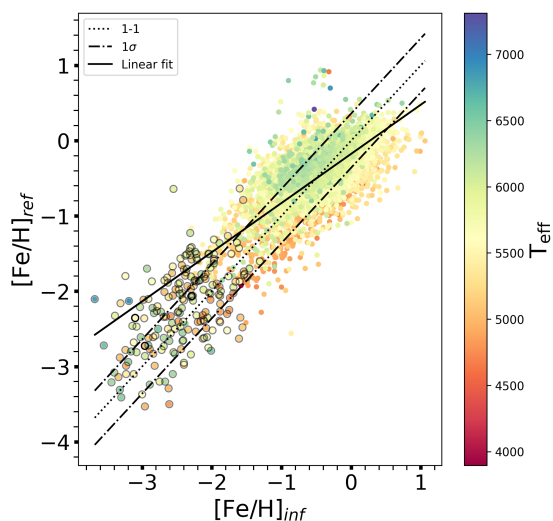


**Fig. 6.** Metallicity estimation of a subset of the GALAH-SAGA dataset. The points that have a black circle around them are located below the black-dotted line in the flux-ratio plane (Figure 3). The color-coding reflects the effective temperature of the stars. We plotted the inferred and reference  $[\text{Fe}/\text{H}]$  on the x- and y-axis respectively.

that masks these stars as metal poor. Therefore, we wished to test to which degree those stars are expected to contaminate a selected metal-poor candidate sample.

We selected a random subset of 200 stars from the OBA stars' golden sample (European Space Agency (ESA) & DPAC Consortium 2022). From those, 193 stars have an externally calibrated BP/RP spectrum, and 173 have a blending fraction  $\beta \leq 0.5$ . We dereddened the externally calibrated spectra as described in Section 2.2 and subsequently computed the flux ratios. In Figure 7 we plot the flux ratios of the OBA golden sample subset. In order to show the effect of extinction, which depends on the color excess rather than on the flux ratios, we used logarithmic axes. The effect of extinction is indicated with an arrow (orange arrow), where its nock and point represent the flux ratios before and after dereddening, respectively, for  $E(B - V) \approx 0.3$  mag. As can be seen, none of the 173 stars appear in the region of the flux-ratio plane where the metal-poor stars are frequently found (Figure 3). However, due to the fact that the location of the stars on the flux-ratio plane depends on the extinction, we caution the reader that highly reddened OBA stars with underestimated color-excess values could appear in the region of metal-

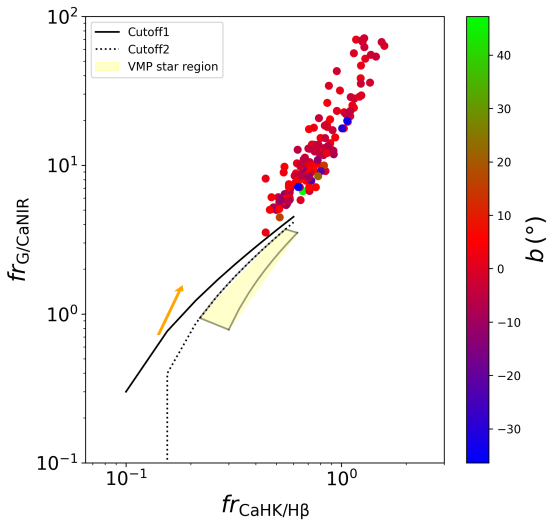


**Fig. 7.** Flux ratios of OBA stars. The solid and dotted lines represent Cutoff1 and Cutoff2, respectively, while the yellow shaded area designates the region that is populated by very metal-poor stars (see Figure 3). The color-coding indicates the Galactic Latitude  $b$  of each star. As can be seen, most of the stars are located on the Galactic plane ( $|b| \leq 10^\circ$ ). The orange arrow illustrates the effect of extinction for a color excess  $E(B-V) \approx 0.3$  mag. The nock and the point of the arrow represent the flux ratios before and after dereddening, respectively.

poor stars (yellow area in Figure 7) and hence contaminate the sample of metal-poor stars selected via this method.

## 5. Observational metal-poor star candidate verification

In order to verify our metal-poor candidate selection method as well as the metallicity estimation presented herein, we selected a sample of stars from *Gaia* DR3 that had not been observed before. We opted to select fairly bright giant stars in order to achieve a good enough signal-to-noise ratio (S/N) for the purpose of deriving precise  $[\text{Fe}/\text{H}]$ . Further, the location of the telescope to be used was known beforehand; hence we used the following selection criteria:  $G=12-13$  mag,  $\text{Ra}=16-02\text{h}$ ,  $\text{Dec}=00^\circ-+20^\circ$ ,  $|b| > 20^\circ$ , and  $\beta \leq 0.5$ , which rendered 90 798 stars. We then computed the flux ratios. From the 90 798 stars, we chose those with flux ratios of  $1 \leq fr_{\text{G}/\text{CaNIR}} \leq 5$ , which left us with 70 509 stars. Next, we selected all the stars below a more stringent cut than Cutoff2, which is a line that is shifted parallel to Cutoff2 by  $0.1 + fr_{\text{CaHK}/\text{H}\beta}$ . This cutoff left us with 77 stars, of which ten had already been observed in high resolution, and their metallicities are, or will be, in the literature. It is worth noting that all ten of the stars that appear in literature are metal poor. The reason we used a more stringent cut was that there is a clear correlation between the inferred metallicity and the position of the star on the flux-ratio plane. We opted to observe candidates with the lowest predicted metallicities, as if we had used Cutoff2, most of the stars above the more stringent cutoff would not have made it into the final target list due to the higher estimated  $[\text{Fe}/\text{H}]_{\text{inf}}$ . We show the distribution of the inferred  $[\text{Fe}/\text{H}]_{\text{inf}}$  for metal-poor candidates that were located between Cutoff2 and our chosen cutoff in Figure A.1. Finally, we estimated the  $[\text{Fe}/\text{H}]$  for the remaining 67 stars, and our final target list was comprised of 32 stars with  $[\text{Fe}/\text{H}]_{\text{inf}} \leq -2.35$ , of which we managed to observe 26. Of the 35 stars that were not included in the target list, eight of them were outside the metal-

licity inference range ( $fr_{\text{G}/\text{CaNIR}} > 3.3$ ). The distribution of the inferred metallicities for the remaining 27 metal-poor candidates that were not included in the final target list is shown in Figure A.2.

### 5.1. Observations and metallicity determinations

The targets were observed at the McDonald Observatory with the Harlan J. Smith 2.7m telescope and the TS23 echelle spectrograph (Tull et al. 1995). The spectra were obtained using a 1.2" slit and 1x1 binning, yielding a resolving power of  $R \sim 60,000$  and covering a wavelength range of 3600-10000 Å. The 26 stars were observed over four nights in August 2023. The data was reduced using standard IRAF packages (Tody 1986, 1993), including correction for bias, flat-field, and scattered light. Table 2 lists the *Gaia* DR3 id, right ascension, declination, Heliocentric Julian Date (HJD), exposure times, the S/N per pixel at 5000Å and heliocentric radial velocities. The heliocentric radial velocities were determined via cross-correlation with a spectrum of the standard star HD 182488 ( $V_{\text{hel}} = -21.2$  kms $^{-1}$ ; Soubiran et al. 2018) obtained on the same run.

We determined the stellar parameters ( $T_{\text{eff}}$ ,  $\log g$ ,  $[\text{Fe}/\text{H}]$ , and  $v_t$ ) for the observed stars from a combination of photometry and equivalent width (EW) measurements of Fe I and Fe II lines and using the software smhr<sup>4</sup> (Casey 2014) to run the radiative transfer code MOOG<sup>5</sup> (Snedden 1973; Sobeck et al. 2011), assuming local thermodynamical equilibrium. We used one dimensional plane-parallel  $\alpha$ -enhanced ( $[\alpha/\text{Fe}] = +0.4$ ) stellar model atmospheres computed from the ATLAS9 grid (Castelli & Kurucz 2003) and line lists from linemake<sup>6</sup> (Placco et al. 2021). Solar abundances were taken from Asplund et al. (2009), and  $T_{\text{eff}}$  for the stars was determined from dereddened *Gaia* G, BP, RP (Anders et al. 2022; Gaia Collaboration et al. 2018), and 2MASS K magnitudes (Cutri et al. 2003) using the color- $T_{\text{eff}}$  relations from Mucciarelli et al. (2021). For the K magnitudes, we used the extinction coefficient from McCall (2004). The  $\log g$  was then determined by requiring ionization equilibrium between the Fe I and Fe II lines and  $v_t$  by requiring no correlation of the Fe I line abundances with reduced EW. Finally, the  $[\text{Fe}/\text{H}]_{\text{spec}}$  of the stars was taken as the mean abundances of the Fe I lines, and the uncertainties are the standard deviation of these. The final stellar parameters are listed in Table 2.

### 5.2. Results

The stellar parameters of the observed stars are shown in Table 2. As the parameters show, all observed stars are metal-poor FGK stars. The uncertainty in our metallicity inference is  $\sigma_{[\text{Fe}/\text{H}]_{\text{inf}}} \sim 0.31$ , which agrees with the uncertainty in deriving metallicities for the GALAH-SAGA sample ( $\sigma_{[\text{Fe}/\text{H}]_{\text{inf}}} \sim 0.36$ ), as described above. Figure 8 shows  $[\text{Fe}/\text{H}]_{\text{inf}}$  versus the spectroscopic-determined  $[\text{Fe}/\text{H}]_{\text{spec}}$ . Further, 100% of the observed stars are very metal-poor, 58% have  $[\text{Fe}/\text{H}] < -2.5$ , and 8% are EMP. Lastly, we did not have any contamination from OBA stars, which agrees with our finding in Section 4.

## 6. Catalog of stellar $[\text{Fe}/\text{H}]$

For the purpose of providing the community with a catalog of metallicities, we used the following criteria from The Milky

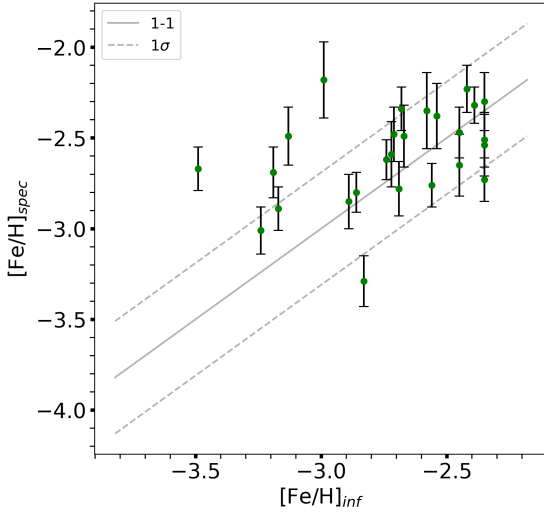
<sup>4</sup> <https://github.com/andycasey/smhr>

<sup>5</sup> <https://github.com/alexji/moog17scat>

<sup>6</sup> <https://github.com/vmplacco/linemake>

**Table 2.** Stellar parameters and observation log of observed metal-poor candidates.

<i>Gaia</i> DR3 ID	RA (J2000) (hrs)	Dec (J2000) (°)	HJD	exp time (s)	S/N 5000Å	$V_{hel} \pm \sigma$ (kms <sup>-1</sup> )	$[Fe/H]_{inf}$ (dex)	G (mag)	$T_{eff}$ (K)	log <i>g</i> (dex)	$[Fe/H]_{spec}$ (dex)	$\sigma_{[Fe/H]_{spec}}$ (dex)	$v_t$ (kms <sup>-1</sup> )	$E(B-V)$ (mag)
4560234719702983552	17 00 58.86	+18 12 48.76	2460177.61	3x1200	38	-200.2 ± 0.7	-3.49	12.95	5512	1.81	-2.67	0.12	2.26	0.067
2770306858573498880	23 54 36.90	+13 43 33.61	2460175.83	3x900	43	-91.8 ± 0.9	-3.19	12.75	5280	2.42	-2.69	0.14	1.63	0.043
2740778202499153280	00 09 13.91	+03 34 27.64	2460175.88	3x1200	29	-63.3 ± 0.7	-3.17	12.52	5172	2.18	-2.89	0.12	1.58	0.024
2783063972298129280	00 42 31.57	+18 34 52.58	2460175.93	3x1200	23	-349.7 ± 0.7	-3.13	12.53	5463	1.92	-2.49	0.16	1.98	0.058
38721161695303808	03 55 46.04	+13 28 40.99	2460178.96	3x1200	11	59.1 ± 1.1	-2.99	12.89	5666	3.09	-2.18	0.21	1.95	0.298
1788649988097920768	21 20 25.52	+19 16 40.19	2460175.75	3x1200	35	2.1 ± 1.4	-3.24	12.84	5868	1.95	-3.01	0.13	2.65	0.078
2739719922558093440	23 50 58.88	+02 36 12.99	2460176.84	3x600	38	15.4 ± 1.3	-2.89	12.10	6488	3.40	-2.85	0.15	1.77	0.033
3268830653286376704	03 15 35.79	+02 25 49.29	2460176.96	3x1200	27	203.3 ± 0.7	-2.72	12.81	5114	2.18	-2.59	0.18	1.49	0.095
4446252678577892224	16 34 16.18	+08 49 40.19	2460178.63	3x900	22	-12.1 ± 0.8	-2.71	12.27	4995	1.88	-2.48	0.15	1.81	0.065
2719036833232602752	22 57 03.19	+12 58 25.60	2460175.80	3x600	41	-242.8 ± 0.5	-2.68	12.15	5316	1.90	-2.34	0.12	2.06	0.047
4229999872631438848	20 32 11.41	+01 02 05.16	2460177.71	3x1200	37	-240.6 ± 0.5	-2.67	12.82	5221	2.71	-2.49	0.17	1.36	0.097
1757147197551005952	21 09 25.50	+11 48 44.80	2460175.70	3x1200	26	71.0 ± 1.3	-2.86	12.60	5440	1.23	-2.80	0.11	2.29	0.108
1730672812979631104	20 56 02.56	+02 07 13.56	2460178.69	3x1200	14	-160.8 ± 1.0	-2.58	12.84	5194	1.09	-2.35	0.21	2.38	0.107
2814304091236720000	23 27 36.00	+15 23 54.70	2460177.80	3x1200	31	-81.5 ± 0.9	-2.56	12.96	5096	1.95	-2.76	0.12	2.05	0.054
4561199025759521920	17 02 37.48	+19 17 21.35	2460177.66	3x1200	31	-174.7 ± 0.5	-2.54	12.79	5267	2.57	-2.38	0.18	1.73	0.088
4503007613380083328	17 53 57.89	+17 45 19.99	2460176.64	3x1200	50	-100.9 ± 1.0	-2.69	12.42	6030	4.22	-2.78	0.15	1.72	0.081
4449403019908847488	16 48 40.46	+13 32 43.83	2460176.61	3x600	36	195.9 ± 0.7	-2.45	12.15	5214	2.33	-2.65	0.17	1.48	0.060
257440079017777408	01 58 30.71	+11 18 42.38	2460177.93	3x1200	38	-101.6 ± 1.0	-2.42	12.58	6547	4.04	-2.23	0.13	1.62	0.116
2554217295745049856	00 39 13.34	+04 23 33.16	2460176.87	3x1200	38	-145.0 ± 0.9	-2.39	12.81	6235	3.51	-2.32	0.10	1.55	0.027
2580053787477560576	01 19 10.86	+10 07 08.75	2460177.85	3x1200	40	-29.0 ± 0.6	-2.45	12.55	5139	2.33	-2.47	0.14	1.68	0.070
2732958716319826048	22 33 41.08	+14 49 05.58	2460178.73	3x900	20	26.8 ± 0.9	-2.35	12.23	5636	2.59	-2.54	0.17	1.24	0.069
2756350516963035904	23 40 19.64	+05 34 00.66	2460176.80	3x1200	33	111.7 ± 1.7	-2.35	12.91	6235	2.40	-2.73	0.12	1.50	0.081
2698131578134995456	21 34 27.89	+04 04 38.23	2460177.76	3x900	39	-299.1 ± 0.6	-2.35	12.27	5294	2.90	-2.51	0.15	1.39	0.054
4432234794379005952	16 34 54.04	+02 06 14.94	2460178.60	3x900	17	85.5 ± 0.8	-2.35	12.23	5257	1.60	-2.30	0.16	1.99	0.062
2706127364131151744	22 41 26.08	+05 07 30.91	2460178.77	3x1000	21	-139.7 ± 2.1	-2.83	12.65	5648	2.56	-3.29	0.14	2.09	0.077
1733398605383859840	21 09 34.21	+05 14 05.85	2460176.69	3x1200	30	-52.3 ± 0.7	-2.74	12.70	5200	1.26	-2.62	0.11	1.97	0.112


**Fig. 8.**  $[Fe/H]_{inf}$  versus  $[Fe/H]_{spec}$ . The solid gray line is the 1 to 1 line, and the dashed gray line designates the  $1\sigma$  uncertainty ( $\sigma_{[Fe/H]_{spec}} = 0.31$  dex) in  $[Fe/H]_{spec}$ .

Way Halo High-Resolution Survey (Christlieb et al. 2019) of the 4-meter Multi-Object Spectroscopic Telescope (4MOST) (De Jong et al. 2019) combined with the criteria developed for this work to select stars from *Gaia* DR3:  $|b| > 10^\circ$ ,  $0.15 \text{ mag} \leq (BP - RP)_0 < 1.1 \text{ mag}$ , blending index  $\beta \leq 0.5$ ,  $1.3 \leq fr_{G/CaNIR} \leq 3.3$ , and  $E(B - V) \leq 1.5 \text{ mag}$ . These criteria yielded 10 861 062 stars, for which we estimated the metallicity. We note that 225 498 stars in this catalog have  $[Fe/H]_{inf} < -2.0$ . Further, in our catalog, 2236 stars have  $[Fe/H]_{inf} < -5.0$ , which suggests that these stars probably have emission lines rather than being metal-poor. We cross-matched the stars of our catalog that have  $[Fe/H]_{inf} < -2.0$  with the *Gaia* OBA golden sample (European Space Agency (ESA) & DPAC Consortium 2022), and we found that 104 of the stars are indeed OBA stars. Out of those OBA contaminants, eight have an estimated metallicity  $[Fe/H]_{inf} < -5.0$  in the catalog. A sample of the catalog is shown in Table 3.

## 7. Comparison to other catalogs

As already described in the introduction, many studies have taken advantage of the wealth of information encapsulated in the *Gaia* BP/RP spectra and have provided to the community catalogs of stellar atmospheric parameters. Specifically, the catalogs of Andrae et al. (2023b) and Martin et al. (2023) have been shown to work very well in the metal-poor regime. We used the GALAH-SAGA verification sub-dataset (Figure 6) to compare the metallicities we estimated versus those of Andrae et al. (2023b) and Martin et al. (2023). The  $[Fe/H]_{inf}$  we estimated for this sub-dataset are independent of the fitting procedure. Figure 9 shows the performance of each catalog. At first glance, it is clear that the catalog of Martin et al. (2023) performs better in the metal-poor regime than ours and that of Andrae et al. (2023b). However, the difference in accuracy of the inferred metallicities in all three catalogs is comparable. Specifically for  $[Fe/H]_{ref} < -2$ , the iron abundances of Martin et al. (2023) and Andrae et al. (2023b) have  $\sigma \sim 0.39$  and are 0.1 dex better than ours. For  $[Fe/H]_{ref} < -3$ , the standard deviation of the estimated metallicities in all three catalogs is the same, that is,  $\sim 0.36$  dex. In the metal-rich regime, our metallicities have uncertainties that are  $\sim 0.2$  dex higher than those of the other two catalogs, whose performance is similar,  $\sigma \sim 0.24$  dex.

## 8. Summary

We applied the metal-poor star candidate selection recipe described in Paper I (Xylakis-Dornbusch et al. 2022) to *Gaia* DR3 BP/RP spectra. In order to do so, we updated the selection method. Specifically, instead of using the effective temperature and surface gravity information, we only used the flux ratios,  $fr_{G/CaNIR}$  and  $fr_{CaHK/H\beta}$ , determined in Paper I to estimate the metallicity of the stars. We addressed the extinction by means of dereddening the spectra before computing the flux ratios, and we found that the method can be applied to stars with color excesses  $E(B - V) \leq 1.5$ . We then used BP/RP spectra through a cross-match between *Gaia* DR3 and GALAH DR3 as well as with the SAGA database to validate the selection method. We were able to estimate the  $[Fe/H]$  solely with the use of the flux ratios, with an uncertainty of  $\sigma_{[Fe/H]_{inf}} \sim 0.36$  dex. Next, we assessed to which degree OBA stars could contaminate a metal-

**Table 3.** Sample of the catalog of metallicities.

<i>source_id</i>	<i>RA</i> (J2000) ( $^{\circ}$ )	<i>DEC</i> (J2000) ( $^{\circ}$ )	<i>E</i> ( <i>B</i> – <i>V</i> ) (mag)	<i>fr</i> <sub>CaHK/H<math>\beta</math></sub>	<i>fr</i> <sub>G/CaNIR</sub>	[Fe/H] <sub>inf</sub> (dex)	<i>G</i> (mag)	<i>G</i> <sub>BP</sub> (mag)	<i>G</i> <sub>RP</sub> (mag)
1736084918450522624	311.672374	6.454326	0.086352	0.395785	3.040589	-0.65	14.839189	15.116240	14.387665
1736086121041383936	311.640473	6.501470	0.080705	0.386366	2.951276	-0.53	12.410907	12.699553	11.959683
1736086464640617472	311.605184	6.517305	0.079810	0.384081	3.279787	-0.51	12.523436	12.753575	12.055906
1736086769579627008	311.686028	6.547942	0.081594	0.440737	2.951817	-1.27	14.591786	14.878093	14.132823
1736089213417835264	311.740409	6.639877	0.088562	0.383000	2.963972	-0.50	14.826837	15.120335	14.363322
1736089934974194688	311.614227	6.572804	0.078512	0.320748	2.815581	0.09	12.647016	12.943399	12.197193
1736090381648971776	311.524228	6.550632	0.083777	0.382586	2.909278	-0.49	13.581572	13.875311	13.124882
1736093847685000960	311.868064	6.611197	0.092579	0.410637	3.239939	-0.84	14.073834	14.347256	13.636151
1736099693138064384	311.706790	6.756967	0.085753	0.351283	2.938921	-0.17	13.712016	14.000586	13.259321
1736099693138065408	311.698148	6.754874	0.084601	0.376363	2.852484	-0.42	15.257664	15.554148	14.791958

**Notes.** The color excess values,  $E(B - V)$ , are from Schlegel et al. (1998) (re-calibrated by Schlafly & Finkbeiner (2011)). The full catalog is available at the CDS.

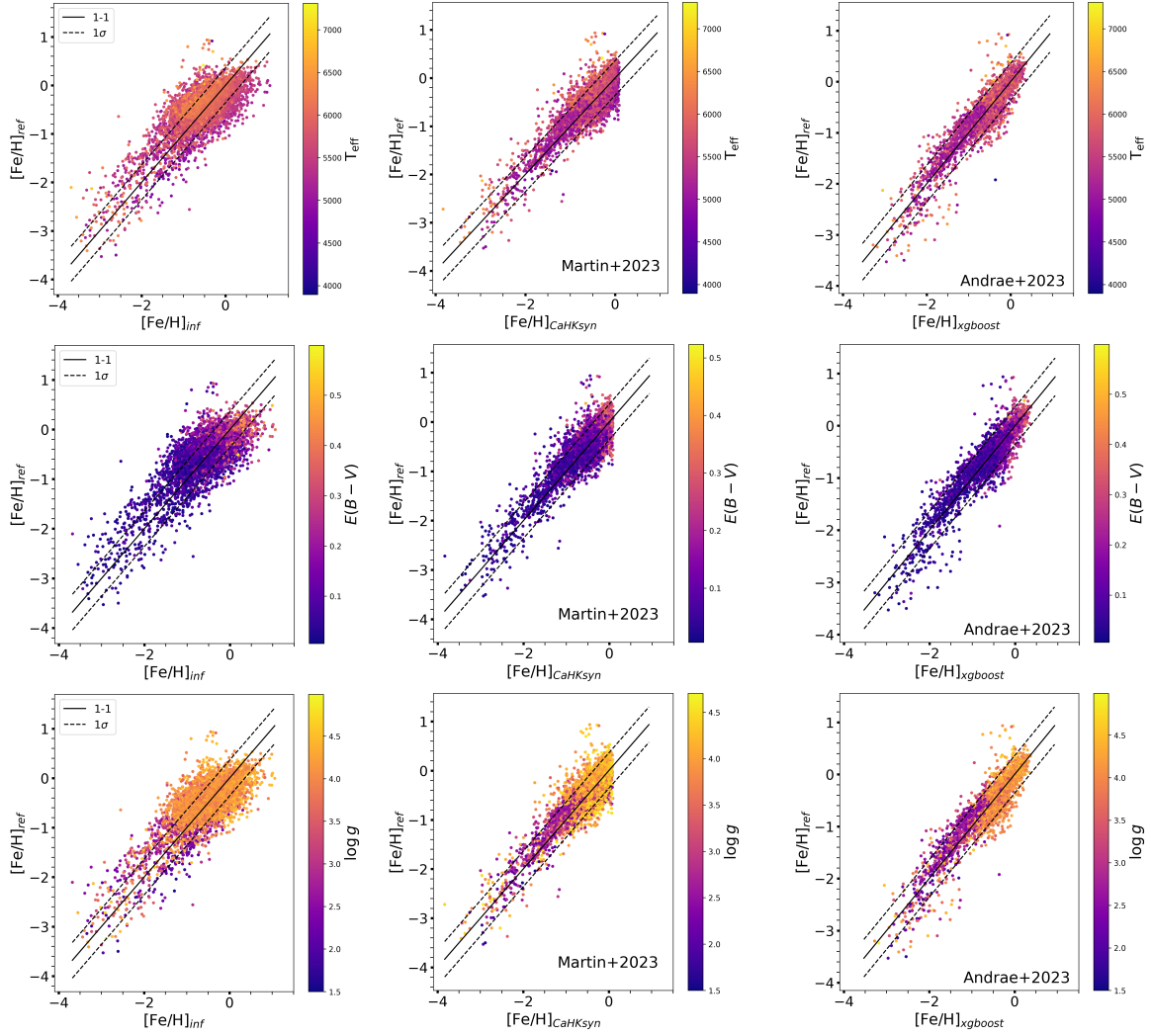


**Fig. 9.** Comparison of our derived metallicities with those from the Andrae et al. (2023b) (XGBOOST) and Martin et al. (2023) (CaHK<sub>synth</sub>) catalogs. Top (from left to right): Metallicities of our, XGBOOST, and CaHK<sub>synth</sub> catalogs are plotted, respectively, for the GALAH-SAGA validation dataset ([Fe/H]<sub>ref</sub>). The color-coding reflects the effective temperature of the stars. Middle and bottom: Same as the top panels but the color-coding depicts the color excess and surface gravity, respectively. The solid black line shows the 1-1 line, while the dashed lines show a  $\sigma = 0.36$  dex uncertainty.

poor candidate sample selected via the method described herein. We found that it is not very likely as long as one has a high level of color excesses at their disposal to perform the dereddening of the spectra. Following this, we selected stars from *Gaia* DR3 via our updated selection procedure for spectroscopic validation.

We observed 26 stars, of which 100% had [Fe/H] < -2.0, 58% had [Fe/H] < -2.5, and 8% had [Fe/H] < -3.0. We inferred the metallicities for this sample of stars prior to observations with an uncertainty  $\sigma_{[\text{Fe}/\text{H}]_{\text{inf}}} \sim 0.31$ . Finally, we assembled a

catalog of metallicities for 10 861 062, of which 225 498 have  $[\text{Fe}/\text{H}]_{\text{inf}} < -2.0$ .

**Acknowledgements.** We thank the anonymous referee for their comments, which helped improve this manuscript. This work was funded by the Deutsche Forschungsgemeinschaft (DFG, German Research Foundation) – Project-ID 138713538 – SFB 881 (“The Milky Way System”, subproject A04). This research was supported by the Australian Research Council Centre of Excellence for All Sky Astrophysics in 3 Dimensions (ASTRO 3D), through project number CE170100013. This work was supported by computational resources provided by the Australian Government through the National Computational Infrastructure (NCI) under the National Computational Merit Allocation Scheme and the ANU Merit Allocation Scheme (project y89). TXD acknowledges support from the Heidelberg Graduate School for Physics (HGSFP). TTH acknowledges support from the Swedish Research Council (VR 2021-05556). This work made use of the Third Data Release of the GALAH Survey (Buder et al. 2021). The GALAH Survey is based on data acquired through the Australian Astronomical Observatory, under programs: A/2013B/13 (The GALAH pilot survey); A/2014A/25, A/2015A/19, A2017A/18 (The GALAH survey phase 1); A2018A/18 (Open clusters with HERMES); A2019A/1 (Hierarchical star formation in Ori OB1); A2019A/15 (The GALAH survey phase 2); A/2015B/19, A/2016A/22, A/2016B/10, A/2017B/16, A/2018B/15 (The HERMES-TESS program); and A/2015A/3, A/2015B/1, A/2015B/19, A/2016A/22, A/2016B/12, A/2017A/14 (The HERMES K2-follow-up program). We acknowledge the traditional owners of the land on which the AAT stands, the Gamilaraay people, and pay our respects to elders past and present. This paper includes data that has been provided by AAO Data Central (datacentral.org.au). This work has made use of data from the European Space Agency (ESA) mission *Gaia* (<https://www.cosmos.esa.int/gaia>), processed by the *Gaia* Data Processing and Analysis Consortium (DPAC, <https://www.cosmos.esa.int/web/gaia/dpac/consortium>). Funding for the DPAC has been provided by national institutions, in particular the institutions participating in the *Gaia* Multilateral Agreement. This work has made use of the Python package *GaiaXPY*, developed and maintained by members of the *Gaia* Data Processing and Analysis Consortium (DPAC) and in particular, Coordination Unit 5 (CU5), and the Data Processing Centre located at the Institute of Astronomy, Cambridge, UK (DPCI).

## References

Abdurro’uf, Accetta, K., Aerts, C., et al. 2022, *ApJS*, 259, 35  
 Anders, F., Khalatyan, A., Queiroz, A. B. A., et al. 2022, *A&A*, 658, A91  
 Andrae, R., Fouesneau, M., Sordo, R., et al. 2023a, *A&A*, 674, A27  
 Andrae, R., Rix, H.-W., & Chandra, V. 2023b, *ApJS*, 267, 8  
 Asplund, M., Grevesse, N., Sauval, A. J., & Scott, P. 2009, *ARA&A*, 47, 481  
 Bailer-Jones, C. A. L., Andrae, R., Arcaj, B., et al. 2013, *A&A*, 559, A74  
 Bailer-Jones, C. A. L., Rybizki, J., Fouesneau, M., Mantelet, G., & Andrae, R. 2018, *AJ*, 156, 58  
 Beers, T. C. & Christlieb, N. 2005, *ARA&A*, 43, 531  
 Bellazzini, M., Massari, D., De Angeli, F., et al. 2023, *A&A*, 674, A194  
 Bonifacio, P., Caffau, E., & Molaro, P. 2000a, *A&AS*, 145, 473  
 Bonifacio, P., Monai, S., & Beers, T. C. 2000b, *AJ*, 120, 2065  
 Buder, S., Sharma, S., Kos, J., et al. 2021, *MNRAS*, 506, 150  
 Cardelli, J. A., Clayton, G. C., & Mathis, J. S. 1989, *ApJ*, 345, 245  
 Casey, A. R. 2014, PhD thesis, Australian National University, Canberra  
 Castelli, F. & Kurucz, R. L. 2003, in *Modelling of Stellar Atmospheres*, ed. N. Piskunov, W. W. Weiss, & D. F. Gray, Vol. 210, A20  
 Chen, T. & Guestin, C. 2016, in *Proceedings of the 22nd ACM SIGKDD International Conference on Knowledge Discovery and Data Mining, KDD ’16 (ACM)*  
 Christlieb, N., Battistini, C., Bonifacio, P., et al. 2019, *The Messenger*, 175, 26  
 Cunningham, E. C., Hunt, J. A. S., Price-Whelan, A. M., et al. 2023, arXiv e-prints, arXiv:2307.08730  
 Cutri, R. M., Skrutskie, M. F., van Dyk, S., et al. 2003, *VizieR Online Data Catalog*, II/246  
 De Angeli, F., Weiler, M., Montegriffo, P., et al. 2023, *A&A*, 674, A2  
 De Jong, R. S., Agertz, O., Berbel, A. A., et al. 2019, *Published in The Messenger* vol. 175, pp. 3-11, March 2019.  
 European Space Agency (ESA) & DPAC Consortium. 2022, *Gaia DR3 source IDs of O, B, and A-type stars*  
 Fitzpatrick, E. L. 1999, *PASP*, 111, 63  
 Fouesneau, M., Frémat, Y., Andrae, R., et al. 2023, *A&A*, 674, A28  
 Gaia Collaboration, Babusiaux, C., van Leeuwen, F., et al. 2018, *A&A*, 616, A10  
 Gaia Collaboration, Prusti, T., de Bruijne, J. H. J., et al. 2016, *A&A*, 595, A1  
 Gaia Collaboration, Vallenari, A., Brown, A. G. A., et al. 2023, *A&A*, 674, A1  
 Green, G. 2018, *The Journal of Open Source Software*, 3, 695  
 Katz, D., Sartoretti, P., Guerrier, A., et al. 2023, *A&A*, 674, A5

Li, H., Aoki, W., Matsuno, T., et al. 2022, *ApJ*, 931, 147  
 Martin, N. F., Starkenburg, E., Yuan, Z., et al. 2023, arXiv e-prints, arXiv:2308.01344  
 McCall, M. L. 2004, *AJ*, 128, 2144  
 Mucciarelli, A., Bellazzini, M., & Massari, D. 2021, *A&A*, 653, A90  
 Placco, V. M., Sneden, C., Roederer, I. U., et al. 2021, *Research Notes of the American Astronomical Society*, 5, 92  
 Riello, M., De Angeli, F., Evans, D. W., et al. 2021, *A&A*, 649, A3  
 Rix, H.-W., Chandra, V., Andrae, R., et al. 2022, *ApJ*, 941, 45  
 Schlafly, E. F. & Finkbeiner, D. P. 2011, *ApJ*, 737, 103  
 Schlafly, E. F., Meisner, A. M., & Green, G. M. 2019, *ApJS*, 240, 30  
 Schlegel, D. J., Finkbeiner, D. P., & Davis, M. 1998, *ApJ*, 500, 525  
 Skrutskie, M. F., Cutri, R. M., Stiening, R., et al. 2006, *AJ*, 131, 1163  
 Sneden, C. A. 1973, PhD thesis, University of Texas, Austin  
 Sobeck, J. S., Kraft, R. P., Sneden, C., et al. 2011, *AJ*, 141, 175  
 Soubiran, C., Jasniewicz, G., Chemin, L., et al. 2018, *A&A*, 616, A7  
 Starkenburg, E., Martin, N., Youakim, K., et al. 2017, *MNRAS*, 471, 2587  
 Suda, T., Hidaka, J., Aoki, W., et al. 2017, *PASJ*, 69, 76  
 Suda, T., Katsuta, Y., Yamada, S., et al. 2008, *PASJ*, 60, 1159  
 Suda, T., Yamada, S., Katsuta, Y., et al. 2011, *MNRAS*, 412, 843  
 Tody, D. 1986, in *Society of Photo-Optical Instrumentation Engineers (SPIE) Conference Series*, Vol. 627, *Instrumentation in astronomy VI*, ed. D. L. Crawford, 733  
 Tody, D. 1993, in *Astronomical Society of the Pacific Conference Series*, Vol. 52, *Astronomical Data Analysis Software and Systems II*, ed. R. J. Hanisch, R. J. V. Brissenden, & J. Barnes, 173  
 Tull, R. G., MacQueen, P. J., Sneden, C., & Lambert, D. L. 1995, *PASP*, 107, 251  
 Wang, C., Huang, Y., Yuan, H., et al. 2022, *ApJS*, 259, 51  
 Xylakis-Dornbusch, T., Christlieb, N., Lind, K., & Nordlander, T. 2022, *A&A*, 666, A58  
 Yamada, S., Suda, T., Komiya, Y., Aoki, W., & Fujimoto, M. Y. 2013, *MNRAS*, 436, 1362  
 Yao, Y., Ji, A. P., Koposov, S. E., & Limberg, G. 2024, *MNRAS*, 527, 10937  
 Zhang, X., Green, G. M., & Rix, H.-W. 2023, *MNRAS*, 524, 1855

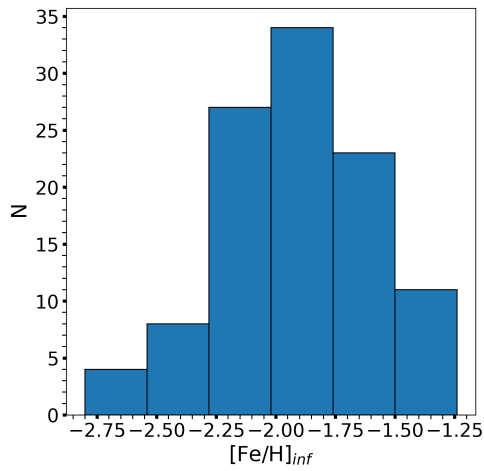


**Fig. A.1.** Distribution of  $[\text{Fe}/\text{H}]_{inf}$  for metal-poor candidates located between Cutoff2 and the cutoff we used to select candidates for observations.

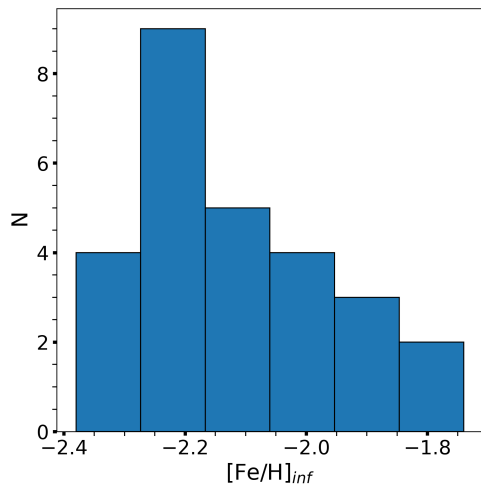


**Fig. A.2.** Distribution of  $[\text{Fe}/\text{H}]_{inf}$  of the 27 metal-poor candidates that were not included in the final target list.

## Appendix A: Additional figures

We present additional figures that are described in Section 5. We show the inferred metallicity distribution of the candidate metal-poor stars that are located on the flux-ratio plane between Cutoff2 and the more stringent cut we used to select stars for observations. Lastly, we show the metallicity distribution of the metal-poor candidates below the stringent cutoff not included in the target list.



## Chapter 5

# The *R*-Process Alliance: Analysis of Limited-*r* Stars

The manuscript presented in this chapter (PaperIII) is accepted for publication in *A&A* with the following author list: T. Xylakis-Dornbusch, T. T. Hansen, T. C. Beers, N. Christlieb, R. Ezzeddine, A. Frebel, E. Holmbeck, V. M. Placco, I. U. Roederer, C. M. Sakari, and C. Sneden. The research that I conducted, was a comprehensive analysis of the abundances and kinematics of three metal-poor stars (two  $r_{lim}$  and one  $r$ -I star). Along with the three stars, I analysed the kinematics of all the  $r_{lim}$  stars that have been discovered to date and can be found in the literature. The *R*-Process Alliance, that is, most of the co-authors of this paper, provided to me the reduced spectra of the three stars, as well as their estimated  $T_{\text{eff}}$  and  $\log g$ . T. T. Hansen computed the uncertainties listed in Table A.1., generated Figure 4, and helped me in the editing of the manuscript. Discussions with T. T. Hansen, and comments from all co-authors helped me improve the manuscript. Part of Table 4, Tables A.1., and inferred orbital parameters are provided in the Appendix B.

# The *R*-Process Alliance: Analysis of limited-*r* stars

T. Xylakis-Dornbusch<sup>1</sup>, T. T. Hansen<sup>2</sup>, T. C. Beers<sup>3,4</sup>, N. Christlieb<sup>1</sup>, R. Ezzeddine<sup>5</sup>, A. Frebel<sup>6,4</sup>, E. Holmbeck<sup>7</sup>, V. M. Placco<sup>8</sup>, I. U. Roederer<sup>9,4</sup>, C. M. Sakari<sup>10</sup>, and C. Sneden<sup>11</sup>

<sup>1</sup> Zentrum für Astronomie der Universität Heidelberg, Landessternwarte, Königstuhl 12, 69117 Heidelberg, Germany  
e-mail: txylaki@lsw.uni-heidelberg.de

<sup>2</sup> Department of Astronomy, Stockholm University, AlbaNova University Center, SE-106 91 Stockholm, Sweden

<sup>3</sup> Department of Physics, University of Notre Dame, Notre Dame, IN 46556, USA

<sup>4</sup> JINA Center for the Evolution of the Elements, USA

<sup>5</sup> Department of Astronomy, University of Florida, 211 Bryant Space Science Center, Gainesville, FL 32601, USA

<sup>6</sup> Department of Physics and Kavli Institute for Astrophysics and Space Research, Massachusetts Institute of Technology, Cambridge, MA 02139, USA

<sup>7</sup> The Observatories of the Carnegie Institution for Science, 813 Santa Barbara St, Pasadena, CA 91101, USA

<sup>8</sup> NSF's NOIRLab, Tucson, AZ 85719, USA

<sup>9</sup> Department of Physics, North Carolina State University, Raleigh, NC 27695, USA

<sup>10</sup> Department of Physics & Astronomy, San Francisco State University, San Francisco CA 94132, USA

<sup>11</sup> Department of Astronomy and McDonald Observatory, The University of Texas, Austin, TX 78712, USA

## ABSTRACT

**Context.** In recent years, the *R*-Process Alliance (RPA) has conducted a successful search for stars that are enhanced in elements produced by the rapid neutron-capture (*r*-)process. In particular, the RPA has uncovered a number of stars that are strongly enriched in light *r*-process elements, such as Sr, Y, and Zr. These so-called limited-*r* stars were investigated to explore the astrophysical production site(s) of these elements.

**Aims.** We investigate the possible formation sites for light neutron-capture elements by deriving detailed abundances for neutron-capture elements from high-resolution spectra with a high signal-to-noise ratio of three limited-*r* stars.

**Methods.** We conducted a kinematic analysis and a 1D local thermodynamic equilibrium spectroscopic abundance analysis of three stars. Furthermore, we calculated the lanthanide mass fraction ( $X_{\text{La}}$ ) of our stars and of limited-*r* stars from the literature.

**Results.** We found that the abundance pattern of neutron-capture elements of limited-*r* stars behaves differently depending on their [Ba/Eu] ratios, and we suggest that this should be taken into account in future investigations of their abundances. Furthermore, we found that the  $X_{\text{La}}$  of limited-*r* stars is lower than that of the kilonova AT2017gfo. The latter seems to be in the transition zone between limited-*r*  $X_{\text{La}}$  and that of *r*-I and *r*-II stars. Finally, we found that unlike *r*-I and *r*-II stars, the current sample of limited-*r* stars is largely born in the Galaxy and is not accreted.

**Key words.**

## 1. Introduction

Since the pioneering work of Burbidge et al. (1957) and Cameron (1957), astronomers have known that elements beyond the iron peak are formed via the slow and rapid neutron-capture processes (*s*-process and *r*-process, respectively). However, the astrophysical site for the *r*-process is still highly debated. It has been hypothesized that two types of *r*-processes or two distinct sites may exist, differing by the available neutron flux. In the main *r*-process, all elements up to uranium can be produced, and in a neutron-starved, so-called limited *r*-process, only the lighter elements can be formed (up to  $\sim$ Ba) (Frebel 2018). This limited *r*-process, also referred to as the weak *r*-process (Hansen et al. 2012) or the light-element primary process (LEPP) (Travaglio et al. 2004), was introduced in order to explain the observed abundance distribution of light *r*-process elements ( $32 < Z < 56$ ) in metal-poor stars, which differs from the behavior of the heavier elements.

The *r*-process-enhanced (RPE) stars are divided into two subcategories, namely *r*-I and *r*-II stars, for which  $+0.3 < [\text{Eu}/\text{Fe}] \leq +0.7$  and  $[\text{Ba}/\text{Eu}] < 0.0$ , and  $[\text{Eu}/\text{Fe}] > +0.7$  and  $[\text{Ba}/\text{Eu}] < 0.0$ , respectively (Christlieb et al. 2004; Beers &

Christlieb 2005; Holmbeck et al. 2020). Multiple studies have found that for the *r*-I and *r*-II stars, a remarkable match is seen between the abundances of the old metal-poor stars and the Sun for elements between the second and third *r*-process peaks ( $55 < Z < 73$ ) (Sneden et al. 2008; Cowan et al. 2021). However, this universality does not extend to the lighter elements, where a larger scatter is seen. In particular, some stars display an enhancement in the light *r*-process elements compared to the heavy elements, which is evident when scaled to the Solar System *r*-process abundance pattern. These stars are characterized by the following abundance ratios:  $[\text{Eu}/\text{Fe}] < +0.3$ ,  $[\text{Sr}/\text{Ba}] > +0.5$  and  $[\text{Sr}/\text{Eu}] > 0.0$ , and they are called limited-*r* ( $r_{\text{lim}}$ ) stars (Frebel 2018).

The first star that was discovered to display this type of abundance pattern in its neutron-capture elements was HD 122563 (Sneden & Parthasarathy 1983; Honda et al. 2006, 2007). This star was found to exhibit an abundance pattern of neutron-capture elements that gradually decreases with growing atomic number. This was unlike any abundance pattern seen before, and it is dissimilar to the pattern seen in *r*-I and *r*-II stars. The main question astronomers have tried to answer since the discovery

of this difference in  $r$ -process stars is whether the limited and main  $r$ -process components are the results of different events, or if they are the product of the same event for which different initial conditions or locations dictate the extent of the range of elements produced.

The community still speculates about the production sites of the  $r$ -process elements, with the exception of neutron star mergers (NSMs), which were confirmed as such after the observation of the kilonova (KN) AT2017gfo, which was the electromagnetic counterpart (Coulter et al. 2017) of the gravitational event GW170817 (Abbott et al. 2017a,b). Other candidate sites are collapsars (Siegel et al. 2019; Brauer et al. 2021), which are fast-rotating massive stars that end their lives as supernovae (SNe), magneto-rotational core-collapse supernovae (MR-SNe) (Winteler et al. 2012), and quark deconfinement SNe (Fischer et al. 2018, 2020). The two former sites can theoretically produce both the main and limited components of the  $r$ -process, whereas the latter is a candidate for a limited  $r$ -process. Specifically, Nishimura et al. (2017) found that core-collapse-SNe that are driven by magneto-rotational instability can produce a variety of  $r$ -process patterns that range from the limited- $r$  to the solar  $r$ -process pattern, when neutrino heating and magnetic fields are similar.

To investigate the abundance signature of the limited- $r$  neutron-capture elements and to thereby constrain the possible production sites for these elements, the  $R$ -Process Alliance (RPA) has included these stars in their search. The search also aims to identify highly  $r$ -process-enhanced stars. Following Frebel (2018), the RPA selected stars with  $[\text{Eu}/\text{Fe}] < +0.3$ ,  $[\text{Sr}/\text{Ba}] > +0.5$  and  $[\text{Sr}/\text{Eu}] > 0.0$  as  $r_{lim}$ ; in the first four data releases, the RPA discovered 42 stars new  $r_{lim}$  stars (Hansen et al. 2018; Sakari et al. 2018; Ezzeddine et al. 2020; Holmbeck et al. 2020). This paper reports the first detailed analysis of three of these  $r_{lim}$  stars. The paper is organized as follows. In Section 2, we describe the observations of the stars, and in Section 3, we report the stellar parameters and determine the elemental abundances. The results are presented in Section 4. In Section 5, we discuss the possible birthplace of the  $r_{lim}$  stars and whether NSMs could be the production site for the elements observed in the atmospheres of these stars.

## 2. Observations

Our sample stars listed in Table 1 were observed as part of the RPA survey for RPE stars. First, snapshot spectra were obtained ( $R \sim 30,000$  and a signal-to-noise ratio (S/N)  $\sim 30$  at  $4100 \text{ \AA}$ ; see Hansen et al. 2018 for details) and analyzed. Analyses of the snapshot spectra of J20313531-3127319 (J2031) and J21402305-1227035 (J2140) were published in Hansen et al. (2018) and Holmbeck et al. (2020), respectively, while this paper presents the first analysis of J00385967+2725516 (J0038). Following the analysis of the snapshot spectra, the three stars were selected as portrait candidates. Higher-resolution portrait spectra of J2031 and J2140 with a higher S/N were obtained with the Magellan Inamori Kyocera Echelle (MIKE) spectrograph (Bernstein et al. 2003) on the Magellan/Clay telescope at the Las Campanas Observatory in Chile in April 2019, while the portrait spectrum of J0038 was obtained with the TS23 echelle spectrograph (Tull et al. 1995) on the Harlan J. Smith 107 in (2.7 m) telescope at McDonald Observatory in August 2020. The MIKE spectra cover a wavelength range of  $3350 \text{ \AA}$  to  $5000 \text{ \AA}$  in the blue and  $4900 \text{ \AA}$  to  $9500 \text{ \AA}$  in the red. The observations were obtained with a  $0.7 \times 5.0''$  slit and  $2 \times 2$  binning, yielding a resolving

power of  $R \sim 37000$  and  $R \sim 30000$  in the blue and red, respectively. The McDonald spectra cover a wavelength range from  $3400 \text{ \AA}$  to  $10900 \text{ \AA}$  and were obtained with the  $1.8''$  slit and  $1 \times 1$  binning. This yielded a resolving power of  $R \sim 35000$ . A snippet of all three spectra around  $4500 \text{ \AA}$  is shown in Figure 1. As depicted, the quality of our spectra is ideal for an accurate determination of the elemental abundances. The MIKE data were reduced with the Carnegie Python (CarPy) MIKE pipeline (Kelson et al. 2000; Kelson 2003), and the McDonald data were reduced using standard IRAF packages (Tody 1986, 1993), including correction for bias, flat field, and scattered light. Multiple spectra of the same star from different nights were subsequently coadded. Table 1 lists the stellar identification of the target (stellar ID), right ascension (RA), and declination (DEC), while Table 2 lists the heliocentric Julian date (HJD), exposure times, S/N per pixel, and heliocentric radial velocities for the spectra. The heliocentric radial velocities of the stars were determined via cross-correlation of the object spectra with spectra of the standard star HD 122563 ( $V_{helio} = -26.13 \text{ km s}^{-1}$ ; Gaia Collaboration 2018) obtained with the same instruments. Thirty-five orders were used for the cross-correlation of the McDonald spectrum, and fifty-five orders were used in the MIKE spectra. This resulted in the mean radial velocities and standard deviations listed in Table 2. The radial velocities of all three stars were reported in the literature. For J2031 and J2140, our velocities are consistent with previous measurements (J2031:  $-221.0 \text{ km s}^{-1}$ ; Kunder et al. 2017,  $-222.5 \text{ km s}^{-1}$ ; Hansen et al. 2018, and  $-221.1 \text{ km s}^{-1}$  Steinmetz et al. 2020; J2140:  $-133.0 \text{ km s}^{-1}$ ; Beers et al. 2017, and  $-130.4 \text{ km s}^{-1}$ ; Gaia Collaboration 2018). For J0038, however, a velocity of  $-97.56 \text{ km s}^{-1}$  was reported by Gaia Collaboration (2018), which is weaker in blueshift by  $\sim 20 \text{ km s}^{-1}$  than what we find it to be. This suggests that this star is part of a binary system. This assumption is supported by the fact that J0038 is included in the table of Gaia DR3 non-single stars (NSSs) `nss_twobody_orbit` (Halbwachs et al. 2023).

## 3. Stellar parameters and abundance analysis

We used the software `smhr` (Casey 2014; Ji et al. 2020) to normalize and then merge the orders of the echelle spectra. Then, we used it to fit Gaussians to measure the equivalent widths (EWs) of spectral absorption lines. Last, with `smhr` we derived the respective abundances from the curve of growth or from spectral synthesis via the 1D local thermodynamic equilibrium (LTE) radiative transfer code MOOG (Snedden (1973); Sobeck et al. (2011), 2017 version 2).

The stellar parameters of effective temperature ( $T_{\text{eff}}$ ), surface gravity ( $\log g$ ), metallicity ( $[\text{Fe}/\text{H}]$ ), and microturbulence ( $\xi$ ) were determined following the procedure outlined in Roediger et al. (2018). The  $T_{\text{eff}}$  for the stars was determined photometrically, that is, from the colors listed in Table 1 using the color-temperature relations of Casagrande et al. (2010). They were dereddened using the Schlafly & Finkbeiner (2011) dust maps and extinction coefficients from McCall (2004). Furthermore, the  $\log g$  was calculated using the following fundamental relation:

$$\log(g/g_{\odot}) = \log(M/M_{\odot}) - 4 \log(T_{\text{eff}}/T_{\text{eff},\odot}) + 0.4(M_{\text{bol}} - M_{\text{bol},\odot})$$

$$\text{where } M_{\text{bol}} = BC_v + V + 5 \log \varpi + 5 - 3.1E(B - V),$$

using  $M_{\text{bol},\odot} = 4.75$ ,  $\log T_{\text{eff},\odot} = 3.7617$ , and  $\log g_{\odot} = 4.438$ , and the parallaxes,  $\varpi$ , listed in Table 1. Finally, EW measurements

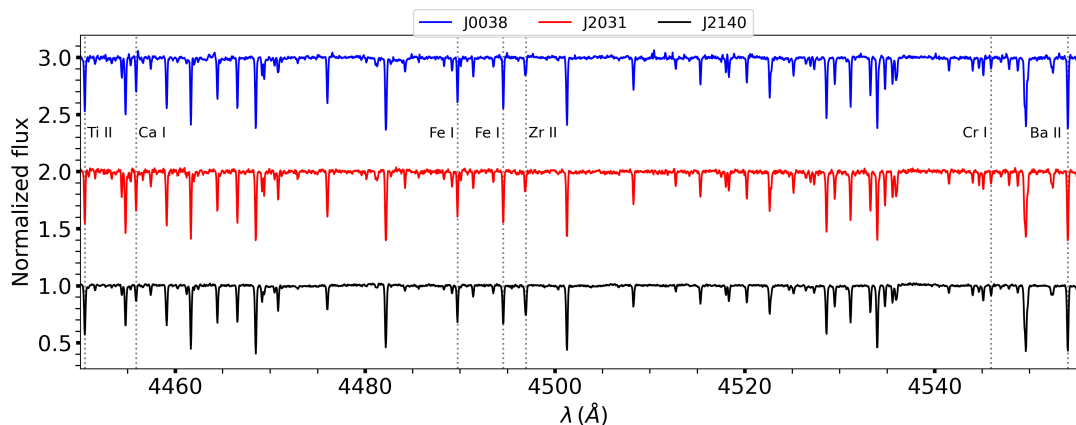
<sup>1</sup> <https://github.com/andycasey/smhr>

<sup>2</sup> <https://github.com/alexji/moog17scat>

**Table 1.** Basic data for the sample stars.

Stellar ID	RA	DEC	<i>B</i>	<i>V</i>	<i>J</i>	<i>H</i>	<i>K</i>	<i>E(B−V)</i>	<i>BC<sub>v</sub></i>	$\varpi$	<i>D</i>
			mag	mag	mag	mag	mag	mag	mag	mag	mas
2MASSJ00385967+2725516	00:39:00.2	+27:25:33.9	12.18	11.44	9.87	9.40	9.35	0.04	−0.37	0.78±0.02	1236 <sup>+42</sup> <sub>−32</sub>
2MASSJ20313531-3127319	20:31:35.0	−31:27:24.3	14.36	13.57	11.94	11.47	11.37	0.08	−0.49	0.38±0.02	2365 <sup>+76</sup> <sub>−107</sub>
2MASSJ21402305-1227035	21:40:23.3	−12:26:59.8	11.94	11.04	9.23	8.76	8.62	0.05	−0.51	0.34±0.03	2669 <sup>+157</sup> <sub>−185</sub>

**References.** References: The *B* and *V* magnitudes were taken from APASS (Henden et al. 2018), and the 2MASS *JHK* magnitudes were taken from Cutri et al. (2003). *E(B−V)* was calculated using the dust maps from Schlafly & Finkbeiner (2011), the bolometric corrections, *BC<sub>v</sub>*, are based on Casagrande & Vandenberg (2014), the distances, *D*, were taken from Bailer-Jones et al. (2018), and the parallaxes,  $\varpi$ , from Gaia Collaboration et al. (2023).


**Fig. 1.** Snippet of the spectra for our three stars. Stars are offset in the direction of the y-axis to avoid overlap.

**Table 2.** Observing log.

Object	HJD	Exposure time	S/N	<i>V<sub>helio</sub></i>
		(sec)	@4500 Å	(km s <sup>−1</sup> )
J0038	2459087	5x1800	85*	−117.5±0.2
	2459088	5x1800		−116.0±0.2
J2031	2458600	4x900	87	−220.6±0.3
J2140	2458601	3x900	197	−129.5±0.4

**Notes.** \* S/N of co-added spectra.

**Table 3.** Stellar parameters of the target stars.

Object	<i>T<sub>eff</sub></i>	log <i>g</i>	[Fe/H]	$\xi$
	(K)			(km s <sup>−1</sup> )
J0038	5203±79	2.45±0.09	−2.39 ± 0.20	1.72±0.10
J2031	5218±67	2.66±0.08	−2.28 ± 0.13	1.65±0.06
J2140	4855±64	1.44±0.12	−3.05 ± 0.14	2.02±0.06

of Fe I and Fe II lines were used to determine the metallicities and  $\xi$ . We adopted the [FeI/H] abundance as the model metallicity, and the value of  $\xi$  ensures that the Fe I abundances are independent of their respective reduced equivalent widths. The [FeI/H] and [FeII/H] abundances agree to within 0.03 dex for all three stars. The final stellar parameters for the stars, along with the associated uncertainties, are listed in Table 3. In Table 3 we list the combined systematic parameter uncertainties (see Roederer et al. 2018 for details) and statistical uncertainties arising from the scatter in individual Fe-line abundances.

Following the parameter determination, the elemental abundances were derived via EW analysis and spectral synthesis. We used  $\alpha$ -enhanced ( $[\alpha/\text{Fe}] = +0.4$ ) ATLAS9 model atmospheres (Castelli & Kurucz 2003), and the solar abundances were taken

from Asplund et al. (2009). The line lists we used for the analysis were generated from linemake<sup>3</sup> (Placco et al. 2021), and they include isotopic and hyperfine structure broadening, where applicable, for which we employed the *r*-process isotope ratios from Sneden et al. (2008). Atomic data, EWs, and derived abundances for individual lines are listed in Table 4. The final abundances were determined as weighted averages of individual line abundances following Ji et al. (2020). We also followed the procedure outlined in Ji et al. (2020) to determine the abundance uncertainties by propagating through the stellar parameter uncertainties (see Table A).

## 4. Results

The abundances of 30 elements, including 10 neutron-capture elements, were determined for the three stars. The final abundances and associated uncertainties are listed in Table 5. In Table 6 we list the abundance ratios for the three stars associated with the *r<sub>lim</sub>* abundance criteria. Figure 2 compares the derived abundances for selected elements to those of normal Milky Way (MW) halo stars (black circles) from Roederer et al. (2014) and *r<sub>lim</sub>* stars (red stars) from the literature. The sample of literature *r<sub>lim</sub>* stars was compiled from the SAGA Database (Suda et al. 2008, 2011; Yamada et al. 2013; Suda et al. 2017), selected so that they fulfill the criteria of *r<sub>lim</sub>* stars (see Table 6). We only included stars that had measured abundances for all three elements (i.e., Sr, Ba and Eu) and excluded those for which only upper limits were available. The abundances from the following studies are included in Figure 2: Barklem et al. (2005); Preston et al. (2006); François et al. (2007); Lai et al. (2008); Cohen et al. (2013); Ishigaki et al. (2013); Hansen et al. (2018); Sakari et al. (2018); Ezzeddine et al. (2020); Holmbeck et al. (2020).

<sup>3</sup> <https://github.com/vmplacco/linemake>

#### 4.1. Light elements Li to Zn

We derived the abundances of elements from Li to Zn using a combination of EW and spectral synthesis analysis (see Table 4 for details of the individual lines). Figure 2 shows that the abundances derived for J0038 and J2031 generally follow the trends seen for other MW halo and  $r_{lim}$  stars for the elements displayed, with the exception of O and K. On the other hand, J2140 generally exhibits higher abundances of the iron-peak elements Cr, Mn, Co, Ni, Cu, and Zn, as well as for O and K, similar to J0038 and J2031. This star is also enhanced in N and Na, suggesting that its chemical-enrichment history is different from typical MW halo stars and from that of the two other stars in our sample. Figure 2 shows that J2140 stands out from all other stars in their iron-peak and Na abundances. This is also very interesting considering that the  $\alpha$ -element abundances of J2140 follow the trend of typical metal-poor MW halo stars, with the exception of O, which is somewhat higher.

In Figure 3, we compare some spectral lines of Cr, Mn, Co, Ni, and Zn from J2140 to those of two other stars with similar stellar parameters in order to demonstrate the enhancement of these elements in this star. The comparison stars are CS 29502–092 and CS 22948–066, with stellar parameters  $T_{\text{eff}}=4820\pm34$  K,  $\log g=1.5\pm0.14$ , and  $[\text{Fe}/\text{H}] = -3.2\pm0.15$ , and  $T_{\text{eff}}=4830\pm34$  K,  $\log g=1.55\pm0.15$ , and  $[\text{Fe}/\text{H}] = -3.18\pm0.16$ , respectively (Roederer et al. 2014). The absolute abundances of these stars as reported by Roederer et al. (2014) are  $\log \epsilon(\text{CrI}) = 2.19$ ,  $\log \epsilon(\text{MnI}) = 2.11$ ,  $\log \epsilon(\text{NiI}) = 3.21$ ,  $\log \epsilon(\text{CoI}) = 1.73$ ,  $\log \epsilon(\text{ZnI}) = 1.70$  for CS29502–092, and  $\log \epsilon(\text{CrI}) = 1.82$ ,  $\log \epsilon(\text{MnI}) = 1.85$ ,  $\log \epsilon(\text{NiI}) = 2.86$ ,  $\log \epsilon(\text{CoI}) = 1.67$ ,  $\log \epsilon(\text{ZnI}) = 1.58$  for CS22948–066.

We used the nonlocal thermodynamic equilibrium (NLTE) corrections from Bergemann et al. (2021) for O I and those from Andrievsky et al. (2010) for K I in order to assess whether the overabundances of these elements for all three stars are merely NLTE effects and not real enhancements. We repeated this for Cr I, Mn I, and Co I only for J2140 using the NLTE corrections from Bergemann & Cescutti (2010), Bergemann et al. (2019), and from Bergemann et al. (2010) with collisional data from Voronov et al. (2022), respectively. In the case of O I, the NLTE corrections for J0038 and J2031 are  $\sim -0.03$  dex, whereas no correction arises for J2140. The NLTE corrections for K I are  $\sim -0.21$  dex for J2140 and  $\sim -0.27$  dex for J0038 and J2031. Concerning Cr I, Mn I, and Co I, the NLTE corrections for J2140 are  $\sim +0.55$  dex,  $\sim +0.4$  dex, and  $\sim +0.87$  dex, respectively. Finally, after applying the evolutionary correction from Placco et al. (2014), J2140 has  $[\text{C}/\text{Fe}] = +1.05$ , which would classify it as a carbon-enhanced metal-poor (CEMP) star (Beers & Christlieb 2005; Aoki et al. 2007; Carollo et al. 2011; Norris et al. 2013).

#### 4.2. Neutron-capture elements

We derived abundances of ten neutron-capture elements, specifically, Sr, Y, Zr, Ba, La, Nd, Eu, Dy, Er, and Yb, via spectral synthesis. The syntheses of neutron-capture element absorption features present in the spectra of the three stars are shown in Figure 4. As demonstrated in Figure 4, the spectral synthesis technique we employed can reproduce very well the observed single (Y II), blended (Zr II), and weak (Er II) lines. In Table 6, we list the  $[\text{Eu}/\text{Fe}]$ ,  $[\text{Sr}/\text{Ba}]$ , and  $[\text{Sr}/\text{Eu}]$  ratios for the stars, along with the limits required for a  $r_{lim}$  classification according to Frebel (2018). Two of our stars, J0038 and J2140, fulfill the criteria of  $r_{lim}$  stars;  $[\text{Eu}/\text{Fe}] < +0.3$ ,  $[\text{Sr}/\text{Ba}] > +0.5$  and  $[\text{Sr}/\text{Eu}] > 0.0$ ,

**Table 4.** Sample of line information.

StellarID	Species	$\lambda$ (Å)	$\chi$ (eV)	$\log gf$	EW (mÅ)	$\sigma_{\text{EW}}$ (mÅ)	$\log \epsilon$	ref
J003859	O I	7771.94	9.15	0.37	20.48	2.62	7.65	1
J003859	O I	7774.17	9.15	0.22	7.73	1.62	7.24	1
J003859	O I	7775.39	9.15	0.00	7.87	1.53	7.47	1
J003859	Na I	5889.95	0.00	0.11	170.38	2.93	4.21	1
J003859	Na I	5895.92	0.00	-0.19	158.03	0.78	4.36	1
J003859	Mg I	4167.27	4.35	-0.74	61.95	1.21	5.66	1
J003859	Mg I	4702.99	4.33	-0.44	80.18	0.71	5.54	1
J003859	Mg I	5528.40	4.35	-0.55	79.94	0.72	5.68	2
J003859	Mg I	5711.09	4.35	-1.84	14.72	0.80	5.79	2
J003859	Al I	3961.52	0.01	-0.33	121.84	1.40	3.35	1
J003859	Si I	5772.15	5.08	-1.75	5.58	1.21	5.98	1
J003859	K I	7664.90	0.00	0.12	65.09	0.89	3.37	1
J003859	K I	7698.96	0.00	-0.18	45.82	0.88	3.33	1

**References.** (1) Kramida et al. (2018a), (2) Pehlivan Rhodin et al. (2017), (3) Yu & Derevianko (2018), (4) Lawler et al. (2013), (5) Wood et al. (2013), (6) Pickering et al. (2001, 2002), (7) Sobek et al. (2007), (8) Lawler et al. (2017), (9) Den Hartog et al. (2014), (10) O’Brian et al. (1991), (11) Belmonte et al. (2017), (12) Ruffoni et al. (2014), (13) Meléndez & Barbuy (2009), (14) Den Hartog et al. (2019), (15) Wood et al. (2014), (16) Roederer & Lawler (2012), (17) Smith et al. (1998), (18) Lawler & Dakin (1989) using hfs from Kurucz & Bell (1995), (19) Lawler et al. (2014) (20) Wood et al. (2014), (21) Den Hartog et al. (2011), (22) Lawler et al. (2015), (23) Kramida et al. (2018b), (24) Biémont et al. (2011), (25) Ljung et al. (2006), (26) Kramida et al. (2018b) using HFS/IS from McWilliam (1998), (27) Lawler et al. (2001) using HFS from Ivans et al. (2006), (28) Den Hartog et al. (2003) using HFS/IS from Roederer et al. (2008), (29) Lawler et al. (2001) using HFS/IS from Ivans et al. (2006) (30) Wickliffe et al. (2000), (31) Lawler et al. (2008), (32) Sneden et al. (2009), (33) Kramida & Ralchenko (1999) using hfs from Kurucz & Bell (1995).

**Notes.** The full table is available online.

while the  $[\text{Eu}/\text{Fe}]$  ratio of J2031 is too high and the  $[\text{Sr}/\text{Eu}]$  ratio is too low, and it can be classified as an  $r$ -I star. A somewhat cooler spectroscopic  $T_{\text{eff}}$  of 4894 K and lower gravity of  $\log g = 1.39$  were derived in Hansen et al. (2018), likely resulting in the lower  $[\text{Eu}/\text{Fe}]$  abundances derived and in the subsequent  $r_{lim}$  classification of this star. Its  $[\text{Eu}/\text{Fe}] = +0.3$  abundance also barely qualify it for the  $r$ -I class, and it may therefore be useful for exploring the transition between the  $r_{lim}$  and  $r$ -I regime.

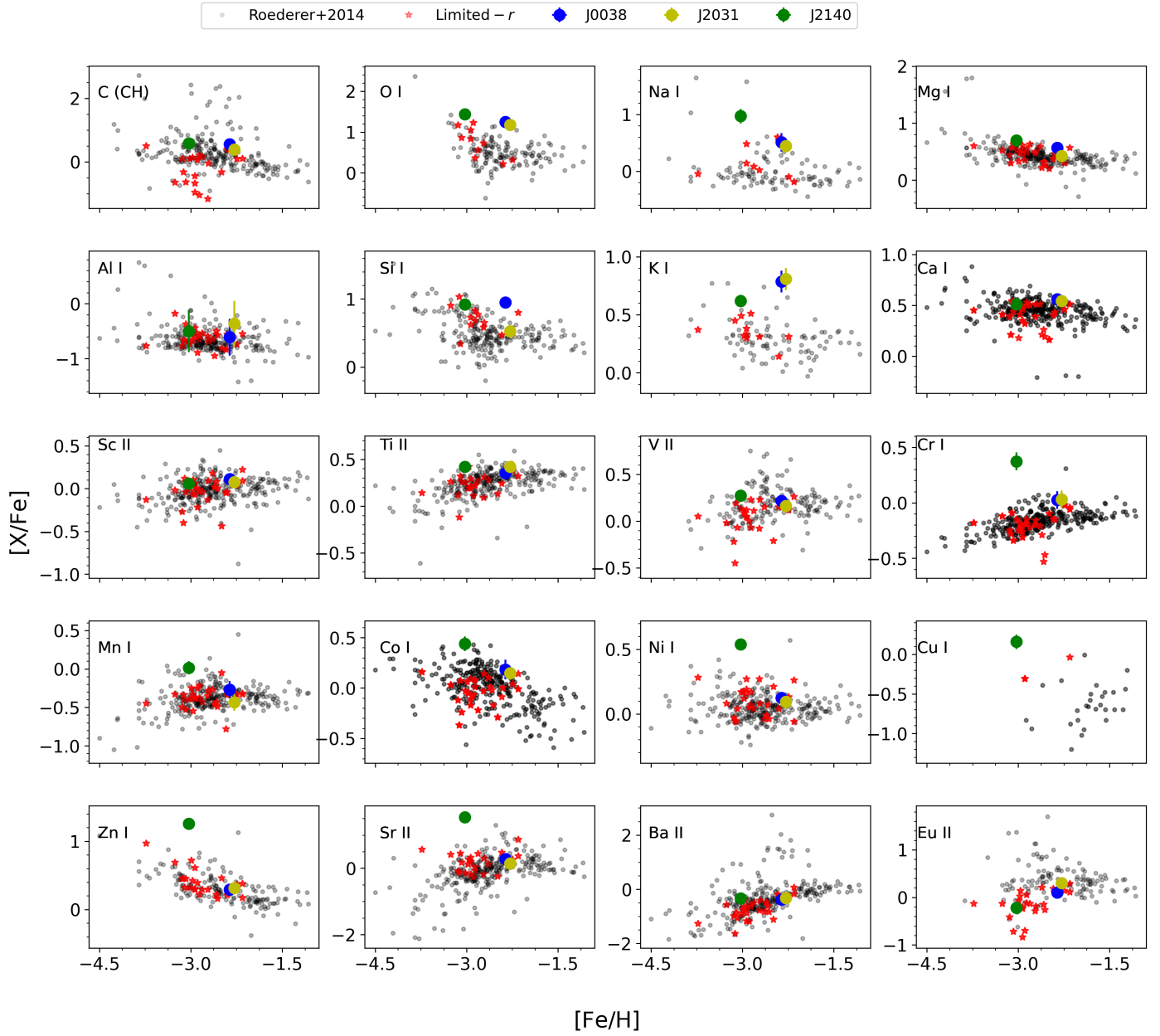


**Fig. 2.** Derived abundances for the three sample stars (blue, yellow, and green dots) compared to abundances of normal MW halo stars (black dots) from [Roederer et al. \(2014\)](#) and from the literature  $r_{lim}$  stars (red stars). The error bars of our three stars, when not visible, are the size of the dots.

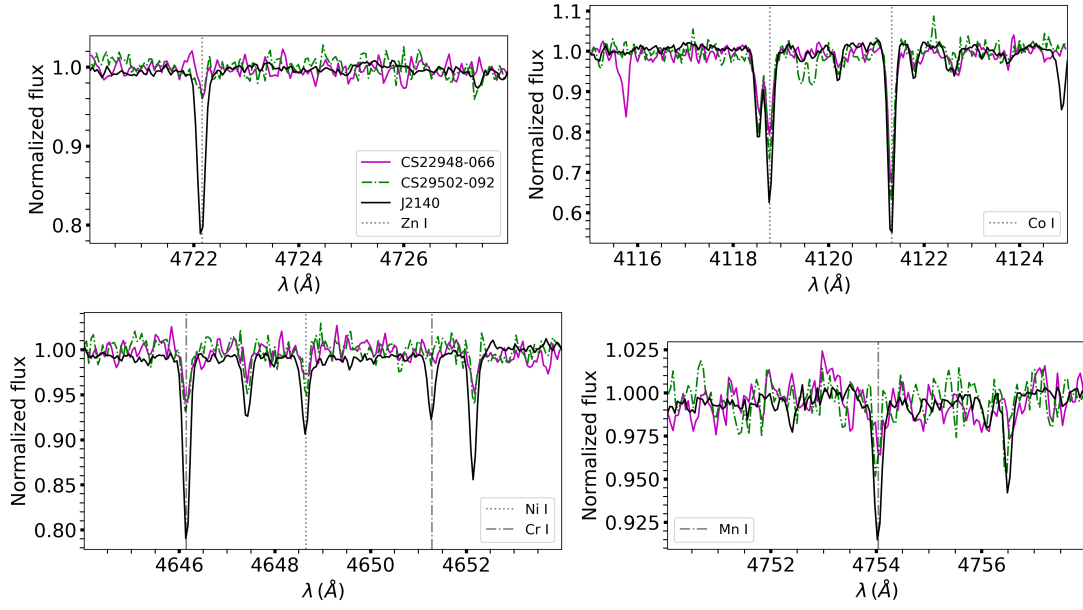


**Fig. 3.** Comparison of spectral lines between J2140 and stars CS 29502–092 and CS 22948–066. We show the spectral lines of Zn I at 4722.16 Å (top left panel), of Co I at 4118.77 Å and 4121.32 Å (top right panel), of Ni I and Cr I (bottom left panel) at 4604.99 Å and 4648.65 Å, and 4646.15 Å and 4651.28 Å, respectively, and of Mn I at 4754.04 Å (bottom right panel).

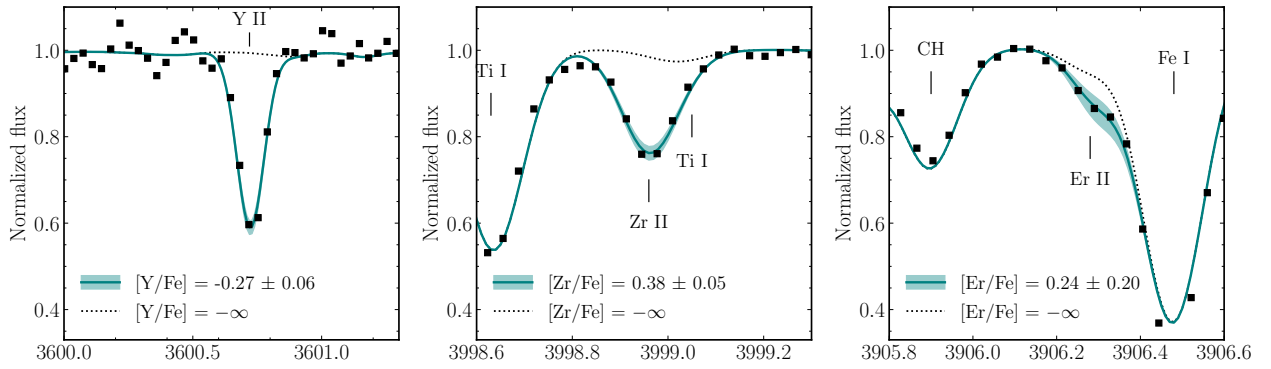


**Fig. 4.** Comparison of the synthesis and observed spectra (black dots) for an Y II line in J2031 (left panel), a Zr II line in J0038 (middle panel), and an Er II line in J2140 (right panel). The blue line is the best-fit synthesis, the blue band shows the uncertainty, and the dotted line is a synthesis without the given element.

**Table 5.** Abundance table. N denotes the number of absorption lines used for the elemental-abundance determination.

2MASSJ00385967+2725516							2MASSJ20313531-3127319						2MASSJ21402305-1227035						
Element	N	$\log \epsilon(X)$	[X/H]	$\sigma_{[X/H]}$ (dex)	[X/Fe]	$\sigma_{[X/Fe]}$ (dex)	N	$\log \epsilon(X)$	[X/H]	$\sigma_{[X/H]}$ (dex)	[X/Fe]	$\sigma_{[X/Fe]}$ (dex)	N	$\log \epsilon(X)$	[X/H]	$\sigma_{[X/H]}$ (dex)	[X/Fe]	$\sigma_{[X/Fe]}$ (dex)	
Li I	1	+1.04	-0.01	0.10	+2.47	0.10	1	+1.16	+0.11	0.06	+2.48	0.06	-	-	-	-	-	-	-
C-H	1	+6.50	-1.93	0.12	+0.55	0.11	1	+6.44	-1.99	0.06	+0.38	0.06	1	+5.88	-2.55	0.08	+0.58	0.07	
C <sub>cor</sub>	-	-	-	-	+0.56*	-	-	-	-	-	+0.39*	-	-	-	-	-	+1.05*	-	-
N-H	-	-	-	-	-	-	-	-	-	-	-	-	1	+6.04	-1.79	0.14	+1.33	0.13	
O I	3	+7.46	-1.23	0.10	+1.25	0.12	2	+7.49	-1.20	0.04	+1.18	0.06	3	+7.00	-1.69	0.12	+1.44	0.13	
Na I	2	+4.27	-1.97	0.17	+0.51	0.16	3	+4.31	-1.93	0.09	+0.44	0.09	2	+4.08	-2.15	0.13	+0.97	0.13	
Mg I	4	+5.69	-1.91	0.08	+0.57	0.08	7	+5.65	-1.95	0.08	+0.42	0.08	8	+5.17	-2.43	0.07	+0.70	0.07	
Al I	2	+3.36	-3.09	0.34	-0.61	0.33	3	+3.71	-2.74	0.42	-0.36	0.41	1	+2.82	-3.63	0.39	-0.50	0.38	
Si I	2	+5.98	-1.53	0.08	+0.95	0.08	4	+5.66	-1.85	0.04	+0.53	0.05	3	+5.30	-2.21	0.06	+0.92	0.06	
K I	2	+3.34	-1.69	0.10	+0.79	0.09	2	+3.46	-1.57	0.10	+0.81	0.10	1	+2.52	-2.51	0.05	+0.62	0.05	
Ca I	24	+4.42	-1.92	0.06	+0.56	0.06	28	+4.51	-1.83	0.04	+0.54	0.04	16	+3.72	-2.62	0.06	+0.51	0.06	
Sc II	8	+0.90	-2.25	0.07	+0.11	0.07	11	+0.94	-2.21	0.06	+0.08	0.06	12	+0.18	-2.97	0.09	+0.06	0.07	
Ti I	16	+2.88	-2.08	0.08	+0.40	0.07	18	+2.99	-1.96	0.06	+0.42	0.06	19	+2.33	-2.62	0.07	+0.51	0.07	
Ti II	25	+2.94	-2.01	0.05	+0.35	0.05	27	+3.08	-1.87	0.04	+0.42	0.05	30	+2.34	-2.61	0.06	+0.42	0.06	
V I	2	+1.58	-2.35	0.05	+0.14	0.06	3	+1.59	-2.34	0.06	+0.03	0.06	2	+1.01	-2.92	0.05	+0.20	0.05	
V II	6	+1.79	-2.14	0.03	+0.22	0.04	8	+1.81	-2.12	0.03	+0.16	0.05	10	+1.17	-2.76	0.06	+0.27	0.06	
Cr I	8	+3.19	-2.45	0.08	+0.02	0.08	7	+3.30	-2.34	0.08	+0.03	0.08	11	+2.89	-2.75	0.08	+0.37	0.08	
Cr II	3	+3.21	-2.43	0.05	-0.07	0.06	3	+3.46	-2.18	0.06	+0.10	0.06	3	+2.96	-2.68	0.05	+0.35	0.04	
Mn I	6	+2.68	-2.75	0.11	-0.27	0.11	7	+2.62	-2.81	0.11	-0.43	0.11	6	+2.32	-3.11	0.08	+0.02	0.09	
Mn II	-	-	-	-	-	-	5	+2.86	-2.57	0.10	-0.28	0.10	3	+2.32	-3.11	0.06	-0.08	0.06	
Fe I	149	+5.02	-2.48	0.04	+0.00	0.00	132	+5.12	-2.38	0.04	+0.00	0.00	120	+4.37	-3.13	0.04	+0.00	0.00	
Fe II	13	+5.14	-2.36	0.04	+0.00	0.00	10	+5.21	-2.29	0.05	+0.00	0.00	11	+4.47	-3.03	0.06	+0.00	0.00	
Co I	6	+2.69	-2.30	0.10	+0.18	0.10	17	+2.76	-2.23	0.06	+0.15	0.06	17	+2.30	-2.69	0.07	+0.44	0.07	
Ni I	15	+3.86	-2.36	0.04	+0.12	0.04	14	+3.94	-2.28	0.05	+0.09	0.06	19	+3.63	-2.59	0.04	+0.54	0.04	
Cu I	-	-	-	-	-	-	-	-	-	-	-	-	1	+1.22	-2.97	0.09	+0.16	0.09	
Zn I	2	+2.37	-2.19	0.07	+0.29	0.07	2	+2.50	-2.06	0.05	+0.31	0.05	3	+2.69	-1.87	0.08	+1.26	0.08	
Sr I	-	-	-	-	-	-	-	-	-	-	-	-	1	+1.01	-1.86	0.05	+1.27	0.05	
Sr II	2	+0.78	-2.09	0.11	+0.28	0.12	2	+0.73	-2.14	0.17	+0.15	0.15	3	+1.38	-1.49	0.06	+1.54	0.06	
Y II	11	-0.23	-2.44	0.06	-0.08	0.06	12	-0.35	-2.56	0.06	-0.27	0.06	17	-0.13	-2.34	0.04	+0.69	0.07	
Zr II	8	+0.60	-1.98	0.04	+0.38	0.05	9	+0.55	-2.04	0.04	+0.25	0.05	20	+0.54	-2.04	0.06	+0.99	0.06	
Ba II	5	-0.56	-2.74	0.10	-0.38	0.09	5	-0.43	-2.61	0.10	-0.32	0.08	5	-1.18	-3.36	0.13	-0.33	0.10	
La II	3	-1.28	-2.38	0.10	-0.02	0.10	2	-1.14	-2.24	0.10	+0.04	0.12	1	-1.77	-2.87	0.29	+0.16	0.25	
Nd II	2	-0.84	-2.26	0.06	+0.10	0.06	2	-0.56	-1.98	0.09	+0.31	0.09	3	-1.55	-2.97	0.08	+0.06	0.06	
Eu II	3	-1.74	-2.26	0.06	+0.10	0.06	3	-1.47	-1.99	0.05	+0.30	0.05	2	-2.73	-3.25	0.07	-0.22	0.08	
Dy II	2	-1.32	-2.42	0.13	-0.06	0.13	2	-0.94	-2.04	0.10	+0.25	0.10	-	-	-	-	-	-	
Er II	1	-1.18	-2.10	0.14	+0.26	0.14	2	-1.01	-1.93	0.11	+0.36	0.10	1	-1.88	-2.80	0.24	+0.24	0.20	
Yb II	1	-1.63	-2.47	0.23	-0.11	0.22	1	-1.20	-2.04	0.12	+0.24	0.10	1	-2.45	-3.29	0.18	-0.26	0.14	

**Notes.** \* C abundance after the evolutionary correction from [Placco et al. \(2014\)](#).

**Table 6.** Limited- $r$  classification criteria.

Object	[Eu/Fe]	[Sr/Ba]	[Sr/Eu]	[Ba/Eu]
$r_{lim}$	$< +0.3$	$> +0.5$	$> 0.0$	$\dots$
J0038	+0.10	+0.66	+0.18	-0.48
J2031	+0.30	+0.47	-0.15	-0.62
J2140	-0.22	+1.87	+1.76	-0.11

## 5. Discussion

### 5.1. $r$ -process patterns for limited- $r$ stars

The classical way to analyze the abundance patterns of RPE stars is to compare them to the scaled abundance pattern of the Solar System  $r$ -process because the pattern of heavy  $r$ -process elements (Ba to Hf) has many times been observed to exhibit a universality consistent with the scaled residual  $r$ -process solar pattern (Snedden et al. 2008; Cowan et al. 2021). However, as described in Section 1, when scaling to Eu, this universality does not extend to the light elements ( $32 < Z < 56$ ), and it neither seems to apply to  $r_{lim}$  stars such as HD 122563 (Honda et al. 2006, 2007). This suggests that a limited  $r$ -process or neutron-poor  $r$ -process could be in operation.

Recently, this picture has been challenged by the RPA by Roederer et al. (2022), who investigated the spread in the abundances of eight stars from the literature with varying  $r$ -process enrichment ( $-0.22 \leq [\text{Eu}/\text{Fe}] \leq +1.32$ ). However, instead of scaling the full pattern to Eu, as is usually done, Roederer et al. (2022) scaled the light  $r$ -process elements (Se to Te) to Zr, and only the elements from Ba and up, to Eu. The authors found that even though the light  $r$ -process elements exhibit variations compared to the heavy elements, they are not entirely decoupled. Furthermore, by scaling to Zr, a universal pattern among the light  $r$ -process elements Se, Sr, Y, Zr, Nb, Mo, and Te appeared. However, for some elements, Ru, Rh, Pd, and Ag, the star-to-star scatter persisted. Roederer et al. (2023) investigated this scatter further and found that in RPE stars, the abundances of Ru, Rh, Pd, and Ag are correlated to those of heavy  $r$ -process elements with  $63 \leq Z \leq 78$ . This is not observed for the neighboring elements with  $34 \leq Z \leq 42$  and  $48 \leq Z \leq 68$ . In order to explain this finding, Roederer et al. (2023) proposed that these correlations appear due to fission-fragment depositions. Specifically, the authors assembled metal-poor stars from the literature with  $[\text{Ba}/\text{Eu}] < -0.3$  to ensure that the  $r$ -process was the main channel of heavy-element production. They then constructed a pattern of the mean neutron-capture element abundances of stars with  $[\text{Eu}/\text{Fe}] \leq +0.3$ , including the  $r_{lim}$  star HD 122563. This so-called baseline pattern is assumed to represent an  $r$ -process without fission. Roederer et al. (2023) found that the  $r$ -process abundance variations in the other stars in the sample that have  $[\text{Eu}/\text{Fe}] > +0.3$  can be explained by the coproduction of the  $r$ -process and fission-fragment depositions of transuranic nuclei, and that this mechanism alters the pattern not only around Ru - Ag, but also for the heavier elements in the regions  $64 \leq Z \leq 78$ . This coproduction of certain light and heavy  $r$ -process elements was previously shown by Vassh et al. (2020). Vassh et al. (2020) applied the fission yields obtained with the finite-range liquid drop model (FRLDM) (Mumpower et al. 2020) on neutron-rich merger ejecta simulations and found that the late-time fission fragments are deposited in the region around Ru - Ag, leading up and into the lanthanides. This process influences the final abundance distribution in these regions most. Lemaître et al. (2021) also found that neutron-rich ejecta in NSMs produce fis-

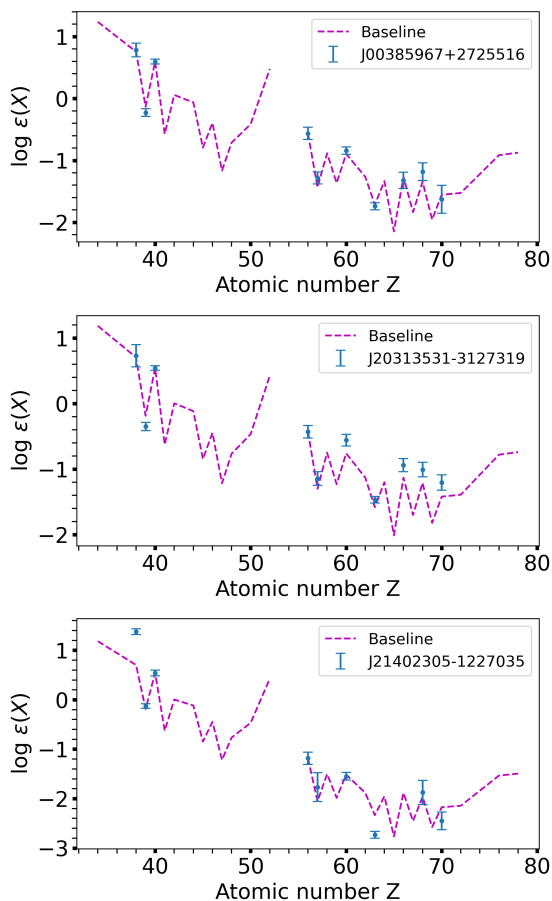
sion fragments that contribute almost entirely to the final abundances of nuclei with  $100 \leq A \leq 180$  (Ru to and including the lanthanides). However, when the ejecta are less rich in neutrons and weak interactions are taken into account, Lemaître et al. (2021) found that the fission fragments deposit in the region  $A = 140 - 180$ , namely the lanthanides. Finally, it should be noted that the intermediate neutron-capture process ( $i$ -process; Cowan & Rose 1977) could also contribute to the abundances of the light neutron-capture elements with  $32 \leq Z \leq 55$  (Roederer et al. 2016).

Figure 5 compares the neutron-capture elemental abundances of our three stars with the baseline pattern from Roederer et al. (2023). In order to do this, we scaled the light  $r$ -process elements to Zr and the heavy ones, that is,  $Z \geq 56$ , to Ba. We find that the abundance pattern for the  $r_{lim}$  star J0038 (top panel) agrees very well with the baseline pattern. This suggests that this star could have been enriched by a similar  $r$ -process as  $r$ -I and  $r$ -II stars, but without fission-fragment deposition. The low  $[\text{Ba}/\text{Eu}]$  ratio for this star of  $-0.48$  also agrees with that of the stars Roederer et al. (2023) used to construct the baseline pattern. J2031 (middle panel), which is an  $r$ -I star, matches the baseline pattern reasonably well for the light elements (Sr, Y, Zr), but appears to be more enhanced in some of the heavy elements. This suggests that it was enriched by an  $r$ -process that experienced some fission cycling. However, J2140 (bottom panel), which also fulfills the  $r_{lim}$  abundance criteria (see Table 6), exhibits a somewhat higher Sr abundance and a much lower Eu abundance than indicated from the baseline pattern. This could suggest that the heavy elements present in the atmosphere of this star are the products of different or multiple nuclear processes. Since J2140 has  $[\text{Ba}/\text{Eu}] = -0.11$ , some contribution from the  $s$ -process is likely present, for example, from rotating massive stars (spin stars) (Meynet et al. 2006; Frischknecht et al. 2015; Limongi & Chieffi 2018). In the models of Frischknecht et al. (2015), spin stars can produce elements up to Ba, which are ejected via stellar winds, while the SN models of Limongi & Chieffi (2018) that include rotation find that heavier elements up to Pb can be produced. In principle, spin stars could also contribute to the Sr-Zr abundances we find for J0038 and J2031, but with their low  $[\text{Ba}/\text{Eu}]$  values ( $-0.48$  and  $-0.62$ , respectively) and the good match to the baseline pattern for Sr-Zr, an  $r$ -process is more likely. However, the neutron-capture elements in the very old stars are probably formed through the  $r$ -process, as first suggested by Truran (1981).

Based on this comparison, we suggest that in order to better study the  $r_{lim}$  stars,  $[\text{Ba}/\text{Eu}]$  also need to be taken into account to be able to distinguish between stars that follow the baseline pattern and those that do not. In Figure 6 we show the  $[\text{Ba}/\text{Eu}]$  ratios as a function of  $[\text{Fe}/\text{H}]$  for our sample stars and the literature  $r_{lim}$  stars. Even though  $[\text{Ba}/\text{Eu}]$  has not been a selection criterion for the categorization of  $r_{lim}$  stars so far, most of them in the literature have  $[\text{Ba}/\text{Eu}] < -0.3$ . Based on the good match between the abundance pattern of star J0038 and the baseline pattern and the lack of it for star J2140, our understanding of the formation of these elements would be helped by studying  $r_{lim}$  stars in two regimes, that is  $[\text{Ba}/\text{Eu}] < -0.3$  and  $\geq -0.3$ .

### 5.2. Lanthanide fractions

Since the  $r_{lim}$  stars are selected to exhibit higher abundances in light  $r$ -process elements compared to the heavy ones, measuring and comparing the ratio of the bulk of light and heavy elements gives us some type of quantification of this overabundance, which can be useful for identifying the nucleosynthetic



**Fig. 5.** Comparison to the baseline pattern. We plot the abundances of neutron-capture elements for stars J0038, J2031, and J2140 and overplot the scaled baseline pattern (Roederer et al. 2023). The light elements ( $Z < 56$ ) are scaled to Zr, while the heavy ( $Z \geq 56$ ) elements are scaled to Ba.

channel that causes the abundance signature of these stars. Because most of the heavy elements in RPE metal-poor stars that are easy to measure belong to the lanthanides, it is straightforward to use the lanthanide mass fraction of the stars in order to quantify the ratio of light to heavy elements. The lanthanide fraction ( $X_{La}$ ) is the ratio of the mass of the elements belonging to the lanthanides to the mass of all other *r*-process elements.

The multimessenger observations of the gravitational wave event of the NSM GW170817 and its KN is the only evidence we have so far that *r*-process elements are being synthesized in such an event (Kasen et al. 2017; Perego et al. 2017; Drout et al. 2017; Rosswog et al. 2018). In addition, the lanthanide fraction of a KN is a measurable quantity because it directly affects the duration and shape of the KN light curve as well as the shape of its spectrum (Kasen et al. 2017). Ji et al. (2019) computed the  $X_{La}$  of *r*-process-dominated very metal-poor stars ( $[\text{Fe}/\text{H}] < -2.3$  and  $[\text{Ba}/\text{Eu}] < -0.4$ ) and compared them to the  $X_{La}$  of the KN AT2017gfo. They found that if this KN is a typical representative of an NSM, then these events cannot be the dominant *r*-process site because most *r*-I and *r*-II stars are richer in lanthanides than this specific KN.

We computed the  $X_{La}$  of our stars, as well as those of the  $r_{lim}$  stars in the literature with abundances measured for Sr, Ba, and Eu at least. To do this, we followed Ji et al. (2019) and used the solar residual *r*-process abundances of Sneden et al. (2008). The  $X_{La}$ 's are shown in Figure 7. This result exhibits a clear sep-

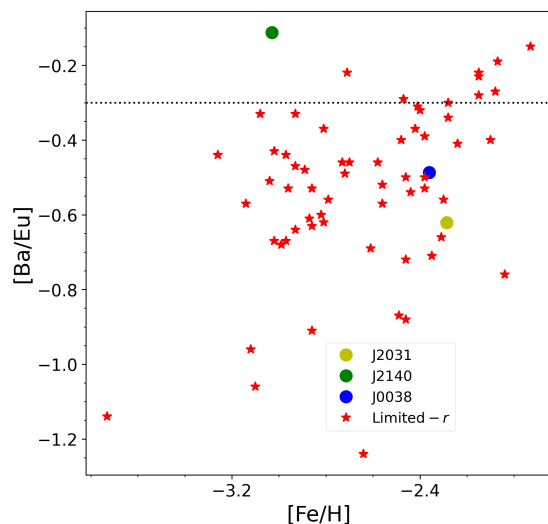


**Fig. 6.**  $[\text{Ba}/\text{Eu}]$  abundance ratios of our sample of stars and of  $r_{lim}$  stars in the literature. The markers are the same as in Figure 2. The dotted black line indicates  $[\text{Ba}/\text{Eu}] = -0.3$ .

aration between  $r_{lim}$  stars and the *r*-I and *r*-II star around the  $X_{La}$  value of the KN, which could suggest that the ratio of the light to heavy elements produced in this KN lies in the transition region from  $r_{lim}$  to *r*-I, *r*-II stars. This is expected because by design, the selection criteria of  $r_{lim}$  stars (Table 6) select stars with low lanthanide fractions. However, while the  $X_{La}$  of AT2017gfo might be a good match to  $r_{lim}$  stars, the time delay of *r*-process element enrichment by NSMs might cause a problem. Figure 6 shows that almost all discovered and analyzed  $r_{lim}$  stars have  $[\text{Fe}/\text{H}] < -2.0$ . This was previously discussed by Côté et al. (2019) and Holmbeck et al. (2020). Thus, due to the time delay in the onset of NSMs and the low metallicity of  $r_{lim}$  stars, if they indeed bear the imprint of NSMs, they would need to have been born in an environment where star formation is inefficient, which in turn would allow the effects of this nucleosynthesis channel to be conspicuous. Recently, however, Kobayashi et al. (2023) showed that NSMs (including both neutron star (NS)-NS and NS-black hole (BH) mergers) can reproduce the evolutionary relations of  $[\text{Eu}/\text{Fe}]-[\text{Fe}/\text{H}]$  and  $[\text{Eu}/\text{O}]-[\text{O}/\text{H}]$  in the solar neighborhood when the delay-time distribution (DTD) between onset of star formation and merger is metallicity dependent. An alternative way to eliminate the problem of the time delay is to consider MR-SNe or collapsars as a significant source of *r*-process material in the early Universe. Ji et al. (2019) calculated theoretical  $\log X_{La}$  values for collapsar models from Siegel et al. (2019) and MR-SN from Nishimura et al. (2015), finding values ranging from  $-1.60$  to  $-2.81$  and  $-0.77$  to  $-1.94$ , respectively, which both overlap with the value derived for AT2017gfo. In the future, more model calculations and larger stellar samples from the RPA will help us to determine which sites are dominant. Finally, we note that there might be a bias in the sample of the  $r_{lim}$  stars discovered to date because they were discovered in surveys aiming to find stars with  $[\text{Fe}/\text{H}] < -2.0$ .

### 5.3. Kinematics of limited-*r* stars

Previous studies have shown that a large fraction of *r*-II stars were likely born in smaller satellite systems and were accreted by the MW (Roederer et al. 2018; Gudin et al. 2021; Shank et al. 2023). To investigate whether this is also the case for the

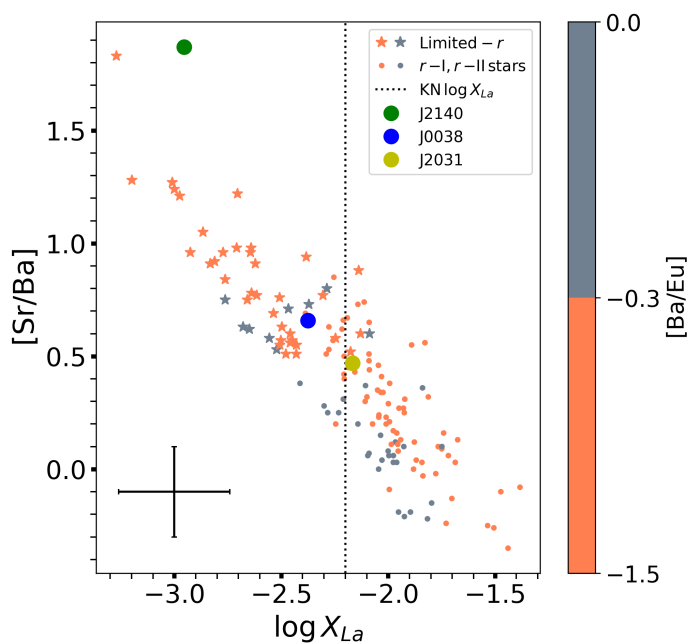


**Fig. 7.** Lanthanide fraction of our sample of stars and of the literature  $r_{lim}$ ,  $r$ -I, and  $r$ -II stars. The symbols are the same as in Figure 2. The points are coral when  $[Ba/Eu] < -0.3$  and gray when  $[Ba/Eu] \geq -0.3$ . The dotted line is the lanthanide fraction of the KN of the neutron star merger GW170817 (Kilpatrick et al. 2017; Chornock et al. 2017; Tanaka et al. 2017; Tanvir et al. 2017; Troja et al. 2017). The error bar shows the mean uncertainty of the  $[Sr/Ba]$  abundances and the derived  $\log X_{La}$ s.

$r_{lim}$  stars, we used *Gaia* DR3 radial velocities and proper motions (Gaia Collaboration et al. 2023) and distances from Bailer-Jones et al. (2021) to study the kinematics of the  $r_{lim}$  stars in our sample and in the literature. The orbits were then calculated with galpy<sup>4</sup> (Bovy 2015). In order to estimate the uncertainties of the orbital parameters, we calculated 500 orbits for each star while varying the proper motions and radial velocities by sampling them from a Gaussian distribution. The distributions had as mean the actual values of the proper motions and radial velocities, while we used their uncertainties as sigma. Figure 8 shows the Toomre diagram, where we plot  $V_{LSR}$  versus  $\sqrt{U_{LSR}^2 + W_{LSR}^2}$ , which are the velocities with respect to the local standard of rest (LSR) in the Cartesian Galactic coordinate frame. As shown, all three stars from our study have retrograde orbits, suggesting they could have been accreted onto the MW from satellite galaxies. However,  $\sim 65\%$  of all the  $r_{lim}$  stars are on prograde orbits. Moreover, 38% of the  $r_{lim}$  stars have  $v_{tot} < 220 \text{ km s}^{-1}$ , suggesting they may be consistent with disk stars. In addition, the  $r_{lim}$  stars considered from the perspective of their  $[Ba/Eu]$  abundance ratio also appear to be different in the two groups. Most of the stars with  $[Ba/Eu] \geq -0.3$  are on prograde orbits. These findings differ from the findings of Roederer et al. (2018) on the kinematics of 35 highly  $r$ -process-enhanced field stars ( $r$ -II for  $[Eu/Fe] > +0.7$ ). Roederer et al. (2018) showed that most if not all of the  $r$ -II stars were probably accreted by the MW from ultrafaint dwarf galaxies or low-luminosity dwarf spheroidal galaxies. The study of Roederer et al. (2018) was extended to significantly larger samples by Gudín et al. (2021) (466  $r$ -I and  $r$ -II stars) and Shank et al. (2023) (1720 stars). These studies confirmed the accreted nature of  $r$ -I and  $r$ -II stars. In

<sup>4</sup> <http://github.com/jobovy/galpy>

particular, Shank et al. (2023) reported that only 17% of the  $r$ -I stars and 8% of the  $r$ -II stars have disk-like kinematics. With the use of an unsupervised learning algorithm, Shank et al. (2023) identified 36 chemo-dynamically tagged groups (CDTGs), and  $\sim 1\%$  of the  $r$ -I and  $r$ -II stars in their sample were identified as belonging to the metal-weak thick disk (MWTD), while  $\sim 2.1\%$  were traced as members of the splashed disk (SD). The SD is described as a part of the MW primordial disk that was kinematically heated by the *Gaia*-Sausage-Enceladus (GSE) merger event (Belokurov et al. 2018; Helmi et al. 2018; Di Matteo et al. 2019; Belokurov et al. 2020).

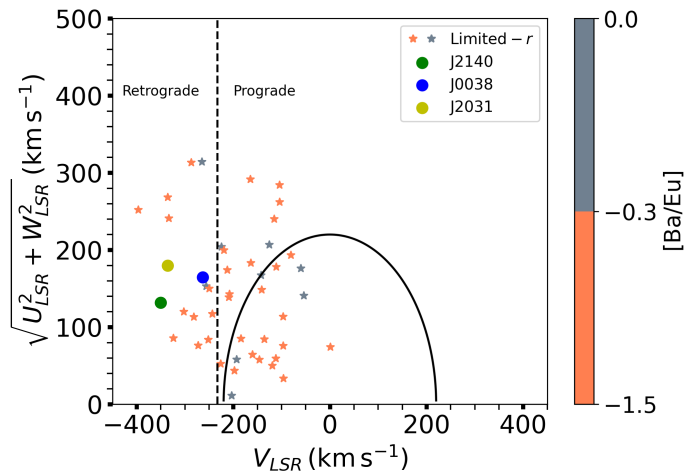


**Fig. 8.** Toomre diagram for the  $r_{lim}$  stars. The velocities depicted were calculated with respect to the LSR. The points are designated as in Figure 7. The dashed black line is  $V_{LSR} = -233.1 \text{ km s}^{-1}$  (McMillan 2016), and stars to the left of it are on retrograde orbits. The solid black line designates the area in which all stars have  $v_{tot} < 220 \text{ km s}^{-1}$ , where  $v_{tot} = \sqrt{U^2 + V^2 + W^2}$ .

We further examined the  $r_{lim}$  stars that appear to be disk-like, that is, their  $v_{tot} = \sqrt{U^2 + V^2 + W^2} < 220 \text{ km s}^{-1}$ . Several studies (e.g., Beers et al. 2014; Sestito et al. 2019, 2020; Cordoni et al. 2020) used the maximum distance of the stars from the Galactic plane,  $Z_{max}$ , to separate disk from halo stars, often in combination with another orbital parameter. Cordoni et al. (2020) used  $Z_{max}$  and the eccentricity of the orbit,  $e$ , in order to identify disk stars. Specifically, they considered stars on prograde orbits with  $|Z_{max}| \leq 3 \text{ kpc}$  and  $e < 0.75$  to belong to the thick disk. In Figure 9 we plot  $e$  versus  $Z_{max}$  of the disk-like  $r_{lim}$  stars. Based on these criteria, it appears that  $\sim 39\%$  of the disk-like  $r_{lim}$  stars belong to the MWTD, which is  $\sim 15\%$  of all the identified  $r_{lim}$  stars (7 stars) to date. Another route to identify disk stars was introduced by Haywood et al. (2018), who studied stars with high transverse velocities ( $v_t > 200 \text{ km s}^{-1}$ ), and used a  $Z_{max} - R_{max}$  plane, where  $R_{max}$  is the apocenter of the orbit projected on the Galactic plane, and discrete wedges appeared. These wedges were also clearly visible in the distribution of the angles  $\arctan(Z_{max}/R_{max})$ . Recently, Hong et al. (2023) followed Haywood et al. (2018) and assigned ranges to the inclination angle ( $IA$ ) -  $IA = \arctan(Z_{max}/R_{max})$  to distinguish thin- and thick-disk and halo stars. Specifically, they identified stars on prograde orbits as being members of the disk if  $|Z_{max}| \leq 3 \text{ kpc}$ , or  $IA \leq 0.65$ . The results following this selection procedure are presented in Figure 10. The use of the  $IA$  doubles the percentage of  $r_{lim}$  disk stars from  $\sim 15\%$  to  $\sim 30\%$  (14 stars). However, 5 out of the 14 stars with these criteria are identified as thin-disk stars ( $IA \leq 0.25$ ), while the rest are attributed to the MWTD

$0.25 < IA \leq 0.65$ . The significant difference between the  $r_{lim}$  and *r*-I, *r*-II stars from the aspect of disk membership still remains, considering that even though Shank et al. (2023) found 17% of the *r*-I stars to have disk-like kinematics, only  $\sim 1\%$  of the *r*-I and *r*-II stars could be chemo-dynamically traced back to the MWTD.

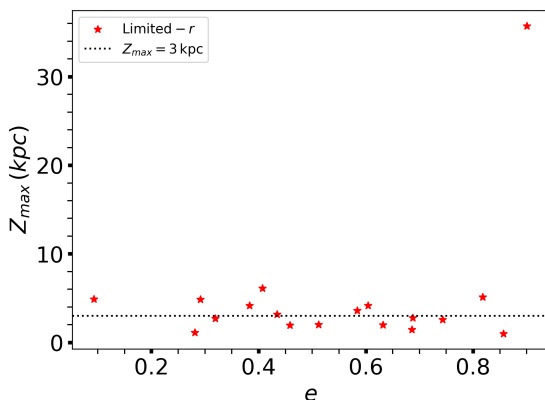


**Fig. 9.** Eccentricity vs.  $Z_{max}$  of the disk-like  $r_{lim}$  stars. The dotted black line designates  $Z_{max} = 3$  kpc. Stars that have  $Z_{max} < 3$  kpc and  $e \leq 0.75$  are very likely MWTD stars (Cordoni et al. 2020). The star with the highest eccentricity,  $e > 0.9$ , also has the largest  $Z_{max} > 30$  kpc.

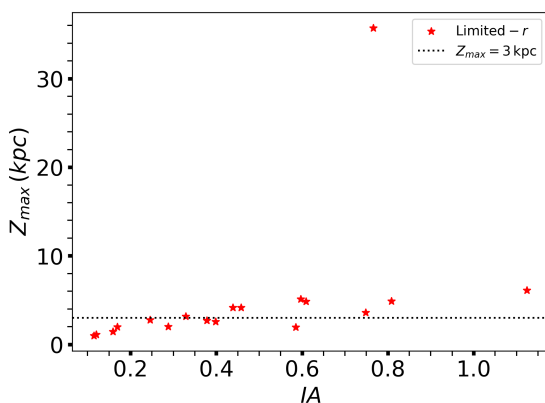


**Fig. 10.** Inclination angle vs.  $Z_{max}$  of the disk-like  $r_{lim}$  stars. As in Figure 9 the dotted black line designates  $Z_{max} = 3$  kpc. Stars that have  $Z_{max} < 3$  kpc or  $0.25 < IA \leq 0.65$  are very likely thick-disk stars, and those with  $IA \leq 0.25$  are probably thin-disk members (Hong et al. 2023). The IA is in radians.

Finally, as our three sample stars all have retrograde orbits, which might indicate that they are accreted by the MW from a satellite galaxy, we investigated their possible association with known structures. The *Gaia* mission (Gaia Collaboration et al. 2016) has provided astrometric information for more than a billion stars so far, enabling astronomers to unravel parts of the hierarchical assembly history of the MW (Helmi 2020). In this context, several accretion events have been identified. However, no definitive way for selecting members of an accretion event exists so far, in the sense that different kinematic or dynamic selection criteria from different studies can favor different stars as members of the same event, with a significant overlap. Gudin et al. (2021) found that 20% of the *r*-I and *r*-II stars are connected to the GSE event, while Shank et al. (2023) reported that 9% of their sample stars were associated with this event. We used the dynamic selection criteria from Myeong et al. (2019) and Feuillet et al. (2021) for the GSE and Sequoia (Myeong et al. 2019)

accretion events. The dynamic criteria of Myeong et al. (2019) are  $-0.07 < J_\phi/J_{tot} < 0.07$  and  $-1.0 < (J_z - J_R)/J_{tot} < -0.3$  for the GSE event and  $-1.0 < J_\phi/J_{tot} < -0.5$  and  $-1.0 < (J_z - J_R)/J_{tot} < 0.1$  for the Sequoia event. Those from Feuillet et al. (2021) are  $-500 \leq L_z \leq 500$  and  $30 \leq \sqrt{J_R} \leq 55$ , and  $-1.0 < J_\phi/J_{tot} < -0.4$  and  $-1.0 < (J_z - J_R)/J_{tot} < 0.1$  for the GSE and Sequoia events, respectively. According to these criteria, star J2140 was probably accreted during the Sequoia accretion event. In total, two  $r_{lim}$  stars seem to be accreted from *Gaia* Sequoia, while two to four others were accreted from GSE, depending on the selection criteria. Cumulatively, we find 4-9% for the  $r_{lim}$  stars associated with the GSE, depending on the dynamic criteria employed. The results are shown in Table A.2

## 6. Summary

We studied a sample of three *r*-process stars that were observed by the RPA and were classified as  $r_{lim}$  stars. With the updated stellar parameters used for this study, one of the stars, J2031, is an *r*-I star, while the other two, J0038 and J2140, qualify as  $r_{lim}$  stars. The abundances of non-neutron-capture elements for J0038 and J2031 resemble those of normal MW halo stars, while J2140 exhibits higher abundances of the iron-peak elements Cr, Mn, Co, Ni, Cu, and Zn and is also enhanced in C, N and Na. This suggests that it underwent a different chemical-enrichment history than stars J0038, J2031, and other typical MW halo stars.

We compared the neutron-capture element abundance patterns of our stars to the baseline pattern of Roederer et al. (2023). For the two  $r_{lim}$  stars we find that the pattern of J0038, which has  $[Ba/Eu] < -0.3$ , agrees very well with the pattern, while that of J2140, which has  $[Ba/Eu] > -0.3$ , does not. This implies that  $r_{lim}$  stars with  $[Ba/Eu] < -0.3$  have been enriched by an *r*-process similar to that which enriched *r*-I and *r*-II stars, while another or multiple nuclear processes caused the abundance pattern seen in  $r_{lim}$  stars with  $[Ba/Eu] \geq -0.3$ . Furthermore, the comparison of the *r*-I star, J2031, with the baseline pattern suggests that the abundances of this star have been affected by fission-fragment deposition.

Next, we calculated  $X_{La}$  of our stars, as well as those of the  $r_{lim}$  stars in the literature. We compared it to that of the KN of the NSM GW170817. We find that the  $X_{La}$  of the KN is in the transition region between  $r_{lim}$  stars and *r*-I, *r*-II stars. This could suggest that NSMs such as GW170817 could be the *r*-process site that causes the abundance signatures observed in  $r_{lim}$  stars. However, because we do not know the time delay between NSMs and the onset of star formation, it is important to assess whether the  $r_{lim}$  stars could have been accreted onto the MW from an environment with a low star-formation rate. To investigate this, we studied the kinematics of the  $r_{lim}$  stars. We find that unlike *r*-I and *r*-II stars that were mostly accreted (Gudin et al. 2021), 65% of  $r_{lim}$  stars are on prograde orbits, suggesting they were probably born in situ. Furthermore, 38% of the  $r_{lim}$  stars present disk-like kinematics, which conveys another distinct difference between these and *r*-I, *r*-II stars, as reported by Shank et al. (2023), who find that 17% of the *r*-I stars and 8% of the *r*-II stars have such kinematics. Last, we find that 15% of the  $r_{lim}$  stars are simultaneously on prograde orbits, have  $Z_{max} \leq 3$  kpc, and have  $e \leq 0.75$ , indicating that they belong to the MWTD, unlike the *r*-I, *r*-II stars, only  $\sim 1\%$  of which were chemo-dynamically attributed to the MWTD (Shank et al. 2023).

The discovery and detailed abundance analysis of more  $r_{lim}$  stars is vital to further explore the kinematic signature of these stars and assess the difference between those with  $[Ba/Eu]$  above and below  $-0.3$ . The measurement of additional neutron-capture

elements for these stars will either reinforce the fact that the latter seems to have been enriched by an  $r$ -process similar to that enriching  $r$ -I and  $r$ -II stars or provide new insight. Future analysis of snapshot stellar spectra, already obtained by the RPA, is expected to double the number of identified  $r_{lim}$  stars.

**Acknowledgements.** We thank the anonymous referee for helpful comments, which helped improve this manuscript. This work was funded by the Deutsche Forschungsgemeinschaft (DFG, German Research Foundation) – Project-ID 138713538 – SFB 881 (“The Milky Way System”, subproject A04). T.X. acknowledges support from the Heidelberg Graduate School for Physics (HGSFP). T.T.H. acknowledges support from the Swedish Research Council (VR 2021-05556). T.C.B. acknowledges partial support for this work from grant PHY 14-30152; Physics Frontier Center/JINA Center for the Evolution of the Elements (JINA-CEE), and OISE-1927130: The International Research Network for Nuclear Astrophysics (iReNA), awarded by the US National Science Foundation. R.E. acknowledges support from NSF grant AST-2206263. A.F. acknowledges support from NSF grants AST-1716251 and 2307436. The work of V.M.P. is supported by NOIRLab, which is managed by the Association of Universities for Research in Astronomy (AURA) under a cooperative agreement with the National Science Foundation. I.U.R. acknowledges support from the U.S. National Science Foundation (NSF), grants PHY 14-30152 (Physics Frontier Center/JINA-CEE), AST 1815403, and AST 2205847, as well as support from the NASA Astrophysics Data Analysis Program, grant 80NSSC21K0627. This paper includes data gathered with the 6.5 meter Magellan Telescopes located at Las Campanas Observatory, Chile, and data taken at The McDonald Observatory of The University of Texas at Austin. This research made extensive use of the SIMBAD database operated at CDS, Strasbourg, France (Wenger et al. 2000), arXiv.org and NASA’s Astrophysics Data System for bibliographic information.

## References

- Abbott, B. P., Abbott, R., Abbott, T. D., et al. 2017a, *Phys. Rev. Lett.*, 119, 161101
- Abbott, B. P., Abbott, R., Abbott, T. D., et al. 2017b, *ApJ*, 848, L12
- Andrievsky, S. M., Spite, M., Korotin, S. A., et al. 2010, *Astronomy and Astrophysics*, 509, A88
- Aoki, W., Beers, T. C., Christlieb, N., et al. 2007, *The Astrophysical Journal*, 655, 492–521
- Asplund, M., Grevesse, N., Sauval, A. J., & Scott, P. 2009, *ARA&A*, 47, 481
- Bailer-Jones, C. A. L., Rybizki, J., Fousneau, M., Demleitner, M., & Andrae, R. 2021, *VizieR Online Data Catalog*, I/352
- Bailer-Jones, C. A. L., Rybizki, J., Fousneau, M., Mantelet, G., & Andrae, R. 2018, *AJ*, 156, 58
- Barklem, P. S., Christlieb, N., Beers, T. C., et al. 2005, *A&A*, 439, 129
- Beers, T. C. & Christlieb, N. 2005, *ARA&A*, 43, 531
- Beers, T. C., Norris, J. E., Placco, V. M., et al. 2014, *The Astrophysical Journal*, 794, 58
- Beers, T. C., Placco, V. M., Carollo, D., et al. 2017, *ApJ*, 835, 81
- Belmonte, M. T., Pickering, J. C., Ruffoni, M. P., et al. 2017, *ApJ*, 848, 125
- Belokurov, V., Erkal, D., Evans, N. W., Koposov, S. E., & Deason, A. J. 2018, *MNRAS*, 478, 611
- Belokurov, V., Sanders, J. L., Fattahi, A., et al. 2020, *Monthly Notices of the Royal Astronomical Society*, 494, 3880–3898
- Bergemann, M. & Cescutti, G. 2010, *A&A*, 522, A9
- Bergemann, M., Gallagher, A. J., Eitner, P., et al. 2019, *A&A*, 631, A80
- Bergemann, M., Hoppe, R., Semenova, E., et al. 2021, *Monthly Notices of the Royal Astronomical Society*, 508, 2236–2253
- Bergemann, M., Pickering, J. C., & Gehren, T. 2010, *Monthly Notices of the Royal Astronomical Society*, 401, 1334–1346
- Bernstein, R., Shectman, S. A., Gunnels, S. M., Mochnacki, S., & Athey, A. E. 2003, in *Society of Photo-Optical Instrumentation Engineers (SPIE) Conference Series*, Vol. 4841, Instrument Design and Performance for Optical/Infrared Ground-based Telescopes, ed. M. Iye & A. F. M. Moorwood, 1694–1704
- Biémont, É., Blagoev, K., Engström, L., et al. 2011, *MNRAS*, 414, 3350
- Bovy, J. 2015, *The Astrophysical Journal Supplement Series*, 216, 29
- Brauer, K., Ji, A. P., Drout, M. R., & Frebel, A. 2021, *The Astrophysical Journal*, 915, 81
- Burbidge, E. M., Burbidge, G. R., Fowler, W. A., & Hoyle, F. 1957, *Reviews of Modern Physics*, 29, 547
- Cameron, A. G. W. 1957, *Publications of the Astronomical Society of the Pacific*, 69, 201
- Carollo, D., Beers, T. C., Bovy, J., et al. 2011, *The Astrophysical Journal*, 744, 195
- Casagrande, L., Ramírez, I., Meléndez, J., Bessell, M., & Asplund, M. 2010, *A&A*, 512, A54
- Casagrande, L. & Vandenberg, D. A. 2014, *MNRAS*, 444, 392
- Casey, A. R. 2014, Australian National Univ.
- Castelli, F. & Kurucz, R. L. 2003, in *Modelling of Stellar Atmospheres*, ed. N. Piskunov, W. W. Weiss, & D. F. Gray, Vol. 210, A20
- Chornock, R., Berger, E., Kasen, D., et al. 2017, *ApJ*, 848, L19
- Christlieb, N., Beers, T. C., Barklem, P. S., et al. 2004, *A&A*, 428, 1027
- Cohen, J. G., Christlieb, N., Thompson, I., et al. 2013, *ApJ*, 778, 56
- Cordoni, G., Da Costa, G. S., Yong, D., et al. 2020, *Monthly Notices of the Royal Astronomical Society*, 503, 2539–2561
- Côté, B., Eichler, M., Arcones, A., et al. 2019, *ApJ*, 875, 106
- Coulter, D. A., Foley, R. J., Kilpatrick, C. D., et al. 2017, *Science*, 358, 1556
- Cowan, J. J. & Rose, W. K. 1977, *ApJ*, 212, 149
- Cowan, J. J., Sneden, C., Lawler, J. E., et al. 2021, *Reviews of Modern Physics*, 93
- Cutri, R. M., Skrutskie, M. F., van Dyk, S., et al. 2003, *VizieR Online Data Catalog*, II/246
- Den Hartog, E. A., Lawler, J. E., Sneden, C., & Cowan, J. J. 2003, *ApJS*, 148, 543
- Den Hartog, E. A., Lawler, J. E., Sneden, C., Cowan, J. J., & Brukhovetsky, A. 2019, *ApJS*, 243, 33
- Den Hartog, E. A., Lawler, J. E., Sobek, J. S., Sneden, C., & Cowan, J. J. 2011, *ApJS*, 194, 35
- Den Hartog, E. A., Ruffoni, M. P., Lawler, J. E., et al. 2014, *ApJS*, 215, 23
- Di Matteo, P., Haywood, M., Lehnert, M. D., et al. 2019, *A&A*, 632, A4
- Drout, M. R., Piro, A. L., Shappee, B. J., et al. 2017, *Science*, 358, 1570
- Ezzeddine, R., Rasmussen, K., Frebel, A., et al. 2020, *ApJ*, 898, 150
- Feuillet, D. K., Sahlholdt, C. L., Feltzing, S., & Casagrande, L. 2021, *Monthly Notices of the Royal Astronomical Society*, 508, 1489–1508
- Fischer, T., Bastian, N.-U. F., Wu, M.-R., et al. 2018, *Nature Astronomy*, 2, 980
- Fischer, T., Wu, M.-R., Wehmeyer, B., et al. 2020, *The Astrophysical Journal*, 894, 9
- François, P., Depagne, E., Hill, V., et al. 2007, *A&A*, 476, 935
- Frebel, A. 2018, *Annual Review of Nuclear and Particle Science*, 68, 237
- Frischknecht, U., Hirschi, R., Pignatari, M., et al. 2015, *Monthly Notices of the Royal Astronomical Society*, 456, 1803
- Gaia Collaboration. 2018, *VizieR Online Data Catalog*, I/345
- Gaia Collaboration, Prusti, T., de Bruijne, J. H. J., et al. 2016, *A&A*, 595, A1
- Gaia Collaboration, Vallenari, A., Brown, A. G. A., et al. 2023, *A&A*, 674, A1
- Gudin, D., Shank, D., Beers, T. C., et al. 2021, *ApJ*, 908, 79
- Halbwachs, J.-L., Pourbaix, D., Arenou, F., et al. 2023, *A&A*, 674, A9
- Hansen, C. J., Primas, F., Hartman, H., et al. 2012, *A&A*, 545, A31
- Hansen, T. T., Holmbeck, E. M., Beers, T. C., et al. 2018, *ApJ*, 858, 92
- Haywood, M., Di Matteo, P., Lehnert, M. D., et al. 2018, *The Astrophysical Journal*, 863, 113
- Helmi, A. 2020, *ARA&A*, 58, 205
- Helmi, A., Babusiaux, C., Koppelman, H. H., et al. 2018, *Nature*, 563, 85–88
- Henden, A. A., Levine, S., Terrell, D., et al. 2018, in *American Astronomical Society Meeting Abstracts*, Vol. 232, American Astronomical Society Meeting Abstracts #232, 223.06
- Holmbeck, E. M., Hansen, T. T., Beers, T. C., et al. 2020, *ApJS*, 249, 30
- Honda, S., Aoki, W., Ishimaru, Y., & Wanajo, S. 2007, *ApJ*, 666, 1189
- Honda, S., Aoki, W., Ishimaru, Y., Wanajo, S., & Ryan, S. G. 2006, *ApJ*, 643, 1180
- Hong, J., Beers, T. C., Lee, Y. S., et al. 2023, *Candidate Members of the VMP/EMP Disk System of the Galaxy from the SkyMapper and SAGES Surveys*
- Ishigaki, M. N., Aoki, W., & Chiba, M. 2013, *ApJ*, 771, 67
- Ivans, I. I., Simmerer, J., Sneden, C., et al. 2006, *ApJ*, 645, 613
- Ji, A. P., Drout, M. R., & Hansen, T. T. 2019, *ApJ*, 882, 40
- Ji, A. P., Li, T. S., Hansen, T. T., et al. 2020, *AJ*, 160, 181
- Kasen, D., Metzger, B., Barnes, J., Quataert, E., & Ramirez-Ruiz, E. 2017, *Nature*, 551, 80
- Kelson, D. D. 2003, *PASP*, 115, 688
- Kelson, D. D., Illingworth, G. D., van Dokkum, P. G., & Franx, M. 2000, *ApJ*, 531, 184
- Kilpatrick, C. D., Foley, R. J., Kasen, D., et al. 2017, *Science*, 358, 1583
- Kobayashi, C., Mandel, I., Belczynski, K., et al. 2023, *ApJ*, 943, L12
- Kramida, A. & Ralchenko, Y. 1999, NIST atomic spectra database, NIST standard reference database 78
- Kramida, A., Ralchenko, Y., Nave, G., & Reader, J. 2018a, in *Molecular and Optical Physics Meeting Abstracts*, M01
- Kramida, A., Ralchenko, Y., Reader, J., & NIST Atomic Spectra Database (ver. 5.5.6). [Online]. 2018b, Available: <https://physics.nist.gov/asd> [2018, May 12]. National Institute of Standards and Technology, Gaithersburg, MD
- Kunder, A., Kordopatis, G., Steinmetz, M., et al. 2017, *AJ*, 153, 75
- Kurucz, R. & Bell, B. 1995, *Atomic Line List*
- Lai, D. K., Bolte, M., Johnson, J. A., et al. 2008, *ApJ*, 681, 1524
- Lawler, J. E., Bonvallet, G., & Sneden, C. 2001, *ApJ*, 556, 452

- Lawler, J. E. & Dakin, J. T. 1989, *Journal of the Optical Society of America B Optical Physics*, 6, 1457
- Lawler, J. E., Guzman, A., Wood, M. P., Sneden, C., & Cowan, J. J. 2013, *ApJS*, 205, 11
- Lawler, J. E., Sneden, C., & Cowan, J. J. 2015, *ApJS*, 220, 13
- Lawler, J. E., Sneden, C., Cowan, J. J., et al. 2008, *ApJS*, 178, 71
- Lawler, J. E., Sneden, C., Nave, G., et al. 2017, *ApJS*, 228, 10
- Lawler, J. E., Wickliffe, M. E., Hartog, E. A. D., & Sneden, C. 2001, *The Astrophysical Journal*, 563, 1075
- Lawler, J. E., Wood, M. P., Hartog, E. A. D., et al. 2014, *The Astrophysical Journal Supplement Series*, 215, 20
- Lemaître, J.-F., Goriely, S., Bauswein, A., & Janka, H.-T. 2021, *Phys. Rev. C*, 103, 025806
- Limongi, M. & Chieffi, A. 2018, *ApJS*, 237, 13
- Ljung, G., Nilsson, H., Asplund, M., & Johansson, S. 2006, *A&A*, 456, 1181
- McCall, M. L. 2004, *AJ*, 128, 2144
- McMillan, P. J. 2016, *Monthly Notices of the Royal Astronomical Society*, 465, 76
- McWilliam, A. 1998, *AJ*, 115, 1640
- Meléndez, J. & Barbuy, B. 2009, *A&A*, 497, 611
- Meynet, G., Ekström, S., & Maeder, A. 2006, *A&A*, 447, 623
- Mumpower, M. R., Jaffke, P., Verriere, M., & Randrup, J. 2020, *Phys. Rev. C*, 101, 054607
- Myeong, G. C., Vasiliev, E., Iorio, G., Evans, N. W., & Belokurov, V. 2019, *Monthly Notices of the Royal Astronomical Society*, 488, 1235–1247
- Nishimura, N., Sawai, H., Takiwaki, T., Yamada, S., & Thielemann, F. K. 2017, *ApJ*, 836, L21
- Nishimura, N., Takiwaki, T., & Thielemann, F.-K. 2015, *ApJ*, 810, 109
- Norris, J. E., Yong, D., Bessell, M. S., et al. 2013, *ApJ*, 762, 28
- O’Brian, T. R., Wickliffe, M. E., Lawler, J. E., Whaling, W., & Brault, J. W. 1991, *Journal of the Optical Society of America B Optical Physics*, 8, 1185
- Pehlivan Rhodin, A., Belmonte, M. T., Engstrom, L., et al. 2017, *arXiv e-prints*, arXiv:1708.06692
- Perego, A., Radice, D., & Bernuzzi, S. 2017, *ApJ*, 850, L37
- Pickering, J. C., Thorne, A. P., & Perez, R. 2001, *ApJS*, 132, 403
- Pickering, J. C., Thorne, A. P., & Perez, R. 2002, *ApJS*, 138, 247
- Placco, V. M., Frebel, A., Beers, T. C., & Stancliffe, R. J. 2014, *The Astrophysical Journal*, 797, 21
- Placco, V. M., Sneden, C., Roederer, I. U., et al. 2021, *Research Notes of the American Astronomical Society*, 5, 92
- Preston, G. W., Sneden, C., Thompson, I. B., Shtetman, S. A., & Burley, G. S. 2006, *AJ*, 132, 85
- Roederer, I. U., Cowan, J. J., Pignatari, M., et al. 2022, *ApJ*, 936, 84
- Roederer, I. U., Hattori, K., & Valluri, M. 2018, *AJ*, 156, 179
- Roederer, I. U., Karakas, A. I., Pignatari, M., & Herwig, F. 2016, *ApJ*, 821, 37
- Roederer, I. U. & Lawler, J. E. 2012, *ApJ*, 750, 76
- Roederer, I. U., Lawler, J. E., Sneden, C., et al. 2008, *The Astrophysical Journal*, 675, 723
- Roederer, I. U., Preston, G. W., Thompson, I. B., et al. 2014, *The Astronomical Journal*, 147, 136
- Roederer, I. U., Sakari, C. M., Placco, V. M., et al. 2018, *The Astrophysical Journal*, 865, 129
- Roederer, I. U., Vassh, N., Holmbeck, E. M., et al. 2023, *Science*, 382, 1177
- Rosswog, S., Sollerman, J., Feindt, U., et al. 2018, *A&A*, 615, A132
- Ruffoni, M. P., Den Hartog, E. A., Lawler, J. E., et al. 2014, *MNRAS*, 441, 3127
- Sakari, C. M., Placco, V. M., Farrell, E. M., et al. 2018, *ApJ*, 868, 110
- Schlafly, E. F. & Finkbeiner, D. P. 2011, *ApJ*, 737, 103
- Sestito, F., Buck, T., Starkenburg, E., et al. 2020, *Monthly Notices of the Royal Astronomical Society*, 500, 3750–3762
- Sestito, F., Longeard, N., Martin, N. F., et al. 2019, *Monthly Notices of the Royal Astronomical Society*, 484, 2166
- Shank, D., Beers, T. C., Placco, V. M., et al. 2023, *ApJ*, 943, 23
- Siegel, D. M., Barnes, J., & Metzger, B. D. 2019, *Nature*, 569, 241
- Smith, V. V., Lambert, D. L., & Nissen, P. E. 1998, *ApJ*, 506, 405
- Sneden, C. 1973, *Univ. Texas*
- Sneden, C., Cowan, J. J., & Gallino, R. 2008, *ARA&A*, 46, 241
- Sneden, C., Lawler, J. E., Cowan, J. J., Ivans, I. I., & Den Hartog, E. A. 2009, *ApJS*, 182, 80
- Sneden, C. & Parthasarathy, M. 1983, *ApJ*, 267, 757
- Sobeck, J. S., Kraft, R. P., Sneden, C., et al. 2011, *AJ*, 141, 175
- Sobeck, J. S., Lawler, J. E., & Sneden, C. 2007, *ApJ*, 667, 1267
- Steinmetz, M., Guiglion, G., McMillan, P. J., et al. 2020, *AJ*, 160, 83
- Suda, T., Hidaka, J., Aoki, W., et al. 2017, *PASJ*, 69, 76
- Suda, T., Katsuta, Y., Yamada, S., et al. 2008, *PASJ*, 60, 1159
- Suda, T., Yamada, S., Katsuta, Y., et al. 2011, *MNRAS*, 412, 843
- Tanaka, M., Utsumi, Y., Mazzali, P. A., et al. 2017, *PASJ*, 69, 102
- Tanvir, N. R., Levan, A. J., González-Fernández, C., et al. 2017, *ApJ*, 848, L27
- Tody, D. 1986, in *Society of Photo-Optical Instrumentation Engineers (SPIE) Conference Series*, Vol. 627, *Instrumentation in astronomy VI*, ed. D. L. Crawford, 733
- Tody, D. 1993, in *Astronomical Society of the Pacific Conference Series*, Vol. 52, *Astronomical Data Analysis Software and Systems II*, ed. R. J. Hanisch, R. J. V. Brissenden, & J. Barnes, 173
- Travaglio, C., Gallino, R., Arnone, E., et al. 2004, *The Astrophysical Journal*, 601, 864
- Troja, E., Piro, L., van Eerten, H., et al. 2017, *Nature*, 551, 71
- Truran, J. W. 1981, *A&A*, 97, 391
- Tull, R. G., MacQueen, P. J., Sneden, C., & Lambert, D. L. 1995, *PASP*, 107, 251
- Vassh, N., Mumpower, M. R., McLaughlin, G. C., Sprouse, T. M., & Surman, R. 2020, *ApJ*, 896, 28
- Voronov, Y. V., Yakovleva, S. A., & Belyaev, A. K. 2022, *The Astrophysical Journal*, 926, 173
- Wenger, M., Ochsenbein, F., Egret, D., et al. 2000, *A&AS*, 143, 9
- Wickliffe, M. E., Lawler, J. E., & Nave, G. 2000, *J. Quant. Spectr. Rad. Transf.*, 66, 363
- Winteler, C., Käppeli, R., Perego, A., et al. 2012, *ApJ*, 750, L22
- Wood, M. P., Lawler, J. E., Sneden, C., & Cowan, J. J. 2013, *ApJS*, 208, 27
- Wood, M. P., Lawler, J. E., Sneden, C., & Cowan, J. J. 2014, *ApJS*, 211, 20
- Yamada, S., Suda, T., Komiya, Y., Aoki, W., & Fujimoto, M. Y. 2013, *MNRAS*, 436, 1362
- Yu, Y. & Derevianko, A. 2018, *Atomic Data and Nuclear Data Tables*, 119, 263

**Table A.1.** Uncertainties in the abundances determination due to the uncertainties in stellar parameters for star J0038.

Element	$\Delta T_{\text{eff}}$ (K)	$\Delta \log g$ (dex)	$\Delta \xi$ ( $\text{km s}^{-1}$ )	$\Delta [\text{M}/\text{H}]$ (dex)	$\sigma_{\text{sys}}$ (dex)
Li I	0.08	-0.00	0.01	0.01	0.07
C-H	0.16	-0.03	0.01	0.04	0.10
O I	-0.08	0.04	-0.01	-0.00	0.04
Na I	0.10	-0.03	-0.10	-0.00	0.16
Mg I	0.04	-0.01	-0.02	0.00	0.06
Al I	0.16	-0.03	-0.11	0.01	0.23
Si I	0.04	0.01	-0.02	-0.00	0.06
K I	0.06	-0.00	-0.03	0.00	0.08
Ca I	0.04	0.00	0.01	0.00	0.04
Sc II	0.02	0.03	-0.01	0.01	0.06
Ti I	0.08	-0.00	0.03	0.01	0.05
Ti II	0.03	0.03	0.04	0.02	0.03
V I	0.02	0.01	0.02	-0.01	0.02
V II	-0.02	0.04	0.01	0.00	0.01
Cr I	0.08	0.00	0.03	0.01	0.05
Cr II	-0.00	0.03	-0.01	0.00	0.03
Mn I	0.06	-0.00	-0.01	0.00	0.06
Fe I	0.04	0.00	0.03	0.01	0.02
Fe II	0.01	0.03	0.02	0.01	0.02
Co I	0.05	0.01	-0.02	-0.01	0.08
Ni I	0.04	0.00	0.03	0.00	0.02
Zn I	0.04	0.01	-0.01	0.00	0.06
Sr II	-0.10	-0.04	-0.19	-0.10	0.11
Y II	-0.00	0.03	-0.00	0.01	0.04
Zr II	-0.02	0.04	0.01	0.00	0.02
Ba II	0.03	0.03	-0.02	0.01	0.08
La II	0.02	0.03	0.03	0.01	0.02
Nd II	0.02	0.02	0.01	0.02	0.03
Eu II	0.02	0.03	0.02	0.01	0.03
Dy II	0.02	0.03	0.01	0.03	0.04
Er II	0.02	0.03	-0.07	-0.01	0.12
Yb II	0.06	0.02	-0.03	0.01	0.11

**Notes.** The full table for all three stars is available online.

**Table A.2.** Accreted  $r_{\text{lim}}$  stars based on dynamic selection criteria.

Stellar ID	GSE member	Sequoia member	Criteria
2MASSJ19534978-5940001	✓	-	Myeong et al. (2019), Feuillet et al. (2021)
2MASSJ19345497-5751400	✓	-	Myeong et al. (2019), Feuillet et al. (2021)
2MASSJ20560913-1331176	✓	-	Feuillet et al. (2021)
2MASSJ19202070-6627202	✓	-	Feuillet et al. (2021)
HD 184266	✓	-	Feuillet et al. (2021)
2MASSJ21402305-1227035	-	✓	Myeong et al. (2019), Feuillet et al. (2021)
CD-24 1782	-	✓	Myeong et al. (2019), Feuillet et al. (2021)

**Table A.3.** Lanthanide mass fractions of  $r_{\text{lim}}$  stars.

Stellar ID	$X_{\text{La}}$	$\sigma_{X_{\text{La}}}$ (dex)
J21402305-1227035	-2.95	0.22
J00385967+2725516	-2.38	0.17
J20313531-3127319	-2.17	0.15
J10344785-4823544	-2.52	0.37
J13085850-2712188	-2.43	0.37
J13335283-2623539	-2.51	0.37
J05384334-5147228	-2.46	0.39
J01094330-5907230	-2.45	0.37
J132604.5-152502	-2.50	0.15
J160642.3-163245	-2.56	0.28
J19594558-2549075	-2.46	0.53
J163931.1-052252	-2.65	0.32
J14533307-4428301	-2.50	0.37
J14435196-2106283	-2.68	0.37
J20560913-1331176	-2.54	0.53
J18121045-4934495	-2.66	0.53
J164551.2-042947	-2.76	0.37
J19534978-5940001	-2.61	0.53
J035509.3-063711	-2.64	0.22
J19202070-6627202	-2.76	0.54
J14164084-2422000	-2.81	0.54
J19345497-5751400	-2.64	0.53
J19494025-5424113	-2.77	0.54
J08025449-5224304	-2.93	0.40
J03563703-5838281	-2.87	0.54
J003052.7-100704	-2.97	0.26
J21370807-0927347	-3.00	0.54
J17285930-7427532	-3.01	0.54
J154755.2-083710	-3.20	0.30
CS 22186-023	-2.83	0.48
CS 22879-103	-2.29	0.30
CS 22891-209	-2.64	0.35
CS 22897-008	-3.27	0.32
CS 22937-072	-2.47	0.36
CS 22940-070	-2.37	0.35
CS 22956-114	-2.25	0.38
CS 30494-003	-2.30	0.34
CD-24 1782	-2.51	0.46
G026-001	-2.48	0.31
HD 13979	-2.13	0.36
HD 19445	-2.43	0.48
HD 26169	-2.38	0.30
HD 88609	-2.70	0.44
HD 122563	-2.71	0.37
HD 175606	-2.18	0.36
HD 184266	-2.09	0.30
HD 237846	-2.62	0.42
HE 1320-1339	-2.14	0.35

## Appendix A: Additional tables.

We present a table showing the uncertainty arising in the abundance estimation from the uncertainty in the stellar parameter determination. Furthermore, a table contains information about the likely accreted  $r_{\text{lim}}$  stars based on the dynamic selection criteria from Myeong et al. (2019) and Feuillet et al. (2021). Last, we include a table that lists the lanthanide fractions and the uncertainties that were computed for the  $r_{\text{lim}}$  stars.



## Chapter 6

# Discussion

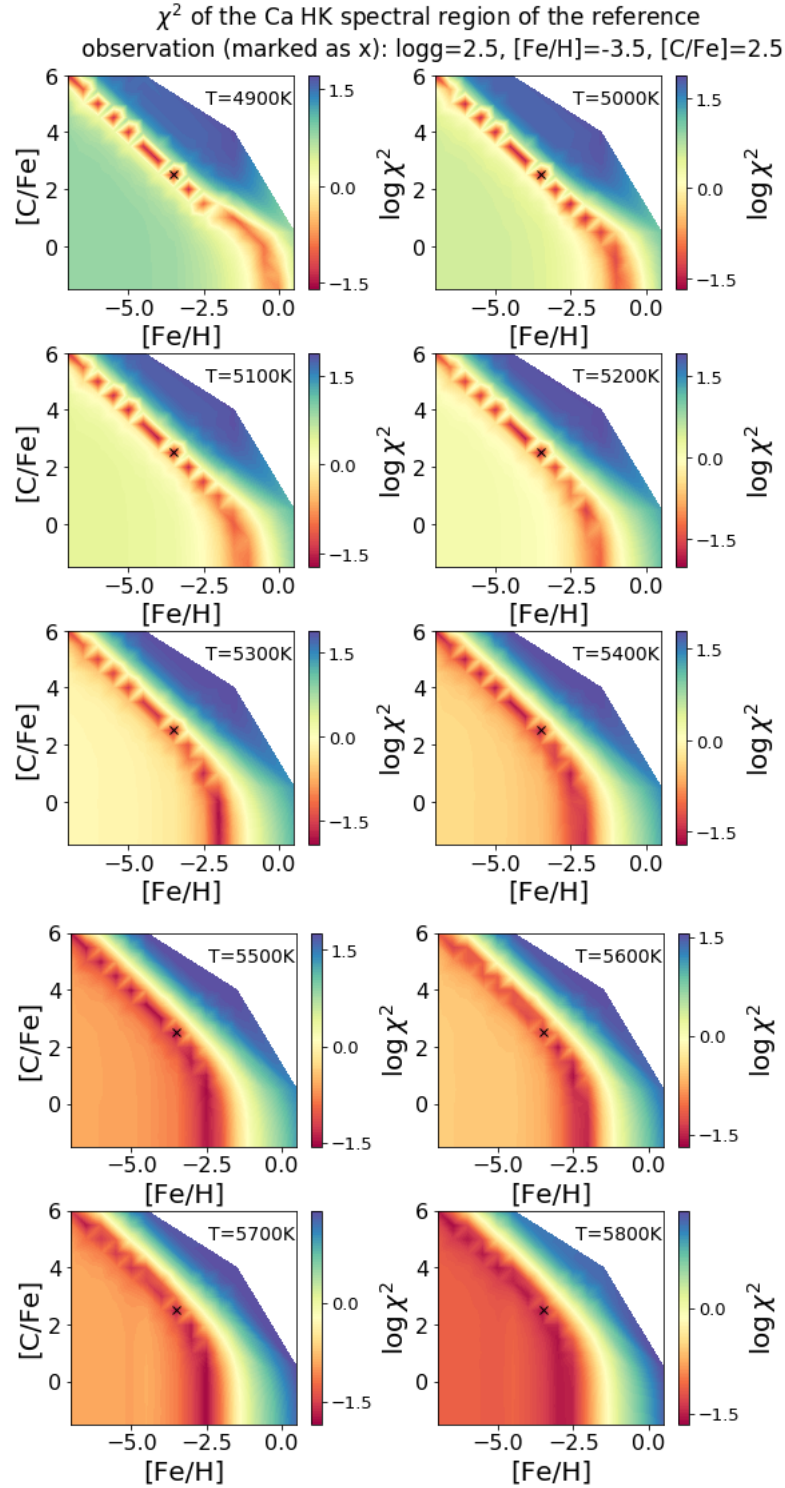
In this dissertation three different studies are presented. The two first were dedicated to the discovery of metal-poor candidates in *Gaia*, while the last one was a study of metal-poor stars that exhibit signatures of *r*-process nucleosynthesis in their abundance patterns. Here I will be discussing about the caveat of the selection method, how the different studies can be linked with each other, and also place them in the broader framework of Galactic archaeology.

### 6.1 Caveat of the selection method

The quest for a method to identify metal-poor stars with *Gaia* BP/RP spectra posed many challenges. The extremely low-resolution – as described in Section 1.4 – required an investigation into whether or not the spectra would carry enough information related to the metallicity of the source. As the BP/RP spectra were not available at the beginning of this project, the first investigation was done on simulated data. Therefore, I proceeded to do a  $\chi^2$  test which was executed as follows: I simulated with Ulysses a model spectrum of specific stellar parameters  $T_{\text{eff}}$ ,  $\log g$ ,  $[\text{Fe}/\text{H}]$ , and  $[\text{C}/\text{Fe}]$ , and noisy spectra of the same temperature and surface gravity, but with varying metallicities and relative carbon abundances. I also varied the  $[\text{C}/\text{Fe}]$ , since it has been shown (e.g. Lucatello et al., 2006; Yong et al., 2013; Lee et al., 2013; Placco et al., 2014; Arentsen et al., 2021) that a significant fraction of metal-poor stars are CEMP stars, and that the fraction increases as the metallicity decreases. Particularly, Placco et al., 2014 found that for Galactic halo stars with  $[\text{Fe}/\text{H}] \leq -2.0$   $\sim$  20% have  $[\text{C}/\text{Fe}] \geq +0.7$ , and that this fraction increases to  $\sim$  43% and  $\sim$  81% for stars with  $[\text{Fe}/\text{H}] \leq -3.0$  and  $[\text{Fe}/\text{H}] \leq -4.0$ , respectively. Arentsen et al., 2021 found that the CEMP fraction of metal-poor stars in the Galactic bulge differs from that of the halo stars. Specifically, they found that when  $[\text{Fe}/\text{H}] < -2.0$   $\sim$  5.7% of the stars have  $[\text{C}/\text{Fe}] \geq +0.7$ , and this increases to  $\sim$  16% and  $\sim$  42% for stars with  $[\text{Fe}/\text{H}] < -2.5$  and  $[\text{Fe}/\text{H}] < -3.0$ , respectively. Therefore, an important requirement for the BP/RP metal-poor identification method was to be able to identify CEMP stars as metal-poor. A contour plot of the  $\chi^2$  of the Ca H & K region of the spectra using the noisy spectra as the observations  $O$ , and the model spectrum as such  $M$ , was used for the assessment.

$$\chi^2 = \sum \frac{(O - M)^2}{M} \quad (6.1)$$

The results are shown in Figure 6.1. As can be seen, the  $\chi^2$  test shows – for that particular set of stellar parameters – that as the temperature increases the information in the spectra suffices for the purpose of distinguishing between metal-rich and metal-poor stars down to  $[\text{Fe}/\text{H}] \sim -2.5$ .



However, in Paper I I found that the minimum metallicity down to which the selection method can distinguish is  $[\text{Fe}/\text{H}] \sim -3.0$ . This was partially confirmed in Paper II: the application on the GALAH-SAGA dataset showed that the method can predict the metallicity down to  $[\text{Fe}/\text{H}] \sim -3.4$  with  $\sigma \sim 0.36$  dex, but the selection and observation of the candidates showed that the method can reliably distinguish down to  $[\text{Fe}/\text{H}] \sim -2.9$  with  $\sigma \sim 0.31$  dex.

This is a caveat of the method, but here I will argue as to why, in practice, it does not really limit its capabilities. All the surveys that have been tailored to look for metal-poor stars, such as the HES, *Pristine*, and the Skymapper surveys, operate in selecting targets – via survey-specific methods – for which they take spectra of medium resolving power ( $R \sim 1000 - 2000$ ) for metal-poor candidate verification. From those spectra they choose targets to follow-up with high-resolution spectroscopy.

The method presented in this dissertation has been shown to be successful in the selection of metal-poor stars, providing already to the community more than 220 000 VMP candidates for observations. Its effectiveness was shown, in addition, via other observations: we were granted 50 nights at the ANU 2.3-metre telescope to perform a follow-up search and we have already discovered hundreds of new metal-poor stars with  $[\text{Fe}/\text{H}] < -2.0$ , and a few with  $[\text{Fe}/\text{H}] < -3.0$  that are highly carbon enriched (Nordlander, Xylakis-Dornbusch et al. in preparation). Along with  $T_{\text{eff}}$  from the color- $T_{\text{eff}}$  relation of Mucciarelli, Bellazzini, and Massari, 2021, a list of candidates for spectroscopic observations can readily be assembled. For example, the RPA has selected its candidates for observations based solely on  $T_{\text{eff}}$  and  $[\text{Fe}/\text{H}]$  from large surveys, such as the RAdial Velocity Experiment (Steinmetz et al., 2006). The RPA selected bright and cool metal-poor stars: cool to assure the detection of Eu, metal-poor in order to trace few nucleosynthesis events, and bright so that the exposure time is short, and in turn maximize the number of observed candidates (Hansen et al., 2018b).

The discovery and detailed abundance analysis of more metal-poor stars is essential in furthering our understanding of Galactic chemical evolution, in better constraining the initial mass function (IMF) of PopIII stars and BB nucleosynthesis, and exploring the nucleosynthesis channels which have enriched the Universe, including the  $r$ -process.

## 6.2 Metal-poor stars in the Galactic bulge

Looking at the Galactic bulge, the ongoing PIGS survey studies the chemistry and kinematics of the bulge with metal-poor stars ( $[\text{Fe}/\text{H}] < -0.5$ ). Recent work of the survey showed that there is a clear relation between metallicity and rotation, and that the latter decreases with decreasing metallicity (Arentsen et al., 2020a). The survey is conducted on the western half of the bulge, since its footprint extends to  $\delta > -30^\circ$  (Arentsen et al., 2020b). This poses a crucial limitation for studying for example the symmetry and the chemo-dynamical distribution of stars. A further limitation is, that PIGS avoids regions of reddening with color-excesses  $E(B - V) > 0.8$  mag.

The method that I developed can be used to select metal-poor stars in the bulge using the footprint of *Gaia*. Alongside the astrometric *Gaia* data, the most complete, to date, chemo-dynamical mapping of the metal-poor constituents of the MW can be undertaken. Furthermore, these candidate metal-poor stars would constitute a perfect catalogue for follow-up observations in wide-field surveys, such as the 4MOST Milky way Disc And BuLge High-Resolution (4MIDABLE-HR) survey (Bensby et al., 2019), possibly uncovering the oldest hidden stars in the Galaxy. Recently, Forsberg et al., 2023 discovered the first RPE star that is, very likely, a member of the Galactic bulge. The discovery and analysis of more RPE stars belonging to the bulge would advance our understanding of the  $r$ -process, but also contribute in various aspects to our understanding of the evolution of the MW.

### 6.3 Kinematics of $r_{lim}$ stars

In the *Gaia* era it is uncomplicated to conduct a kinematic analysis alongside an abundance analysis, since the astrometric and kinematic data for most of the stars are readily available in the *Gaia* database.

The kinematic analysis of the  $r_{lim}$  stars that is presented in PaperIII, showed that from the kinematics aspect, the  $r_{lim}$  stars show significant differences when compared to the  $r$ -I and  $r$ -II stars. 15 – 30% of  $r_{lim}$  stars belong to the disk, while only 1% of  $r$ -I and  $r$ -II stars have been, to date, chemo-dynamically linked to the MWTD (Shank et al., 2023), and a large fraction of them have been shown to have been accreted on to the MW (Roederer, Hattori, and Valluri, 2018; Gudin et al., 2021; Shank et al., 2023). Roederer, Hattori, and Valluri, 2018 showed that almost all of the 35  $r$ -II stars in their study were probably accreted from ultra-faint dwarf (UFD) galaxies or low-luminosity dwarf spheroidal galaxies. This was confirmed by Gudin et al., 2021, who studied 466  $r$ -I and  $r$ -II stars. Additionally, the discovery of RPE stars in the UFD galaxy Reticulum II (Ji et al., 2016b; Ji et al., 2019; Roederer et al., 2016), supports the idea that such galaxies are among the primary birthplaces of halo RPE stars. In the light of these evidence, the search of  $r_{lim}$  stars in dwarf and UFD galaxies is important, since it would add key pieces of information that could help us understand better the differences and similarities exhibited between the  $r_{lim}$  and  $r$ -I,  $r$ -II stars, as well as the responsible nucleosynthesis channel.

Recent studies, such as those of Pace and Li, 2019, McConnachie and Venn, 2020, Battaglia et al., 2022, and Divakar et al., 2024 have provided to the community new candidate members of dwarf and UFD galaxies, based on *Gaia* astrometric and photometric information, and in some cases photometry from other surveys such as Pan-STARRS1 Surveys (Chambers et al., 2016). The method developed in this dissertation could be used to select new metal-poor candidates from dwarf and UFD galaxies to search for  $r$ -process stars, and specifically  $r_{lim}$  stars.

Furthermore, in PaperIII I found that the  $r_{lim}$  star J0038 with  $[Ba/Eu] < -0.3$  is consistent with the baseline pattern from Roederer et al., 2023a, suggesting that  $r_{lim}$  stars with  $[Ba/Eu] < -0.3$  have been enriched by the same  $r$ -process the  $r$ -I and  $r$ -II stars have. On the other hand, the  $r_{lim}$  stars with  $[Ba/Eu] > -0.3$  do not agree with the pattern, pointing to other or multiple nucleosynthesis channels. The detailed abundance analysis of more  $r_{lim}$  stars, can shed more light on the nature of the difference between those with  $[Ba/Eu]$  above or below  $-0.3$ , and will either support or dismiss the idea that the latter seem to have been supplied their  $r$ -process material by the same  $r$ -process channel that the  $r$ -I and  $r$ -II stars have. Additionally, the presence or lack of them in dwarf galaxies can help us understand the influence of the environment on the  $r$ -process, and potentially add constraints on the IMF of such galaxies. Nevertheless, the study of Kobayashi et al., 2023 showed, that NSMs can reproduce the evolutionary relations of  $[Eu/Fe]$ - $[Fe/H]$  and  $[Eu/O]$ - $[O/H]$  in the Solar Neighborhood, when the delay-time distribution between onset of star formation and merger is metallicity dependent. Thus, the discovery of more  $r_{lim}$  stars in the Galaxy with disk-like kinematics, could suggest that maybe NSMs – like GW170817 – are the primary channel of  $r$ -process nucleosynthesis in the MW.

### 6.4 J2140 and the Sequoia accretion event

The consistently lower values of the  $X_{La}$ 's of the  $r_{lim}$  stars compared to that of the KN AT2017gfo, suggest that KNe like AT2017gfo could be the supplying channel

of the  $r$ -process material in  $r_{lim}$  stars. However, there is the issue of time delay between onset of star formation and NSMs, so I assessed whether the  $r_{lim}$  stars could have been accreted onto the MW from satellite galaxies with low star formation rate. Therefore, I proceeded with a kinematic analysis, which showed that the three stars in my sample are on prograde orbits. Further, I proceeded with the application of the dynamical selection criteria of Myeong et al., 2019 and Feuillet et al., 2021 for the GSE and Sequoia (Myeong et al., 2019) accretion events, to find whether the stars could be kinematically linked to any of these two events.

I found that the  $r_{lim}$  star J2140 appears to have been accreted onto the MW during the Sequoia accretion event. J2140 exhibits peculiarity in its abundances. It classifies as an  $r_{lim}$  CEMP star with  $[Ba/Eu] = -0.11$ , and appears to have been enriched by multiple nuclear processes. The abundances relative to iron of J2140 for Cr, Mn, Co, Ni, and Zn are among the highest derived for any star, while its  $[Sr/Ba] = +1.87$  is the highest ratio among the  $r_{lim}$  stars ( $[Cr/Fe] = +0.37$ ,  $[Mn/Fe] = +0.02$ ,  $[Co/Fe] = +0.44$ ,  $[Ni/Fe] = +0.54$ , and  $[Zn/Fe] = +1.26$ ).

The other  $r_{lim}$  star that was kinematically associated with Sequoia is CD-24 1782, which is, with  $[Fe/H] = -3.05$ , as metal-poor as J2140. The abundances of CD-24 1782 for the light and iron peak elements (Roederer et al., 2014) follow those of the typical MW halo stars, while for the neutron-capture elements  $[Sr/Ba] = +0.76$  and  $[Ba/Eu] = -0.67$ . The very low  $[Ba/Eu]$  ratio of this EMP star suggests that the neutron-capture elements present in its atmosphere are probably - dissimilar to J2140 - products solely of the  $r$ -process.

Matsuno et al., 2022 conducted a high precision differential abundance analysis of stars that appear, dynamically, to be members of Sequoia. The stars in this study, however, have  $[Fe/H] > -1.8$ , and due to the differential analysis, a straightforward comparison between the abundances is not possible. However, Matsuno et al., 2022 report two stars that were also dynamically selected as members, but were too metal-poor to include in the differential study. For one of those stars, HE1509-0252, abundances of light, iron-peak, and neutron-capture elements have been derived in the high-resolution abundance analysis study of Cohen et al., 2013. Star HE 1509-0252 is a giant with  $T_{eff} = 5750$  K,  $\log g = 3.5$  dex, and  $[Fe/H] = -2.85$ , and abundance ratios  $[Cr/Fe] = -0.40$ ,  $[Mn/Fe] = -0.81$ ,  $[Co/Fe] = +0.14$ ,  $[Ni/Fe] = -0.24$ , and  $[Zn/Fe] = +0.13$  (Cohen et al., 2013). The abundances of Co and Zn follow those of typical MW halo stars, while those of Cr, Mn, and Ni are low in comparison (see Figure 2 in Paper III, MW halo stars from Roederer et al., 2014). Cohen et al., 2013 give an upper limit for Eu  $[Eu/Fe] \leq +1.10$ . In total, HE 1509-0252 does not show similarities to J2140.

Recently, Aguado et al., 2021 conducted a high-resolution abundance analysis of 9 stars that are kinematically attributed to the GSE and Sequoia accretion events, and found high  $r$ -process enrichment in both. All 5 stars in this study that are attributed to Sequoia, have  $[Eu/Fe] > 0.5$ ,  $[Ba/Eu] \leq -0.64$ ,  $[Sr/Fe] < -0.04$ , and a metallicity range of  $-2.14 \leq [Fe/H] \leq -1.72$ . Furthermore, the  $[\alpha/Fe]$  of J2140 agrees, within the errors, with the highest  $[\alpha/Fe]$  of the Sequoia stars in the study of Aguado et al., 2021, where it is defined as  $[\alpha/Fe] = ([Mg/Fe] + [Ca/Fe] + [Ti/Fe])/3$ . However, the  $[Sr/Ba]$  ratios of the Sequoia stars with  $-0.51 \leq [Sr/Ba] \leq -0.11$ , are much lower than that of J2140. The lower  $[Fe/H]$  of J2140 compared to the Sequoia stars, in addition to the significant  $[Ba/Eu]$  difference could suggest a different  $r$ -process enrichment channel for the later than for J2140.

Furthermore, Aoki, Aoki, and François, 2020 did a high-resolution abundance analysis of five EMP stars ( $-3.06 \leq [Fe/H] \leq -2.82$ ) that are members of the dwarf spheroidal galaxy Sextans. They found that the  $[Ca/Fe]$ ,  $[Mg/Fe]$ , and  $[Sr/Ba]$  ratios

of the five stars are in agreement. Particularly, Aoki, Aoki, and François, 2020 claim that the clustering of the  $[\text{Sr}/\text{Ba}]$  ratios supports the hypothesis that these stars were formed from a chemically homogeneous gas cloud. A small scatter in  $[\text{Sr}/\text{Ba}]$  is also found by Ji et al., 2016a for stars in the UFD galaxy Reticulum II, but for stars with a wide range of metallicities ( $-3.5 < [\text{Fe}/\text{H}] < -2.0$ ). However, Aoki, Aoki, and François, 2020 note that this small scatter in  $[\text{Sr}/\text{Ba}]$  that is found in Reticulum II must be the result of a different mechanism than the one that leads to the  $[\text{Sr}/\text{Ba}]$  clustering observed in Sextans. Ji et al., 2016b argue that probably a single  $r$ -process event is responsible for most of the neutron-capture material in Reticulum II, however, according to Ji et al., 2016a, inhomogeneous metal mixing is needed to explain the level of scatter observed in the abundances. Recently, however, Hansen et al., 2024 found that stars in the UFD galaxy Tucana V exhibit great variation in their abundances. The study of Hansen et al., 2024 included one star from the central region of the galaxy, and two stars from the outskirts. They note that their results are a testament to the inhomogeneous enrichment of Tucana V.

In conclusion, based on these studies of stars associated with Sequoia, star J2140 does not appear to be chemically compatible to the stars that are kinematically linked to Sequoia. Furthermore, it has been shown that stars in some dwarf galaxies (e.g. Sextans and Reticulum II) exhibit homogeneity in their abundances, whereas stars in other galaxies (e.g. in Tucana V) exhibit diversity. Therefore, the study of more stars with kinematics consistent with Sequoia and with  $[\text{Fe}/\text{H}] < -2.5$ , would shed more light on the birthplace of J2140 and on Sequoia itself.

## 6.5 $X_{La}$ of the $r_{lim}$ stars

The lanthanide mass fraction  $X_{La}$  of a star is the fraction of the mass of lanthanides to the mass of the rest of the  $r$ -process material found in the star. This mass fraction is a great tool for the study of RPE stars, since it can be used to probe the possible nucleosynthesis enrichment channels.

In Paper III I found that the  $r_{lim}$  stars have fractions of heavy to light neutron-capture elements that are lower than those in the  $r$ -I and  $r$ -II stars, and particularly, there is a clear separation of the  $X_{La}$ 's of the two groups around the  $X_{La}$  of the KN AT2017gfo. That is, there appears to be a transition region of  $r_{lim}$  to  $r$ -I,  $r$ -II  $X_{La}$ 's, suggesting that the production of  $r$ -process material by KN should have a limited weight constrained depending on whether the event could account for the enrichment of  $r_{lim}$  or of  $r$ -I,  $r$ -II stars.

Furthermore, models of KN have shown that their light curves are very sensitive to the KN  $X_{La}$ . Even et al., 2020 showed how the light-curves of the KN change, depending on the  $X_{La}$ , by testing whether or not the variation of the abundance of some lanthanide species – for constant  $X_{La}$  – could affect the light-curve. They found that the broad-band light curves are sensitive to the variation of the mass fractions of Nd in the lanthanide ejecta. In addition, studies of fission cycling during the  $r$ -process nucleosynthesis in NSMs, have shown that fission fragment deposition in neutron-rich ejecta shape the final abundances of elements with  $100 \leq A \leq 180$ , that is from Ru and up into – and including – the lanthanides (Vassh et al., 2020; Lemaître et al., 2021). Ergo, the use of the limited weight constrained in the transition region of  $r_{lim}$  to  $r$ -I,  $r$ -II  $X_{La}$ 's, in combination with the lack of fission fragment deposition in  $r_{lim}$  stars with  $[\text{Ba}/\text{Eu}] < -0.3$ , and an  $X_{Nd}$  representative of  $r_{lim}$  stars, could be considered in a recipe for a KN consistent with an  $r_{lim}$  chemical-enrichment pattern.

## Chapter 7

# Outlook

The search and thorough studies of metal-poor stars have advanced greatly our understanding of the Galactic chemical enrichment history and of galaxy assembly. The latter has seen a revolutionary progress since the advent of *Gaia* that has provided the community astrometric and kinematic information for more than a billion stars. However, there are still many open questions pertaining to the formation and chemical enrichment of metal-poor stars, which is in direct link with the nature of their progenitors and the nucleosynthesis channels that were operating in the early Universe.

The studies that were conducted as part of this dissertation aimed at both finding more metal-poor stars and exploring the origin of their abundance signatures. Especially, the metal-poor candidate selection method can be applied in different fields of Galactic astronomy and archaeology. The metal-poor star selection method or in general the metallicity determination method can be applied in various regions of the MW, including those regions that have relatively high extinctions. Therefore, the Galactic bulge, disk, dwarf satellites, and even star forming regions could be explored with the recipe that is presented herein.

As discussed in Section 6.2, finding and deriving detailed abundances for metal-poor stars in the Galactic bulge could immensely promote our understanding of the formation, the mass ranges and explosive deaths of the first galactic stars, of the timescale and nature of the nucleosynthesis processes that took place. Further, it would provide constraints for the existing chemodynamical models of the bulge, none of which is yet fully self-consistent in the cosmological frame-work. Furthermore, observations of more stars that are selected via this method can be used to assess whether further calibration and thus improvement of its performance is possible.

Additionally, this method could be used to find metal-poor stars for which asteroseismic data are available (e.g. in the Kepler footprint; Borucki et al., 2010), in order to improve their metallicities and chemical abundances, and derive precise masses and ages (e.g. Valentini et al., 2019). Abundances of higher precision could for example give us new clues for the  $r$ -process nucleosynthesis, while the ages of metal-poor stars could provide constraints for the age of the Galaxy.

Moreover, it was shown that the selection method can extrapolate. Particularly, even though the method was initially developed for stars with  $T_{\text{eff}} < 6300$  K, the follow-up study indicated that metal-poor stars with  $T_{\text{eff}} > 6300$  K could be recovered as being metal-poor. That means, that even though the method cannot determine the  $[\text{Fe}/\text{H}]$  for those stars because the flux ratio is  $fr_{G/CaNIR} > 3.3$ , it can, nevertheless, select them as metal-poor. Therefore, selecting and observing metal-poor candidates with  $fr_{G/CaNIR} > 3.3$  is also an option for finding and studying metal-poor main sequence turnoff stars. Such stars were not selected for observations with surveys like SkyMapper due to the performed color cuts, so it is highly

likely that many interesting stars have not yet been discovered.

The discovery of more  $r_{lim}$  stars in the next years will bring about a clearer view and understanding about their nature. The RPA has already obtained spectra for  $\sim 1000$  stars, and their analysis is expected to double the number of  $r_{lim}$  stars (Holmbeck et al., 2020b). An  $r_{lim}$  sample of  $\sim 100$  stars will provide some statistical significance to their kinematic signatures, that show, so far, that they were largely born in the Galaxy. Furthermore, much more light will be shed on their chemical enrichment history, and therefore on the  $r$ -process. However, the sample will still have a bias towards low metallicities, since the newly discovered stars will have been selected in searches for metal-poor stars. This bias could be balanced by large high-resolution surveys such as 4MOST (de Jong et al., 2019).

## Chapter 8

# Summary

For the completion of this PhD dissertation I conducted three studies. In the first study, I developed an empirical method for the selection of candidate metal-poor stars from the *Gaia* BP/RP spectra, which have a very low resolving power ( $R < 100$ ). This method employs flux ratios of spectral regions that are sensitive to the metallicity, and it can be applied to FGK stars that have  $4800 \text{ K} \leq T_{\text{eff}} \leq 6300 \text{ K}$ . In order to develop this method, I considered the fact that the fraction of CEMP stars increases with decreasing metallicity, by using a grid of synthetic spectra with a variety of  $[\text{Fe}/\text{H}]$ - $[\text{C}/\text{Fe}]$  combinations. I found that  $[\text{Fe}/\text{H}]$  increases while  $fr_{\text{CaHK}/\text{H}\beta}$  decreases exponentially, for a quasi-constant  $fr_{\text{G}/\text{CaNIR}}$ . Since  $fr_{\text{CaHK}/\text{H}\beta}$  depends on temperature and surface gravity, the method was developed in a manner that both of those stellar parameters are needed as priors. As a first test, I applied the method to the very same data-set that was used for its development, that is, noiseless synthetic spectra with  $G = 15$  mag. I was able to predict the metallicity at  $[\text{Fe}/\text{H}] \geq -3.0$ , with an uncertainty  $\sigma \lesssim 0.6$  dex. When I used noisy spectra of the same brightness or fainter ( $G = 15, 16, 17$  mag) to verify the method, the results were very similar, particularly,  $\sigma \lesssim 0.65$  dex for  $[\text{Fe}/\text{H}] \geq -3.0$ . Furthermore, I found that the effectiveness of the method depends on temperature and  $[\text{C}/\text{Fe}]$ , simultaneously. Particularly, for Solar and sub-Solar  $[\text{C}/\text{Fe}]$  the method performs somewhat better for lower temperatures of the same  $\log g$ , when determining  $[\text{Fe}/\text{H}] \leq -3.5$ . However, for  $[\text{Fe}/\text{H}] \geq -3.0$ , the temperature does not influence the performance of the method. For super-Solar  $[\text{C}/\text{Fe}]$  and  $[\text{Fe}/\text{H}] > -3.5$ , the performance is better for higher temperatures of the same  $\log g$ . When determining  $[\text{Fe}/\text{H}] \leq -3.5$ , the performance is, as for the Solar  $[\text{C}/\text{Fe}]$  case. Lastly, the effectiveness of the method depends also, separately, on the relative  $[\text{C}/\text{Fe}]$  when it is super-Solar.

This empirical selection method can be applied to stars as faint as  $G = 18$  mag, considering that I was able to predict the metallicity of such synthetic spectra down to  $[\text{Fe}/\text{H}] = -2.0$  with an uncertainty  $\sigma < 0.6$  dex, which is good enough for the purpose of discovering new metal-poor stars. Even though the method can go quite deep and predict metallicities of faint stars, it can not be applied in regions where reddening has to be taken into account. Finally, the application of the empirical flux ratio method on a dataset drawn from a realistic MDF, showed that the method is expected to have a success rate of 50% in selecting EMP stars, when selecting all stars with predicted  $[\text{Fe}/\text{H}] \leq -2.5$ .

The second study that I conducted is a follow-up work on the empirical metal-poor candidate selection method. In this study I applied the method developed in Paper I to *Gaia* DR3 BP/RP spectra. I found, that the method had to be updated. The update consisted of turning away from the use of priors – no  $T_{\text{eff}}$  and  $\log g$  needed – and using only the flux ratios  $fr_{\text{G}/\text{CaNIR}}$  and  $fr_{\text{CaHK}/\text{H}\beta}$  to predict stellar metallicity. In this study I addressed the issue of extinction, by means of dereddening the spectral flux. I found that in that way, the refined method can be applied to

stars with  $E(B - V) \leq 1.5$ . Further, I used a dataset comprised of GALAH DR3 and SAGA database stars – for which *Gaia* DR3 BP/RP spectra were available – in order to test the refined method. I was able to estimate the metallicity with an uncertainty  $\sigma_{[\text{Fe}/\text{H}]_{\text{inf}}} \sim 0.36$  dex. Following, I assessed whether or not OBA stars are probable contaminants in a metal-poor candidate sample set up through this method. I found that it is not a prominent issue, as long as the dereddening is as of a high standard. As a next step, I selected metal-poor candidates from *Gaia* DR3 for spectroscopic validation. 26 candidates were observed, of which all (100%) were VMP ( $[\text{Fe}/\text{H}] < -2.0$ ), 58% had  $[\text{Fe}/\text{H}] < -2.5$ , and 8% had  $[\text{Fe}/\text{H}] < -3.0$ . The final product of this study was a catalogue of metallicities for more than 10 million stars, of which 225 498 have  $[\text{Fe}/\text{H}]_{\text{inf}} < -2.0$ .

In my final study, I conducted a comprehensive abundance and kinematic analysis of three  $r$ -process stars, that were observed by the RPA. These stars were, at first, classified as  $r_{\text{lim}}$  stars, but the new stellar parameters derived in this study classify star J2031 as an  $r$ -I star. However, the other two stars, J0038 and J2031, still qualify as  $r_{\text{lim}}$  stars. I found that the abundances of the light and the iron-peak element for J2031 and J0038, follow the trend of typical MW halo stars. On the other hand, J2140 manifests higher abundances of the following iron-peak elements: Cr, Mn, Co, Ni, Cu, and Zn. This star is also enhanced in C, N, and Na. These differences indicate that J2140 underwent a different chemical-enrichment history than J2031 and J0038, and other normal halo stars.

I compared the neutron-capture element abundance patterns of the three stars with the baseline pattern from Roederer et al., 2023b. This comparison showed that there appears to be a difference between  $r_{\text{lim}}$  stars that have  $[\text{Ba}/\text{Eu}]$  below or above  $-0.3$ . Particularly, star J0038 that has  $[\text{Ba}/\text{Eu}] < -0.3$  matches very well with the baseline pattern, whereas J2140 that has  $[\text{Ba}/\text{Eu}] > -0.3$ , does not. This result suggests that  $r_{\text{lim}}$  stars with  $[\text{Ba}/\text{Eu}] < -0.3$  have been enriched by the same  $r$ -process that  $r$ -I and  $r$ -II stars have, while those with  $[\text{Ba}/\text{Eu}] > -0.3$  have probably been enriched by another or a combination of other nucleosynthesis processes. Furthermore, J2031 which is an  $r$ -I star does not match the pattern and it appears that this star's abundance pattern is the result of an  $r$ -process that experienced fission cycling.

Following, I computed the  $X_{\text{La}}$  of my three stars and of all the RPE stars –including the  $r_{\text{lim}}$  stars – in the literature, in order to compare them with the  $X_{\text{La}}$  of the KN AT2017gfo. I found that the  $X_{\text{La}}$  of the  $r_{\text{lim}}$  stars and of the  $r$ -I and  $r$ -II stars are clearly separated. Specifically, the  $X_{\text{La}}$  of the KN lies in the transition region between the  $X_{\text{La}}$  of the  $r_{\text{lim}}$  stars and that of the  $r$ -I and  $r$ -II stars. This result could suggest that KN like the one from the NSM GW170817 could be responsible for the abundance pattern seen in  $r_{\text{lim}}$  stars. However, this leap is not that easy to make, since the time delay between the onset of star formation and NSMs, poses a problem. So next, I investigated the kinematics of the  $r_{\text{lim}}$  stars to find out whether accretion on to the MW from a galaxy with inefficient star formation could solve the time delay problem. I found that 65% of the  $r_{\text{lim}}$  stars are on prograde orbits, which suggests that they were probably born in the Galaxy. This is in contrast with the findings of Gudin et al., 2021, that the  $r$ -I and  $r$ -II stars were mostly accreted. Furthermore, 38% of the  $r_{\text{lim}}$  stars exhibit disk-like kinematics, which is also different that what has been reported for the  $r$ -I and  $r$ -II stars. Specifically, Shank et al., 2023 found that 17% of the  $r$ -I stars and 8% of the  $r$ -II stars have disk-like kinematics. Ultimately, I found that 15 – 30% of the  $r_{\text{lim}}$  stars appear to belong to the disk of the Galaxy, which is also unlike the  $r$ -I and  $r$ -II stars; Shank et al., 2023 found that only  $\sim 1\%$  of them could be chemo-dynamically linked to the MWTD.

Finally, the discovery of new  $r_{\text{lim}}$  stars is of paramount importance, since only the

detailed abundances and kinematics of more stars of this kind can allow us to draw conclusions about their birthplace(s), their chemical-enrichment history, and the differences they exhibit depending on  $[\text{Ba}/\text{Eu}]$ . More neutron-capture abundance patterns of  $r_{lim}$  stars will either support the finding that those with  $[\text{Ba}/\text{Eu}] < -3.0$  were enriched by the same  $r$ -process that enriched the  $r$ -I and  $r$ -II stars, or will bring about new understanding.



## Appendix A

# The effect of extinction on the flux-ratios and selection of the blending fraction $\beta$ .

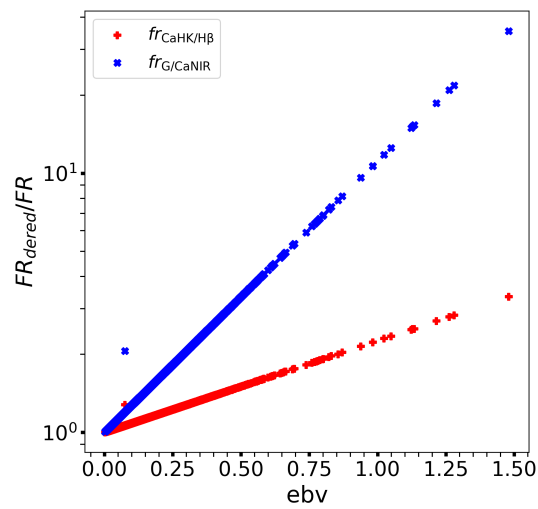


FIGURE A.1: Ratio of the flux-ratios post- and pre-dereddening. The effect of reddening has a greater impact on the  $fr_{\text{G}/\text{CaNIR}}$  flux-ratio compared to the  $fr_{\text{CaHK}/\text{H}\beta}$ . This would be expected, since the Calcium Near Infrared Triplet (Ca NIR) is located far more in the red than the other components of the flux-ratios, and is thus much less affected by extinction.

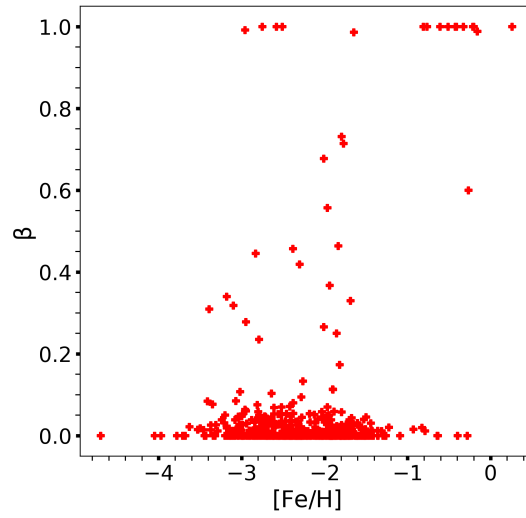


FIGURE A.2: Blending fraction  $\beta$  versus the metallicity of the stars selected from Cutoff2. A significant fraction of false positives, with  $[\text{Fe}/\text{H}] < -1$ , are found to have large values of the blending fraction  $\beta$ .

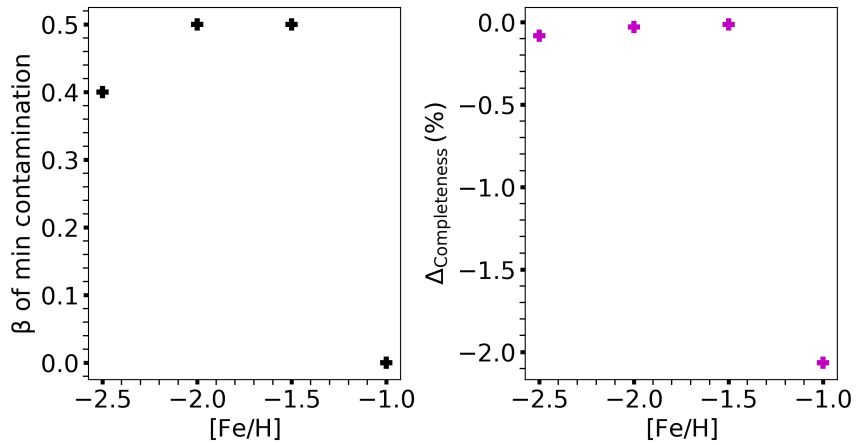


FIGURE A.3: Selection of the maximum value of the blending fraction  $\beta$  for the quality cut purpose. The  $\beta$  of the minimum contamination for stars at and below the metallicity shown on the x-axis, is shown in the left panel. In the right panel we calculated the difference between the completeness achieved with the  $\beta$  from the left plot, and the maximum possible completeness at the same metallicity bin. All stars were selected through Cutoff1.

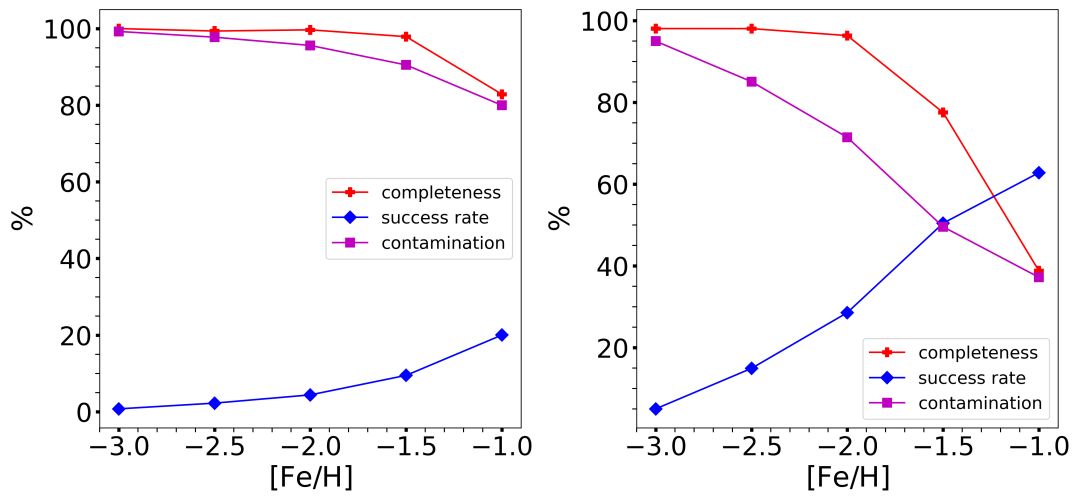


FIGURE A.4: Completeness, success rate and contamination of the stars that were selected from below Cutoff1 (left panel) and Cutoff2 (right panel). The stars were selected from a reddened flux-ratio plane, i.e. no dereddening was performed.



## Appendix B

# Additional data on the abundance analysis and kinematics of the sample and literature $r_{lim}$ stars.

Tables for the abundance uncertainties and line list information for the neutron-capture elements of the sample stars, and their inferred orbital parameters and uncertainties (including those for the  $r_{lim}$  stars in the literature). References for the atomic data of neutron-capture elements: (23) Kramida et al., 2018, (24) Biémont et al., 2011, (25) Ljung et al., 2006, (26) Kramida et al., 2018 using HFS/IS from McWilliam, 1998, (27) Lawler, Bonvallet, and Sneden, 2001 using HFS from Ivans et al., 2006, (28) Den Hartog et al., 2003 using HFS/IS from Roederer et al., 2008, (29) Lawler et al., 2001 using HFS/IS from Ivans et al., 2006 (30) Wickcliffe, Lawler, and Nave, 2000, (31) Lawler et al., 2008, (32) Sneden et al., 2009

TABLE B.6: Line information.

StellarID	Species	$\lambda$ (Å)	$\chi$ (eV)	$\log gf$	EW (mÅ)	$\sigma_{EW}$ (mÅ)	$\log \epsilon$	ref
J003859	Sr II	4077.71	0.00	0.15	synth	synth	0.81	23
J003859	Sr II	4215.52	0.00	-0.17	synth	synth	0.78	23
J003859	Y II	3710.29	0.18	0.51	synth	synth	-0.36	24
J003859	Y II	3747.55	0.10	-0.95	synth	synth	0.01	24
J003859	Y II	3774.33	0.13	0.29	synth	synth	-0.15	24
J003859	Y II	3832.89	0.18	-0.34	synth	synth	-0.24	24
J003859	Y II	3982.59	0.13	-0.56	synth	synth	-0.09	24
J003859	Y II	4235.73	0.13	-1.27	synth	synth	-0.26	24
J003859	Y II	4358.72	0.10	-1.15	synth	synth	-0.40	24
J003859	Y II	4883.68	1.08	0.19	synth	synth	-0.30	24
J003859	Y II	4900.12	1.03	0.03	synth	synth	-0.40	24
J003859	Y II	5087.42	1.08	-0.16	synth	synth	-0.42	24
J003859	Y II	5200.41	0.99	-0.47	synth	synth	-0.34	24
J003859	Zr II	3766.82	0.41	-0.83	synth	synth	0.60	25
J003859	Zr II	3998.96	0.56	-0.52	synth	synth	0.64	25
J003859	Zr II	4050.32	0.71	-1.06	synth	synth	0.49	25
J003859	Zr II	4149.20	0.80	-0.04	synth	synth	0.48	25
J003859	Zr II	4161.20	0.71	-0.59	synth	synth	0.52	25
J003859	Zr II	4208.98	0.71	-0.51	synth	synth	0.60	25
J003859	Zr II	4211.88	0.53	-1.04	synth	synth	0.68	25
J003859	Zr II	4258.04	0.56	-1.20	synth	synth	0.66	25
J003859	Ba II	4554.03	0.00	0.14	synth	synth	-0.58	26

J003859	Ba II	4934.08	0.00	-0.16	synth	synth	-0.61	26
J003859	Ba II	5853.68	0.60	-0.91	synth	synth	-0.56	26
J003859	Ba II	6141.71	0.70	-0.03	synth	synth	-0.56	26
J003859	Ba II	6496.90	0.60	-0.41	synth	synth	-0.58	26
J003859	La II	3794.77	0.24	0.21	synth	synth	-1.55	27
J003859	La II	4077.34	0.24	-0.06	synth	synth	-1.23	27
J003859	La II	4123.22	0.32	0.13	synth	synth	-1.30	27
J003859	Nd II	4109.45	0.32	0.35	synth	synth	-0.86	28
J003859	Nd II	4303.57	0.00	0.08	synth	synth	-0.81	28
J003859	Eu II	3819.67	0.00	0.51	synth	synth	-1.75	29
J003859	Eu II	4129.72	0.00	0.22	synth	synth	-1.71	29
J003859	Eu II	4205.04	0.00	0.21	synth	synth	-1.74	29
J003859	Dy II	3944.68	0.00	0.11	synth	synth	-1.37	30
J003859	Dy II	4077.97	0.10	-0.04	synth	synth	-1.22	30
J003859	Er II	3906.31	0.00	0.12	synth	synth	-1.18	31
J003859	Yb II	3694.19	0.00	-0.30	synth	synth	-1.63	32
J20313531	Sr II	4077.71	0.00	0.15	synth	synth	0.72	23
J20313531	Sr II	4215.52	0.00	-0.17	synth	synth	0.69	23
J20313531	Y II	3549.00	0.13	-0.29	synth	synth	-0.17	24
J20313531	Y II	3600.73	0.18	0.34	synth	synth	-0.41	24
J20313531	Y II	3601.92	0.10	-0.15	synth	synth	-0.39	24
J20313531	Y II	3611.04	0.13	0.05	synth	synth	-0.21	24
J20313531	Y II	3710.29	0.18	0.51	synth	synth	-0.35	24
J20313531	Y II	3774.33	0.13	0.29	synth	synth	-0.23	24
J20313531	Y II	3832.89	0.18	-0.34	synth	synth	-0.31	24
J20313531	Y II	3982.59	0.13	-0.56	synth	synth	-0.18	24
J20313531	Y II	4398.01	0.13	-0.75	synth	synth	-0.48	24
J20313531	Y II	4883.68	1.08	0.19	synth	synth	-0.50	24
J20313531	Y II	4900.12	1.03	0.03	synth	synth	-0.50	24
J20313531	Y II	5205.72	1.03	-0.28	synth	synth	-0.47	24
J20313531	Zr II	3430.53	0.47	-0.16	synth	synth	0.54	25
J20313531	Zr II	3479.02	0.53	-0.67	synth	synth	0.33	25
J20313531	Zr II	3505.67	0.16	-0.39	synth	synth	0.53	25
J20313531	Zr II	3551.95	0.10	-0.36	synth	synth	0.54	25
J20313531	Zr II	3998.96	0.56	-0.52	synth	synth	0.57	25
J20313531	Zr II	4149.20	0.80	-0.04	synth	synth	0.52	25
J20313531	Zr II	4161.20	0.71	-0.59	synth	synth	0.55	25
J20313531	Zr II	4208.98	0.71	-0.51	synth	synth	0.56	25
J20313531	Zr II	4211.88	0.53	-1.04	synth	synth	0.57	25
J20313531	Ba II	4554.03	0.00	0.14	synth	synth	-0.44	26
J20313531	Ba II	4934.08	0.00	-0.16	synth	synth	-0.47	26
J20313531	Ba II	5853.68	0.60	-0.91	synth	synth	-0.41	26
J20313531	Ba II	6141.71	0.70	-0.03	synth	synth	-0.54	26
J20313531	Ba II	6496.90	0.60	-0.41	synth	synth	-0.36	26
J20313531	La II	3949.10	0.40	0.49	synth	synth	-1.35	27
J20313531	La II	4077.34	0.24	-0.06	synth	synth	-1.03	27
J20313531	Nd II	3991.74	0.00	-0.26	synth	synth	-0.76	28
J20313531	Nd II	4303.57	0.00	0.08	synth	synth	-0.50	28
J20313531	Eu II	3819.67	0.00	0.51	synth	synth	-1.57	29
J20313531	Eu II	4129.72	0.00	0.22	synth	synth	-1.43	29
J20313531	Eu II	4205.04	0.00	0.21	synth	synth	-1.49	29

J20313531	Dy II	3944.68	0.00	0.11	synth	synth	-0.98	30
J20313531	Dy II	4077.97	0.10	-0.04	synth	synth	-0.90	30
J20313531	Er II	3499.10	0.06	0.29	synth	synth	-1.04	31
J20313531	Er II	3906.31	0.00	0.12	synth	synth	-0.97	31
J20313531	Yb II	3694.19	0.00	-0.30	synth	synth	-1.20	32
J21402305	Sr I	4607.33	0.00	0.28	synth	synth	1.01	23
J21402305	Sr II	4077.71	0.00	0.15	synth	synth	1.41	23
J21402305	Sr II	4161.80	2.94	-0.47	synth	synth	1.37	23
J21402305	Sr II	4215.52	0.00	-0.17	synth	synth	1.46	23
J21402305	Y II	3600.73	0.18	0.34	synth	synth	-0.08	24
J21402305	Y II	3611.04	0.13	0.05	synth	synth	-0.04	24
J21402305	Y II	3628.70	0.13	-0.70	synth	synth	0.04	24
J21402305	Y II	3710.29	0.18	0.51	synth	synth	0.28	24
J21402305	Y II	3747.55	0.10	-0.95	synth	synth	0.01	24
J21402305	Y II	3774.33	0.13	0.29	synth	synth	0.03	24
J21402305	Y II	3832.89	0.18	-0.34	synth	synth	-0.14	24
J21402305	Y II	3982.59	0.13	-0.56	synth	synth	0.09	24
J21402305	Y II	4358.72	0.10	-1.15	synth	synth	-0.19	24
J21402305	Y II	4398.01	0.13	-0.75	synth	synth	-0.17	24
J21402305	Y II	4854.86	0.99	-0.27	synth	synth	-0.16	24
J21402305	Y II	4900.12	1.03	0.03	synth	synth	-0.23	24
J21402305	Y II	4982.13	1.03	-1.32	synth	synth	0.05	24
J21402305	Y II	5087.42	1.08	-0.16	synth	synth	-0.18	24
J21402305	Y II	5123.21	0.99	-0.79	synth	synth	-0.29	24
J21402305	Y II	5200.41	0.99	-0.47	synth	synth	-0.20	24
J21402305	Y II	5205.72	1.03	-0.28	synth	synth	-0.14	24
J21402305	Zr II	3430.53	0.47	-0.16	synth	synth	0.37	25
J21402305	Zr II	3499.57	0.41	-1.06	synth	synth	0.65	25
J21402305	Zr II	3505.67	0.16	-0.39	synth	synth	0.60	25
J21402305	Zr II	3551.95	0.10	-0.36	synth	synth	0.68	25
J21402305	Zr II	3630.02	0.36	-1.11	synth	synth	0.57	25
J21402305	Zr II	3714.78	0.53	-0.96	synth	synth	0.52	25
J21402305	Zr II	3718.83	0.36	-1.76	synth	synth	0.55	25
J21402305	Zr II	3998.96	0.56	-0.52	synth	synth	0.56	25
J21402305	Zr II	4048.67	0.80	-0.53	synth	synth	0.41	25
J21402305	Zr II	4053.32	0.71	-1.06	synth	synth	0.53	25
J21402305	Zr II	4071.09	1.00	-1.66	synth	synth	0.61	25
J21402305	Zr II	4149.20	0.80	-0.04	synth	synth	0.34	25
J21402305	Zr II	4161.20	0.71	-0.59	synth	synth	0.41	25
J21402305	Zr II	4208.98	0.71	-0.51	synth	synth	0.40	25
J21402305	Zr II	4258.04	0.56	-1.20	synth	synth	0.63	25
J21402305	Zr II	4317.31	0.71	-1.45	synth	synth	0.66	25
J21402305	Zr II	4440.45	1.21	-1.04	synth	synth	0.34	25
J21402305	Zr II	4442.99	1.49	-0.42	synth	synth	0.49	25
J21402305	Zr II	4496.96	0.71	-0.89	synth	synth	0.62	25
J21402305	Zr II	4613.95	0.97	-1.54	synth	synth	0.57	25
J21402305	Ba II	4554.03	0.00	0.14	synth	synth	-1.27	26
J21402305	Ba II	4934.08	0.00	-0.16	synth	synth	-1.34	26
J21402305	Ba II	5853.68	0.60	-0.91	synth	synth	-1.27	26
J21402305	Ba II	6141.71	0.70	-0.03	synth	synth	-1.20	26
J21402305	Ba II	6496.90	0.60	-0.41	synth	synth	-1.04	26

J21402305	La II	4077.34	0.24	-0.06	synth	synth	-1.77	27
J21402305	Nd II	3991.74	0.00	-0.26	synth	synth	-1.36	28
J21402305	Nd II	4109.45	0.32	0.35	synth	synth	-1.55	28
J21402305	Nd II	4303.57	0.00	0.08	synth	synth	-1.78	28
J21402305	Eu II	4129.72	0.00	0.22	synth	synth	-2.73	29
J21402305	Eu II	4205.04	0.00	0.21	synth	synth	-2.73	29
J21402305	Er II	3906.31	0.00	0.12	synth	synth	-1.88	31
J21402305	Yb II	3694.19	0.00	-0.30	synth	synth	-2.45	32

---

TABLE B.1: Uncertainties for the abundances of J003859+272551 due to the uncertainties in stellar parameters.

Element	$\Delta T_{eff}$ (dex)	$\Delta \log g$ (dex)	$\Delta \zeta$ (dex)	$\Delta [M/H]$ (dex)	$\sigma_{sys}$ (dex)
Li I	0.08	-0.00	0.01	0.01	0.07
C-H	0.16	-0.03	0.01	0.04	0.10
O I	-0.08	0.04	-0.01	-0.00	0.04
Na I	0.10	-0.03	-0.10	-0.00	0.16
Mg I	0.04	-0.01	-0.02	0.00	0.06
Al I	0.16	-0.03	-0.11	0.01	0.23
Si I	0.04	0.01	-0.02	-0.00	0.06
K I	0.06	-0.00	-0.03	0.00	0.08
Ca I	0.04	0.00	0.01	0.00	0.04
Sc II	0.02	0.03	-0.01	0.01	0.06
Ti I	0.08	-0.00	0.03	0.01	0.05
Ti II	0.03	0.03	0.04	0.02	0.03
V I	0.02	0.01	0.02	-0.01	0.02
V II	-0.02	0.04	0.01	0.00	0.01
Cr I	0.08	0.00	0.03	0.01	0.05
Cr II	-0.00	0.03	-0.01	0.00	0.03
Mn I	0.06	-0.00	-0.01	0.00	0.06
Fe I	0.04	0.00	0.03	0.01	0.02
Fe II	0.01	0.03	0.02	0.01	0.02
Co I	0.05	0.01	-0.02	-0.01	0.08
Ni I	0.04	0.00	0.03	0.00	0.02
Zn I	0.04	0.01	-0.01	0.00	0.06
Sr II	-0.10	-0.04	-0.19	-0.10	0.11
Y II	-0.00	0.03	-0.00	0.01	0.04
Zr II	-0.02	0.04	0.01	0.00	0.02
Ba II	0.03	0.03	-0.02	0.01	0.08
La II	0.02	0.03	0.03	0.01	0.02
Nd II	0.02	0.02	0.01	0.02	0.03
Eu II	0.02	0.03	0.02	0.01	0.03
Dy II	0.02	0.03	0.01	0.03	0.04
Er II	0.02	0.03	-0.07	-0.01	0.12
Yb II	0.06	0.02	-0.03	0.01	0.11

TABLE B.2: Uncertainties for the abundances of J20313531 due to the uncertainties in stellar parameters.

Element	$\Delta T_{eff}$ (dex)	$\Delta \log g$ (dex)	$\Delta \xi$ (dex)	$\Delta [M/H]$ (dex)	$\sigma_{sys}$ (dex)
Li I	0.06	-0.01	-0.00	0.00	0.04
C-H	0.11	-0.04	0.02	0.05	0.05
O I	-0.07	0.04	-0.01	-0.01	0.02
Na I	0.04	-0.01	-0.04	-0.00	0.07
Mg I	0.06	-0.03	-0.03	0.01	0.06
Al I	0.14	-0.00	-0.01	0.03	0.14
Si I	0.02	-0.00	-0.00	0.00	0.02
K I	0.05	-0.01	-0.04	-0.00	0.08
Ca I	0.04	-0.00	0.02	0.00	0.02
Sc II	0.01	0.02	-0.00	0.01	0.03
Ti I	0.07	-0.00	0.04	0.01	0.04
Ti II	0.02	0.03	0.04	0.02	0.02
V I	0.02	0.01	0.01	-0.01	0.03
V II	-0.01	0.02	0.01	0.01	0.02
Cr I	0.07	-0.00	0.02	0.01	0.04
Cr II	-0.01	0.03	-0.01	0.01	0.03
Mn I	0.05	-0.01	-0.02	0.00	0.06
Mn II	-0.03	0.01	-0.06	-0.00	0.05
Fe I	0.04	-0.00	0.03	0.01	0.02
Fe II	0.00	0.03	-0.00	0.01	0.03
Co I	0.02	0.00	-0.01	-0.01	0.03
Ni I	0.04	0.00	0.03	0.00	0.02
Zn I	0.03	0.01	-0.01	0.01	0.05
Sr II	0.06	0.01	-0.09	0.03	0.15
Y II	0.01	0.02	-0.01	0.02	0.04
Zr II	-0.01	0.04	0.00	0.00	0.02
Ba II	0.02	0.03	-0.02	0.02	0.07
La II	-0.00	0.03	0.03	0.02	0.02
Nd II	0.02	0.02	0.02	0.03	0.03
Eu II	0.01	0.03	0.01	0.02	0.03
Dy II	0.01	0.02	-0.01	0.02	0.04
Er II	0.02	0.02	-0.02	0.02	0.06
Yb II	0.05	0.03	-0.03	0.02	0.10

TABLE B.3: Uncertainties for the abundances of J21402305 due to the uncertainties in stellar parameters.

Element	$\Delta T_{eff}$ (dex)	$\Delta \log g$ (dex)	$\Delta \xi$ (dex)	$\Delta [M/H]$ (dex)	$\sigma_{sys}$ (dex)
C-H	0.14	-0.04	0.04	0.01	0.07
N-H	0.16	-0.08	-0.05	-0.02	0.14
O I	-0.07	0.04	-0.00	-0.00	0.04
Na I	0.13	-0.09	-0.08	-0.02	0.12
Mg I	0.04	-0.01	-0.02	0.00	0.04
Al I	0.25	-0.09	-0.09	-0.01	0.25
Si I	0.01	0.00	-0.01	-0.02	0.04
K I	0.05	-0.00	-0.01	0.00	0.05
Ca I	0.04	-0.00	0.00	0.00	0.04
Sc II	0.02	0.03	-0.01	0.00	0.06
Ti I	0.07	-0.00	0.01	0.00	0.06
Ti II	0.04	0.05	0.06	0.01	0.04
V I	0.02	0.00	0.02	-0.01	0.02
V II	0.00	0.04	0.00	0.00	0.04
Cr I	0.07	-0.00	0.03	0.01	0.05
Cr II	0.00	0.04	-0.01	0.00	0.05
Mn I	0.04	-0.02	-0.02	-0.00	0.04
Mn II	-0.01	0.02	-0.04	0.01	0.05
Fe I	0.05	0.00	0.04	0.01	0.03
Fe II	0.02	0.04	0.01	0.01	0.05
Co I	0.04	-0.00	-0.02	-0.01	0.05
Ni I	0.04	0.00	0.04	0.00	0.02
Cu I	0.04	0.00	0.01	0.01	0.03
Zn I	0.04	0.01	-0.02	0.00	0.07
Sr I	0.04	-0.01	-0.00	0.00	0.04
Sr II	-0.00	0.03	-0.01	0.00	0.03
Y II	-0.03	0.03	-0.01	0.01	0.02
Zr II	0.01	0.05	0.02	0.01	0.04
Ba II	0.05	0.03	-0.03	0.00	0.10
La II	0.24	0.05	0.01	0.05	0.26
Nd II	0.04	0.04	0.02	0.01	0.06
Eu II	-0.01	0.06	0.03	0.01	0.03
Er II	0.05	0.05	-0.15	-0.01	0.24
Yb II	0.09	0.04	-0.05	0.01	0.17

TABLE B.4: Inferred orbital parameters for the  $r_{lim}$  stars.  $R_{max}$  is the projection of the apocenter of the orbit on the Galactic plane  
 $R_{max} = \sqrt{r_{ap}^2 - Z_{max}^2}$ , and  $IA = \arctan(Z_{max}/R_{max})$ .

StellarID	$Z_{max}$ (kpc)	$V$ ( $km\ s^{-1}$ )	$U$ ( $km\ s^{-1}$ )	$W$ ( $km\ s^{-1}$ )	$J_p$ ( $km\ s^{-1}\ kpc$ )	$J_z$ ( $km\ s^{-1}\ kpc$ )	$J_\phi$ ( $km\ s^{-1}\ kpc$ )	$J_\psi$ ( $km\ s^{-1}\ kpc$ )	$r_{ap}$ (kpc)	$r_{peri}$ (kpc)	$e$	$IA$ radians	$R_{max}$ (kpc)
J12402305-1227035	2.987288	-362.640779	115.962365	27.341385	-62.4213570	427.497869	69.008545	9.332915	1.743630	0.686673	0.325815	8.841912	
J00385967+2725516	1.501081	-275.349300	-171.497297	-45.122887	-402.118778	760.676887	19.822063	11.260869	0.899050	0.852812	0.133699	11.160373	
J20313531-3127319	5.480708	-348.021217	-92.740369	153.028760	-677.541433	64.695020	483.794640	7.171142	3.984476	0.287087	0.869193	4.624621	
J10344785-4823544	7.945123	-236.521093	159.557445	104.504508	-160.356481	795.389566	212.712504	11.230081	0.517431	0.911950	0.785934	7.936607	
J13335283-2623539	0.910945	-345.459934	-251.057685	15.143045	-600.547576	939.271149	359.892553	29.391493	0.583291	0.902635	0.760727	21.289723	
J10385850-2712188	20.263905	-238.159592	-8.733880	-59.618183	-59.918183	420.152791	15.198980	14.324722	1.278603	0.836219	0.066655	14.295728	
J13335283-2623539	0.910945	-345.459934	-251.057685	15.143045	-600.547576	939.271149	359.892553	29.391493	0.583291	0.902635	0.760727	21.289723	
J05384334-5147228	5.546939	-263.853633	14.842739	72.299835	-231.543438	537.113237	194.345763	9.409491	0.706958	0.860923	0.630446	7.600656	
J01094330-5907230	7.201983	-293.714165	-101.986089	60.226376	-207.673852	394.521573	381.783382	8.657761	1.002773	0.795059	0.982438	4.805026	
J1326045-152520	2.705447	-108.781135	-65.531467	-59.918183	1006.818696	78.171023	134.106336	7.327424	3.782005	0.319386	0.378122	6.809676	
J160642-3-163245	6.690205	-137.536382	-130.265054	-176.178348	-176.178348	163.423483	488.867778	8.872731	3.806459	0.399565	0.854159	5.828079	
J19594558-2549075	6.120813	-92.795841	-120.014513	133.075028	133.075028	99.847960	89.360699	6.53145187	6.787289	2.854263	0.406912	2.933076	
J169931.1-052252	3.955823	-268.059367	-120.344362	99.847960	-184.597263	481.509927	137.221443	7.842813	0.500620	0.879991	0.528673	6.772088	
J14533307-4428301	1.100557	-11.111981	50.158915	34.584715	1516.885819	93.408129	23.317873	9.181940	2.281177	0.120150	1.123929	9.115744	
J14453196-2106283	4.846901	-72.181377	-100.517418	144.464177	1043.917900	81.464377	318.211773	8.473801	4.641371	0.291664	0.608926	6.950744	
J20560913-1331176	16.063814	-299.074266	276.409983	-131.662209	-269.294771	1376.309480	312.733384	19.363496	1.108895	0.892062	0.978378	10.811978	
J18121045-4934495	1.953550	-108.257169	-2.200357	-39.485659	315.856973	65.200108	124.891597	3.535916	1.321712	0.458467	0.585346	2.947260	
J164551.2-042947	4.766936	-154.462606	-152.155285	-97.026305	267.382385	225.243935	306.960118	6.161314	1.303650	0.651806	0.884642	3.903602	
J19534978-5940001	5.692686	-176.692668	260.911182	97.693525	11.7599335	1134.072745	107.727245	14.167146	0.330063	0.954439	0.413507	12.973101	
J035509.3-063711	3.997295	-221.226052	-143.254855	-49.296261	311.954512	850.679084	44.308687	12.221133	0.943626	0.856684	0.333213	11.548927	
J19202070-6627202	5.873663	-347.729848	-260.689688	-105.584049	104.282502	162.282502	163.038174	12.815358	0.304833	0.954439	0.413507	12.973101	
J14164084-2422000	2.002110	-147.803921	-135.366306	-3.288430	723.629657	196.041970	1542.63946616	7.052370	2.279634	0.511760	0.287815	6.762209	
J19345497-5751400	21.888942	-408.679207	-135.366306	211.938129	453.905477	1366.369203	13.938029	4.932300	0.466474	0.953482	0.476115	11.390061	
J19494025-5424113	3.598250	-158.087055	-13.186270	-64.990858	324.921213	91.558082	238.280983	5.287962	1.378227	0.584164	0.748391	3.874938	
J08025449-5224304	2.756704	-131.227996	17.971028	-47.931223	804.593302	490.621700	78.42412	11.336453	2.090497	0.687743	0.245634	7.395554	
J0563703-5838281	8.712907	-255.442585	-121.650630	31.382720	441.410441	418.279953	482.052421	11.430370	1.904131	0.718234	0.866739	7.395554	
J12370807-0927347	13.739742	-314.483678	64.841424	-100.076607	842.428902	224.476306	1366.084335	15.228775	7.612713	0.413199	1.124895	6.567731	
J17285930-7427532	11.929498	-116.132928	167.803981	-198.761416	87.663848	386.037882	1150.396632	12.096291	3.140028	0.588857	1.404540	2.001833	
J154755.2-083710	5.123834	-196.193347	-62.090606	60.791043	210.316286	214.476627	195.424691	9.117353	0.647493	0.817898	0.596736	7.541382	
BPS CS 22186-023	3.171058	-123.971291	-33.601158	47.663707	1171.663778	191.064206	124.309177	9.824736	3.873793	0.434575	0.328647	9.298916	
BPS CS 22879-103	35.728787	-215.427374	-20.685719	-1.503819	125.046722	232.468653	211.293669	51.540249	0.436602	0.900310	0.765949	37.146346	
BPS CS 22891-209	2.348948	-284.747957	-64.845456	-61.272575	-133.907911	377.905539	95.681859	6.270164	0.778439	0.779501	0.383990	5.813553	
BPS CS 22897-008	7.514046	-231.415856	163.951338	-103.385271	-237.717386	235.974199	621.239626	8.061762	2.106342	0.585486	1.200058	2.920807	
BPS CS 22937-072	4.875248	-66.052507	-75.892306	-107.329208	873.514119	6.386132	482.512297	6.743850	5.593899	0.983599	0.743096	6.074137	
BPS CS 22940-070	2.555371	-205.119913	-47.570476	-52.355300	280.806573	310.364745	109.989979	6.589770	0.983599	0.743096	0.398220	6.074137	
BPS CS 22956-114	6.677440	-219.949345	-77.457415	119.106251	87.642533	87.642533	677.869666	7.238927	2.719105	0.454440	1.174340	2.793328	
BPS CS 30494-003	4.150200	-108.894761	33.894334	97.002180	1195.734017	152.981316	198.654042	9.763324	4.355204	0.383073	0.439052	8.837323	
CD-24 1782	0.523631	-336.070452	74.249461	-14.300412	-780.487085	388.017156	4.412435	9.103489	2.011275	0.638168	0.057552	9.088417	
G026-001	8.682504	-224.483072	70.155499	-161.106658	179.918467	535.209149	506.330088	9.129127	1.894265	0.656814	1.256704	2.820478	
HD 13979	0.930571	-209.734681	29.29131	-23.2171691	294.098892	620.166169	15.797487	14.606551	3.100948	0.649710	0.487081	12.907852	
HD 26169	6.836570	-127.373971	-219.111749	112.652772	104.905194	620.166169	44.772637	9.196519	1.712945	0.686039	0.158976	9.080551	
HD 88609	1.455873	-261.906528	-158.290077	31.549227	660.879456	794.734792	794.734792	8.572170	2.312305	0.604346	0.457762	8.411405	
HD 12563	3.118707	-153.264567	-94.172489	-111.822829	737.276627	370.234230	105.328653	20.518245	0.650774	0.938541	0.391026	18.96497	
HD 175606	4.143998	-276.97582	3.01708577	-101.901753	1173.610031	767.023399	686.90301	20.446782	4.807320	0.619284	0.848290	13.520783	
HD 184266	7.820268	-116.324123	190.212372	-207.771563	1173.610031	767.023399	686.90301	20.446782	4.807320	0.619284	0.848290	13.520783	
HD 237846	15.338166	-175.715326	-71.994077	165.473091	565.557411	161.956788	600.923005	8.784099	3.430330	0.438284	0.984950	4.856769	
HE 1320-1339	7.319303	-123.177305	156.682245	-66.718549	1009.039047	481.768610	37.314334	11.644034	2.624947	0.632077	0.169368	11.477424	

TABLE B.5: Mean uncertainties of the inferred orbital parameters for the  $r_{lim}$  stars.

StellarID	$\sigma_{Z_{max}}$ (kpc)	$\sigma_V$ ( $km\ s^{-1}$ )	$\sigma_U$ ( $km\ s^{-1}$ )	$\sigma_W$ ( $km\ s^{-1}$ )	$\sigma_{l_p}$ ( $km\ s^{-1}\ kpc$ )	$\sigma_{l_r}$ ( $km\ s^{-1}\ kpc$ )	$\sigma_{l_z}$ ( $km\ s^{-1}\ kpc$ )	$\sigma_{r_{ep}}$ (kpc)	$\sigma_{r_{peri}}$ (kpc)	$\sigma_e$
J21402305-1227035	0.087786	21.788053	13.616697	4.475168	105.421399	13.535400	9.887892	0.643337	0.244875	0.020859
J00385967+2725516	0.515703	6.577098	6.398225	3.528241	66.574588	18.045164	2.590651	0.266149	0.161094	0.021769
J20313531-3127319	0.261782	12.774654	3.863937	1.673944	72.301936	25.263409	14.998662	0.116989	0.407670	0.053656
J10344785-4823544	0.135725	0.554748	1.660580	0.978460	3.378187	3.719621	5.108092	0.061340	0.065951	0.010681
J13085850-2712188	57.558961	31.349637	12.546547	24.044318	90.058126	79.974154	259.192677	85.858083	0.764465	0.120397
J13335283-2623539	0.040737	4.837265	4.535612	0.433138	30.176666	20.834203	0.267051	0.410607	0.070199	0.004588
J05384334-5147228	0.462815	3.864517	1.309859	4.998962	38.423825	33.659495	28.915997	0.064265	0.171950	0.030304
J01094330-5907230	0.234973	9.433689	4.198852	4.033969	55.788639	50.019028	51.596536	0.132337	0.322119	0.056860
J132604.5-152502	0.156980	5.686506	2.620234	2.102933	40.550866	6.006835	12.058246	0.018008	0.149089	0.016630
J160642.3-163245	0.104738	4.190527	1.068618	2.717359	32.447198	22.187250	22.294865	0.084556	0.028696	0.001669
J19594558-2549075	0.076981	4.713994	3.769201	4.881941	112.648712	26.440636	113.810560	0.386530	0.114465	0.037588
J163931.1-052252	0.063156	6.703554	0.674371	3.994344	43.166540	28.346735	10.709869	0.176009	0.139901	0.033200
J14533307-4428301	0.023586	0.486672	0.305231	0.525237	6.692309	1.913953	0.796568	0.007472	0.032401	0.003178
J14435196-2106283	0.465430	4.699826	9.610374	9.714499	42.054767	23.232383	32.223574	0.379381	0.193401	0.039137
J20560913-1331176	0.392928	5.600534	3.037150	1.016845	38.041336	17.845517	5.843948	0.481570	0.182370	0.015254
J18121045-4934495	0.136834	5.910182	2.267261	1.844274	59.654777	3.712747	17.506388	0.180901	0.187796	0.037204
J164551.2-042947	0.181135	9.991940	2.732015	0.849986	83.313570	12.587007	42.319395	0.418993	0.155747	0.015663
J19534978-5940001	0.113329	4.060854	3.493145	7.942643	46.463541	28.482405	9.176406	0.315883	0.065222	0.009068
J035509.3-063711	0.136028	7.134570	0.773407	2.807665	66.779477	43.890156	1.657516	0.098132	0.121344	0.018089
J19202070-6627202	0.762773	14.105197	10.857543	4.202909	4.924421	92.571802	11.110095	1.034483	0.101223	0.014827
J14164084-2422000	0.417883	7.142351	4.583014	0.273568	43.725264	13.795474	4.814415	0.010439	0.135022	0.021568
J19345497-5751400	31.946511	113.884485	17.016616	44.863251	463.922036	1704746.329938	490.359894	82.513643	1.329016	0.225501
J19494025-5424113	0.690030	10.917563	4.918307	2.679507	63.441512	2.905953	27.509787	0.639234	0.237959	0.073491
J08025449-5224304	0.729847	0.658567	10.223894	2.515770	30.767527	39.896810	23.489898	0.573608	0.088390	0.024250
J03563703-5838281	1.620804	11.979399	10.223894	11.790593	9.839333	40.104070	182.722097	0.572075	0.507759	0.048807
J21370807-0927347	7.007872	65.540685	23.557561	33.486341	559.848167	192.207968	804.871677	7.620101	5.692800	0.222000
J17285930-7427532	0.236146	2.357990	0.979872	5.389544	36.143184	24.840812	97.332267	0.143720	0.357225	0.035424
J154755.2-083710	9.976435	12.962099	3.324165	4.570191	67.459939	16.682933	19.609332	17.183970	0.214374	0.081619
BPS CS 22186-023	0.183678	3.660909	1.772385	4.024897	28.720598	11.933976	10.950776	0.051437	0.145634	0.015489
BPS CS 22879-103	0.110647	16.966813	2.383198	2.481696	80.502242	16.275839	26.440344	145.912685	0.202166	0.087740
BPS CS 22891-209	0.022600	12.476217	1.863431	6.142963	64.834760	35.257748	7.315477	0.063981	0.098199	0.024250
BPS CS 22897-008	0.128589	3.623491	2.873797	2.617251	96.544104	84.005204	21.223586	0.381900	0.341903	0.067777
BPS CS 22937-072	0.177072	21.813485	12.169265	3.895649	56.337377	2.060825	35.399613	0.203120	0.028659	0.013482
BPS CS 22940-070	0.340680	13.088734	3.492446	5.524402	118.792019	41.738318	16.241669	0.064638	0.307164	0.067707
BPS CS 22956-114	0.092075	2.119480	0.294748	1.103127	55.385628	10.971126	92.911166	0.138172	0.194935	0.025126
BPS CS 30494-003	0.002603	2.499501	1.036196	0.569849	21.567652	8.052239	0.041012	0.024636	0.069037	0.009372
CD-24 1782	0.180825	4.889915	2.836367	3.743280	39.414710	19.107635	35.095971	0.099678	0.168936	0.023166
G026-001	0.499992	2.154173	0.470989	0.313342	18.174521	9.868952	0.137420	0.020308	0.043734	0.008778
HD 13979	0.189637	2.124500	2.714156	1.388844	16.051605	18.320415	6.532431	0.189896	0.050863	0.007497
HD 26169	0.028924	3.253722	0.374850	1.211272	27.577142	12.492552	2.798187	0.025645	0.081159	0.013270
HD 88609	1.557436	2.834841	1.587014	0.501101	22.813772	7.923870	0.260482	0.046929	0.049468	0.009201
HD 122563	0.113951	0.986694	2.929215	1.245889	8.096363	7.663722	4.755520	0.077598	0.022915	0.005057
HD 175606	0.047065	0.689959	0.126774	0.941292	5.616941	1.678401	2.463287	0.046114	0.075318	0.006842
HD 184266	0.016287	0.306505	0.103766	0.163618	1.581178	1.180490	0.928684	0.019684	0.012096	0.000792
HE 1320-1339	0.168251	3.262328	5.353872	1.268839	20.190483	12.785435	7.938108	0.119815	0.096986	0.016899
HD 19445	0.011133	0.124009	0.131138	0.199742	1.012322	0.763897	0.305134	0.004736	0.005148	0.000643



# Bibliography

- Abbott, B. P. et al. (2017). “GW170817: Observation of Gravitational Waves from a Binary Neutron Star Inspiral”. In: *Phys. Rev. Lett.* 119 (16), p. 161101. DOI: [10.1103/PhysRevLett.119.161101](https://doi.org/10.1103/PhysRevLett.119.161101). URL: <https://link.aps.org/doi/10.1103/PhysRevLett.119.161101>.
- Aguado, David S. et al. (Feb. 2021). “Elevated r-process Enrichment in Gaia Sausage and Sequoia\*”. In: *The Astrophysical Journal Letters* 908.1, p. L8. ISSN: 2041-8213. DOI: [10.3847/2041-8213/abdbb8](https://doi.org/10.3847/2041-8213/abdbb8). URL: <http://dx.doi.org/10.3847/2041-8213/abdbb8>.
- Aoki, M., W. Aoki, and P. François (Apr. 2020). “Chemical abundance analysis of extremely metal-poor stars in the Sextans dwarf spheroidal galaxy”. In: *Astronomy and Astrophysics* 636, A111. ISSN: 1432-0746. DOI: [10.1051/0004-6361/201936535](https://doi.org/10.1051/0004-6361/201936535). URL: <http://dx.doi.org/10.1051/0004-6361/201936535>.
- Aoki, Wako et al. (Jan. 2007). “Carbon-enhanced Metal-poor Stars. I. Chemical Compositions of 26 Stars”. In: 655.1, pp. 492–521. DOI: [10.1086/509817](https://doi.org/10.1086/509817). arXiv: [astro-ph/0609702](https://arxiv.org/abs/astro-ph/0609702) [astro-ph].
- Arentsen, A. et al. (Jan. 2020a). “The Pristine Inner Galaxy Survey (PIGS) I: tracing the kinematics of metal-poor stars in the Galactic bulge”. In: 491.1, pp. L11–L16. DOI: [10.1093/mnrasl/slz156](https://doi.org/10.1093/mnrasl/slz156). arXiv: [1910.06337](https://arxiv.org/abs/1910.06337) [astro-ph.GA].
- Arentsen, Anke et al. (Aug. 2020b). “The Pristine Inner Galaxy Survey (PIGS) II: Uncovering the most metal-poor populations in the inner Milky Way”. In: 496.4, pp. 4964–4978. DOI: [10.1093/mnras/staa1661](https://doi.org/10.1093/mnras/staa1661). arXiv: [2006.08641](https://arxiv.org/abs/2006.08641) [astro-ph.GA].
- Arentsen, Anke et al. (July 2021). “The Pristine Inner Galaxy Survey (PIGS) III: carbon-enhanced metal-poor stars in the bulge”. In: 505.1, pp. 1239–1253. DOI: [10.1093/mnras/stab1343](https://doi.org/10.1093/mnras/stab1343). arXiv: [2105.03441](https://arxiv.org/abs/2105.03441) [astro-ph.GA].
- Arlandini, Claudio et al. (Nov. 1999). “Neutron Capture in Low-Mass Asymptotic Giant Branch Stars: Cross Sections and Abundance Signatures”. In: 525.2, pp. 886–900. DOI: [10.1086/307938](https://doi.org/10.1086/307938). arXiv: [astro-ph/9906266](https://arxiv.org/abs/astro-ph/9906266) [astro-ph].
- Asplund, M., A. M. Amarsi, and N. Grevesse (Sept. 2021). “The chemical make-up of the Sun: A 2020 vision”. In: 653, A141, A141. DOI: [10.1051/0004-6361/202140445](https://doi.org/10.1051/0004-6361/202140445). arXiv: [2105.01661](https://arxiv.org/abs/2105.01661) [astro-ph.SR].
- Asplund, Martin et al. (Sept. 2009). “The Chemical Composition of the Sun”. In: 47.1, pp. 481–522. DOI: [10.1146/annurev.astro.46.060407.145222](https://doi.org/10.1146/annurev.astro.46.060407.145222). arXiv: [0909.0948](https://arxiv.org/abs/0909.0948) [astro-ph.SR].
- Astraatmadja, Tri L. (2015). “Ulysses: Principles and practice.” In: *Technical Report GAIA-C8-TN-MPIA-TLA-001, Max Planck Institute for Astronomy, Heidelberg*.
- Bailer-Jones, C. A. L. et al. (Mar. 2021). “Estimating Distances from Parallaxes. V. Geometric and Photogeometric Distances to 1.47 Billion Stars in Gaia Early Data Release 3”. In: 161.3, 147, p. 147. DOI: [10.3847/1538-3881/abd806](https://doi.org/10.3847/1538-3881/abd806). arXiv: [2012.05220](https://arxiv.org/abs/2012.05220) [astro-ph.SR].
- Battaglia, G. et al. (Jan. 2022). “Gaia early DR3 systemic motions of Local Group dwarf galaxies and orbital properties with a massive Large Magellanic Cloud”. In: *Astronomy and Astrophysics* 657, A54. ISSN: 1432-0746. DOI: [10.1051/0004-6361/202141528](https://doi.org/10.1051/0004-6361/202141528). URL: <http://dx.doi.org/10.1051/0004-6361/202141528>.

- Beers, T. C., G. W. Preston, and S. A. Shectman (Oct. 1985). "A search for stars of very low metal abundance. I." In: 90, pp. 2089–2102. DOI: [10.1086/113917](https://doi.org/10.1086/113917).
- Beers, Timothy C. and Norbert Christlieb (Sept. 2005). "The Discovery and Analysis of Very Metal-Poor Stars in the Galaxy". In: 43.1, pp. 531–580. DOI: [10.1146/annurev.astro.42.053102.134057](https://doi.org/10.1146/annurev.astro.42.053102.134057).
- Beers, Timothy C., George W. Preston, and Stephen A. Shectman (June 1992). "A Search for Stars of Very Low Metal Abundance. II". In: 103, p. 1987. DOI: [10.1086/116207](https://doi.org/10.1086/116207).
- Belokurov, V. et al. (July 2018). "Co-formation of the disc and the stellar halo". In: 478.1, pp. 611–619. DOI: [10.1093/mnras/sty982](https://doi.org/10.1093/mnras/sty982). arXiv: [1802.03414](https://arxiv.org/abs/1802.03414) [astro-ph.GA].
- Bensby, T. et al. (Mar. 2019). "4MOST Consortium Survey 4: Milky Way Disc and Bulge High-Resolution Survey (4MIDABLE-HR)". In: *The Messenger* 175, pp. 35–38. DOI: [10.18727/0722-6691/5123](https://doi.org/10.18727/0722-6691/5123). arXiv: [1903.02470](https://arxiv.org/abs/1903.02470) [astro-ph.GA].
- Bergemann, Maria and Thomas Nordlander (2014). "NLTE Radiative Transfer in Cool Stars". In: *Determination of Atmospheric Parameters of B*, pp. 169–185. DOI: [10.1007/978-3-319-06956-2\\_16](https://doi.org/10.1007/978-3-319-06956-2_16).
- Biémont, É. et al. (July 2011). "Lifetime measurements and calculations in  $Y^+$  and  $Y^{2+}$  ions". In: 414.4, pp. 3350–3359. DOI: [10.1111/j.1365-2966.2011.18637.x](https://doi.org/10.1111/j.1365-2966.2011.18637.x).
- Binney, James and Scott Tremaine (Dec. 2008). *Galactic Dynamics: Second Edition*. Princeton University Press. ISBN: 9781400828722. DOI: [10.1515/9781400828722](https://doi.org/10.1515/9781400828722). URL: <http://dx.doi.org/10.1515/9781400828722>.
- Bissantz, Nicolai and Ortwin Gerhard (Mar. 2002). "Spiral arms, bar shape and bulge microlensing in the Milky Way". In: *Monthly Notices of the Royal Astronomical Society* 330.3, 591–608. ISSN: 1365-2966. DOI: [10.1046/j.1365-8711.2002.05116.x](https://doi.org/10.1046/j.1365-8711.2002.05116.x). URL: <http://dx.doi.org/10.1046/j.1365-8711.2002.05116.x>.
- Borucki, William J. et al. (Feb. 2010). "Kepler Planet-Detection Mission: Introduction and First Results". In: *Science* 327.5968, p. 977. DOI: [10.1126/science.1185402](https://doi.org/10.1126/science.1185402).
- Bovy, Jo (Feb. 2015). "galpy: A python LIBRARY FOR GALACTIC DYNAMICS". In: *The Astrophysical Journal Supplement Series* 216.2, p. 29. ISSN: 1538-4365. DOI: [10.1088/0067-0049/216/2/29](https://doi.org/10.1088/0067-0049/216/2/29). URL: <http://dx.doi.org/10.1088/0067-0049/216/2/29>.
- Burbidge, E. Margaret et al. (Jan. 1957). "Synthesis of the Elements in Stars". In: *Reviews of Modern Physics* 29.4, pp. 547–650. DOI: [10.1103/RevModPhys.29.547](https://doi.org/10.1103/RevModPhys.29.547).
- Busso, Maurizio et al. (Feb. 2021). "s-processing in AGB Stars Revisited. III. Neutron Captures from MHD Mixing at Different Metallicities and Observational Constraints". In: 908.1, 55, p. 55. DOI: [10.3847/1538-4357/abca8e](https://doi.org/10.3847/1538-4357/abca8e). arXiv: [2011.07469](https://arxiv.org/abs/2011.07469) [astro-ph.SR].
- Cameron, A. G. W. (1957). "NUCLEAR REACTIONS IN STARS AND NUCLEOGENESIS". In: *Publications of the Astronomical Society of the Pacific* 69.408, p. 201. DOI: [10.1086/127051](https://doi.org/10.1086/127051). URL: <https://dx.doi.org/10.1086/127051>.
- Carrasco, J. M. et al. (Aug. 2021). "Internal calibration of Gaia BP/RP low-resolution spectra". In: 652, A86, A86. DOI: [10.1051/0004-6361/202141249](https://doi.org/10.1051/0004-6361/202141249). arXiv: [2106.01752](https://arxiv.org/abs/2106.01752) [astro-ph.IM].
- Casagrande, L. et al. (Mar. 2010). "An absolutely calibrated  $T_{eff}$  scale from the infrared flux method. Dwarfs and subgiants". In: 512, A54, A54. DOI: [10.1051/0004-6361/200913204](https://doi.org/10.1051/0004-6361/200913204). arXiv: [1001.3142](https://arxiv.org/abs/1001.3142) [astro-ph.SR].
- Casey, Andrew R. (2014). "PhD thesis". In: *Australian National Univ.*
- Chambers, K. C. et al. (Dec. 2016). "The Pan-STARRS1 Surveys". In: *arXiv e-prints*, arXiv:1612.05560, arXiv:1612.05560. DOI: [10.48550/arXiv.1612.05560](https://doi.org/10.48550/arXiv.1612.05560). arXiv: [1612.05560](https://arxiv.org/abs/1612.05560) [astro-ph.IM].

- Christlieb, N. et al. (Dec. 2004). “The Hamburg/ESO R-process Enhanced Star survey (HERES). I. Project description, and discovery of two stars with strong enhancements of neutron-capture elements”. In: 428, pp. 1027–1037. DOI: [10.1051/0004-6361:20041536](https://doi.org/10.1051/0004-6361:20041536). arXiv: [astro-ph/0408389](https://arxiv.org/abs/astro-ph/0408389) [astro-ph].
- Christlieb, N. et al. (June 2008). “The stellar content of the Hamburg/ESO survey. IV. Selection of candidate metal-poor stars”. In: 484.3, pp. 721–732. DOI: [10.1051/0004-6361:20078748](https://doi.org/10.1051/0004-6361:20078748). arXiv: [0804.1520](https://arxiv.org/abs/0804.1520) [astro-ph].
- Cohen, Judith G. et al. (Nov. 2013). “Normal and Outlying Populations of the Milky Way Stellar Halo at  $[\text{Fe}/\text{H}] < -2$ ”. In: 778.1, 56, p. 56. DOI: [10.1088/0004-637X/778/1/56](https://doi.org/10.1088/0004-637X/778/1/56). arXiv: [1310.1527](https://arxiv.org/abs/1310.1527) [astro-ph.GA].
- Cowan, J. J. and W. K. Rose (Feb. 1977). “Production of  $^{14}\text{C}$  and neutrons in red giants.” In: 212, pp. 149–158. DOI: [10.1086/155030](https://doi.org/10.1086/155030).
- Cowan, John J. et al. (Jan. 2021). “Origin of the heaviest elements: The rapid neutron-capture process”. In: *Reviews of Modern Physics* 93.1, 015002, p. 015002. DOI: [10.1103/RevModPhys.93.015002](https://doi.org/10.1103/RevModPhys.93.015002). arXiv: [1901.01410](https://arxiv.org/abs/1901.01410) [astro-ph.HE].
- De Angeli, F. et al. (June 2023). “Gaia Data Release 3. Processing and validation of BP/RP low-resolution spectral data”. In: 674, A2, A2. DOI: [10.1051/0004-6361/202243680](https://doi.org/10.1051/0004-6361/202243680). arXiv: [2206.06143](https://arxiv.org/abs/2206.06143) [astro-ph.IM].
- de Jong, R. S. et al. (Mar. 2019). “4MOST: Project overview and information for the First Call for Proposals”. In: *The Messenger* 175, pp. 3–11. DOI: [10.18727/0722-6691/5117](https://doi.org/10.18727/0722-6691/5117). arXiv: [1903.02464](https://arxiv.org/abs/1903.02464) [astro-ph.IM].
- Den Hartog, E. A. et al. (Oct. 2003). “Improved Laboratory Transition Probabilities for Nd II and Application to the Neodymium Abundances of the Sun and Three Metal-poor Stars”. In: 148.2, pp. 543–566. DOI: [10.1086/376940](https://doi.org/10.1086/376940).
- Diemand, Jürg, Piero Madau, and Ben Moore (Dec. 2005). “The distribution and kinematics of early high- $\sigma$  peaks in present-day haloes: implications for rare objects and old stellar populations”. In: 364.2, pp. 367–383. DOI: [10.1111/j.1365-2966.2005.09604.x](https://doi.org/10.1111/j.1365-2966.2005.09604.x). arXiv: [astro-ph/0506615](https://arxiv.org/abs/astro-ph/0506615) [astro-ph].
- Divakar, Devika K. et al. (Jan. 2024). “Possibilities of identifying members from Milky Way satellite galaxies using unsupervised machine learning algorithms”. In: *Journal of Astrophysics and Astronomy* 45.1, 5, p. 5. DOI: [10.1007/s12036-023-09990-4](https://doi.org/10.1007/s12036-023-09990-4). arXiv: [2311.14102](https://arxiv.org/abs/2311.14102) [astro-ph.IM].
- Eichler, M. et al. (July 2015). “THE ROLE OF FISSION IN NEUTRON STAR MERGERS AND ITS IMPACT ON THE r-PROCESS PEAKS”. In: *The Astrophysical Journal* 808.1, p. 30. ISSN: 1538-4357. DOI: [10.1088/0004-637x/808/1/30](https://doi.org/10.1088/0004-637x/808/1/30). URL: <http://dx.doi.org/10.1088/0004-637X/808/1/30>.
- Even, Wesley et al. (Aug. 2020). “Composition Effects on Kilonova Spectra and Light Curves. I”. In: 899.1, 24, p. 24. DOI: [10.3847/1538-4357/ab70b9](https://doi.org/10.3847/1538-4357/ab70b9). arXiv: [1904.13298](https://arxiv.org/abs/1904.13298) [astro-ph.HE].
- Ezzeddine, Rana et al. (Aug. 2020). “The R-Process Alliance: First Magellan/MIKE Release from the Southern Search for R-process-enhanced Stars”. In: 898.2, 150, p. 150. DOI: [10.3847/1538-4357/ab9d1a](https://doi.org/10.3847/1538-4357/ab9d1a). arXiv: [2006.07731](https://arxiv.org/abs/2006.07731) [astro-ph.SR].
- Feuillet, Diane K et al. (Sept. 2021). “Selecting accreted populations: metallicity, elemental abundances, and ages of the Gaia-Sausage-Enceladus and Sequoia populations”. In: *Monthly Notices of the Royal Astronomical Society* 508.1, 1489–1508. ISSN: 1365-2966. DOI: [10.1093/mnras/stab2614](https://doi.org/10.1093/mnras/stab2614). URL: <http://dx.doi.org/10.1093/mnras/stab2614>.
- Forsberg, R. et al. (Jan. 2023). “First r-process enhanced star confirmed as a member of the Galactic bulge”. In: 669, A17, A17. DOI: [10.1051/0004-6361/202244305](https://doi.org/10.1051/0004-6361/202244305). arXiv: [2210.05688](https://arxiv.org/abs/2210.05688) [astro-ph.SR].

- Frebel, Anna (Oct. 2018). "From Nuclei to the Cosmos: Tracing Heavy-Element Production with the Oldest Stars". In: *Annual Review of Nuclear and Particle Science* 68.1, pp. 237–269. DOI: [10.1146/annurev-nucl-101917-021141](https://doi.org/10.1146/annurev-nucl-101917-021141). arXiv: [1806.08955](https://arxiv.org/abs/1806.08955) [astro-ph.SR].
- Frebel, Anna and John E. Norris (2013). "Metal-Poor Stars and the Chemical Enrichment of the Universe". In: *Planets, Stars and Stellar Systems. Volume 5: Galactic Structure and Stellar Populations*. Ed. by Terry D. Oswalt and Gerard Gilmore. Vol. 5, p. 55. DOI: [10.1007/978-94-007-5612-0\\_3](https://doi.org/10.1007/978-94-007-5612-0_3).
- Gaia Collaboration et al. (Nov. 2016). "The Gaia mission". In: 595, A1, A1. DOI: [10.1051/0004-6361/201629272](https://doi.org/10.1051/0004-6361/201629272). arXiv: [1609.04153](https://arxiv.org/abs/1609.04153) [astro-ph.IM].
- Gaia Collaboration et al. (June 2023). "Gaia Data Release 3. Summary of the content and survey properties". In: 674, A1, A1. DOI: [10.1051/0004-6361/202243940](https://doi.org/10.1051/0004-6361/202243940). arXiv: [2208.00211](https://arxiv.org/abs/2208.00211) [astro-ph.GA].
- Goswami, Partha Pratim and Aruna Goswami (Dec. 2020). "i-Process nucleosynthesis: Observational evidences from CEMP stars". In: *Journal of Astrophysics and Astronomy* 41.1. ISSN: 0973-7758. DOI: [10.1007/s12036-020-09670-7](https://doi.org/10.1007/s12036-020-09670-7). URL: <http://dx.doi.org/10.1007/s12036-020-09670-7>.
- Gudin, Dmitrii et al. (Feb. 2021). "The R-Process Alliance: Chemodynamically Tagged Groups of Halo r-process-enhanced Stars Reveal a Shared Chemical-evolution History". In: 908.1, 79, p. 79. DOI: [10.3847/1538-4357/abd7ed](https://doi.org/10.3847/1538-4357/abd7ed). arXiv: [2012.13808](https://arxiv.org/abs/2012.13808) [astro-ph.GA].
- Gull, Maude et al. (Aug. 2018). "The R-Process Alliance: Discovery of the First Metal-poor Star with a Combined r- and s-process Element Signature". In: 862.2, 174, p. 174. DOI: [10.3847/1538-4357/aacbc3](https://doi.org/10.3847/1538-4357/aacbc3). arXiv: [1806.00645](https://arxiv.org/abs/1806.00645) [astro-ph.SR].
- Hempel, Melanie et al. (Nov. 2016). "The Intermediate Neutron-capture Process and Carbon-enhanced Metal-poor Stars". In: 831.2, 171, p. 171. DOI: [10.3847/0004-637X/831/2/171](https://doi.org/10.3847/0004-637X/831/2/171). arXiv: [1608.08634](https://arxiv.org/abs/1608.08634) [astro-ph.SR].
- Hansen, C. J. et al. (Sept. 2012). "Silver and palladium help unveil the nature of a second r-process". In: 545, A31, A31. DOI: [10.1051/0004-6361/201118643](https://doi.org/10.1051/0004-6361/201118643). arXiv: [1205.4744](https://arxiv.org/abs/1205.4744) [astro-ph.SR].
- Hansen, Terese T. et al. (May 2018a). "The R-process Alliance: First Release from the Southern Search for R-process-enhanced Stars in the Galactic Halo". In: 858.2, 92, p. 92. DOI: [10.3847/1538-4357/aabacc](https://doi.org/10.3847/1538-4357/aabacc). arXiv: [1804.03114](https://arxiv.org/abs/1804.03114) [astro-ph.SR].
- (May 2018b). "The R-process Alliance: First Release from the Southern Search for R-process-enhanced Stars in the Galactic Halo". In: 858.2, 92, p. 92. DOI: [10.3847/1538-4357/aabacc](https://doi.org/10.3847/1538-4357/aabacc). arXiv: [1804.03114](https://arxiv.org/abs/1804.03114) [astro-ph.SR].
- Hansen, Terese T. et al. (Mar. 2024). "Chemical Diversity on Small Scales – Abundance Analysis of the Tucana V Ultra-Faint Dwarf Galaxy". In: *arXiv e-prints*, arXiv:2403.13060, arXiv:2403.13060. DOI: [10.48550/arXiv.2403.13060](https://doi.org/10.48550/arXiv.2403.13060). arXiv: [2403.13060](https://arxiv.org/abs/2403.13060) [astro-ph.GA].
- Helmi, Amina et al. (Oct. 2018). "The merger that led to the formation of the Milky Way's inner stellar halo and thick disk". In: 563.7729, pp. 85–88. DOI: [10.1038/s41586-018-0625-x](https://doi.org/10.1038/s41586-018-0625-x). arXiv: [1806.06038](https://arxiv.org/abs/1806.06038) [astro-ph.GA].
- Hinkel, Natalie R., Patrick A. Young, and III Wheeler Caleb H. (Dec. 2022). "A Concise Treatise on Converting Stellar Mass Fractions to Abundances to Molar Ratios". In: 164.6, 256, p. 256. DOI: [10.3847/1538-3881/ac9bfa](https://doi.org/10.3847/1538-3881/ac9bfa). arXiv: [2210.10800](https://arxiv.org/abs/2210.10800) [astro-ph.EP].
- Holmbeck, E. M., T. M. Sprouse, and M. R. Mumpower (Feb. 2023). "Nucleosynthesis and observation of the heaviest elements". In: *The European Physical Journal A* 59.2. ISSN: 1434-601X. DOI: [10.1140/epja/s10050-023-00927-7](https://doi.org/10.1140/epja/s10050-023-00927-7). URL: <http://dx.doi.org/10.1140/epja/s10050-023-00927-7>.

- Holmbeck, Erika M. et al. (Aug. 2020a). “The R-Process Alliance: Fourth Data Release from the Search for R-process-enhanced Stars in the Galactic Halo”. In: 249.2, 30, p. 30. DOI: [10.3847/1538-4365/ab9c19](https://doi.org/10.3847/1538-4365/ab9c19). arXiv: [2007.00749](https://arxiv.org/abs/2007.00749) [astro-ph.SR].
- (Aug. 2020b). “The R-Process Alliance: Fourth Data Release from the Search for R-process-enhanced Stars in the Galactic Halo”. In: 249.2, 30, p. 30. DOI: [10.3847/1538-4365/ab9c19](https://doi.org/10.3847/1538-4365/ab9c19). arXiv: [2007.00749](https://arxiv.org/abs/2007.00749) [astro-ph.SR].
- Honda, S. et al. (June 2006). “Neutron-Capture Elements in the Very Metal Poor Star HD 122563”. In: 643.2, pp. 1180–1189. DOI: [10.1086/503195](https://doi.org/10.1086/503195). arXiv: [astro-ph/0602107](https://arxiv.org/abs/astro-ph/0602107) [astro-ph].
- Honda, Satoshi et al. (Sept. 2007). “Neutron-Capture Elements in the Very Metal-poor Star HD 88609: Another Star with Excesses of Light Neutron-Capture Elements”. In: 666.2, pp. 1189–1197. DOI: [10.1086/520034](https://doi.org/10.1086/520034). arXiv: [0705.3975](https://arxiv.org/abs/0705.3975) [astro-ph].
- Howes, L. M. et al. (Nov. 2015). “Extremely metal-poor stars from the cosmic dawn in the bulge of the Milky Way”. In: 527.7579, pp. 484–487. DOI: [10.1038/nature15747](https://doi.org/10.1038/nature15747). arXiv: [1511.03930](https://arxiv.org/abs/1511.03930) [astro-ph.GA].
- Ivans, Inese I. et al. (July 2006). “Near-Ultraviolet Observations of HD 221170: New Insights into the Nature of r-Process-rich Stars”. In: 645.1, pp. 613–633. DOI: [10.1086/504069](https://doi.org/10.1086/504069). arXiv: [astro-ph/0604180](https://arxiv.org/abs/astro-ph/0604180) [astro-ph].
- Ji, Alexander P., Maria R. Drout, and Terese T. Hansen (Sept. 2019). “The Lanthanide Fraction Distribution in Metal-poor Stars: A Test of Neutron Star Mergers as the Dominant r-process Site”. In: 882.1, 40, p. 40. DOI: [10.3847/1538-4357/ab3291](https://doi.org/10.3847/1538-4357/ab3291). arXiv: [1905.01814](https://arxiv.org/abs/1905.01814) [astro-ph.HE].
- Ji, Alexander P. et al. (Oct. 2016a). “Complete Element Abundances of Nine Stars in the r-process Galaxy Reticulum II”. In: 830.2, 93, p. 93. DOI: [10.3847/0004-637X/830/2/93](https://doi.org/10.3847/0004-637X/830/2/93). arXiv: [1607.07447](https://arxiv.org/abs/1607.07447) [astro-ph.GA].
- Ji, Alexander P. et al. (Mar. 2016b). “R-process enrichment from a single event in an ancient dwarf galaxy”. In: 531.7596, pp. 610–613. DOI: [10.1038/nature17425](https://doi.org/10.1038/nature17425). arXiv: [1512.01558](https://arxiv.org/abs/1512.01558) [astro-ph.GA].
- Ji, Alexander P. et al. (Jan. 2019). “Chemical Abundances in the Ultra-faint Dwarf Galaxies Grus I and Triangulum II: Neutron-capture Elements as a Defining Feature of the Faintest Dwarfs\*”. In: *The Astrophysical Journal* 870.2, p. 83. ISSN: 1538-4357. DOI: [10.3847/1538-4357/aaf3bb](https://doi.org/10.3847/1538-4357/aaf3bb). URL: <http://dx.doi.org/10.3847/1538-4357/aaf3bb>.
- Ji, Alexander P. et al. (Oct. 2020). “The Southern Stellar Stream Spectroscopic Survey (S<sup>5</sup>): Chemical Abundances of Seven Stellar Streams”. In: 160.4, 181, p. 181. DOI: [10.3847/1538-3881/abac6b](https://doi.org/10.3847/1538-3881/abac6b). arXiv: [2008.07568](https://arxiv.org/abs/2008.07568) [astro-ph.SR].
- Jordi, C. et al. (Nov. 2010). “Gaia broad band photometry”. In: 523, A48, A48. DOI: [10.1051/0004-6361/201015441](https://doi.org/10.1051/0004-6361/201015441). arXiv: [1008.0815](https://arxiv.org/abs/1008.0815) [astro-ph.IM].
- Käppeler, F. et al. (Jan. 2011). “The s process: Nuclear physics, stellar models, and observations”. In: *Reviews of Modern Physics* 83.1, pp. 157–194. DOI: [10.1103/RevModPhys.83.157](https://doi.org/10.1103/RevModPhys.83.157). arXiv: [1012.5218](https://arxiv.org/abs/1012.5218) [astro-ph.SR].
- Klessen, Ralf S. and Simon C.O. Glover (Aug. 2023). “The First Stars: Formation, Properties, and Impact”. In: *Annual Review of Astronomy and Astrophysics* 61.1, 65–130. ISSN: 1545-4282. DOI: [10.1146/annurev-astro-071221-053453](https://doi.org/10.1146/annurev-astro-071221-053453). URL: <http://dx.doi.org/10.1146/annurev-astro-071221-053453>.
- Kobayashi, Chiaki et al. (Feb. 2023). “Can Neutron Star Mergers Alone Explain the r-process Enrichment of the Milky Way?” In: 943.2, L12, p. L12. DOI: [10.3847/2041-8213/acad82](https://doi.org/10.3847/2041-8213/acad82). arXiv: [2211.04964](https://arxiv.org/abs/2211.04964) [astro-ph.HE].
- Komatsu, E. et al. (Feb. 2011). “Seven-year Wilkinson Microwave Anisotropy Probe (WMAP) Observations: Cosmological Interpretation”. In: 192.2, 18, p. 18. DOI: [10.1088/0067-0049/192/2/18](https://doi.org/10.1088/0067-0049/192/2/18). arXiv: [1001.4538](https://arxiv.org/abs/1001.4538) [astro-ph.CO].

- Kramida, A. et al. (Apr. 2018). "NIST Atomic Spectra Database (ver. 5.5.6)". In: *Available: <https://physics.nist.gov/asd> [2018, May 12]. National Institute of Standards and Technology, Gaithersburg, MD.*
- Lawler, J. E., G. Bonvallet, and Christopher Sneden (July 2001). "Experimental Radiative Lifetimes, Branching Fractions, and Oscillator Strengths for La II and a New Determination of the Solar Lanthanum Abundance". In: 556.1, pp. 452–460. DOI: [10.1086/321549](https://doi.org/10.1086/321549).
- Lawler, J. E. et al. (2001). "Improved Laboratory Transition Parameters for Eu II and Application to the Solar Europium Elemental and Isotopic Composition". In: *The Astrophysical Journal* 563.2, p. 1075. DOI: [10.1086/323407](https://doi.org/10.1086/323407). URL: <https://dx.doi.org/10.1086/323407>.
- Lawler, J. E. et al. (Sept. 2008). "Improved Laboratory Transition Probabilities for Er II and Application to the Erbium Abundances of the Sun and Five r-Process-rich, Metal-poor Stars". In: 178.1, pp. 71–88. DOI: [10.1086/589834](https://doi.org/10.1086/589834). arXiv: [0804.4465 \[astro-ph\]](https://arxiv.org/abs/0804.4465).
- Lee, Young Sun et al. (Nov. 2013). "Carbon-enhanced Metal-poor Stars in SDSS/SEGUE. I. Carbon Abundance Estimation and Frequency of CEMP Stars". In: 146.5, 132, p. 132. DOI: [10.1088/0004-6256/146/5/132](https://doi.org/10.1088/0004-6256/146/5/132). arXiv: [1310.3276 \[astro-ph.SR\]](https://arxiv.org/abs/1310.3276).
- Lemaître, J.-F. et al. (2021). "Fission fragment distributions and their impact on the r-process nucleosynthesis in neutron star mergers". In: *Phys. Rev. C* 103 (2), p. 025806. DOI: [10.1103/PhysRevC.103.025806](https://doi.org/10.1103/PhysRevC.103.025806). URL: <https://link.aps.org/doi/10.1103/PhysRevC.103.025806>.
- Lippuner, Jonas et al. (Aug. 2017). "Signatures of hypermassive neutron star lifetimes on r-process nucleosynthesis in the disc ejecta from neutron star mergers". In: *Monthly Notices of the Royal Astronomical Society* 472.1, 904–918. ISSN: 1365-2966. DOI: [10.1093/mnras/stx1987](https://doi.org/10.1093/mnras/stx1987). URL: <http://dx.doi.org/10.1093/mnras/stx1987>.
- Ljung, G. et al. (Sept. 2006). "New and improved experimental oscillator strengths in Zr II and the solar abundance of zirconium". In: 456.3, pp. 1181–1185. DOI: [10.1051/0004-6361:20065212](https://doi.org/10.1051/0004-6361:20065212).
- Lodders, K., H. Palme, and H. P. Gail (Jan. 2009). "Abundances of the Elements in the Solar System". In: *Landolt B&ouml;rstein* 4B, p. 712. DOI: [10.1007/978-3-540-88055-4\\_34](https://doi.org/10.1007/978-3-540-88055-4_34). arXiv: [0901.1149 \[astro-ph.EP\]](https://arxiv.org/abs/0901.1149).
- Lucatello, Sara et al. (Nov. 2006). "The Frequency of Carbon-enhanced Metal-poor Stars in the Galaxy from the HERES Sample". In: 652.1, pp. L37–L40. DOI: [10.1086/509780](https://doi.org/10.1086/509780). arXiv: [astro-ph/0609730 \[astro-ph\]](https://arxiv.org/abs/astro-ph/0609730).
- Lugaro, Maria et al. (Sept. 2023). "The s Process and Beyond". In: *Annual Review of Nuclear and Particle Science* 73.1, 315–340. ISSN: 1545-4134. DOI: [10.1146/annurev-nucl-102422-080857](https://doi.org/10.1146/annurev-nucl-102422-080857). URL: <http://dx.doi.org/10.1146/annurev-nucl-102422-080857>.
- Matsuno, Tadafumi et al. (May 2022). "High-precision chemical abundances of Galactic building blocks: The distinct chemical abundance sequence of Sequoia". In: *Astronomy and Astrophysics* 661, A103. ISSN: 1432-0746. DOI: [10.1051/0004-6361/202142752](https://doi.org/10.1051/0004-6361/202142752). URL: <http://dx.doi.org/10.1051/0004-6361/202142752>.
- McConnachie, Alan W. and Kim A. Venn (Aug. 2020). "Revised and New Proper Motions for Confirmed and Candidate Milky Way Dwarf Galaxies". In: *The Astronomical Journal* 160.3, p. 124. ISSN: 1538-3881. DOI: [10.3847/1538-3881/aba4ab](https://doi.org/10.3847/1538-3881/aba4ab). URL: <http://dx.doi.org/10.3847/1538-3881/aba4ab>.
- McMillan, Paul J. (Feb. 2017). "The mass distribution and gravitational potential of the Milky Way". In: 465.1, pp. 76–94. DOI: [10.1093/mnras/stw2759](https://doi.org/10.1093/mnras/stw2759). arXiv: [1608.00971 \[astro-ph.GA\]](https://arxiv.org/abs/1608.00971).

- McWilliam, Andrew (Apr. 1998). "Barium Abundances in Extremely Metal-poor Stars". In: 115.4, pp. 1640–1647. DOI: [10.1086/300289](https://doi.org/10.1086/300289).
- Montegriffo, P. et al. (June 2023). "GaiaData Release 3: External calibration of BP/RP low-resolution spectroscopic data". In: *Astronomy and Astrophysics* 674, A3. ISSN: 1432-0746. DOI: [10.1051/0004-6361/202243880](https://doi.org/10.1051/0004-6361/202243880). URL: <http://dx.doi.org/10.1051/0004-6361/202243880>.
- Moster, Benjamin P., Thorsten Naab, and Simon D. M. White (Feb. 2013). "Galactic star formation and accretion histories from matching galaxies to dark matter haloes". In: 428.4, pp. 3121–3138. DOI: [10.1093/mnras/sts261](https://doi.org/10.1093/mnras/sts261). arXiv: [1205.5807](https://arxiv.org/abs/1205.5807) [astro-ph.CO].
- Mucciarelli, A., M. Bellazzini, and D. Massari (Sept. 2021). "Exploiting the Gaia EDR3 photometry to derive stellar temperatures". In: 653, A90, A90. DOI: [10.1051/0004-6361/202140979](https://doi.org/10.1051/0004-6361/202140979). arXiv: [2106.03882](https://arxiv.org/abs/2106.03882) [astro-ph.SR].
- Myeong, G C et al. (July 2019). "Evidence for two early accretion events that built the Milky Way stellar halo". In: *Monthly Notices of the Royal Astronomical Society* 488.1, 1235–1247. ISSN: 1365-2966. DOI: [10.1093/mnras/stz1770](https://doi.org/10.1093/mnras/stz1770). URL: <http://dx.doi.org/10.1093/mnras/stz1770>.
- Navarro, Julio F., Carlos S. Frenk, and Simon D. M. White (May 1996). "The Structure of Cold Dark Matter Halos". In: 462, p. 563. DOI: [10.1086/177173](https://doi.org/10.1086/177173). arXiv: [astro-ph/9508025](https://arxiv.org/abs/astro-ph/9508025) [astro-ph].
- Nishimura, N. et al. (Feb. 2017). "The Intermediate r-process in Core-collapse Supernovae Driven by the Magneto-rotational Instability". In: 836.2, L21, p. L21. DOI: [10.3847/2041-8213/aa5dee](https://doi.org/10.3847/2041-8213/aa5dee). arXiv: [1611.02280](https://arxiv.org/abs/1611.02280) [astro-ph.HE].
- Nishimura, Nobuya, Tomoya Takiwaki, and Friedrich-Karl Thielemann (Sept. 2015). "THE r-PROCESS NUCLEOSYNTHESIS IN THE VARIOUS JET-LIKE EXPLOSIONS OF MAGNETOROTATIONAL CORE-COLLAPSE SUPERNOVAE". In: *The Astrophysical Journal* 810.2, p. 109. ISSN: 1538-4357. DOI: [10.1088/0004-637x/810/2/109](https://doi.org/10.1088/0004-637x/810/2/109). URL: <http://dx.doi.org/10.1088/0004-637x/810/2/109>.
- Pace, Andrew B. and Ting S. Li (Apr. 2019). "Proper Motions of Milky Way Ultrafaint Satellites with Gaia DR2 × DES DR1". In: 875.1, 77, p. 77. DOI: [10.3847/1538-4357/ab0aee](https://doi.org/10.3847/1538-4357/ab0aee). arXiv: [1806.02345](https://arxiv.org/abs/1806.02345) [astro-ph.GA].
- Placco, Vinicius M. et al. (Dec. 2014). "Carbon-enhanced Metal-poor Star Frequencies in the Galaxy: Corrections for the Effect of Evolutionary Status on Carbon Abundances". In: 797.1, 21, p. 21. DOI: [10.1088/0004-637x/797/1/21](https://doi.org/10.1088/0004-637x/797/1/21). arXiv: [1410.2223](https://arxiv.org/abs/1410.2223) [astro-ph.SR].
- Rafelski, Marc et al. (Aug. 2012). "Metallicity Evolution of Damped Ly $\alpha$  Systems Out to  $z \sim 5$ ". In: 755.2, 89, p. 89. DOI: [10.1088/0004-637x/755/2/89](https://doi.org/10.1088/0004-637x/755/2/89). arXiv: [1205.5047](https://arxiv.org/abs/1205.5047) [astro-ph.CO].
- Reggiani, Henrique et al. (Oct. 2020). "The Most Metal-poor Stars in the Inner Bulge". In: 160.4, 173, p. 173. DOI: [10.3847/1538-3881/aba948](https://doi.org/10.3847/1538-3881/aba948). arXiv: [2007.12728](https://arxiv.org/abs/2007.12728) [astro-ph.SR].
- Riello, M. et al. (May 2021). "Gaia Early Data Release 3. Photometric content and validation". In: 649, A3, A3. DOI: [10.1051/0004-6361/202039587](https://doi.org/10.1051/0004-6361/202039587). arXiv: [2012.01916](https://arxiv.org/abs/2012.01916) [astro-ph.IM].
- Rix, Hans-Walter et al. (Dec. 2022). "The Poor Old Heart of the Milky Way". In: 941.1, 45, p. 45. DOI: [10.3847/1538-4357/ac9e01](https://doi.org/10.3847/1538-4357/ac9e01). arXiv: [2209.02722](https://arxiv.org/abs/2209.02722) [astro-ph.GA].
- Roederer, I. U. et al. (Jan. 2023a). "Element abundance patterns in stars indicate fission of nuclei heavier than uranium." In: *Science* 382, pp. 1177–1180. DOI: [10.48550/arXiv.2312.06844](https://doi.org/10.48550/arXiv.2312.06844). arXiv: [2312.06844](https://arxiv.org/abs/2312.06844) [astro-ph.SR].
- Roederer, Ian U., Kohei Hattori, and Monica Valluri (Oct. 2018). "Kinematics of Highly r-process-enhanced Field Stars: Evidence for an Accretion Origin and Detection

- of Several Groups from Disrupted Satellites". In: 156.4, 179, p. 179. DOI: [10.3847/1538-3881/aadd9c](https://doi.org/10.3847/1538-3881/aadd9c). arXiv: [1808.09467](https://arxiv.org/abs/1808.09467) [astro-ph.SR].
- Roederer, Ian U. et al. (2008). "Europium, Samarium, and Neodymium Isotopic Fractions in Metal-Poor Stars". In: *The Astrophysical Journal* 675.1, p. 723. DOI: [10.1086/526452](https://doi.org/10.1086/526452). URL: <https://dx.doi.org/10.1086/526452>.
- Roederer, Ian U. et al. (May 2014). "A SEARCH FOR STARS OF VERY LOW METAL ABUNDANCE. VI. DETAILED ABUNDANCES OF 313 METAL-POOR STARS". In: *The Astronomical Journal* 147.6, p. 136. ISSN: 1538-3881. DOI: [10.1088/0004-6256/147/6/136](https://doi.org/10.1088/0004-6256/147/6/136). URL: <http://dx.doi.org/10.1088/0004-6256/147/6/136>.
- Roederer, Ian U. et al. (Feb. 2016). "DETAILED CHEMICAL ABUNDANCES IN THE r-PROCESS-RICH ULTRA-FAINT DWARF GALAXY RETICULUM 2\*". In: *The Astronomical Journal* 151.3, p. 82. ISSN: 1538-3881. DOI: [10.3847/0004-6256/151/3/82](https://doi.org/10.3847/0004-6256/151/3/82). URL: <http://dx.doi.org/10.3847/0004-6256/151/3/82>.
- Roederer, Ian U. et al. (Sept. 2022). "The R-Process Alliance: Abundance Universality among Some Elements at and between the First and Second R-Process Peaks". In: 936.1, 84, p. 84. DOI: [10.3847/1538-4357/ac85bc](https://doi.org/10.3847/1538-4357/ac85bc). arXiv: [2210.15105](https://arxiv.org/abs/2210.15105) [astro-ph.SR].
- Roederer, Ian U. et al. (Dec. 2023b). "Element abundance patterns in stars indicate fission of nuclei heavier than uranium". In: *arXiv e-prints*, arXiv:2312.06844, arXiv:2312.06844. arXiv: [2312.06844](https://arxiv.org/abs/2312.06844) [astro-ph.SR].
- Sakari, Charli M. et al. (Dec. 2018). "The R-Process Alliance: First Release from the Northern Search for r-process-enhanced Metal-poor Stars in the Galactic Halo". In: 868.2, 110, p. 110. DOI: [10.3847/1538-4357/aae9df](https://doi.org/10.3847/1538-4357/aae9df). arXiv: [1809.09156](https://arxiv.org/abs/1809.09156) [astro-ph.SR].
- Shank, Derek et al. (Jan. 2023). "The R-Process Alliance: Chemodynamically Tagged Groups. II. An Extended Sample of Halo r-process-enhanced Stars". In: 943.1, 23, p. 23. DOI: [10.3847/1538-4357/aca322](https://doi.org/10.3847/1538-4357/aca322). arXiv: [2208.09712](https://arxiv.org/abs/2208.09712) [astro-ph.GA].
- Siegel, Daniel M., Jennifer Barnes, and Brian D. Metzger (May 2019). "Collapsars as a major source of r-process elements". In: *Nature* 569.7755, 241–244. ISSN: 1476-4687. DOI: [10.1038/s41586-019-1136-0](https://doi.org/10.1038/s41586-019-1136-0). URL: <http://dx.doi.org/10.1038/s41586-019-1136-0>.
- Smartt, S. J. et al. (Nov. 2017). "A kilonova as the electromagnetic counterpart to a gravitational-wave source". In: 551.7678, pp. 75–79. DOI: [10.1038/nature24303](https://doi.org/10.1038/nature24303). arXiv: [1710.05841](https://arxiv.org/abs/1710.05841) [astro-ph.HE].
- Snedden, C. and M. Parthasarathy (Apr. 1983). "The r- and s- process nuclei in the early history of the galaxy : HD 122563." In: 267, pp. 757–778. DOI: [10.1086/160913](https://doi.org/10.1086/160913).
- Snedden, Christopher (1973). "PhD thesis". In: *Univ. Texas*.
- Snedden, Christopher, John J. Cowan, and Roberto Gallino (Sept. 2008). "Neutron-Capture Elements in the Early Galaxy". In: *Annual Review of Astronomy and Astrophysics* 46.1, 241–288. ISSN: 1545-4282. DOI: [10.1146/annurev.astro.46.060407.145207](https://doi.org/10.1146/annurev.astro.46.060407.145207). URL: <http://dx.doi.org/10.1146/annurev.astro.46.060407.145207>.
- Snedden, Christopher et al. (May 2009). "New Rare Earth Element Abundance Distributions for the Sun and Five r-Process-Rich Very Metal-Poor Stars". In: 182.1, pp. 80–96. DOI: [10.1088/0067-0049/182/1/80](https://doi.org/10.1088/0067-0049/182/1/80). arXiv: [0903.1623](https://arxiv.org/abs/0903.1623) [astro-ph.SR].
- Sobeck, Jennifer S. et al. (June 2011). "The Abundances of Neutron-capture Species in the Very Metal-poor Globular Cluster M15: A Uniform Analysis of Red Giant Branch and Red Horizontal Branch Stars". In: 141.6, 175, p. 175. DOI: [10.1088/0004-6256/141/6/175](https://doi.org/10.1088/0004-6256/141/6/175). arXiv: [1103.1008](https://arxiv.org/abs/1103.1008) [astro-ph.SR].
- Starkenburger, Else et al. (2017). "The Pristine survey – I. Mining the Galaxy for the most metal-poor stars". In: *Monthly Notices of the Royal Astronomical Society* 471.3,

- 2587–2604. ISSN: 1365-2966. DOI: [10.1093/mnras/stx1068](https://doi.org/10.1093/mnras/stx1068). URL: <http://dx.doi.org/10.1093/mnras/stx1068>.
- Steinmetz, M. et al. (Oct. 2006). “The Radial Velocity Experiment (RAVE): First Data Release”. In: 132.4, pp. 1645–1668. DOI: [10.1086/506564](https://doi.org/10.1086/506564). arXiv: [astro-ph/0606211](https://arxiv.org/abs/astro-ph/0606211) [astro-ph].
- Travaglio, Claudia et al. (Feb. 2004). “Galactic Evolution of Sr, Y, And Zr: A Multiplicity of Nucleosynthetic Processes”. In: 601.2, pp. 864–884. DOI: [10.1086/380507](https://doi.org/10.1086/380507). arXiv: [astro-ph/0310189](https://arxiv.org/abs/astro-ph/0310189) [astro-ph].
- Trypsteen, Marc F. M. and Richard Walker (2017). “Analysis of the Spectra”. In: *Spectroscopy for Amateur Astronomers: Recording, Processing, Analysis and Interpretation*. Cambridge University Press, 76–84.
- Tumlinson, Jason (Dec. 2009). “CHEMICAL EVOLUTION IN HIERARCHICAL MODELS OF COSMIC STRUCTURE. II. THE FORMATION OF THE MILKY WAY STELLAR HALO AND THE DISTRIBUTION OF THE OLDEST STARS”. In: *The Astrophysical Journal* 708.2, 1398–1418. ISSN: 1538-4357. DOI: [10.1088/0004-637x/708/2/1398](https://doi.org/10.1088/0004-637x/708/2/1398). URL: <http://dx.doi.org/10.1088/0004-637x/708/2/1398>.
- Valentini, M. et al. (July 2019). “Masses and ages for metal-poor stars: A pilot programme combining asteroseismology and high-resolution spectroscopic follow-up of RAVE halo stars”. In: *Astronomy and Astrophysics* 627, A173. ISSN: 1432-0746. DOI: [10.1051/0004-6361/201834081](https://doi.org/10.1051/0004-6361/201834081). URL: <http://dx.doi.org/10.1051/0004-6361/201834081>.
- Vangioni-Flam, Elisabeth and Michel Cassé (1999). In: *Astrophysics and Space Science* 265.1/4, 77–86. ISSN: 0004-640X. DOI: [10.1023/a:1002197712862](https://doi.org/10.1023/a:1002197712862). URL: <http://dx.doi.org/10.1023/A:1002197712862>.
- Vassh, Nicole et al. (June 2020). “Coproduction of Light and Heavy r-process Elements via Fission Deposition”. In: 896.1, 28, p. 28. DOI: [10.3847/1538-4357/ab91a9](https://doi.org/10.3847/1538-4357/ab91a9). arXiv: [1911.07766](https://arxiv.org/abs/1911.07766) [astro-ph.HE].
- Wickliffe, M. E., J. E. Lawler, and G. Nave (Aug. 2000). “Atomic transition probabilities for Dy I and Dy II”. In: 66, pp. 363–404. DOI: [10.1016/S0022-4073\(99\)00173-9](https://doi.org/10.1016/S0022-4073(99)00173-9).
- Wolf, Christian et al. (Feb. 2018). “SkyMapper Southern Survey: First Data Release (DR1)”. In: 35, e010, e010. DOI: [10.1017/pasa.2018.5](https://doi.org/10.1017/pasa.2018.5). arXiv: [1801.07834](https://arxiv.org/abs/1801.07834) [astro-ph.IM].
- Wu, Meng-Ru et al. (Aug. 2016). “Production of the entire range of r-process nuclides by black hole accretion disc outflows from neutron star mergers”. In: *Monthly Notices of the Royal Astronomical Society* 463.3, 2323–2334. ISSN: 1365-2966. DOI: [10.1093/mnras/stw2156](https://doi.org/10.1093/mnras/stw2156). URL: <http://dx.doi.org/10.1093/mnras/stw2156>.
- Yong, David et al. (Jan. 2013). “The Most Metal-poor Stars. II. Chemical Abundances of 190 Metal-poor Stars Including 10 New Stars with  $[Fe/H] \leq -3.5$ ”. In: 762.1, 26, p. 26. DOI: [10.1088/0004-637x/762/1/26](https://doi.org/10.1088/0004-637x/762/1/26). arXiv: [1208.3003](https://arxiv.org/abs/1208.3003) [astro-ph.GA].
- Zhao, Gang (2005). “Search for Metal-poor Stars with LAMOST”. In: *AIP Conference Proceedings*. AIP. DOI: [10.1063/1.1893348](https://doi.org/10.1063/1.1893348). URL: <http://dx.doi.org/10.1063/1.1893348>.



## *Acknowledgements*

First I would like to thank my supervisor N. Christlieb for giving me the opportunity and scientific guidance to conduct this research, for giving me ample freedom to develop and pursue my own ideas, and for encouraging new collaborations. Then, I would like to thank K. Lind for bridge funding and the opportunity to participate in work done for WEAVE. Further, I would like to thank T. T. Hansen for teaching me all about spectra and abundance analysis, for sharing her enthusiasm and interest on the  $r$ -process, and for always being prepared to answer any question and help me in any way. Further, I also want to thank the HGSFP for financial support at the final stage of my PhD.

Furthermore, I would like to thank T. Nordlander for fruitful discussions and collaborations, for the detailed answers to any questions that I had. Then, I would like to thank Saskia Hekker for kindly agreeing to referee my thesis, and Ralf Klessen and Mario Tieloff for being part of my thesis committee. I would also like to thank H. G. Ludwig for always being prepared to engage in scientific discussions with me.

I want to thank my friend Sepideh Sadegi for her friendship and discussions during times of joy and need. I would also like to thank my office mate Chiara Battistini for making warm human interaction in the desolate office possible. I further want to thank the LSW PhD-student community for being so friendly and welcoming.

At last, I would like to thank my mother for her continuous support and devotion. I would have not been able to write the final chapters of this thesis without her support. I would also like to thank my sister Anna for being who she is; like-minded and supportive. Moreover, I want to thank in general my family and friends for being there for me and supporting me, everyone in their own way. Further, I would like to thank my husband Boris for hanging in there and understanding my prolonged preoccupation with this research. Finally, I want to thank my son Iων for granting me insight into the meaningful and the meaningless, and ultimately easing the route towards the completion of this PhD.



## Declaration of Authorship

I, Theodora XYLAKIS-DORNBUSCH, declare that this thesis titled, “Investigation of the Galactic chemical enrichment history with searches for and chemical abundance analysis of metal-poor stars” and the work presented in it are my own. I confirm that:

- This work was done wholly or mainly while in candidature for a research degree at this University.
- Where any part of this thesis has previously been submitted for a degree or any other qualification at this University or any other institution, this has been clearly stated.
- Where I have consulted the published work of others, this is always clearly attributed.
- Where I have quoted from the work of others, the source is always given. With the exception of such quotations, this thesis is entirely my own work.
- I have acknowledged all main sources of help.
- Where the thesis is based on work done by myself jointly with others, I have made clear exactly what was done by others and what I have contributed myself.

Signed:

---

Date:

---